Modelling of a Packed-Bed Methanol Steam Reformer for HT-PEM Fuel Cell Applications

Zhu, Jimin

DOI (link to publication from Publisher):
10.54337/aau513444640

Publication date:
2022

Document Version
Publisher's PDF, also known as Version of record

MODELLING OF A PACKED-BED METHANOL STEAM REFORMER FOR HT-PEM FUEL CELL APPLICATIONS

BY
JIMIN ZHU

DISSERTATION SUBMITTED 2022

AALBORG UNIVERSITY
DENMARK

MODELLING OF A PACKED-BED METHANOL STEAM REFORMER FOR HT-PEM FUEL CELL APPLICATIONS

AALBORG UNIVERSITY
DENMARK

Ph.D. Dissertation

Jimin Zhu

Dissertation submitted April, 2022

Dissertation submitted: April 2022

PhD supervisors: Assoc. Prof. Samuel Simon Araya
Aalborg University

Prof. Søren Knudsen Kær
Aalborg University

PhD committee: Associate Professor Thomas Helmer Pedersen
Aalborg University, Denmark

Professor Brant A. Peppley
Queen's University, Canada

Professor Qingfeng Li
Technical University of Denmark, Denmark

PhD Series: Faculty of Engineering and Science, Aalborg University

Department: AAU Energy

ISSN (online): 2446-1636
ISBN (online): 978-87-7573-914-1

Published by:
Aalborg University Press
Kroghstræde 3
DK – 9220 Aalborg Ø
Phone: +45 99407140
aauf@forlag.aau.dk
forlag.aau.dk

Printed in Denmark by Stibo Complete, 2022

CURRICULUM VITAE

Jimin Zhu

PhD student - Aalborg University, Department of Energy Technology

e-mail: jzu@energy.aau.dk

tel: +45 9356 2443

Education

- November 2017 – October 2021, Aalborg University, Denmark
  PhD student at the AAU Energy, Aalborg University

- September 2014 – June 2017, Shandong University, China
  Master of Science (M.Sc.), Control Engineering

- September 2010 – June 2014, Shandong University, China
  Bachelor of Science (B.Sc.), Material Shaping & Control Engineering

LIST OF PUBLICATIONS

The following papers provide the foundation for the main body of this dissertation:

[A] Jimin Zhu, Samuel Simon Araya, Xiaoti Cui, Simon Lennart Sahlin, and Søren Knudsen Kær. "Modeling and Design of a Multi-Tubular Packed-Bed Reactor for Methanol Steam Reforming over a Cu/ZnO/Al2O3 Catalyst." published in Energies 13, no. 3 (2020): 610.

[B] Jimin Zhu, Samuel Simon Araya, Xiaoti Cui, and Søren Knudsen Kær. "The role of effectiveness factor on the modeling of methanol steam reforming over CuO/ZnO/Al2O3 catalyst in a multi-tubular reactor." International Journal of Hydrogen Energy (2022).

[C] Jimin Zhu, Xiaoti Cui, Samuel Simon Araya. "Comparison between 1D and 2D numerical models of a multi-tubular packed-bed reactor for methanol steam reforming." Submitted to International Journal of Hydrogen Energy February 2022. Status: Under Review.

This dissertation based on the above listed scientific papers has been submitted for assessment in partial fulfilment of the PhD degree. The main papers are included directly or indirectly in the extension summary of the dissertation which the readers are referred to for more details. As part of the assessment, co-author statements have been made available to the assessment committee and are also available at the faculty.

In addition to the main papers, the following paper has also been published during the PhD period, however, is not presented in this dissertation:

[1] Samuel Simon Araya, Vincenzo Liso, Xiaoti Cui, Na Li, Jimin Zhu, Simon Lennart Sahlin, Søren Højgaard Jensen, Mads Pagh Nielsen, and Søren Knudsen Kær. "A review of the methanol economy: the fuel cell route." published in *Energies* 13, no. 3 (2020): 596.

Additionally, the following conference poster has been conducted during the PhD period:

- Jimin Zhu, Samuel Simon Araya, Simon Lennart Sahlin, Thomas Egsgaard Pedersen, Xiaoti Cui, and Søren Knudsen Kær. "Modeling and experimental characterization of a methanol steam reformer for a high temperature polymer electrolyte membrane (HT-PEM) fuel cell system." In 6th CARISMA International Conference on Medium and High Temperature Proton Exchange Membrane Fuel Cells. 2019.

ENGLISH SUMMARY

Fuel cells, especially the high temperature polymer electrolyte membrane (HT-PEM) fuel cell, are attracting more attention in backup power, transportation and stationary applications. The HT-PEM fuel cells convert hydrogen directly into electricity, making it possible to have a higher efficiency than conventional generators. Nevertheless, technical problems in hydrogen storage and transportation are still the essential obstacles to the widespread adoption of hydrogen powered fuel cell systems. As an alternative method, the methanol steam reforming (MSR) process has been considered promising for the in-situ hydrogen generation in HT-PEM fuel cell systems.

The hydrogen-rich gas produced in-situ by the MSR process has a significant impact on the performance and durability of the HT-PEM fuel cell stack. Hence, the performance of the reformer should be studied. Special attentions should be paid to the contents of carbon monoxide and methanol in the reformate. The experiments for the reformer provide us the direct and concise results of the system. However, it can be costly and time-consuming, especially when multiple variables should be tested. The tested results could also be affected by certain objective factors such as unnoticed catalyst deactivation, errors in measuring devices (e.g., incorrect fitting of the measuring scale), and inappropriate research design. The mathematical modelling of packed bed reactors allows a deep insight into the chemical reactions and transport processes in the reactor.

A multi-tubular packed-bed MSR reformer for hydrogen production is designed to be integrated with a 5 kW HT-PEM fuel cell stack in this study. A co-current stream of burner gas passes by the shell side of the reformer acting as an external heat source for the catalyst bed. Simultaneously, the reactants flow through the tubular packed-bed reactor with MSR reactions occurring on the commercial $CuO/ZnO/Al_2O_3$ based catalyst. As the reactants flow through the packed bed, complex physical and chemical phenomena at different scales occur in the reactor. Several assumptions are made to simplify the modeling of packed bed reactors.

The one-dimensional pseudo-homogeneous model considers the reforming reactions and the axial transfer phenomena in the reactor. Since no mixing in the axial direction and complete mixing in the radial direction are assumed, this model is referred as an ideal plug-flow model. The effectiveness factor in this model is calculated as a function of the Thiele modulus. The pressure drop in the axial direction through the catalyst bed is also considered, though it generally does not significantly affect the overall reformer performance. Hence, based on the one-dimensional model, the effect of operating parameters such as the steam to carbon ratio (S/C), the contact time (W_{cat}/F_{CH_3OH}) and the inlet temperature of burner gas can be investigated. According to the simulation results of the one-dimensional model, the increase in the inlet

temperature of burner gas and W_{cat}/F_{CH_3OH} is observed to improve the methanol conversion of the reformer. Simultaneously, the CO concentration in the reformate gas is also increased due to the enhanced temperature in the catalyst bed. Additionally, a higher S/C value leads to a lower methanol conversion due to the increased heat consumption for evaporating and heating the additional steam. This will also reduce the amount of CO in the MSR process.

The one-dimensional pseudo-homogeneous model can be extended to a two-dimensional pseudo-homogeneous model by additionally considering the radial gradients of temperature and concentrations in the reactor tube. For a tubular reactor with rather non-uniformly distributed temperature and concentration in the radial direction, this two-dimensional model can make more accurate predictions of the reformer performance. Moreover, the two-dimensional model can be used to estimate the hot-spot temperature and the local catalyst deactivation when the reactor operates at relatively high temperature. Nevertheless, it requires slightly more computation time than the one-dimensional model. According to the simulated temperature distributions in the catalyst bed, the lowest temperature appears at the centre of the reactor tube, and the hot spot is generally formed at the location about 3 cm from the reactor entrance near the tube wall. The increase in the inlet temperature of the burner gas significantly enhances the hot spot temperature of the catalyst bed. In addition, the tube diameter is found to be the most important factor that affects the difference of the simulation results between the one-dimensional model and the two-dimensional model. Besides, this difference between these two models becomes less noticeable when the methanol conversion of the reformer is approaching 100%.

Due to the porous structure of the catalyst, not all the catalytically active surface are exposed to the bulk conditions. Therefore, the reaction-diffusion process within a catalyst particle is modelled considering the interphase and intraparticle transfer resistances. Therefore, the effectiveness factor can be calculated by solving the intraparticle mass and energy balance equations. This method provides an insight into the interaction between the intrinsic kinetics and the heat and mass transport characteristics of the porous catalyst pellet. According to the simulation results in the particle scale, the interphase and intraparticle heat and mass transfer resistances are enhanced with the increasing bulk fluid temperature and the catalyst diameter. Therefore, at the inlet conditions of the reactor, it can be observed that the effectiveness factors for the MSR and MD reactions decrease with the increasing burner temperature and particle diameter. Another method used to estimate the effectiveness factor in this study is by regarding the effectiveness factor as a function of the Thiele modulus. This Thiele modulus-effectiveness factor method requires shorter computation time but is less accurate for the calculation of effectiveness factors.

DANSK RESUMÉ

Brændselsceller, især brændselscellen med høj temperatur polymer elektrolytmembran (HT-PEM), tiltrækker sig mere opmærksomhed inden for backup power, transport og stationære applikationer. HT-PEM brændselscellen omdanner brint direkte til elektricitet, hvilket gør det muligt at have en højere effektivitet end konventionelle generatorer. Ikke desto mindre er tekniske problemer inden for brintlagring og -transport væsentlige forhindringer der skal overvindes. Som en alternativ metode anses methanol steam reforming (MSR) processen for lovende for in-situ brintgenerering i HT-PEM brændselscellesystemer.

Ydeevne og holdbarhed af højtemperatur polymer elektrolytmembran (HT-PEM) brændselscellestak er stærkt påvirket af den hydrogenrige gas, der produceres in-situ ved methanol dampreformering (MSR) processen. Derfor bør reformerens ydeevne studeres. Der skal lægges særlig vægt på indholdet af carbonmonoxid og metanol i reformatet. Forsøgene med reformeren kan give os direkte og præcise resultater af hele systemet. Det kan dog være dyrt og tidskrævende, især når flere variabler skal testes. De testede resultater kan også blive påvirket af visse objektive faktorer, såsom uforudset deaktivering af katalysator, fejlagtige målinger eller uhensigtsmæssige målemetoder (f.eks. unøjagtige termoelementer og flowmåleanordninger) og fejl i forskningsdesignet. Den matematiske modellering af reaktorer med packed-bed design kan give et dybdegående indblik i de kemiske reaktioner og transportprocesser i reaktoren.

MSR-reaktoren af typen shell-and-tube, til brug i forbindelse med hydrogen produktion, er designet til at blive integreret med en 5 kW HT-PEM-brændselscellestak. En medløbende strøm af brændergas passerer gennem siden af reformeren og fungerer som en ekstern varmekilde for reformeren. Samtidig strømmer reaktanterne gennem den rørformede reaktor af packed-bed design med MSR-reaktioner, der foregår på den kommercielle CuO / ZnO / Al_2O_3 baserede katalysator. Når reaktanterne strømmer gennem denne packed-bed reaktor, opstår komplekse fysiske og kemiske fænomener i forskellige skalaer. Derfor antages der flere forudsætninger for at forenkle modelleringen af reaktorer med packed-bed.

Den en-dimensionelle pseudo-homogene model betragter reformeringsreaktionerne kun i reaktorens aksiale retning. Siden der ikke antages blanding i den axiale retning og fuldstændig blanding i den radiale retning er det antaget af modellen er en ideel plug-flow model. Effektivitetsfaktoren i denne model er beregnet som funktion af Thiele modulus. Trykfaldet i den aksiale retning gennem katalysatoren er taget i betragtning, men det antages at det ikke påvirker den samlede reformer ydelse i væsentlig grad. Baseret på den en-dimensionelle model kan virkningen af driftsparametre som damp til kulstof-forholdet (S/C), kontakttiden (W_{cat}/F_{CH_3OH}) og indgangstemperaturen for brændergas derfor undersøges. Ifølge disse

simuleringsresultater fra denne en-dimensionelle model er en forøgelse af indgangstemperaturen af brændergas og forholdet W_{cat}/F_{CH_3OH} observeret for at forbedre konverteringen af metanol i reformeren. Samtidig er CO koncentrationen i reformeren også forøget på grund af den højere temperatur af katalysten. Derudover vil et højere S/C forhold resultere i en lavere konvertering af metanol på grund af det højere varme forbrug i forbindelse med fordampning og opvarming af damp. Dette vil også nedbringe mængden af CO i MSR processen.

Den en-dimensionelle pseudo-homogene model kan udvides til en to-dimensionel pseudo-homogen model ved at overveje de radiale gradienter af temperatur og koncentrationer i reaktorrøret. For en rørreaktor med umiddelbar uensartede temperatur- og koncentrationsfordelinger i radial retning, kan denne todimensionelle model simulere mere nøjagtige forudsigelser af reformerens ydeevne. Desuden kan den todimensionelle model bruges til at forudsige hot-spot-temperatur og lokal deaktivering katalysator, når reaktoren arbejder ved relativt høj temperatur. Ikke desto mindre kræver det en anelse mere beregningstid end den endimensionelle model.

Ifølge den simulerede temperaturfordeling i katalysten er den laveste temperatur observeret i centeret af reaktor røret og den højeste temperatur er generelt omkring 3cm fra toppen, langs væggen af reaktor røret. En forøgning af temperaturen ved inlet vil også forøge dannelsen af hotspots i reaktoren. Derudover er det konkluderet at diameteren af reaktor-røret har en særdeles stor indvirkning på forskellen mellem den en-dimensionelle og to-dimensionelle model. Forskellen på disse to modeller er mindre mærkbar når konverteringen af metanol nærmer sig 100%.

På grund af katalysatorens porøse struktur er ikke hele den katalytisk aktive overflade der er udsat for bulkbetingelserne. Derfor modelleres reaktionsdiffusionsprocessen i katalysatorpartikelen under hensyntagen til interfase-og intrapartikeloverførselsmodstanden. Denne metode giver et indblik i samspillet mellem kinetik og varme/massetransport for den porøse katalysatorpellet. Simuleringsresultaterne viser på partilel skala at interfacet og intrapartikel varme og masse transport modstande er forbedret med forøgning af bulk fluid temperatur og katalyst partikel diameter. Derfor kan det observeres, ved området omkring inlet af reaktoren, at effektivitetsfaktore for MSR og MD reaktionerne bliver sænket under højere brændertemperatur og partikel diameter. En anden metode til at estimere effektivitetsfaktoren er ved at betragte den som en funktion af Thiele-modulet. Denne Thiele-modulus-effektivitetsfaktormetode kræver kortere beregningstid, men er mindre nøjagtig til beregning af effektivitetsfaktorer.

ACKNOWLEDGEMENTS

Finally, I can see the end of my PhD study, after 4 years hard-working and struggling. It has been a special journey in my life, full of ups and downs, laughs and tears. Now I think it is time to show appreciation to people who helped and supported me in the last 4 years, without whom I would never have finished my PhD thesis.

Søren Knudsen Kær and Samuel Simon Araya are my supervisors. You provided me the chance to participate in this fabulous research project as a PhD student in Aalborg University and gave me the guidance and freedom all the way through my PhD study. Also thank you for all the support and encouragement you have given me. Your kindness and positivity encouraged me and inspired me to take responsibility for my career and well-being. Likewise, I would like to thank Simon Lennart Sahlin and Xiaoti Cui who gave me lots of valuable suggestion and feedback on my modelling and simulation results.

Thanks also go to other colleagues and friends in AAU Energy, especially Vincenzo Liso, Mads Pagh Nielsen, Na Li and Diogo Loureiro Martinho. I would never forget the courage and kindly help you gave me when I was upset, and the wonderful times we spent together discussing and sharing ideas. Life gets much better with you guys.

A big thank you to Søren Juhl Andreasen and Advent Technologies A/S (formerly SerEnergy A/S) for hosting me and providing reformers tested in this work. The valuable discussion with you and technical supporting for the reformer test setup are vital to my experimental work.

Besides, I would like to acknowledge the financial supports provided by China Scholarship Council (CSC).

The most special thank you to my husband who is my warmest sunshine, to my parents who give me their sweetest love, and to my marvellous friends who are so lovely and supportive. I feel so grateful and lucky to have you in my life.

Jimin Zhu

Aalborg University, March 2022

TABLE OF CONTENTS

CHAPTER 1. INTRODUCTION

1.1. ENERGY AND ENVIRONMENTAL OUTLOOK

Fossil fuels, such as petroleum, coal, and natural gas, have played a significant role in the modern world since the industrial revolution and allowed unprecedented growth in agriculture, transportation, and industrial processes. Consequently, fossil fuels still dominate today's global energy system, providing more than 80% of global energy consumption [1]. Figure 1.1 shows the increasing global energy consumption from 1965 to 2020 with fossil fuels consistently accounting for a large portion. As seen from the report of the Energy Transitions Commission (ETC), fossil fuels will still provide 60% of energy in 2040 [2]. Furthermore, according to the International Energy Outlook 2021 (IEO2021), worldwide energy consumption would increase by approximately 50% over the next 30 years even if current policy and technology trends continue [3]. The increasing demand of energy and the overdependence on fossil fuels have become critical challenges, bringing energy and economic security threats. The European Union (EU) heavily depends on Russian energy imports, with around 45% of gas imports, 27% of crude oil imports, and 46% of hard coal imports come from Russian [4]. Russia's invasion of Ukraine in 2022 has exacerbated the security of the energy supply situation and driven up energy prices dramatically. Consequently, the European Commission announced a plan called REPowerEU which aims to reduce the dependence on Russian fossil fuels and accelerate the energy transition for more “affordable, secure, and sustainable energy” [5].

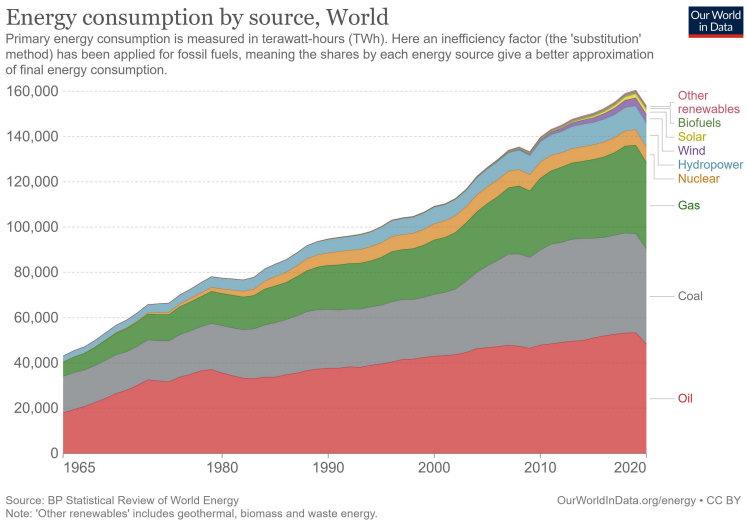

Figure 1.1 Global energy consumption by source from 1965 to 2020 [6]

Fossil fuels contribute to several environmental issues, including air pollution and global warming. Primary air pollutants, such as fine particulate matter (PM), nitrogen oxides (NO_x), sulphur oxides (SO_x), and carbon monoxide (CO), are emitted directly from the combustion of fossil fuels. Research shows that a variety of health problems are associated with short-term and long-term exposure to these air pollutants [7,8]. As a result, the problem of air pollution is viewed as a severe threat to global public health. Furthermore, carbon dioxide (CO2) is the most important human-produced greenhouse gas released from the burning of fossil fuels. Studies show that global CO_2 emission from fossil fuels has increased by 480% since 1950 and primarily driven global climate change [8]. The acceleration of climate change has, directly and indirectly, led to glacier retreat, sea-level rise, infectious diseases, food shortages, and more frequent and intense extreme weather events (floods, heat waves, droughts, and storms). Therefore, a drastic reduction in fossil fuel use is needed to reverse years of out-of-control CO_2 emission.

Greenhouse gas reduction has become a vital agenda for the international community, bringing global academic researchers, technology professionals, policymakers, and other related practitioners working together to create new possibilities for delivering the emissions reductions. The 2015 Paris Agreement established a long-term goal aims to keep the global temperature rise well below 2°C in this century and pursue efforts to limit the temperature increase even further to 1.5°C [9]. To meet the 1.5°C carbon budget, two points have been proposed: (1) leave fossil fuels in the ground; (2) apply carbon capture and storage (CCS) technologies [10]. Leaving most global fossil fuel reserves to remain “in the ground” is widely accepted as a direct approach to limit extra CO_2 from emitting into the atmosphere. It has been estimated that nearly 60% of oil and fossil methane gas and 90% of coal reserves must remain unextracted by 2050 to meet the 1.5°C target [11]. As a political strategy, it will in turn eliminate the reliance on fossil fuels, enhance the energy efficiency in end-use sectors, and promote the development of cost-effective, sustainable, and pollution-free energy sources such as wind, solar, biomass, hydro and nuclear energy [12]. The CCS technologies also play a critical role in facilitating the net removal of CO_2 from the atmosphere and compensating for some carbon emissions [13]. The captured CO_2 can be converted into fuels such as methane and methanol through biological and chemical conversion. As a result, the produced CO_2-based fuels offer a solution to raise the proportion of renewable energy in the power systems [13,14].

An increase in clean energy investments is required for massive clean energy deployments and net zero emissions by 2050. As shown in Figure 1.2, the estimated market size for clean technologies such as wind turbines, solar panels, lithium-ion batteries, electrolysers, and fuel cells will gradually grow by 2050 [1]. Though fuel cells only share a small amount in the global market, they play a crucial role in the carbon neutral future. A fuel cell is an electrochemical device that converts chemical energy into electricity. Compared to conventional technologies such as internal combustion engines (ICEs) and gas turbines, it offers advantages such as high

electrical efficiency, low pollutant emission, low noise, better fuel flexibility and modularity [15]. Fuel cells can be utilized as an uninterruptible power supply or a time-shifted electricity generation in remote off-grid systems, typically consisting of wind turbines and photovoltaic panels [16]. In addition, fuel cells are used in various transportation applications, especially heavy-duty vehicles (trucks, buses, trains, and marine applications), as a path towards de-carbonization. Compared to battery electric vehicles (BEVs), hydrogen fuel cell vehicles (HFCVs) show advantages in terms of a more extended cruising range, a shorter refuelling time, a high specific energy, and no heavy battery on board [17,18]. Fuel cells also play an essential role in the Power-to-X (PtX) solutions to cut CO_2 substantially. The rapid growth in PtX technologies makes it possible to convert the excess renewable electricity into carbon-neutral fuels, which can be stored and transported for end-use [19]. Instead of being blended into the national gas grids, the produced H_2 and H_2-based substances can be used (directly or after in-situ reforming) in fuel cell-powered applications for re-electrification (regarded as power-to-fuel-to-power pathway).

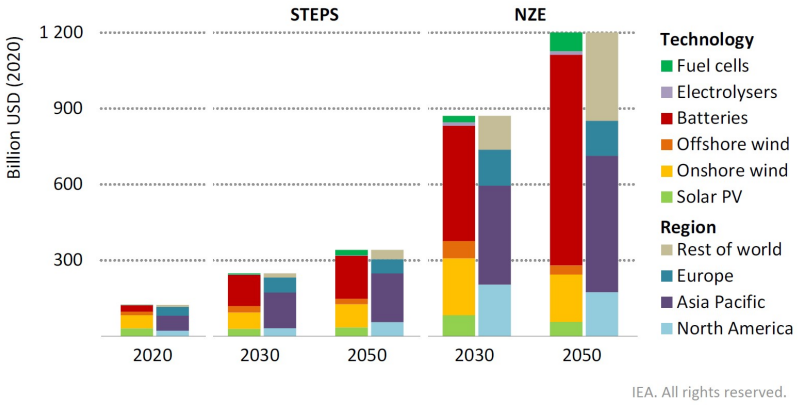

Figure 1.2 Estimated market size for certain clean energy technologies, 2020-2050 [1] *[1]*

1.2. FUEL CELLS

As a type of high efficiency and zero-emission device, hydrogen fuel cell has the potential to be used in both stationary and automotive applications. Although Sir William Robert Grove proposed the first concept of fuel cell in 1893, the first operational fuel cell did not appear until the 1950s. During the early 1960s, NASA put a lot of effort into fuel cell technologies used in space vehicles, bringing the technology to a level that is currently feasible for the private sector [20]. Stationary fuel cell systems can be used as primary power, grid-connected, or off-grid backup power to provide uninterrupted power supplies for critical infrastructure and commercial, industrial, and residential buildings. Because fuel cells have the

[1] *Net Zero Emissions by 2050 Scenario (NZE), Stated Policies Scenario (STEPS)*

advantage of providing a continuous and reliable power supply, they can be added to hybrid systems, which consist of intermittent renewable energy sources (such as wind turbines or photovoltaics) as primary power, to generate power when such energy sources cannot meet the demand. Compared with combustion engines, fuel cell stacks do not consist of any moving parts, allowing a silent operation [21]. There is a well-known fact that fuel cells can escape the Carnot-cycle limitation. Unlike other ICEs, which convert chemical energy into thermal energy and then into mechanical energy, hydrogen fuel cells can directly and effectively convert chemical energy in hydrogen into electrical energy. Therefore, hydrogen and fuel cell technologies provide a critical benefit of higher energy efficiency than a comparably sized ICE. In addition, fuel cell systems using hydrogen sources can eliminate greenhouse gas emissions and air pollution. Fuel cell applications include shipping, aviation, and heavy-duty transportation, which are superior to batteries in many ways, have also gained much attention. Compared with batteries, hydrogen fuel cells have the advantages such as high energy density, durability, shorter re-fuelling time, and can operate as long as the fuel is supplied [22]. In automobiles, fuel cells are normally connected with the propulsion motor in four different ways: fuel cell provides all the power with battery for start-up, fuel cell provides the baseload while the battery provides peak power, fuel cell recharges the battery and the battery provides all the power, fuel cell serves only as an auxiliary power unit [23]. The attempt to develop, produce and bring fuel cell systems into the market started in the 1990s. There are already several FCEV models in and out of production, such as Hyundai ix35 FCEV, Toyota Mirai, Honda FCX Clarity, etc. However, the main obstacles of the commercialization of fuel cell automobiles are still the cost of fuel cells and the costs and availability of hydrogen supply. The market requirements of both automotive and stationary fuel cell systems are shown in Table 1.1 [24].

Requirement	**Automotive**	**Stationary**	
		Primary power	**Backup power**
Power output	50 – 100 kW	1 – 10 kW & 200 kW	1 – 10 kW
Fuel	Hydrogen	Reformate	Hydrogen
Lifetime (operational)	5000 hrs	> 40,000 hrs	< 2000 hrs
High efficiency	Critical	Critical	Not critical
Instant start	Very important	Not important	Very important
Output mode	Highly variable	Variable	~ Constant

Requirement	Automotive	Stationary	
		Primary power	Backup power
Operation	Intermittent	Constant	Intermittent
Preferred voltage	> 300 V	110/220 VAC	24 or 48 VDC or 110/220 VAC
Heat recovery	Not needed	Very important	Not needed
Water balance	Very important	Very important	Not critical
Size and weight	Critical	Not critical	Not critical
Cost	< $50/kW	< $1000/kW	< $5000/kW

Table 1.1 Market requirements of automotive and stationary fuel cell systems [24]

Fuel cells can be divided into several types based on the kind of reactant, electrolyte material, and temperature range of operation [21]. Table 1.2 summarizes the key characteristics, as well as the benefits and drawbacks, of the most prevalent fuel cell types on the market or in development [20,25]. Proton exchange membrane (PEM) fuel cells are among the most promising choices because of has high power density and quick start-up [26]. In a PEM fuel cell, hydrogen and oxygen flow, respectively, to two sides of a polymer electrolyte membrane coated with platinum-based electrode layers. Protons migrate through the membrane from the anode side. At the same time, electrons flow through an external load to generate current. The protons then react with electrons and oxygen on the cathode side to form water and heat [27].

The proton exchange membranes of conventional low-temperature proton exchange membrane (LT-PEM) fuel cells are made of perfluoro sulphonic acid (PFSA) polymers. However, this kind of material can only function in the highly hydrated state, while limiting the operating temperature of the fuel cell up to 80 °C at ambient pressure [28]. As a result of the low operating temperature, LT-PEM fuel cell technologies face a number of challenges. PEM fuel cells need to be fed with high-purity hydrogen, since the anode Pt-based catalyst is tolerant of less than 10 ppm of CO. Hence, external fuel processors, such as CO removers, are usually associated with LT-PEM fuel cells because of the high requirement for hydrogen purity, which increases the complexity and costs of the systems. Water management is critical to the efficiency and durability of LT-PEM fuel cells. To maintain an equilibrium, the balance of water production and removal must be maintained. Proper thermal management of a fuel cell stack is also important for ensuing that fuel cells operate

within the specified temperature range. Moreover, the heat of LT-PEM fuel cells is considered as low-grade heat.

The high temperature proton exchange membrane (HT-PEM) fuel cell operating at a temperature range from 160 to 220 °C has been regarded as a promising option to solve these challenges due to high operating temperature. The advantages of working at a higher temperature are as follows: increased tolerance of fuel impurities (especially CO), easier or even no water management, easier thermal management, and higher grade of waste heat [29]. The reactions and structure of a HT-PEM fuel cell can be seen in Figure 1.3.

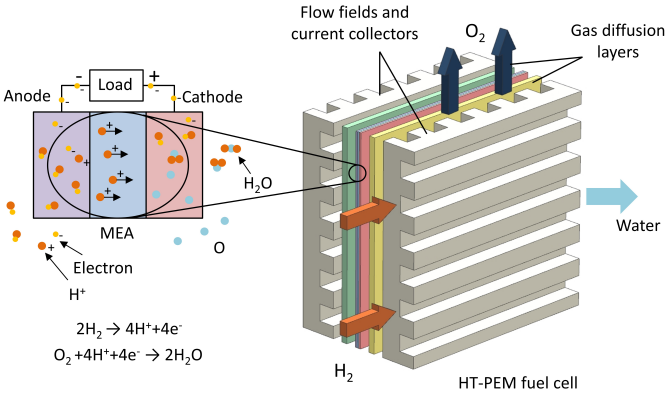

Figure 1.3 HT-PEM fuel cell structure

Because of its exceptional qualities and recent advancements in technology and manufacturing, hydrogen is gaining unprecedented popularity in decarbonization projects and sustainable energy systems. The hydrogen supply chain is depicted in Figure 1.4, from hydrogen production to end-user [30]. Hydrogen is the most prevalent element in the universe and is non-toxic. Whether used in ICEs or fed into fuel cell systems, it is a clean fuel that emits only water. It can be produced from a variety of sources including natural gas (by steam reforming, pyrolysis, plasma reforming), coal or oil (by gasification, partial oxidation), solar energy (by electrolysis, photolytic splitting of water, thermal splitting of water), wind or hydro or wave (by electrolysis of water), fission or fusion (by electrolysis of water, thermal splitting of water), biomass (by fermentation, gasification, pyrolysis) [31–33]. In addition, hydrogen gas has a high energy density by weight (~ 120 MJ/kg), which is three times higher than gasoline's (~ 44 MJ/kg) [34]. Hydrogen as a zero-carbon energy carrier that can be stored and transported, making it a means of storage for renewable electricity. Because the production of hydrogen from some renewable resources is intermittent and location dependent, the storage and transportation of hydrogen are significantly important.

Fuel cell type	Fuel	Catalyst	Electrolyte	Operation temperature (°C)	Specific advantages	Specific disadvantages
Low-temperature proton exchange membrane fuel cells (LT-PEMFCs)	Hydrogen	Platinum supported on carbon	Solid polymer membrane (Nafion)	$60-80$	• Good modular design • High power density • Compact structure • Rapid start-up • Excellent dynamic response	• Complex water and thermal management • Low-grade heat • High sensitivity to contaminants • Expensive catalyst
High-temperature proton exchange membrane fuel cells (HT-PEMFCs)		Platinume-Ruthenium supported on carbon	Nafion/PBI doped in phosphoric acid	$110-180$	• Simple water and thermal management • Accelerated reaction kinetics • High-grade heat • High tolerance to contaminants	• Accelerated stack degradation • Humidification issues • Expensive catalyst
Phosphoric acid fuel cells (PAFCs)	Hydrogen	Platinum supported on carbon	Liquid phosphoric acid (H_3PO_4) in silicon carbide (SiC)	$160-220$	• Technologically mature and reliable • Simple water management • Good tolerance to contaminants • High-grade heat	• Relatively slow start-up • Low power density • High sensitivity to contaminants • Expensive auxiliary systems • Low electrical efficiencies

Fuel cell type	Fuel	Catalyst	Electrolyte	Operation temperature (°C)	Specific advantages	Specific disadvantages
						• Relatively large system size • Electrolyte acid loss • Expensive catalyst • High cost
Direct Methanol fuel cells (DMFCs)	Liquid methanol-water solution	Platinum /Platinume-Ruthenium supported on carbon	Solid polymer membrane (Nafion)	Ambient − 110	• Compact size • Simple system • High fuel volumetric energy density • Easy fuel storage and delivery • Simple thermal management for liquid methanol systems	• Low cell voltage and efficiency • Low power density • Lack of efficient catalysts for direct oxidation of methanol • Fuel and water crossover • Complex water management • High catalyst loading • High cost • CO_2 removal system • Fuel toxicity

Fuel cell type	Fuel	Catalyst	Electrolyte	Operation temperature (°C)	Specific advantages	Specific disadvantages
Alkaline fuel cells (AFCs)	Hydrogen	Nickel /Silver supported on carbon	Potassium hydroxide (KOH) in water solution/Anion exchange membrane (AEM)	Below zero − 230	• High electrical efficiency • Wide range of operation temperature and pressure • Inexpensive catalyst • Catalyst flexibility • Relatively low costs	• Extremely high sensitivity to contaminants • Pure hydrogen and oxygen required • Low power density • Highly corrosive electrolyte leads to sealing issues • Complex and expensive electrolyte management
Molten Carbonate fuel cells (MCFCs)	Methane	Nickel Chromium (NiCr) /Lithiated nickel (NiO)	Liquid alkali carbonate (Li_2Co_3 /Na_2CO_3 /K_2CO_3) in Lithium aluminate ($LiAlO_2$)	600 − 700	• High electrical efficiencies • High-grade heat • High tolerance to contaminants • Possibility of internal reforming • Less strict material requiements • Fuel flexibility • Inexpensive catalyst	• Slow start-up • Low power density • Electrolyte corrosion and evaporative losses • Corrosion of metallic parts • Air crossover • Catalyst dissolution in electrolyte • Cathode CO_2 injection requirement

Fuel cell type	Fuel	Catalyst	Electrolyte	Operation temperature (°C)	Specific advantages	Specific disadvantages
Solid oxide fuel cells (SOFCs)	Methane	Nickel-YSZ composite /Strontium-doped lanthanum manganite (LSM)	Solid yttria-stabilized zirconia (YSZ)	$800 - 1000$	• High electrical efficiencies • High-grade heat • High tolerance to contaminants • Possibility of internal reforming • Eliminated electrolyte issues • Fuel flexibility • Inexpensive catalyst	• Slow start-up • Low power density • Strict material requirements • High thermal stresses • Sealing issues • Durability issues • High manufacturing costs

Table 1.2 Main features of different types of fuel cells

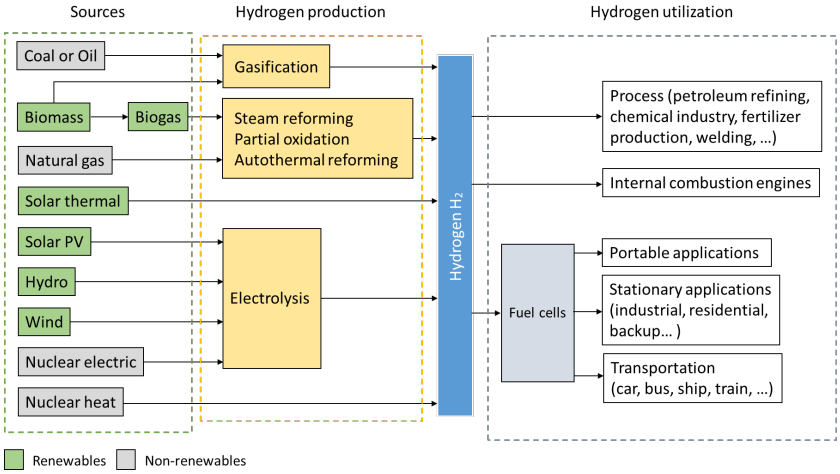

Figure 1.4 Hydrogen supply chain

The difficulty in developing safe, compact, lightweight, and cost-efficient technologies for on-board hydrogen storage is one of the primary hurdles to the widespread use of hydrogen. Figure 1.5 shows various methods for hydrogen storage [34,35]. Typically, hydrogen can be physically stored in as a gas or a liquid. Nowadays, hydrogen compression is the most widely utilized method. In this way, hydrogen gas can be stored as compressed gas in high-pressure tanks with pressures ranging from 20 to 70 MPa [36]. This high-pressure storage technology is used for onboard hydrogen storage in commercial fuel cell electric vehicles (FCEVs), such as the Toyota Mirai and Honda Clarity. Hydrogen embrittlement and gas leakage are two of the most severe possible dangers [34]. Hydrogen, particularly high-pressure and high-purity hydrogen, has a considerable negative impact on the mechanical properties of metals at room temperature, which is known as high-pressure hydrogen embrittlement [37]. This phenomenon causes hydrogen-induced cracks, which increases the likelihood of high-pressure hydrogen components collapsing suddenly. Furthermore, due to its destructive characteristics and small molecular size, hydrogen can easily escape through materials. Hydrogen leakage is not easily perceived since hydrogen gas is colourless and odourless, and it burns with a pale blue flame which is nearly invisible in daylight. Worse yet, compared to other fuels, hydrogen has a wide flammability range ($4-74\%$ vol in air and $4-94\%$ vol in oxygen) and a low ignition energy (0.02 MJ), posing a fire and explosion risk if not handled properly [32,38,39]. Hydrogen gas is also highly diffusive and buoyant. It can swiftly combine with the air around it, resulting in combustible mixtures [40,41]. In addition to this high-pressure storage method, hydrogen stored in dewars or tanks as a cryogenic liquid can result in a volumetric density approximately double that of compressed hydrogen at 70 MPa. Due to its boiling point of -253°C at atmospheric pressure, the tanks or storage facilities for liquid hydrogen require a cryogenic temperature. As a

result, the complexity of the insulation technique required to maintain the storage vessel at an extremely low temperature renders this hydrogen storage method impractical.

Hydrogen can also be stored by physisorption and chemisorption, in addition to the methods mentioned above. In physisorption process, molecular hydrogen is adsorbed on solid surfaces by van der Waals interactions [12]. A wide range of materials, including carbon nanostructures, metal-organic frameworks (MOFs), zeolites, and covalent organic frameworks (COFs), can be utilized as hydrogen storage medium due to their light weight, large specific surface area, and ability to physically adsorb hydrogen molecules [42]. The physisorption method shows advantages in reversibility and fast kinetics, but also restrictions, such as low temperatures or high pressures for hydrogen adsorption [43]. The appropriate tank insulation and thermal management systems are also required. In the chemisorption process, on the other hand, materials chemically interact with atomic hydrogen through chemical bonds, forming hydrides such as metal hydrides, complex hydrides, and chemical hydrides. Although these hydrides offer high hydrogen storage capacity, they also exhibit some disadvantages, including slow kinetic and thermodynamic reactions and relatively high cost. There are also potential safety risks with the use of metallic materials, as metal hydrides (such as magnesium hydride) are highly reactive and can catch fire when exposed to air and water [36]. Therefore, research studies are still required to improve the cost, security, storage capacity, and sorption-desorption kinetics of the following methods [12,44]. Table 1.3 shows typical hydrogen storage technologies and their storage features.

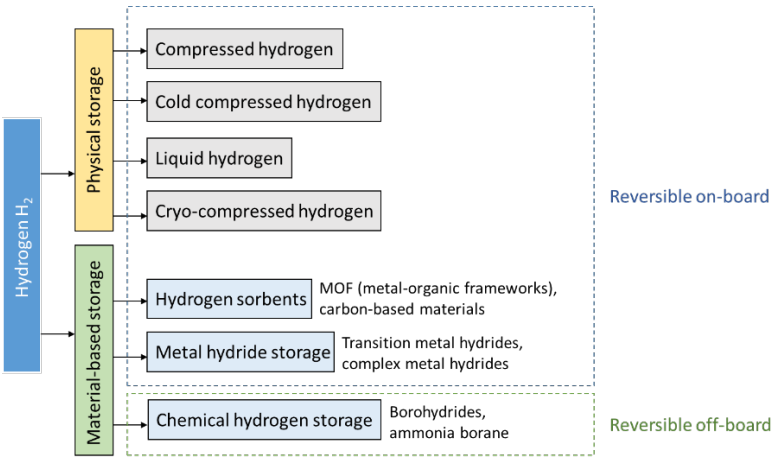

Figure 1.5 Hydrogen storage methods

Parameters	Compressed storage	Liquid storage	Chemical storage	Physisorption
Gravimetric capacity (wt%)	< 13	Size dependent	< 21.7	10
Volumetric capacity (g H_2/L)	< 40	70.8	40-150	40
Temperature (K)	Room temperature	20	typically, > 573 (metal hydrides), 347-441 (complex hydrides)	Varies
Pressure (bar)	200-800	1	1	20-100
System cost ($/kWh)	12-16	6	8-16	13-36
Method of storage	Compressed gas storage	Cryogenic storage	Metal hydrides, complex hydrides, and chemical hydrogen	Metal-organic framework, carbon nanostructures
Benefits	Reversible on-board, lightweight, no need for a thermal management, good kinetics	Reversible on-board, relatively high storage density, low pressure, good kinetics	High storage density,	Reversible on-board, no accumulation of impurities, fast refuelling
Limitations	Extremely high pressure, low storage density	High requirement of thermal insulation, large energy loss due to liquefaction and boil-off process, high tank cost	Regenerable off-board, extremely reactive when exposed to air or water, thermal management required, absorption of impurities, slow kinetics	Thermal management required, poor cycling stability, relatively high pressure
Reference	[12,36,45–47]	[12,45,46]	[12,36,43,48,49]	[12,36,43,48,50]

Table 1.3 Common hydrogen storage technologies and their storage features

1.3. METHANOL STEAM REFORMER

Due to the challenges posed by hydrogen storage and transport, sustainable and economical in-situ hydrogen production methods through the chemical conversion of hydrocarbons and alcohols into hydrogen-rich gases have received particular attention. This chemical process, known as reforming, usually requires the presence of an oxidant. According to the different oxidants used, the reforming process can be classified into steam reforming (SR) (water is the oxidant), partial oxidation (POx) (air is the oxidant), and autothermal reforming (ATR) (both water and air are oxidants) [51]. Many large-scale hydrogen generation systems employ the POx of hydrocarbon. Due to the highly exothermic reaction of the POx process, the high operating temperatures (800 – 1000°C) would make it difficult to prevent the hot spot formation and catalyst deactivation. In contrast, the SR process is endothermic and requires an external heating source. As for the ATR process, it is regarded as a combination of the SR and POx processes. Hence, its effective heat management and adiabatic condition can be achieved by properly selecting the ratios of the reactants (steam-to-carbon ratio and air-to-fuel ratio) independently. This characteristic makes the ATR process superior with a less complicated reactor design, a faster start-up and a shorter response time than SR, and a higher hydrogen yield than POx [52,53]. However, there are some technical issues when using ATR for hydrogen production, such as the sophisticated thermal management, low concentration of H_2 and high concentration of CO in the produced fuel gas compared with SR [54].

In Table 1.4, several hydrogen carriers are compared for hydrogen distribution and on-board production [49]. Methanol is more favorable than other hydrogen carriers because it is liquid at room temperature, giving it a high energy density. This property also allows more commercial and practical fuel storage and transportation. Methanol has a high hydrogen/carbon (H/C) ratio (4: 1), a low temperature for vaporization (65℃), a low temperature for reforming ($200 - 300$℃). This mild reaction condition makes it suitable to be integrated with an HT-PEM fuel cell stack in a reformed methanol fuel cell (RMFC) system. Moreover, methanol also indefinitely miscible with water and can be made from a variety of carbon-based fuel sources [55–57].

Carriers	Annual production (ton)	Hydrogen content (%)	Temperature (K)	Catalysts	Advantages	Disadvantages	Requirements for next-generation catalysts
$CH_4 + 2H_2O$	$\sim 7 \times 10^8$	15.4	> 1073	Ni- or Pt-based (Ni/Al_2O_3, Pt/Al_2O_3)	Mature technique, low cost	Energy demanding, CO_2 emission, CO by-product	Resistance to coking, sintering, and poisoning
$CH_3OH + H_2O$	4.1×10^7	12.0	$433 - 623$	Cu- and Pt-based ($Cu/ZnO/Al_2O_3$, Pt/ZnO)	Mature technique, relatively simple process, moderate conditions	Relatively high cost, CO_2 emission, CO by-product	High selectivity, stability, non-noble metal, wide operating temperature range
HCOOH	7.2×10^5	4.4	$293 - 373$	Noble metal complexes	Mild conditions	Noble metal catalysts, low hydrogen content	Stability, recyclability, non-noble metal
NH_3	$\sim 1.4 \times 10^8$	17.6	$673 - 973$	Ru- and Ni-based	Mature technique, CO_x-free H_2, simple process and set-up	Energy-demanding dehydrogenation, corrosive and toxic NH_3	High efficiency, non-noble metal catalysts, lower operating temperature
C_6H_{11}-CH_3	1×10^7	6.1	~ 573	Pt-based (Pt/Al_2O_3, Pt/AC)	Recyclable, high-purity H_2, CO_x-free H_2	Energy-demanding, coking, noble metal catalysts	Resistance to coking, stability, non-noble metal

Table 1.4 Carriers for hydrogen distribution and on-site production [49]

The comparison of four typical methanol reforming processes is shown in Table 1.5. Under appropriate conditions, the most favored reaction stoichiometry is the MSR because of the highest H_2 yield and relatively low CO concentration compared to other reactions. The process of MSR is strongly endothermic. In this reforming process, the gas mixture of water and methanol can be converted into a hydrogen-rich gas, which contains H_2, CO_2, CO, and unconverted CH_3OH and H_2O, with the operating temperature ranging from 180℃ to 300℃. MSR is also a well-established technology and the most common method for producing hydrogen from methanol [58].

	Advantages	**Disadvantages**
Methanol decomposition (MD)	simplest	high CO production
Partial oxidation of methanol (POM)	compactness, fast start-up, rapid responses	exothermic reaction, hot-spots formation
Steam reforming of methanol (MSR)	well-developed, highest H_2 concentration per mole of methanol	highly endothermic, require continuous heat supply, difficult for transient operation
Oxidative steam reforming of methanol (OSRM)	higher concentrations of H_2, fast dynamics, no need of additional heat supply	complicated thermal behaviour and operating control

Table 1.5 The advantages and disadvantages of different types of methanol reforming processes for hydrogen production

The performance of the catalytic MSR reactions significantly depends on the catalyst. The high activity and fast kinetics at low temperature, low CO selectivity and good stability at high temperature are preferred when selecting catalysts, especially for compact reformers for on-board hydrogen production. Compared with other noble metal-based catalysts, copper-based catalysts represented mainly by the $Cu/ZnO/Al_2O_3$ catalyst are the most commonly used catalysts for MSR due to their higher reaction activity and lower cost [59]. It is generally accepted that the behaviour of copper-based catalysts strongly depends on the morphology and physicochemical properties of copper, which are affected by interactions between metal components and supporting materials [60]. The addition of promoters, such as alkaline metals and acidic oxides, usually improves catalyst performance by affecting the status of copper. It has been reported that when ZnO is used as a promoter, it can improve the dispersion of copper on the catalyst surface, promote the reducibility of copper, stabilize the crystal size of copper, and prevent the aggregation of copper particles during the reaction [61,62]. Furthermore, Al_2O_3 is widely used as a support material for copper-based catalysts due to its high thermal stability, low cost, and high surface area for the loading of active metal [63,64]. However, due to the thermal instability of the copper-

based catalysts, the active sites on the catalyst surface are still easily deactivated by thermal sintering at high operating temperatures [60].

Besides copper-based catalysts, the group 8-10 metal-based catalysts are also used for catalytic reaction of MSR. The most commonly used catalyst in this group is Pd/ZnO [60]. When compared to copper-based catalysts, group 8-10 metal-based catalysts have superior thermal and long-term stability while maintaining similar selectivity. Their costs, on the other hand, are relatively high, and their catalytic activity can still be improved.

The reformer's design is another important aspect in the reforming process. The goal of reactor design is to maximize conversion and selectivity while keeping costs low. Due to their low cost and ease of operation, conventional fixed or packed-bed reactors using a pelleted form of the catalyst are still exceedingly adaptable at both the laboratory and industrial scale. This type of reactor has the advantage in that any catalyst formulation can be made in a suitable shape and poured into the reactor. It also provides the convenience in replacing the catalyst after it is deactivated. To achieve adequate volume for the required amount of catalyst, multiple tubes may be arranged in parallel by welding the tube ends to a sheet header. Such reformers, typically consist of tubes that are packed with catalyst particles or pellets, play an important role in the chemical industry. In addition to conventional reactors, the applications of membranes combined with chemical reactors, called membrane reactors (MRs), have been proposed to intensify the process [55]. In such reactors, Pd-based membranes are generally used, so that the desired product (hydrogen) obtained is selectively separated from the reaction side through the membrane. The selective separation of hydrogen enhances the methanol conversion, which is higher than in conventional reactors. However, some of their disadvantages, such as low mechanical resistance and high costs, become potential restrictions to their commercialization [55]. In wall-coated reactors, a thin layer of catalyst is coated to the inside walls of the reactor, allowing for less heat and mass transfer constraints. As a result, the reactors will be operated in a fairly isothermal state, making temperature management much easier. Furthermore, the pressure drop common in packed bed reactors can be avoided. The main disadvantage of the wall-coated reactors, however, is the reduced specific catalyst load [56]. Furthermore, as compared to conventional packed-bed reactors, reformers with patterned microchannels have been observed to present a better performance [56]. These microchannel reactors show obvious advantages in higher surface-to-volume ratio, longer reactant residence time, better heat and mass transfer properties and flow patterns, and a flat shape that is suitable for integration with a fuel cell stack [55]. The cost of creating intricate pathways inside the reformer, however, is substantial. As a consequence, packed-bed reformers continue to be the most widely used in industry.

1.4. REFORMED METHANOL FUEL CELL SYSTEM

The development of integrated RMFC systems brings a great potential for HT-PEM fuel cells in backup, automotive and stationary power applications, where a MSR reformer is used for the in-situ hydrogen production. HT-PEM fuel cells possess a high tolerance towards CO up to 3 – 5% vol, making them suitable for integration with an in-situ hydrogen generation system without multiple steps for CO removal [65]. Furthermore, similar operating temperatures enable better integration of HT-PEM fuel cells (160 – 220℃) with the MSR process (180 – 300℃) [66,67]. An RMFC system is commonly made up of four basic parts: an evaporator, a burner, a reformer, and a fuel cell stack. Figure 1.6 depicts a simplified illustration of the system's structure.

Liquid methanol and water are sent to the evaporator and then to the catalyst bed of the reformer. The reactants in the bulk flow reach the catalyst particles' outer surface first. Then, from there, it diffuses into and via the pores within the particles. Subsequently, the reaction takes place at the pore surface. The reformate gas can be transferred to the anode side of the fuel cell stack. Through electrochemical reactions, the fuel cell stack generates electricity employing hydrogen from the anode side and oxygen from the cathode side. The CO, H_2, and CH_3OH that remain in the fuel cell exhaust gas are redirected to the burner. They are combusted with the incoming air in the burner to generate thermal energy. As a result, the hot gas from the burner can provide the heat required for the reforming process.

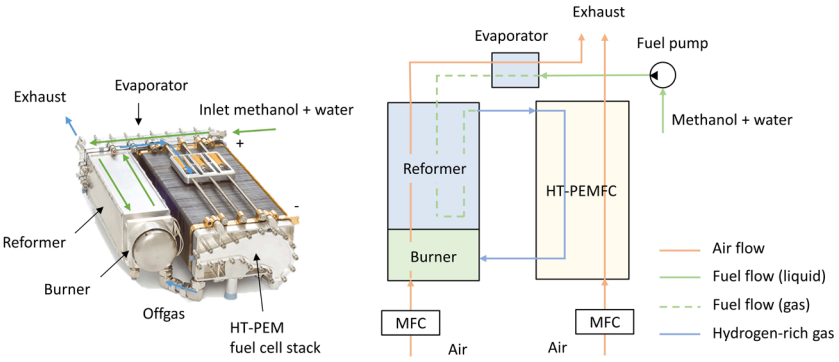

Figure 1.6 A simplified schematic illustration depicting the operating principle of a reformed methanol fuel cell system

Much research has been done on the modelling and experimental tests for the system design and performance study [68–71], the system optimization and control [72–74], as well as the study of heat integration of RMFC systems [75–77]. For example, in the study by Sahlin et al. [78], a dynamic model of the RMFC system has been

developed and validated with experimental results. The model was used to predict the energy flow through each component and the transient behaviour of the RMFC system. Justesen et al. [72] used the ANFIS approach to create a model of the RMFC system. This model was used to examine the effect of the composition in reformate gas on the fuel cell voltage and to determine the most efficient reformer temperature for the RMFC system. Ribeirinha et al. [76] experimentally studied the thermal integration of a low-temperature MSR cell with an HT-PEM fuel cell in a combined stack configuration. They noticed that the constant presence of methanol in the reformate stream led the membrane electrode assembly to degrade. At the same time, catalyst deactivation in the reformer was also observed after several hours of operation at different fuel flow rates and operating temperatures. As a result of the decreased catalyst activity, the hydrogen partial pressure decreases, increasing the fuel cell's anode resistance.

Accordingly, the hydrogen yield, fuel conversion, concentration of undesired by-products (primarily CO) in the reformed gas, and degree of catalyst deactivation are all important elements in the operation of a fuel cell power system coupled with a fuel processor for hydrogen generation. For this reason, experimental and numerical evaluations of the MSR reformer's performance in the RMFC system should be conducted.

1.5. PROJECT OBJECTIVE

The primary objective of this PhD project is to use mathematical models to describe chemical reactions and transport phenomena in the MSR reformer. Although the experiments for the reformer could provide us the direct and concise results of the system, it can be costly and time-consuming, especially when multiple variables or long-term performance should be tested. The tested results can also be affected by certain factors such as unnoticed catalyst deactivation, errors in measuring devices (e.g., incorrect fitting of the measuring scale), and inappropriate research design (e.g., test without reaching a steady state). On the other hand, the mathematical modelling of packed-bed reactors does not have such disadvantages. It allows a deep insight into the chemical reactions and transport processes in the reactor. However, the complexity of the physical and chemical phenomena occurring at different scales in the reactor leads to difficulty and uncertainty with the mathematical description of these phenomena. Hence, several assumptions must be made to simplify the modeling of packed bed reactors by considering the feasibility, sacrificing some accuracy, and determining the most critical characteristics of the investment.

In this dissertation, a steady-state one-dimensional pseudo-homogeneous model, a steady-state two-dimensional pseudo-homogeneous model are developed. At the particle scale, two methods are adopted and compared to compute the effectiveness factors for the chemical reactions. Taking into account the properties of these models, it is possible to choose the most suitable model and adjust it when particular attention

is devoted to certain problems specific to the packed bed reactor. Numerical methods for solving the differential equations in these models using MATLAB® are mentioned. The effects of operation and geometric parameters on the reformer performance are studied using different models. Moreover, a study on optimization of the multi-tubular packed bed reformer is presented for the performance improvement so that a high methanol conversion and hydrogen production yield, as well as a low CO concentration in the reformate gas and a low hotspot temperature in the catalyst bed could be achieved.

CHAPTER 2. MATHEMATICAL MODELLING OF METHANOL STEAM REFORMERS

The performance of a multi-tubular packed-bed reformer for the MSR process is investiageted in this study. Because the MSR process is endothermic, it requires an external heating source to activate the reaction sites and keep the catalyst bed temperature from declining. It indicates that the reformer should be combined with a heat supply device, such as a catalytic combustor or burner, for on-site applications [70,79,80]. As shown in Figure 2.1, this shell-and-tube reformer consists of a number of baffles and tubes mounted inside a cylindrical shell. The reactor shell is generally surrounded by a thick layer of insulating material to reduce the heat losses. Specially designed baffles are installed in the reformer shell to ensure the most efficient distribution of thermal flow in the intertubular space. On the tube sheet, the tubes are organized in equilateral triangles (more compact) or squares. These tubes are randomly packed with $Cu/ZnO/Al_2O_3$ catalyst particles of uniform size. The reactants are transferred from the bulk fluid to the outer surface of the catalyst particles and then delivered through the catalyst pores, as the bulk fluid passes by the catalyst bed. The reactants are adsorbed on the pores surface where the chemical reactions occur. The formed products are then desorbed and transported back to the fluid body. Since the MRS process is accompanied with strong heat consumption, the extra heat should be supplied through the tube wall.

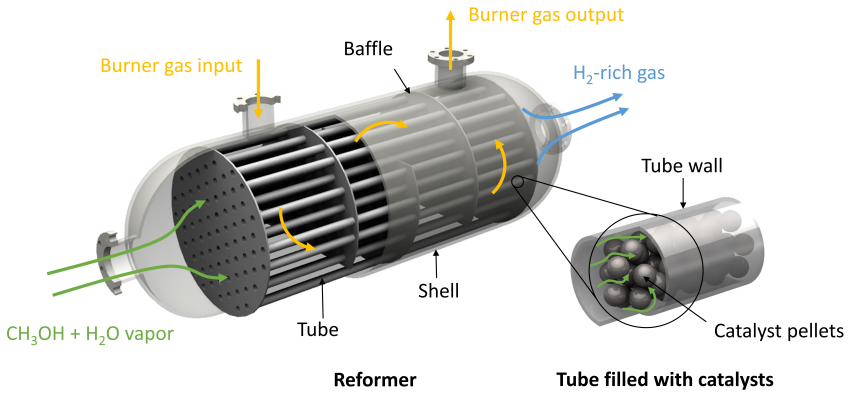

Figure 2.1 Schematic diagram of a multi-tubular packed-bed reactor for methanol steam reforming

To efficiently evaluate the performance of the MSR reformer, modelling and numerical methods have been widely used to save time and cost in extensive experimental tests. Therefore, the catalytic performance of MSR reaction needs to be accurately simulated by kinetic models. The MSR process is affected by heat and mass transport phenomena in catalyst beds. However, due to the complex transport phenomena and chemical reactions in catalyst beds, the accurate estimation of their behaviour becomes impossible or requires very detailed mathematical models. In this case, we should rely on simplified models that can capture the most crucial and salient features of the complex mathematical problem to achieve almost accurate descriptions for most MSR reformers [81].

2.1. KINETIC MODEL

To estimate the performance of the MSR reformer, the appropriate reaction rate expressions are required. Three main sub-reactions that take place within the MSR reformers over the most widely used $CuO/ZnO/Al_2O_3$ catalysts are as shown in the following equations:

Methanol steam reforming reaction (MSR):

$$CH_3OH + H_2O \leftrightarrow CO_2 + 3H_2 \qquad \Delta H = +49.7 \left(\frac{kJ}{mol}\right) \tag{1}$$

Water-gas shift reaction (WGS):

$$CO + H_2O \leftrightarrow CO_2 + H_2 \qquad \Delta H = -41.2 \left(\frac{kJ}{mol}\right) \tag{2}$$

Methanol decomposition reaction (MD):

$$CH_3OH \leftrightarrow CO + 2H_2 \qquad \Delta H = +90.2 \left(\frac{kJ}{mol}\right) \tag{3}$$

According to the main reactions considered in the MSR process, the kinetic models of the MSR process can be classified into three categories [82]: single rate models [83–85], double rate models [86–88], and triple rate models [89–91]. Jiang et al. [92,93] developed an overall power-law and a Langmuir-Hinshelwood-Hougen-Watson model for the MSR process over a $Cu/ZnO/Al_2O_3$ catalyst. They discovered that CO only has limited effect on the reaction rate. They also assumed that all adsorbed compounds are competing for a single active site on the catalyst surface. The WGS reaction was considered neglectable because the competitive adsorption favoured methanol and methyl formate rather than CO. In contrast with the above mentioned reaction mechanism, Lee et al. [94] developed a Langmuir–Hinselwood rate expression for the reforming reaction based on two distinct types of active sites,

one for adsorbed methoxy and the other for adsorbed hydrogen. They assumed that the MD reaction was negligible, and that CO was only produced by the reverse water gas shift (rWGS) reaction. The dehydrogenation of the adsorbed methoxy to the adsorbed oxymethylene was considered the rate-determining step (RDS). To consider the CO production in the MSR process, many studies have introduced double rate models. Amphlett et al. [95] developed a semi-empirical model for the kinetics of the MSR process over a $CuO/ZnO/Al_2O_3$ catalyst. They described the rate expressions for the MSR and MD reactions under specific conditions without considering the WGS reaction in this study. Purnama et al. [96] also developed a double rate model for the MSR process. On the contrary, they used the rWGS reaction to explain the CO formation in this study. The power rate laws for both the MSR and rWGS reactions were used to refine the rate equations from experimental data. They found that the experimental data could be accurately fitted when employing the rWGS reaction rather than the MD reaction to describe the CO formation as a consecutive product. Furthermore, the adsorption of methanol and methyl formate on the catalyst surface was found to be stronger than that of CO. Peppley et al. [89,90] developed a kinetic model considering MSR, WGS, and MD reactions in the MSR process. Two distinct types of actives sites were proposed in this model: one type for the MD reaction, and the other type for the MSR and WGS reactions. Furthermore, the model assumed that hydrogen adsorption did not compete for active sites on which oxygen-containing species adsorb; the RDS for both the MSR and MD reactions is the dehydrogenation of adsorbed methoxy groups; and the RDS for the WGS reaction is the formation of an intermediate formate species. This triple rate model has been widely used in theoretical analysis studies of MSR processes. Sá et al. [97] and Herdem et al. [98] compared several kinetics reaction rates of MSR process over a commercial $CuO/ZnO/Al_2O_3$ catalyst. The kinetic LangmuirHinshelwood model proposed by Peppley et al. [89,90] was found to have the best agreement with their experimental data.

The rate expressions for key reactions involved in the MSR process are provided below, based on the Langmuir-Hinshelwood kinetic model published by Peppley et al. [89,90]:

$$r_R = \frac{k_R K^*_{CH_3O^{(1)}} \left(p_{CH_3OH} / p_{H_2}^{\frac{1}{2}} \right) \left(1 - p_{H_2}^3 p_{CO_2} / K_R^{eq} p_{CH_3OH} p_{H_2O}\right) C_{S_1}^T C_{S_{1a}}^T}{\left(1 + K^*_{CH_3O^{(1)}} \left(p_{CH_3OH} / p_{H_2}^{\frac{1}{2}} \right) + K^*_{HCOO^{(1)}} p_{CO_2} p_{H_2}^{\frac{1}{2}} + K^*_{OH^{(1)}} \left(p_{H_2O} / p_{H_2}^{\frac{1}{2}} \right)\right)\left(1 + K_{H^{(1a)}}^{\frac{1}{2}} p_{H_2}^{\frac{1}{2}}\right)} \quad (4)$$

$$r_W = \frac{k_W K^*_{OH^{(1)}} \left(p_{CO} p_{H_2O} / p_{H_2}^{\frac{1}{2}} \right) \left(1 - p_{H_2} p_{CO_2} / K_W^{eq} p_{CO}\, p_{H_2O}\right) C_{S_1}^{T^2}}{\left(1 + K^*_{CH_3O^{(1)}} \left(p_{CH_3OH} / p_{H_2}^{\frac{1}{2}} \right) + K^*_{HCOO^{(1)}} p_{CO_2} p_{H_2}^{\frac{1}{2}} + K^*_{OH^{(1)}} \left(p_{H_2O} / p_{H_2}^{\frac{1}{2}} \right)\right)^2} \quad (5)$$

$$r_D = \frac{k_D K^*_{CH_3O^{(2)}} \left(p_{CH_3OH}/p_{H_2}^{\frac{1}{2}}\right)\left(1 - p_{H_2}^2 p_{CO}/K_D^{eq} p_{CH_3OH}\right) C_{S_2}^T C_{S_{2a}}^T}{\left(1 + K^*_{CH_3O^{(2)}}\left(p_{CH_3OH}/p_{H_2}^{\frac{1}{2}}\right) + K^*_{OH^{(2)}}\left(p_{H_2O}/p_{H_2}^{\frac{1}{2}}\right)\right)\left(1 + K_{H^{(2a)}}^{\frac{1}{2}} p_{H_2}^{\frac{1}{2}}\right)} \quad (6)$$

where r_j ($\mathrm{mol\,m^{-2}s^{-1}}$) denotes the rate of reaction j ($j = R, W, D$), k_j ($\mathrm{m^2\,s^{-1}mol^{-1}}$) is the rate constant of reaction j, K_j^{eq} is the equilibrium constant of reaction j, K_i^* ($\mathrm{bar^{-0.5}}$) is the adsorption coefficient for species i, p_i (bar) is the partial pressure of component i. $C_{S_1}^T$, $C_{S_{1a}}^T$, $C_{S_2}^T$ and $C_{S_{2a}}^T$ ($\mathrm{mol\,m^{-2}}$) represent the surface concentrations of the hypothetical active sites, where '1' and '1a' sites are for the MSR and WGS reactions, and '2' and '2a' sites are for the MD reaction.

The Arrhenius or van't Hoff expressions can be used to express the temperature dependency of each constant [89,99,100]:

$$k_R = k_R^{\infty}\, exp\left(\frac{-E_R}{RT}\right) \quad (7)$$

$$k_D = k_D^{\infty}\, exp\left(\frac{-E_D}{RT}\right) \quad (8)$$

$$k_w = k_R^{\infty}\, exp\left(\frac{-E_W}{RT}\right) \quad (9)$$

$$K_R^{eq} = \exp\left(-\frac{50240 - 170.98T - 2.64 \times 10^{-2}T^2}{RT}\right) \quad (10)$$

$$K_W^{eq} = \exp\left(-\frac{-41735 + 46.66T - 7.55 \times 10^{-3}T^2}{RT}\right) \quad (11)$$

$$K_D^{eq} = \frac{K_R^{eq}}{K_W^{eq}} \quad (12)$$

$$K^*_{CH_3O^{(1)}} = exp\left(\frac{\Delta S^*_{CH_3O^{(1)}}}{R} - \frac{\Delta H^*_{CH_3O^{(1)}}}{RT}\right) \quad (13)$$

$$K^*_{HCOO^{(1)}} = exp\left(\frac{\Delta S^*_{HCOO^{(1)}}}{R} - \frac{\Delta H^*_{HCOO^{(1)}}}{RT}\right) \quad (14)$$

$$K^*_{OH^{(1)}} = exp\left(\frac{\Delta S^*_{OH^{(1)}}}{R} - \frac{\Delta H^*_{OH^{(1)}}}{RT}\right) \quad (15)$$

$$K_{H^{(1a)}} = exp\left(\frac{\Delta S_{H^{(1a)}}}{R} - \frac{\Delta H_{H^{(1a)}}}{RT}\right) \tag{16}$$

$$K^*_{CH_3O^{(2)}} = exp\left(\frac{\Delta S^*_{CH_3O^{(2)}}}{R} - \frac{\Delta H^*_{CH_3O^{(2)}}}{RT}\right) \tag{17}$$

$$K^*_{OH^{(2)}} = exp\left(\frac{\Delta S^*_{OH^{(2)}}}{R} - \frac{\Delta H^*_{OH^{(2)}}}{RT}\right) \tag{18}$$

$$K_{H^{(2a)}} = exp\left(\frac{\Delta S_{H^{(2a)}}}{R} - \frac{\Delta H_{H^{(2a)}}}{RT}\right) \tag{19}$$

The parameters required for the calculation of the above constants can be found in Table 2.1 and Table 2.2.

Rate constants	**Kinetic parameters**	
	$k^{\infty}(\mathrm{m^2 s^{-1} mol^{-1}})$	E (kJ $\mathrm{mol^{-1}}$)
k_R ($\mathrm{m^2 s^{-1} mol^{-1}}$)	7.4×10^{14}	102.8
k_D ($\mathrm{m^2 s^{-1} mol^{-1}}$)	3.8×10^{20}	170.0
k_w ($\mathrm{m^2 s^{-1} mol^{-1}}$)	5.9×10^{13}	87.6

Table 2.1 Parameters for rate constants in the comprehensive kinetic model

Adsorption coefficients	**Kinetic parameters**	
	$\Delta S^*(J\ mol^{-1}K^{-1})$	$\Delta H^*(kJ\ mol^{-1})$
$K^*_{CH_3O^{(1)}}$ ($\mathrm{bar^{-0.5}}$)	-41.8	-20.0
$K^*_{OH^{(1)}}$ ($\mathrm{bar^{-0.5}}$)	-44.5	-20.0
$K_{H^{(1a)}}$ ($\mathrm{bar^{-0.5}}$)	-100.8	-50.0
$K^*_{HCOO^{(1)}}$ ($\mathrm{bar^{-0.5}}$)	179.2	100.0
$K^*_{CH_3O^{(2)}}$ ($\mathrm{bar^{-0.5}}$)	30.0	-20.0
$K^*_{OH^{(2)}}$ ($\mathrm{bar^{-0.5}}$)	30.0	-20.0
$K_{H^{(2a)}}$ ($\mathrm{bar^{-0.5}}$)	-46.2	-50.0

Table 2.2 Parameters for adsorption coefficients in the comprehensive kinetic model

The production rate of component i per time per unit mass of catalyst r_i (mol s^{-1} (kg of catalyst)$^{-1}$) can be calculated by the rate r_j (mol s^{-1} m^{-2}) of individual reaction j and the surface area per unit mass of fresh catalyst S_c (m^2 kg^{-1}):

$$r_{CO_2} = (r_R + r_W)S_c \tag{20}$$

$$r_{CO} = (r_D - r_W)S_c \tag{21}$$

$$r_{H_2} = (3r_R + 2r_D + r_W)S_c \tag{22}$$

$$-r_{CH_3OH} = (r_R + r_D)S_c \tag{23}$$

$$-r_{H_2O} = (r_R + r_W)S_c \tag{24}$$

2.2. EFFECTIVENESS FACTORS

The solid phase catalysts, as well as the gas phase reactants and products, are involved in the catalytic MSR process. The process of molecule adsorption, reaction, and desorption occurs on the catalyst surface in this heterogeneous catalytic system. The laws of thermodynamics and the empirical science of heat and mass transfer, chemical kinetics, and fluid dynamics control the rate of this process. Therefore, relevant variables from micro to macro should be considered in the reactor and process design.

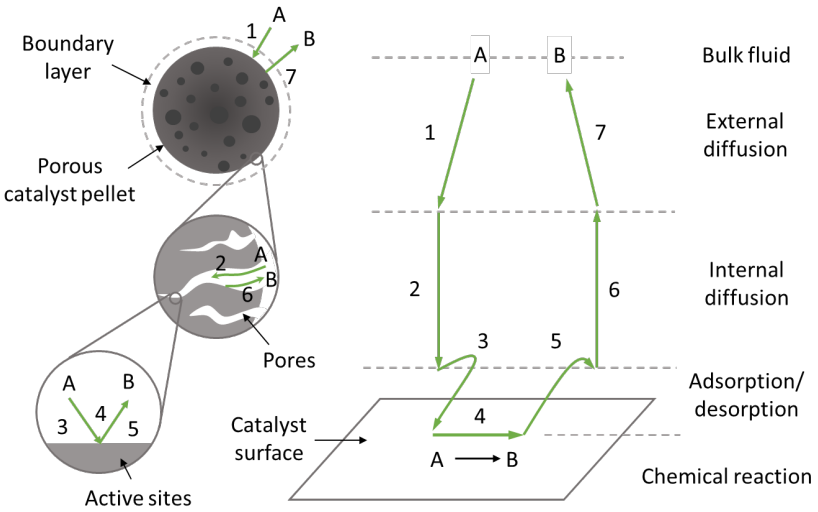

Figure 2.2 Seven-step sequence of microkinetic analysis in a heterogeneous catalytic system

Since the catalytic reaction occurs when the reactant molecules diffuse from the bulk fluid through the catalyst pores and come into contact with the active sites on the pores surface, the entire process of a heterogeneous catalytic reaction can be subdivided into a seven-step sequence which is shown in Figure 2.2 [101]. This seven-step sequence for a catalytic reaction process includes: (1) diffusion of reactant(s) A from the bulk fluid to the external surface of a catalyst pellet; (2) diffusion of reactant(s) A from the external surface of the catalyst pellet to the vicinity of the internal catalytic surface through catalyst pores; (3) adsorption of reactant(s) A onto the catalyst surface; (4) catalytic reaction (A → B) on the catalyst surface; (5) desorption of the product(s) B from the catalyst surface; (6) diffusion of the product(s) B from the interior of the pellet to the external surface of the catalyst pellet; (7) transfer of the product(s) B from the external surface of the catalyst pellet to the bulk fluid [101].

Diffusion, adsorption, surface reaction, and desorption simultaneously happen in catalyst pores, making it a complex mathematical problem. The slowest step's rate limits the overall reaction rate in this sequence. The rates of the three reaction steps in the sequence (adsorption, surface reaction, and desorption) can be determined according to their reaction mechanisms, where the chemical kinetics have been discussed above. At the same time, the internal diffusion of the molecules competes with the catalytic reaction inside the catalyst pellet. The internal diffusion resistance mainly restricts the movement of reactants and products within the catalyst's intricate pore network, which corresponds to the second and sixth steps (internal diffusions) in the seven-step sequence of microkinetic. During the internal diffusion, reactants diffuse from the external surface into and through the pores within the catalyst pellet. As the reactants diffuse toward the centre of the pellet, the concentration of reactants inside the pores C_i will be lower than at the external surface C_i^s if the internal diffusion resistance is high. In this case, not the entire catalyst surface is accessible to the same conditions as the external surface, which leads to variations in reaction rate throughout the catalyst pellet. In addition, the external diffusion, which depends on the stagnant film thickness δ, can affect the reaction rate by restricting the mass transfer from the bulk fluid to the external surface of the catalyst pellet through a boundary layer. This boundary layer provides a considerable transfer resistance at a slow fluid flow velocity. Conversely, at a very high fluid flow velocity, the thickness of the boundary layer becomes extremely small so that it no longer resists the external diffusion. This external resistance also increases with the increasing particle size. Hence, as the fluid flow rate increases and the particle size decreases, the external diffusion resistance becomes a less critical factor concerning the overall reaction rate [102]. Moreover, the heat and mass transfer correlations are analogous in this reaction-diffusion process and share analogous heat and molar flux equations.

As a result, the effectiveness factor η is used to model non-isothermal steady diffusion-reaction processes within catalyst particles. The effectiveness factor, which links global and intrinsic rates, can be defined as the ratio of the actual reaction rate

inside the catalyst particle to the reaction rate without internal and external diffusion limitations:

$$\eta = \frac{(-r_A)_p}{(-r_A)_b} = \frac{\text{Actual or global reaction rate in catalyst particle}}{\text{Reaction rate that would result if entire interior surface were exposed to the bulk fluid conditions}}$$

There are different approaches to calculating the effectiveness factor for a catalytic reaction. When assuming an isothermal, first-order reaction in a spherical catalyst pellet, one of the most widely used approaches to compute an effectiveness factor is as a function of the Thiele modulus [101,103]. The Thiele modulus, which is employed in this example, is a dimensionless quantity that expresses the link between diffusion and reaction rates in porous catalyst particles.

Furthermore, the effectiveness factor obtained from numerically computing the temperature and concentration distributions, as well as the local reaction rates within a catalyst pellet, has received much interest. Ziarati et al. [104] developed a dynamic model of the MSR process in a packed-bed reactor that took into account the effectiveness factors. The efficiency factor for the MSR reaction was estimated by deriving methanol intraparticle concentration profiles using species continuity equations. The WGS reaction, on the other hand, was not considered in this study, and the MD reaction's effectiveness factor was set to one. Olatunde et al. [105] numerically calculated the effectiveness factor for the catalytic MSR process in spherical catalyst pellets. They evaluated the concentration distributions of CH_3OH and H_2, as well as the temperature distributions within catalytic pellets. Effects of the reaction kinetics, thermal conductivity, diffusion coefficient, catalyst particle size, and surface temperature on the effectiveness factor were examined. The external diffusion resistances between the gas and solid phases, on the other hand, were not considered in their study. The presence of CO in the products was also ignored. Tesser et al. [85] conducted an experimental and simulation work on a pilot-scale tubular packed-bed reactor for MSR. Since a commercial catalyst with a size of 3–7 mm was used, the catalyst effectiveness factor was taken into account in this model. A reliable approach for estimating the effectiveness factor was provided by solving mass and heat balance equations, which govern a catalyst particle's simultaneous reactions and diffusion. The temperature and concentration profiles inside the pellet were measured using this method. However, the reaction mechanisms, particularly the formation of CO, needed to be further studied and clarified.

2.2.1. DIFFUSION-REACTION PROCESS IN A CYLINDRICAL CATALYST PARTICLE

Because the concept of the effectiveness factor is brought out to account for the effect of transport resistances on variations of reaction rates throughout the catalyst pellet, it could be calculated by:

$$\eta_j = \frac{\iiint r_j(C_i,T)dV_p}{r_j(C_i^b,T^b)V_p} = \frac{\int_0^{r_p} 4\pi\xi^2 r_j(c_i,T)d\xi}{(4/3)\pi r_p^3 r_j(c_i^b,T^b)} \tag{25}$$

where η_j is the effectiveness factor for reaction j, V_p (m^3) is the volume of a single catalyst particle, $r_j(C_i^b,T^b)$ ($\mathrm{mol\ m^{-2}\ s^{-1}}$) is the production rate of the reaction j at the bulk fluid conditions, $r_j(C_i,T)$ ($\mathrm{mol\ m^{-2}\ s^{-1}}$) is the production rate of the reaction j at different radial positions within a spherical catalyst pellet, r_p (m) is the radius of the catalyst pellet, and ξ (m) is the radial distance of pellet.

The reaction rates inside the catalyst pellet are generally non-uniform, considering the presence of considerable heat and mass transfer resistances. As shown in Figure 2.3, it takes two steps for the reactants to transfer from the bulk fluid to the surface of the pores inside a catalyst pellet: the external diffusion and the internal diffusion. The model of the intraparticle mass and energy balances, which govern the simultaneous diffusion and MSR process in a catalyst pellet, can be developed by assuming a similar behaviour between mass and heat transfer:

Intraparticle mass balance

$$D_{i,ep}\left(\frac{\partial^2 c_i}{\partial\xi^2} + \frac{2}{\xi}\frac{\partial c_i}{\partial\xi}\right) = \rho_c \sum_{j=1}^{N_R} \nu_{ij} r_j S_c \tag{26}$$

Intraparticle energy balance

$$\lambda_{ep}\left(\frac{\partial^2 T}{\partial\xi^2} + \frac{2}{\xi}\frac{\partial T}{\partial\xi}\right) = \rho_c \sum_{j=1}^{N_R} (-\Delta H_j) r_j S_c \tag{27}$$

where $D_{i,ep}$ ($\mathrm{m^2\ s^{-1}}$) denotes the effective diffusivity of the component i in small porous particles, λ_{ep} ($\mathrm{W\ m^{-1}\ K^{-1}}$) denotes the effective thermal conductivity in small porous particles, ν_{ij} is the stoichiometric coefficient of the component i in reaction j, N_R is the number of primary reactions in the MSR process, and r_j ($\mathrm{mol\ m^{-2}\ s^{-1}}$) is the local rate of reaction j inside the catalyst particle.

Boundary conditions:

$$\xi = 0: \qquad \frac{\partial c_i}{\partial\xi} = 0 \qquad \frac{\partial T}{\partial\xi} = 0 \tag{28}$$

$$\xi = \frac{d_p^v}{2}: \qquad -D_{i,ep}\frac{\partial c_i}{\partial \xi} = k_{i,fs}\left(c_i - c_i^b\right)$$

$$-\lambda_{ep}\frac{\partial T}{\partial \xi} = h_{fs}(T - T^b)$$

where $k_{i,fs}$ (m s^{-1}) is the interphase mass transfer coefficient, h_{fs} (W m^{-2} K^{-1}) is the interphase heat transfer coefficient, and d_p^v (m) is the volume-equivalent spherical diameter, defined as the diameter of a sphere with the same volume as this particle.

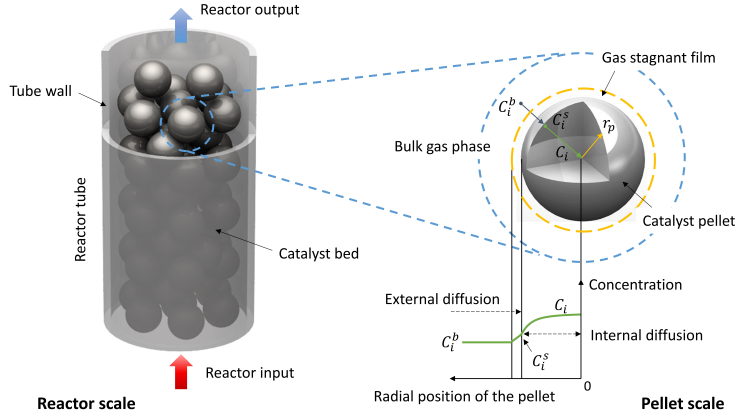

Figure 2.3 Interphase and intraparticle transfer phenomena in a catalytic pellet

Volume-equivalent (surface-equivalent) spherical diameter d_p^v and d_p^s

The catalyst particle used in this study is cylindrical with a diameter of d and a height of h. Therefore, the volume-equivalent (surface-equivalent) spherical diameter should be introduced to simplify the calculation, since a sphere is a readily understood geometry and can be characterised by a single dimension (its radius or diameter).

The volume-equivalent (surface-equivalent) spherical diameter is defined as the diameter of a single spherical pellet having the same volume (surface) as the non-spherical particle.

For a cylinder catalyst, the volume-equivalent particle diameter d_p^v can be calculated by:

$$d_p^v = \left(\frac{6V_p}{\pi}\right)^{\frac{1}{3}} = d\left(\frac{3}{2}\frac{h}{d}\right)^{\frac{1}{3}} \tag{29}$$

In addition, the surface-equivalent spherical diameter d_p^s (m) can be calculated by:

$$d_p^s = \left(\frac{S_p}{\pi}\right)^{\frac{1}{2}} \tag{30}$$

where S_p (m^2) is the external surface area of a single non-spherical particle.

Particle effective diffusivity $D_{i,ep}$

The effective diffusivity $D_{i,ep}$ ($m^2\ s^{-1}$) is defined to describe the diffusion of species i inside the catalyst particle, which is based on the ordinary bulk diffusivity $D_{i,M}$ ($m^2\ s^{-1}$) and the Knudsen diffusivity $D_{i,K}$ ($m^2\ s^{-1}$) [106]:

$$\frac{1}{D_{i,ep}} = \frac{1}{D_{i,M}} + \frac{1}{D_{i,K}} \tag{31}$$

where $D_{i,M}$ ($m^2\ s^{-1}$) is the effective multicomponent diffusion coefficient of species i, and $D_{i,K}$ ($m^2\ s^{-1}$) is the Knudsen diffusivity of component i. This Knudsen diffusivity can be expressed as:

$$D_{i,K} = \frac{\bar{d}}{3}\sqrt{\frac{8RT}{\pi M_i}} \tag{32}$$

where $\bar{d}$ (m) is the average pore diameter (6.4×10^{-9} m) [107].

The ordinary bulk diffusivity $D_{i,M}$ of species i is calculated using the Maxwell-Stefan equation [106]:

$$\frac{1}{D_{i,M}} = \sum_{\substack{j=1 \\ j\neq i}}^{n} \frac{x_j}{D_{ij}}\left(1 - \frac{x_i N_j}{x_j N_i}\right) \tag{33}$$

where n is the number of components in gas mixture, x_i is the mole fraction of specie i, N_i is the molar flux of species i referred to a stationary coordinate reference frame (mol $m^{-2}\ s^{-1}$), N_j/N_i is the flux ratio of species j to i (when diffusion limits the rate of chemical reactions), and D_{ij} ($m^2\ s^{-1}$) is the diffusivity for a binary mixture of i and j.

The Chapman-Enskog equation is used for the calculation of binary diffusivity at a low density:

$$D_{ij} = 0.0018583 \frac{T^{3/2}\left(1/M_i + 1/M_j\right)^{1/2}}{P\sigma_{ij}^2 \Omega_D} \tag{34}$$

where M_i is the molar mass of component i (g mol^{-1}), Ω_D is the collision integral for diffusion, and σ_{ij} is the characteristic length. The calculation of σ_{ij} can be expressed as:

$$\sigma_{ij} = \frac{\sigma_i + \sigma_j}{2} \tag{35}$$

An empirical equation is proposed to estimate Ω_D using the following correlations:

$$\Omega_D = \left(44.54 T_{ij}^{*-4.909} + 1.911 T_{ij}^{*-1.575}\right)^{0.10} \tag{36}$$

where

$$T_{ij}^{*} = \frac{kT}{\varepsilon_{ij}} \tag{37}$$

$$\varepsilon_{ij} = \left(\varepsilon_i \varepsilon_j\right)^{1/2} \tag{38}$$

To estimate the ε_i and σ_i:

$$\sigma = 0.841 V_c^{1/3} \tag{39}$$

$$\frac{\varepsilon}{k} = 0.75 T_c \tag{40}$$

Parameters mentioned in above equations for the calculation of gas diffusivities can be found in Table 2.3.

Particle effective thermal conductivity λ_{ep}

According to the study of Bert Koning [108], for a Cu/ZnO/Al_2O_3 cylinder catalyst with a particle diameter of $d_p = 5.5$ mm, the effective thermal conductivity of catalyst particles can be assumed to be linear with temperature:

$$\lambda_{ep} = 0.21 + 1.5 \times 10^{-4} T \tag{41}$$

The effect of particle size on the value of λ_{ep} has been approved to be insignificant in catalyst beds [109,110]. Therefore, the expression of particle effective thermal conductivity can be directly used in our study.

Solid-fluid heat transfer coefficient h_{fs}

Heat and mass transfer coefficients between the bulk fluid and catalyst particle are introduced to calculate the temperature and concentrations on the external surface of the catalyst particle. According to the studies of Gnielinski [111], the solid-fluid heat transfer coefficient h_{fs} can be predicted by means of the form factor f_a and the Nusself number Nu:

$$\mathrm{Nu}_{fs} = f_a \mathrm{Nu}_{pa} \tag{42}$$

$$\mathrm{Nu}_{pa} = 2 + \sqrt{\mathrm{Nu}_{lam}^2 + \mathrm{Nu}_{turb}^2} \tag{43}$$

$$\mathrm{Nu}_{lam} = 0.664 {\mathrm{Re}_{pa}}^{0.5} \mathrm{Pr}^{1/3} \tag{44}$$

$$\mathrm{Nu}_{turb} = \frac{0.037 Re_{pa}^{0.8} Pr}{1 + 2.443 Re_{pa}^{-0.1} (Pr^{2/3} - 1)} \tag{45}$$

$$\mathrm{Re}_{pa} = \frac{d_p^s u_s \rho_f}{\varepsilon \mu_f} \tag{46}$$

$$\mathrm{Pr} = \frac{c_p \mu_f}{\lambda_f} \tag{47}$$

$$\mathrm{Nu}_{fs} = \frac{h_{fs} d_p^s}{\lambda_f} \tag{48}$$

where Nu is Nusselt number, Nu_{fs} is the fluid/solid Nusselt number, Re is Reynolds number, Pr is Prandtl number, ε is the void fraction of catalyst, μ_f is the fluid viscosity (kg $\mathrm{m}^{-1}\mathrm{s}^{-1}$), λ_f is the thermal conductivity of the fluid (W m^{-1} K^{-1}), and u_s is the superficial velocity of the bulk fluid (m s^{-1}).

For a cylindrical catalytic particle with a length of l (m) and a diameter of d (m), if $0.24 < l/d < 1.2$, the value of f_a can be inserted as $f_a = 1.6$.

Solid-fluid mass transfer coefficient $k_{i,fs}$

The solid-fluid mass transfer coefficient $k_{i,fs}$ can be estimated by:

$$\mathrm{Re}_{pa} = \frac{d_p^s u_s \rho_f}{\mu_f} \tag{49}$$

$$\mathrm{Sc}_i = \frac{\mu_f}{\rho_f D_{i,f}} \tag{50}$$

$$\frac{1}{D_{i,f}} = \sum_{\substack{j=1 \\ j \neq i}}^{n} \frac{x_j}{D_{ij}} \left(1 - \frac{x_i N_j}{x_j N_i}\right) \tag{51}$$

According to the Thoenes-Kramers correlation for the flow through packed beds [112,113] (for $0.25 < \varepsilon < 0.5$, $40 < \mathrm{Re}_{pa}{}' < 4000$, and $1 < \mathrm{Sc}_i < 4000$), the mass transfer coefficient $k_{i,fs}$ can be calculated by:

$$\mathrm{Re}_{pa}{}' = \frac{\mathrm{Re}_{pa}}{(1-\varepsilon)\gamma} \tag{52}$$

$$\mathrm{Sh}_i{}' = 1.0 Re'^{1/2}_{pa} \mathrm{Sc}_i{}^{1/3} \tag{53}$$

$$k_{i,fs} = \frac{D_{i,f}(1-\varepsilon)}{d_p^v \varepsilon} \gamma (\mathrm{Sh}_i{}') \tag{54}$$

For cylindrical pellets

$$\gamma = \frac{2\pi r_p l_p + 2\pi r_p^2}{\pi \left(d_p^v\right)^2} \tag{55}$$

where $D_{i,f}$ is the gas diffusivity of species i ($\mathrm{m^2\ s^{-1}}$), Sc is Schmidt number, Sh is Sherwood number, and γ is the shape factor (external surface area divided by πd_p^2).

Gas mixture viscosity μ_f

The gas mixture viscosity was calculated by Wilke's method described by the following correlation [114]:

$$\mu_f = \sum_{i=1}^{Nc} \frac{x_i \mu_i}{\sum_{j=1}^{Nc} x_j \Phi_{ij}} \tag{56}$$

$$\Phi_{ij} = \frac{\left[1 + \left(\mu_i/\mu_j\right)^{1/2} \left(M_j/M_i\right)^{1/4}\right]^2}{\sqrt{8}\left[1 + \left(M_i/M_j\right)\right]^{1/2}} \tag{57}$$

where μ_f (Pa s) is the viscosity of fluid mixture, μ_i (Pa s) is the viscosity of component i, M is the molecular weight. The first-order solution for the viscosity μ_i (μP) of pure gas i can be written as [115]:

$$\mu_i = 40.785 \frac{F_c (M_i T)^{\frac{1}{2}}}{V_c^{\frac{2}{3}} \Omega_v} \tag{58}$$

$$F_c = 1 - 0.2756\omega + 0.059035\mu_r^4 + \kappa \tag{59}$$

$$\kappa = 0.0682 + 4.704[(number\ of - OH\ groups)/(molecular\ weight)] \tag{60}$$

$$\mu_r = 131.3 \frac{\mu}{(V_c T_c)^{\frac{1}{2}}} \tag{61}$$

$$T^* = 1.2593 \frac{T}{T_c} \tag{62}$$

$$\Omega_v = [A(T^*)^{-B}] + C[\exp(-DT^*)] + E[\exp(-FT^*)] \tag{63}$$

where $A = 1.16145$, $B = 0.14874$, $C = 0.52487$, $D = 0.77320$, $E = 2.16178$ and $F = 2.43787$. Parameter required for the calculation of gas viscosities can be found in Table 2.3.

Gas component	V_c $(\mathbf{cm^3\ mol^{-1}})$	T_c (K)	ω	μ (D)
H_2	118.00	512.64	0.565	1.70
H_2O	55.95	647.14	0.344	1.84
CO_2	64.20	32.98	-0.217	0
CO	93.10	132.85	0.045	0.122
CH_3OH	94.07	304.12	0.225	0

Table 2.3 Parameters for the calculation of gas diffusivity and gas viscosity

2.2.2. EFFECTIVENESS FACTOR AS A FUNCTION OF THIELE MODULUS

Another common approach to calculate the effectiveness factor η is to obtain it as a function of the Thiele modulus ϕ. Here, the Thiele modulus ϕ is established to represent the relationship between diffusion and reaction rate in porous catalyst particles that were not subjected to mass transfer limitations. The following relations can be valid for studying the effects of the diffusion and reaction processes assuming isothermal spherical catalyst particles, pseudo-homogeneous diffusivity, and a pseudo-first-order reaction [101,116]:

$$\eta = \frac{3}{\phi_1^2}(\phi_1 \coth \phi_1 - 1) \tag{64}$$

For a first-order reaction, ϕ_1 is the Thiele modulus, which can be written as:

$$\phi_1^2 = \frac{r_j^s \rho_s r_p^2 S_c}{D_{i,\mathrm{ep}} C_i^s} \tag{65}$$

where r_j^s (mol m^{-2} s^{-1}) and C_i^s (mol m^{-3}) signify the rate of reaction j and the concentration of component i, respectively, when the internal surface is exposed to the surface conditions. r_p (m) is the catalyst pellet's radius, ρ_s (kg m^{-3}) is the density of catalyst bed, and $D_{i,\mathrm{ep}}$ (m^2 s^{-1}) is the effective diffusivity of component i inside catalyst pellets.

It can be observed that as the catalyst pellet size decreases, the Thiele modulus ϕ_1 turns smaller, bringing the effectiveness factor closer to 1 and indicating the reaction process to be surface reaction limited. On the contrary when the Thiele modulus ϕ_1 is big (e.g., ~30), the effectiveness factor will be minimal (e.g., ~0.1), and the reaction process can be characterized as diffusion limited [101]. Therefore, the Weisz-Prater criterion was proposed to determine whether the internal diffusion or the surface reaction limited the entire reaction process. The Weisz-Prater parameter C_{WP} can be expressed as:

$$\begin{aligned} C_{WP} = \eta \times \phi_1^2 &= \frac{\text{Observed (actual) reaction rate}}{\text{Reaction rate evaluated at } C_i^s} \times \frac{\text{Reaction rate evaluated at } C_i^s}{\text{A diffusion rate}} \\ &= \frac{\text{Observed (actual) reaction rate}}{\text{A diffusion rate}} \end{aligned} \tag{66}$$

Diffusion limits and concentration gradients within the catalyst pellet should be insignificant if $C_{WP} \ll 1$. Instead, if $C_{WP} \gg 1$, the internal diffusion limitations are believed to significantly limit the reaction.

2.3. CONTINUUM MODELS

In this system, the MSR process reaction rates are primarily influenced by local temperature and concentrations associated to heat and mass transfer processes, which should be considered before constructing a reactor. As the reactants flow through the packed bed, a variety of physical and chemical processes will occur in the reactor. It is virtually impossible to describe the enormous complexity of these phenomena using mathematical models. Therefore, several assumptions should be made to simplify the modeling of packed bed reactors by considering the accuracy and feasibility of the model and the particular phenomena dictating its most critical features [117]. The most crucial features for modeling a packed-bed reactor are the reaction rates in the catalyst bed and the transport phenomena that simultaneously occur in the catalyst

pellet, bulk fluid, and their interfaces. In this study, the transport phenomena involved in the catalyst bed are divided into the following categories [81]:

- intraparticle diffusion of heat and mass
- heat and mass exchange between the solid catalyst particles and the bulk fluid
- convective heat and mass transfer of the fluid
- heat and mass dispersion in the fluid phase
- thermal conduction in the solid phase
- heat exchange with the shell-side fluid

There are several types of models used to simulate the packed-bed reactors, and the continuum models are the most commonly used [81]. The classification of continuum models is shown in Table 2.4. It is widely accepted that continuum models can be divided into pseudo-homogeneous and heterogeneous models. Pseudo-homogeneous models do not explicitly account for the presence of catalyst particles, which means that no fluid-to-particle heat and mass transfer resistances are assumed. For heterogeneous models, in contrast to pseudo-homogeneous models, the conservation equations for both catalyst and bulk fluid should be considered separately.

		A. Pseudo-Homogeneous (T=Ts; c=cs)	B. Heterogeneous (T≠Ts; c≠cs)
Steady-state	One-dimensional	A.I Basic, plug-flow	B.I + interfacial gradients
		A.II + axial mixing	B.II + intraparticle gradients
	Two-dimensional	A.III + radial mixing	B.III + radial mixing
Dynamic		A.IV + time variable (t)	B.IV + time variable (t)

Table 2.4 Classification of packed bed reactor models

The models within each category are further classified according to the increasing complexity. The basic and most employed model is the one-dimensional pseudo-homogeneous model (A.I). In this model, the catalyst surface and the bulk fluid are regarded to have essentially the same conditions and are mathematically treated as a continuum. The reactants are considered to flow through the catalyst bed in a plug without radial or axial mixing, resulting in a uniform temperature and composition across the cross-section. Unlike the ideal one-dimensional pseudo-homogeneous model, the one-dimensional heterogeneous model considers the interfacial gradients of temperature and concentration between the bulk gas phase and the catalyst surface (B.I). Studies have shown that the temperature on the catalyst surface (T_s) significantly differs from that of the bulk fluid (T_b), but the concentration gradients are quite small under most practical conditions [118,119]. Therefore, this one-dimensional pseudo-homogeneous model can be transformed into a one-dimensional

heterogeneous model by simply adding the heat balance equation between the catalyst surface and the bulk fluid.

The axial mixing effects, caused by the transfer mechanisms such as the mixing due to the presence of packing, molecular diffusion, thermal conduction, and radiation etc, in tubular packed bed reactors can be investigated by introducing an effective axial thermal conductivity and effective axial mass diffusivity in one-dimension pseudo-homogeneous and heterogeneous models (A.II). However, the heat and mass dispersion in axial direction is often neglected in reactor models because it greatly increases the computational time without considerable improvement for the model accuracy [108]. For heterogeneous systems, heat and mass must first be transferred from the bulk fluid to the external surface of the catalyst particles and then through the pores within the particles, where the MSR reactions occur on catalyst surfaces of the pores (B.II) [101]. In this dissertation, the interphase and intraparticle heat and mass transfer limitations are taken into account to represent the two-step diffusion process for a catalyst particle. The effects of the particle size or the intraparticle temperature and concentration profiles can be investigated by calculating heat and mass balance equations within a catalyst pellet.

Two-dimensional models (A.III and B.III) are recommended, especially for heat exchanger reactors (non-adiabatic) with considerable minimum or maximum temperature excursions in catalyst bed, which result in significant radial temperature and concentration gradients. For MSR reactors (endothermic system), the extent of hot spots in catalyst beds requires special attention and can be predicted by such two-dimension models. Despite the fact that actual radial transport mechanisms are extremely complex, the radial heat and mass transfer can be calculated by introducing an effective radial diffusivity and effective radial conductivity and by defining some reasonable simplifications.

Besides the steady-state reactor models, the dynamic models can be developed by describing how some time-dependent variables change over time. Usually, the dynamic models convey more information about the reformer performance than the steady state ones. They can be used to study important practical problems including on-line optimal control [120,121], start-up and shut down [122], transients during process disturbances [123], process design and safety [78,124], and catalyst deactivation [125]. Typically, the dynamic models consist of several partial differential equations (PDEs). The most common way to solve the PDEs is to reduce them to a set of ordinary differential equations (ODEs) and use the well-known algorithms for ODEs to solve the time-dependent models [126]. Table 2.5 shows the conservation equations (and pressure drop equation) of typical models with their initial conditions (ICs), boundary conditions (BCs) and assumptions for MSR reactors.

Model	Equations	Assumptions
One-dimensional, ideal plug-flow, pseudo-homogeneous, steady-state model	$u_s \frac{dC_i}{dz} = -R_i(C,T)$ $u_s \rho_f c_p \frac{dT}{dz} = R_T(C,T) - \frac{4U_w}{d_t}(T - T_w)$ $\frac{dP}{dz} = -\frac{u_s}{\rho_f d_p}\left(\frac{1-\varepsilon}{\varepsilon^3}\right)\left[\frac{150(1-\varepsilon)\mu_f}{d_p} + 1.75u_s\right]$ Initial conditions: $z = 0: \quad C_i = C_{i,0}, T = T_0, P = P_0$	• Ideal gas behaviour • Negligible radial and axial dispersions • Negligible interphase gradients • Negligible intraparticle gradients • Constant bed void fraction in reactors • No deactivation of catalysts
One-dimensional, plug-flow, heterogeneous, steady-state model	Fluid phase: $u_s \frac{dC_i}{dz} = k_f a_v (C_i^s - C_i)$ $u_s \rho_f c_p \frac{dT}{dz} = h_f a_v (T^s - T) - \frac{4U_w}{d_t}(T - T_w)$ Solid phase: $k_f a_v (C_i^s - C_i) = -R_i(C^s, T^s)$ $h_f a_v (T^s - T) = R_T(C^s, T^s)$ Initial conditions: $z = 0: \quad C_i = C_{i,0}, T = T_0, P = P_0$	• Ideal gas behaviour • Negligible radial and axial dispersions • Negligible intraparticle gradients • Negligible direct thermal conduction between simple-shape particles • Constant bed void fraction in reactors • No deactivation of catalysts
One-dimensional, heterogeneous, steady-state model with axial dispersions	Fluid phase: $u_s \frac{dC_i}{dz} - D_{ez} \frac{d^2 C_i}{dz^2} = k_f a_v (C_i^s - C_i)$	• Ideal gas behaviour • Negligible radial dispersions

	$u_s\rho_f c_p \frac{dT}{dz} - \lambda_{ez}\frac{d^2T}{dz^2} = h_f a_v(T^s - T) - \frac{4U_w}{d_t}(T - T_w)$ Solid phase: $k_f a_v(C_i^s - C_i) = -R_i(C^s, T^s)$ $h_f a_v(T^s - T) = R_T(C^s, T^s)$ Boundary conditions: $z = 0$: $u_s C_{i,0} = u_s C_i - D_{ez}\frac{dC_i}{dz}$ $u_s\rho_f c_p T_0 = u_s\rho_f c_p T - \lambda_{ez}\frac{dT}{dz}$ $z = L$: $\frac{dC_i}{dz} = 0$ $\frac{dT}{dz} = 0$	• Negligible intraparticle gradients • Constant bed void fraction in reactors • No deactivation of catalysts
One-dimensional, plug-flow, steady-state model accounting for interface and intraparticle resistances for simple shape particles	Bulk fluid: $u_s\frac{dC_i}{dz} = k_f a_v\left(C_i^{s,s} - C_i\right)$ $u_s\rho_f c_p \frac{dT}{dz} = h_{fs} a_v(T^{s,s} - T) - \frac{4U_w}{d_t}(T - T_w)$ Catalyst particle: $\frac{D_{ep}}{\xi^p}\frac{\partial}{\partial\xi}\left(\xi^p\frac{\partial C_i^s}{\partial\xi}\right) = -R_i(C^s, T^s)$ $\frac{\lambda_{ep}}{\xi^p}\frac{\partial}{\partial\xi}\left(\xi^p\frac{\partial T^s}{\partial\xi}\right) = R_T(C^s, T^s)$	• Ideal gas behaviour • Negligible radial dispersions • Constant bed void fraction in reactors • No deactivation of catalysts • Uniform size, porosity, and activity of catalyst particles.

	Boundary conditions: $z = 0$: $C_i = C_{i,0}, T = T_0$ $\xi = 0$: $\frac{\partial C_i^s}{\partial \xi} = 0, \frac{\partial T}{\partial \xi} = 0$ $\xi = \frac{d_p}{2}$: $-D_{ep}\frac{\partial C_i^s}{\partial \xi} = k_f(C_i^s - C_i)$ $-\lambda_{ep}\frac{\partial T^s}{\partial \xi} = h_{fs}(T^s - T)$	
Two-dimensional, plug-flow, pseudo-homogeneous, steady-state model	$u_s\frac{\partial C_i}{\partial z} - \frac{D_{er}}{r}\frac{\partial}{\partial r}\left(r\frac{\partial C_i}{\partial r}\right) = -R_i(C,T)$ $u_s\rho_f c_p\frac{\partial T}{\partial z} - \frac{\lambda_{er}}{r}\left(r\frac{\partial T}{\partial r}\right) = R_T(C,T)$ Boundary conditions: $z = 0$: $C_i = C_{i,0}, T = T_0$ $r = 0$: $\frac{\partial C_i}{\partial r} = 0, \frac{\partial T}{\partial r} = 0$ $r = \frac{d_t}{2}$: $\frac{\partial C_i}{\partial r} = 0$ $\frac{\partial T}{\partial r} = -Bi(T - T_w)$	• Ideal gas behaviour • Negligible axial dispersions • Negligible interphase gradients • Negligible intraparticle gradients • Constant bed void fraction in reactors • No deactivation of catalysts
Two-dimensional, plug-flow, heterogeneous, steady-state model	$u_s\frac{\partial C_i}{\partial z} - \frac{D_{er}}{r}\frac{\partial}{\partial r}\left(r\frac{\partial C_i}{\partial r}\right) = k_f a_v(C_i^s - C_i)$ $u_s\rho_f c_p\frac{\partial T}{\partial z} - \frac{\lambda_{er}^f}{r}\left(r\frac{\partial T}{\partial r}\right) = h_f a_v(T^s - T)$	• Ideal gas behaviour • Negligible axial dispersions • Negligible intraparticle gradients

41

	$k_f a_v(C_i^s - C_i) = -R_i(C^s, T^s)$ $h_f a_v(T^s - T) = R_T(C^s, T^s) + \frac{\lambda_{er}^s}{r}\left(r\frac{\partial T^s}{\partial r}\right)$ Boundary conditions: $z = 0$: $C_i = C_{i,0}, T = T_0$ $r = 0$: $\frac{\partial C_i}{\partial r} = 0, \frac{\partial T}{\partial r} = \frac{\partial T^s}{\partial r} = 0$ $r = \frac{d_t}{2}$: $\frac{\partial C_i}{\partial r} = 0$ $\frac{\partial T}{\partial r} = -Bi_f(T - T_w)$ $\frac{\partial T^s}{\partial r} = -Bi_s(T - T_w)$	• Constant bed void fraction in reactors • No deactivation of catalysts
One-dimensional, plug-flow, pseudo-homogeneous, dynamic model with axial dispersions	$\varepsilon\frac{\partial C_i}{\partial t} = -u_s\frac{\partial C_i}{\partial z} + \frac{\partial}{\partial z}\left(D_{ez}\frac{\partial C_i}{\partial z}\right) - R_i(C,T)$ $\left(\varepsilon\rho_f c_{p,f} + (1-\varepsilon)\rho_s c_{p,s}\right)\frac{\partial T}{\partial t} = -u_s\rho_f c_p\frac{\partial T}{\partial z} + \frac{\partial}{\partial z}\left(\lambda_{ez}\frac{\partial T}{\partial z}\right) + R_T(C,T) - \frac{4U_w}{d_t}(T - T_w)$ Boundary conditions: $t = 0$: $C_i = C_i^0, T = T^0$ $z = 0$: $u_s C_{i,0} = u_s C_i - D_{ez}\frac{\partial C_i}{\partial z}$	• Ideal gas behaviour • Negligible radial dispersions • Negligible interphase gradients • Negligible intraparticle gradients • Constant bed void fraction in reactors • No deactivation of catalysts

	$u_s\rho_f c_p T_0 = u_s\rho_f c_p T - \lambda_{ez}\frac{\partial T}{\partial z}$ $z = L$: $\frac{\partial C_i}{\partial z} = 0$ $\frac{\partial T}{\partial z} = 0$	
Two-dimensional, plug-flow, pseudo-homogeneous, dynamic model	$\varepsilon\frac{\partial C_i}{\partial t} = -u_s\frac{\partial C_i}{\partial z} + \frac{\partial}{\partial z}\left(D_{ez}\frac{\partial C_i}{\partial z}\right) + \frac{D_{er}}{r}\frac{\partial}{\partial r}\left(r\frac{\partial C_i}{\partial r}\right) - R_i(C,T)$ $\left(\varepsilon\rho_f c_{p,f} + (1-\varepsilon)\rho_s c_{p,s}\right)\frac{\partial T}{\partial t} = -u_s\rho_f c_p\frac{\partial T}{\partial z} + \frac{\partial}{\partial z}\left(\lambda_{ez}\frac{\partial T}{\partial z}\right) + \frac{\lambda_{er}}{r}\left(r\frac{\partial T}{\partial r}\right) + R_T(C,T) - \frac{4U_w}{d_t}(T - T_w)$ Boundary conditions: $t = 0$: $C_i = C_i^0, T = T^0$ $z = 0$: $u_s C_{i,0} = u_s C_i - D_{ez}\frac{\partial C_i}{\partial z}$ $u_s\rho_f c_p T_0 = u_s\rho_f c_p T - \lambda_{ez}\frac{\partial T}{\partial z}$ $z = L$: $\frac{\partial C_i}{\partial z} = 0$ $\frac{\partial T}{\partial z} = 0$	• Ideal gas behaviour • Negligible interphase gradients • Negligible intraparticle gradients • Constant bed void fraction in reactors • No deactivation of catalysts

43

	$r = 0$: $\frac{\partial C_i}{\partial r} = 0, \frac{\partial T}{\partial r} = 0$ $r = \frac{d_t}{2}$: $\frac{\partial C_i}{\partial r} = 0$ $\frac{\partial T}{\partial r} = -Bi(T - T_w)$	

Table 2.5 Typical models for packed-bed reactors

2.3.1. ONE-DIMENSIONAL PSEUDO-HOMOGENEOUS MODEL

To evaluate the performance of a multi-tubular packed bed MSR reformer, a one-dimensional pseudo-homogeneous model was developed using MATLAB®. In most simulation studies, the performance of a single-tube reactor is studied assuming a constant wall temperature [127–129]. However, in industrial applications, there is typically a bundle of tubes in a MSR reformer. The temperature of the shell-side fluid is also non-uniformly distributed in the axial direction, which significantly affects the performance of the reactor. In this study, the multi-tubular packed-bed MSR reformer is set up as a co-current plug-flow heat exchanger reactor as shown in Figure 2.3. It is assumed that:

- steady-state;
- uniform distribution of shell-side fluid in the radial direction;
- ideal gas behaviour;
- negligible radial and axial dispersions (plug-flow);
- negligible interphase and intraparticle transfer resistances;
- constant bed void fraction;
- no deactivation of catalysts.

Moreover, all the parallel tubes in the multi-tubular reformer are assumed to have the same performance as a single reactor tube, which is simulated in this study. The heat transfer coefficient is considered between the tube and shell sides. The porous cylindrical catalyst particles are randomly packed inside the reactor tubes. The axial pressure drop in the reactor is also included in this model.

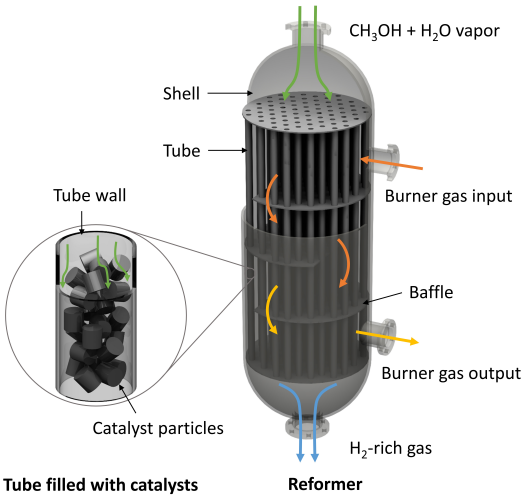

Figure 2.3 Schematic diagram of a multi-tubular packed-bed reactor packed with porous cylindrical catalyst particles

Steady-state mass and energy balance

Only the axial profiles of radially averaged temperatures and concentrations are considered in the one-dimensional pseudo-homogeneous model. The following mole-balance equation gives the continuity equation for the species i in the catalyst bed:

$$u_s \frac{dC_i}{dz} = -\eta_i \rho_c r_i \tag{67}$$

where u_s (m s^{-1}) is the superficial velocity of the fluid phase, C_i (mol m^{-3}) is the concentration of species i in the fluid phase, z (m) is the axial position of the reactor tube, η_i is the effectiveness factor for the production (consumption) of species i, ρ_c (kg m^{-3}) is the density of catalyst bed, and r_i (mol s^{-1}(kg of catalyt)$^{-1}$) is the production (consumption) rate of species i per unit catalyst weight.

The steady-state energy balance equation in the tube side is written as:

$$u_s \rho_f c_p \frac{dT}{dz} = \sum_{j=R,W,D} \eta_j \rho_c \left(-\Delta H_j\right) r_j S_c - \frac{4U_w}{d_t}(T - T_b) \tag{68}$$

where ρ_f (kg m^{-3}) is the fluid density, c_p (J $kg^{-1}K^{-1}$) is the specific heat capacity of the fluid phase, η_j is the effectiveness factor for the reaction j, ΔH_j (J mol^{-1}) is the heat consumed by the reaction j, r_j (mol $m^{-2}s^{-1}$) is the reaction rate of reaction j, U_w (W $m^{-2}K^{-1}$) is the overall heat transfer coefficient between the tube and shell sides, d_t (m) is the tube diameter, T (K) is the operating temperature in the catalyst bed, and T_b (K) is the burner gas temperature in the shell side.

The steady-state energy balance equation in the shell side is written as:

$$u_{s,b} \rho_{f,b} c_{p,b} \frac{dT_b}{dz} = N_t \frac{4U_w}{d_t}(T - T_b) \tag{69}$$

where u_s (m s^{-1}) is the superficial velocity of the burner gas, $\rho_{f,b}$ (kg m^{-3}) is the density of the burner gas, $c_{p,b}$ (J $kg^{-1}K^{-1}$) is the specific heat capacity of the burner gas, and N_t is the number of tubes in the reformer.

Pressure drop

In this research, a collection of uniformly sized porous cylindrical catalyst particles is put inside cylindrical reactor tubes. Pressure changes generally have little effect on the overall performance of the model. Nonetheless, especially when the catalyst particle size is small, the pressure drop may be crucial in determining the reactor's operating costs (e.g. pump power consumption) [81]. The pressure drop in the catalyst bed can be approximately calculated by the semiempirical Ergun equation [101]:

$$\frac{dP}{dz} = -\frac{u_s}{\rho_f d_p}\left(\frac{1-\varepsilon}{\varepsilon^3}\right)\left[\frac{150(1-\varepsilon)\mu_f}{d_p} + 1.75u_s\right] \tag{70}$$

where P (Pa) is the operating pressure in the catalyst bed.

Specific heat capacity

The specific heat capacity of the gas mixture is calculated as follow:

$$C_{p,mix} = \sum_{i=1}^{Nc} C_{p,i} y_i \tag{71}$$

where $C_{p,mix}$ (J mol^{-1}K^{-1}) is the specific heat capacity of the multicomponent mixture, Nc is the number of components in gas mixture, and $C_{p,i}$ (J mol^{-1}K^{-1}) is the specific heat capacity of component i, which can be calculated using the following relationship and data for parameters a, b, c, d and e:

$$t = \frac{T}{1000} \tag{72}$$

$$C_{p,i} = a + b \times t + c \times t^2 + d \times t^3 + e \times \left(\frac{1}{t}\right)^2 \tag{73}$$

where the values of constants a, b, c, d and e are given in Table 2.6.

Gas component	a	b	c	d	e
H_2	33.066178	-11.363417	11.432816	-2.772874	-0.158558
H_2O	30.92000	6.832514	6.7934356	-2.534480	0.0821398
CO_2	24.99735	55.18696	-33.69137	7.948387	-0.136638
CO	25.56759	6.096130	4.054656	-2.671301	0.131021
CH_3OH	13.93945	111.30774	-41.59074	5.482564	0.052037

Table 2.6 Constants for components's specific heat capacity

Reaction enthalpy

The temperature dependence of reaction enthalpies (J mol^{-1}) can be presented as:

$$\Delta H_R = 4.95 \times 10^4 + \left(C_{P,CO_2} + 3 \times C_{P,H_2} - C_{P,CH_3OH} - C_{P,H_2O}\right) \times (T - 298) \tag{74}$$

$$\Delta H_D = 9.07 \times 10^4 + \left(C_{P,CO} + 2 \times C_{P,H_2} - C_{P,CH_3OH}\right) \times (T - 298) \quad (75)$$

$$\Delta H_W = -4.12 \times 10^4 + \left(C_{P,CO_2} + C_{P,H_2} - C_{P,H_2O} - C_{P,CO}\right) \times (T - 298) \quad (76)$$

Overall heat transfer coefficient

As can be seen from the cross-section of a single tube (in Figure 2.4), the heat exchange between the shell side and the tube side can be divided into three steps which occur in three regions with drastic temperature changes. These regions, including (1) the fluid film on the inside of the tube, (2) the wall of the tube, and (3) the fluid film on the outside of the tube, are associated with three types of heat transfer resistance. Assuming the steady-state heat transfer, the overall heat transfer coefficient U_w ($\mathrm{W\,m^{-2}K^{-1}}$) through the tube wall can be described by [130]:

$$\frac{1}{U_w} = \frac{1}{h_t} + \frac{x_w}{k_w}\frac{d_{t,i}}{d_{lm}} + \frac{1}{h_s}\frac{d_{t,i}}{d_{t,o}} \quad (77)$$

where h_t ($\mathrm{W\,m^{-2}\,K^{-1}}$) is the heat transfer coefficient in the tube-side film, h_s ($\mathrm{W\,m^{-2}\,K^{-1}}$) is the heat transfer coefficient in the shell-side film, $d_{t,i}$ (m) is the inner diameter of the reactor tube, $d_{t,o}$ (m) is the outer diameter of the reactor tube, x_w (m) is the thickness of the tube wall, k_w ($\mathrm{W\,m^{-1}K^{-1}}$) is the thermal conductivity of the tube wall, and d_{lm} (m) is the log-mean diameter which is expressed as:

$$d_{lm} = \frac{d_{t,o} - d_{t,i}}{\ln\left(d_{t,o}/d_{t,i}\right)} \quad (78)$$

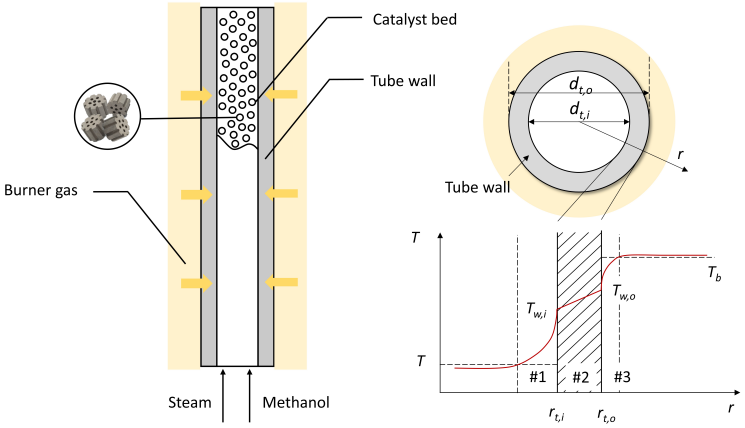

Figure 2.4 Scheme of a single reactor tube

The heat transfer resistance between the tube wall and the catalyst bed is mainly caused by the gas film. According to the study of Mears et al. [131], the heat transfer resistance between the tube wall and the catalyst bed should be considered when the

ratio of tube to particle diameter is small ($D/d_p < 100$). Therefore, the heat transfer coefficient of the inner film h_t is calculated in this study as:

$$h_t = \left(0.4R_e^{\frac{1}{2}} + 0.2R_e^{\frac{2}{3}}\right) P_r{}^{0.4} \frac{1-\varepsilon}{\varepsilon} \frac{k_m}{d_p} \tag{79}$$

where R_e is the Reynolds number, P_r is the Prandtl number, ε is the void fraction of the catalyst bed, and k_m (W m^{-1}K^{-1}) is the thermal conductivity of the gas mixture inside tubes. For the catalyst packed bed, the Reynolds number is defined as:

$$R_e = \frac{d_p G}{\mu_f} \frac{1}{1-\varepsilon} \tag{80}$$

The Donohue equation is widely used to estimate the heat transfer coefficient h_s in the shell-side film of a shell-tube heat exchanger:

$$h_s = 0.2 \left(\frac{d_{t,o} G_e}{\mu_s}\right)^{0.6} \left(\frac{c_{p,s}\mu_s}{k_s}\right)^{0.33} \frac{k_s}{d_{t,o}} \tag{81}$$

$$G_e = \sqrt{G_b G_p} \tag{82}$$

$$G_b = \frac{\dot{m}_s}{S_b} \tag{83}$$

$$S_{ba} = f_b \left(\frac{\pi d_s^2}{4}\right) - N_b \left(\frac{\pi d_{t,o}^2}{4}\right) \tag{84}$$

$$G_p = \frac{\dot{m}_s}{S_p} \tag{85}$$

$$S_{pe} = P_b d_s \left(1 - \frac{d_{t,o}}{p_t}\right) \tag{86}$$

where the G_e (kg m^{-2}s^{-1}) is the mass velocity of gas mixture, G_b (kg m^{-2}s^{-1}) is the mass velocity through the baffle window, and G_p (kg m^{-2}s^{-1}) is the mass velocity for crossflow perpendicular to the tubes. Moreover, S_{ba} (m^2) is the area available for the shell-side fluid flow through the baffle window, and S_{pe} (m^2) is the interstitial area available for crossflow perpendicular to the bank of tubes at the widest point in the shell. In addition, k_s (W m^{-1}K^{-1}) is thermal conductivity of the shell-side fluid, $c_{p,s}$ (J kg^{-1}K^{-1}) is the specific heat capacity of the shell-side fluid, $\dot{m}_s$ (kg s^{-1}) is the mass flow rate of shell-side fluid, and μ_s (Pa s) is the average viscosity of the shell-side fluid. As for geometric parameters, d_s (m) is the diameter of the reformer shell,

p_t (m) is the tube pitch, P_b (m) is the baffle spacing, f_b is the area fraction of baffle plate that is window (for 25% baffle plate, $f_b = 0.1955$), and N_b is the number of tubes in baffle window. Figure 2.5 illustrates the different geometric parameters of the reformer.

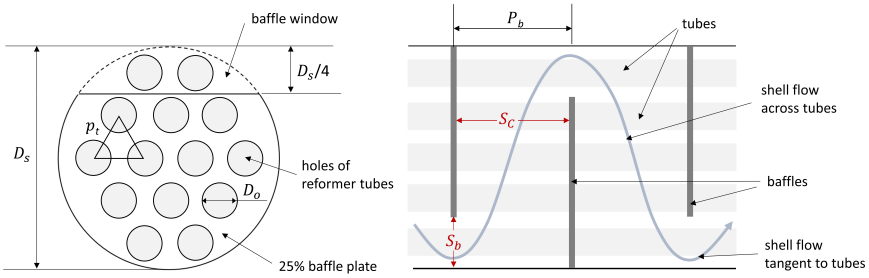

Figure 2.5 Arrangement of tubes and baffles in the shell of reformer

2.3.2. TWO-DIMENSIONAL PSEUDO-HOMOGENEOUS MODEL

In this study, a two-dimensional pseudo-homogeneous model for a pilot-scale multi-tubular packed-bed MSR reactor was developed using MATLAB®. The assumptions adopted in this model are as follows:

- absence of axial heat and mass dispersion (plug flow);
- no temperature or concentration gradients between the particle's exterior surface and the bulk fluid (pseudo-homogeneous);
- variation of the burner gas temperature along the axial direction;
- uniform size, porosity, and activity of catalyst particles;
- constant bed void fraction throughout the entire catalyst bed;
- effectiveness factors for considering intraparticle diffusion resistances;
- no deactivation of catalysts.

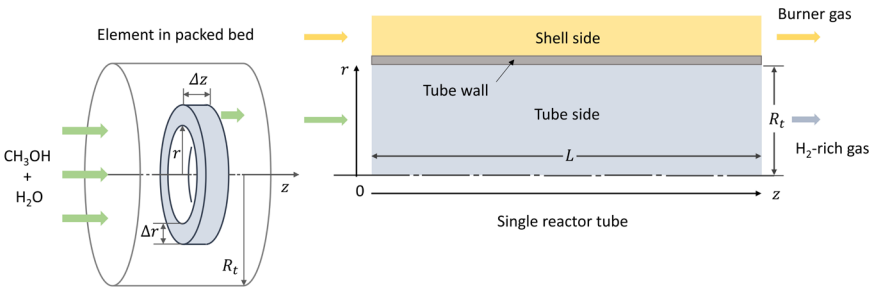

Figure 2.6 An element in packed bed experiencing radial transport and axial flow

This steady-state model considering the typical transport and chemical reaction phenomena in the catalyst bed was developed to investigate the profiles of temperature and concentrations along the length and across the cross-section of the reactor tube. As shown in Figure 2.6, the general steady-state equations in the packed-bed reactor are solved in two-dimensional axi-symmetrical cylindrical coordinates. The mass and energy balance equation are expressed as:

Mass balance

$$u_s \frac{\partial C_i}{\partial z} = D_{er}\left(\frac{\partial^2 C_i}{\partial r^2} + \frac{1}{r}\frac{\partial C_i}{\partial r}\right) + \eta_i \rho_c r_i \tag{87}$$

Energy balance

$$u_s \rho_f C_{p,f} \frac{\partial T}{\partial z} = \lambda_{er}\left(\frac{\partial^2 T}{\partial r^2} + \frac{1}{r}\frac{\partial T}{\partial r}\right) + \sum \eta_j \rho_c \left(-\Delta H_j\right) r_j S_c \tag{88}$$

where D_{er} ($\mathrm{m^2\ s^{-1}}$) is the effective radial mass diffusion coefficient and λ_{er} ($\mathrm{W\ m^{-1}\ K^{-1}}$) is the effective thermal conductivity in the radial direction.

The initial and boundary conditions are given as follows:

$$\begin{aligned} c = c_0, T = T_0 \quad & \text{at } z = 0, 0 \le r \le R_t \\ \frac{\partial c}{\partial r} = 0 \quad & \text{at } r = 0 \text{ and } r = R_t \\ \frac{\partial T}{\partial r} = 0 \quad & \text{at } r = 0, \text{ all } z \\ \frac{\partial T}{\partial r} = -\frac{U_t}{\lambda_{er}}(T - T_s) \quad & \text{at } r = R_t \end{aligned} \tag{89}$$

The reactor tubes are heated by a co-current burner gas stream on the shell side of the reformer. The temperature of the shell-side burner gas is considered to be non-isothermal in the axial direction of the reactor. A simple one-dimensional steady-state model that account for the energy balance in the shell-side burner gas can be expressed as:

$$u_{s,b} \rho_{f,b} c_{p,b} \frac{dT_b}{dz} = N_t \frac{4U_w}{d_t}(T - T_b) \tag{90}$$

where u_s (m s^{-1}) is the superficial velocity of the burner gas, $\rho_{f,b}$ (kg m^{-3}) is the density of the burner gas, $c_{p,b}$ (J $kg^{-1}K^{-1}$) is the specific heat capacity of the burner gas, and N_t is the number of tubes in the reformer.

Effective radial diffusion coefficient in packed bed D_{er}

The effective radial diffusion coefficient D_{er} (m^2 s^{-1}) in packed bed can be calculated by [81,132,133]:

$$D_{er} = \frac{u_s d_p}{11\left[1 + 19.4\left(\frac{d_p}{d_{t,i}}\right)^2\right]} \tag{91}$$

where d_p (m) is the diameter of catalyst particle, $d_{t,i}$ (m) is the inner diameter of reactor tubes.

Radial thermal conductivity in packed bed λ_{er}

The radial heat transfer in the packed bed can be evaluated by the effective radial thermal conductivity λ_{er} (W m^{-1} K^{-1}) according to the following expression [108]:

$$\lambda_{er} = \lambda_r^0 + \lambda_r^f \tag{92}$$

where λ_r^0 is the effective stagnant thermal conductivity due to molecular heat conduction in the fluid and the solid phase, which is independent of the fluid velocity, and λ_r^f is the effective thermal conductivity due to fluid convection.

The above equation is usually expressed in a dimensionless form by using a molecular Peclet number:

$$\frac{\lambda_{er}}{\lambda_f} = \frac{\lambda_r^0}{\lambda_f} + \frac{Pe_h^0}{Pe_{h,r}^\infty} \tag{93}$$

where λ_f is the thermal conductivity of the fluid, Pe_h^0 is fluid Peclet number for heat transfer, and $Pe_{h,r}^\infty$ is Peclet radial heat transfer for fully developed turbulent flow. The values of Pe_h^0 and $Pe_{h,r}^\infty$ can be calculated as:

$$\mathrm{Pe}_h^0 = \frac{u_s \rho_f c_{p,f} d_p^v}{\lambda_f} = RePr \tag{94}$$

$$Pe_{h,r}^{\infty} = 8\left[2 - \left(1 - \frac{2}{N}\right)^2\right] \tag{95}$$

where N is the aspect ratio, or the number of particles on the tube diameter:

$$N = \frac{d_{t,i}}{d_p^v} \tag{96}$$

The correlation for the stagnant thermal conductivity in packed beds λ_r^0 is given by [108,134]:

$$\frac{\lambda_r^0}{\lambda_f} = \left(1 - \sqrt{1-\varepsilon}\right) + \frac{2\sqrt{1-\varepsilon}}{1 - B\kappa^{-1}}\left[\frac{B(1-\kappa^{-1})}{(1-B\kappa^{-1})^2}\ln\left(\frac{\kappa}{B}\right) - \frac{B-1}{1-B\kappa^{-1}} - \frac{B+1}{2}\right] \tag{97}$$

$$B = C_f\left(\frac{1-\varepsilon}{\varepsilon}\right)^{\frac{10}{9}} \tag{98}$$

$$C_f = 1.25\ \text{(sphere)},\ \ 2.5\ \text{(cylinder) or}\ 2.5\left(1 + \frac{d_i}{d_p}\right)\ \text{(rings)} \tag{99}$$

where κ is the ratio of the thermal conductivity of the solid catalyst particle and the gas fluid:

$$\kappa = \frac{\lambda_p}{\lambda_f} \tag{100}$$

For CuO/ZnO/Al_2O_3 cylinder catalyst particles with a diameter of $d_p = 5.5$ mm, the thermal conductivity of catalyst particles can be assumed as linearly dependent on temperature based on the study of Bert Koning [108]:

$$\lambda_p = 0.21 + 1.5 \times 10^{-4} T \tag{101}$$

Because the effect of particle size on effective thermal conductivity of packed beds is approved to be insignificant [109,110], the above equation can be used to calculate λ_p in our study.

The thermal conductivity of gas mixture λ_f can be calculated by:

$$\lambda_f = \sum_{i=1}^{Nc} \frac{x_i \lambda_i}{\sum_{j=1}^{Nc} x_j \Phi_{ij}} \tag{102}$$

$$\Phi_{ij} = \left(\frac{M_j}{M_i}\right)^{\frac{1}{2}} = {\Phi_{ji}}^{-1} \tag{103}$$

where λ_i (mW $m^{-1}K^{-1}$) is the thermal conductivity of the component i, which can be calculated by:

$$\lambda_i = a + b \times T + c \times T^2 + d \times T^3 + e \times \left(\frac{1}{T}\right)^2 \tag{104}$$

where the constants for thermal conductivities can be found in Table 2.7.

Gas component	a	b	c	d	e
CO_2	0.6395	0.0190	1.5214e-04	-1.1666e-07	7.8815e-05
CO	0.0185	0.0918	-3.1038e-05	8.1127e-09	9.7460e-07
H_2	-11.9000	0.8870	-9.2345e-04	5.6111e-07	-0.0026
CH_3OH	8.0364e-05	0.0130	1.4250e-04	-2.8336e-08	1.2646e-09
H_2O	0.4365	0.0529	1.0053e-05	4.8426e-08	2.3506e-05

Table 2.7 Constants for components's thermal conductivity

2.4. SIMULATION METHODS

The MSR models are established in MATLAB®, where the temperature and concentrations of main gas species in the catalyst bed are defined as functions of radial (r) and axial (z) coordinates. In addition, when considering the intraparticle diffusion limitations, the temperature and concentrations within the catalyst particle are defined as functions of the radial coordinate (ξ).

For the one-dimensional steady-state pseudo-homogeneous model, we can obtain the axial temperature and concentration profiles in the catalyst bed by solving the ordinary differential equations (ODEs) using Simulink or MATLAB®.

To numerically estimate the intraparticle distributions of temperature and concentrations, the heat and mass balance equations inside a catalyst particle, which contains a system of second-order ODEs, should be solved. In this study, it is treated as a boundary value problem in this study, so these ODEs can be solved by using the bvp4c function in MATLAB®.

For the two-dimension steady-state pseudo-homogeneous model, the heat and mass transfer phenomena are described by a set of partial differential equations (PDEs). The method of lines (MOL) is applied to solve the PDEs in this study. This method for solving PDEs has been described in detail in the work of Schiesser et al. [135] with excellent examples and MATLAB scripts. The MOL's core idea is to use finite differences (FDs) to replace the PDE spatial (boundary-value) partial derivatives with algebraic approximations (FDs). A second-order upwind FD approximation was used in this model. A system of ODEs thus approximates the original PDE system with only one remaining independent variable. In addition to this method, the pdepe function (PDE solver) in MATLAB® can be used to solve the system of PDEs. However, the pdepe function can only be used to solve certain types of problems (e.g., initial-boundary value problems for systems of parabolic and elliptic PDEs), hence it has less flexibility than the MOL.

2.5. SUMMARY

This chapter has described the mathematical models developed to simulate the MSR process in the catalytic packed bed reactor. The comprehensive Langmuir-Hinshelwood kinetic model based on the studies of Peppley et al. [89,90] was proposed to express the rate of MSR, WGS and MD reactions. Due to the porous structure of the catalyst, not all the catalytically active surface are exposed to the bulk conditions. Therefore, the reaction-diffusion process within a catalyst particle was modelled considering both the interphase and intraparticle transfer resistances. The expressions of the solid-fluid heat transfer coefficient h_{fs}, solid-fluid mass transfer coefficient $k_{i,fs}$, particle effective thermal conductivity λ_{ep}, and particle effective diffusivity $D_{i,ep}$ were described in this chapter. Since the catalyst particles used in this study is cylindrical, the volume-equivalent (surface-equivalent) spherical diameter was introduced to simplify the calculations. This is because the sphere is a well-understood geometric shape and can be simplify characterised by a single dimension (its radius or diameter). Another method to estimate the effectiveness factor by regarding the effectiveness factor as a function of the Thiele modulus was also explained in this chapter.

Furthermore, eight classical continuum models and their assumptions were listed in this chapter. Among them, the steady-state one-dimensional pseudo-homogeneous model and the steady-state two-dimensional pseudo-homogeneous model were described and developed specifically in this study. For the one-dimensional model, it is referred to be a plug-flow model. The heat exchange between the shell and tube sides were expressed by the heat transfer coefficient U taking into account the shell-and-tube structure of the reformer. The pressure drop in the axial direction through the catalyst bed was also calculated by Ergun equation. This one-dimensional pseudo-homogeneous model can be extended to a two-dimensional pseudo-homogeneous model by accounting for the radial gradients of temperature and concentrations. The

calculations of effective radial diffusion coefficient D_{er} and the radial thermal conductivity λ_{er} in the catalyst bed were described in this chapter.

In addition to these models, this chapter reported the simulation methods used in MATLAB® to solve the systems of differential equations. In this study, the ode15s function was used to solve the systems of ODEs, the bvp4c function was used to solve the boundary value problem, and the MOL and pdepe function were used to solve the system of PDEs.

CHAPTER 3. SIMULATION RESULTS OF THE ONE-DIMENSIONAL MODEL

A one-dimensional pseudo-homogeneous model of the multi-tubular packed-bed reformer has been developed in this work. According to the simulation results, the performance of the reformer is mainly affected by the inlet temperatures of the burner gas, the pressure in the catalyst bed, the molar ratio of steam to carbon (S/C), and the ratio of catalyst weight to the molar flow rate of methanol (W_{cat}/F_{CH_3OH}). The hydrogen yield and selectivity of the reformer are critical factors when designing an MSR reformer for onboard hydrogen production in an RMFC system. Additionally, attentions should be paid to the methanol and CO concentrations in the reformate gas due to their poisoning effects on HT-PEM fuel cells.

3.1. SIMULATION RESULTS OF THE ONE-DIMENSIONAL MODEL

The steady-state one-dimensional pseudo-homogeneous model has been developed in this study with the reactor specifications and operating conditions given in Table 3.1. It is considered a plug flow model that takes into account the reaction kinetics, pressure drop, and mass and heat balance in the catalyst bed.

Parameter	Value
Diameter of cylindrical catalyst particles, d_p (m)	1.5×10^{-3}
Height of cylindrical catalyst particle, h (m)	1.5×10^{-3}
Density of catalyst, ρ_c (kg m^{-3})	1300
BET area, S_c $(\text{m}^2\text{kg}^{-1})$	102000
Average pore diameter, Å (m)	6.4×10^{-9}
Void fraction of catalyst bed, ε	0.38
Concentration of active site '1', C_{S1}^T (mol m^{-2})	7.5×10^{-6}
Concentration of active site '1a', C_{S1a}^T (mol m^{-2})	1.5×10^{-5}
Concentration of active site '2', C_{S2}^T (mol m^{-2})	7.5×10^{-6}

Concentration of active site '2a', C_{S2a}^{T} (mol m^{-2})	1.5×10^{-5}
Operating temperature of catalyst bed, T (K)	$503 - 563$
Molar ratio of steam to methanol, S/C	1.3
Pressure in catalyst bed, P (bar)	1
Tube dimension, (m)	0.016×0.001
Number of tubes, N_t	36
Tube pitch, p_t (m)	0.027
Diameter of reformer shell, D_s (m)	0.24
Spacing between baffle plates, P_b (m)	0.12
Number of baffle plates, N_b	4
Reactor length, L (m)	0.48
Area fraction of baffle plate that is window, f_b (for 25% baffle plate)	0.1955

Table 3.1 Reactor specifications and operating conditions

The one-dimensional model enables the prediction of different components' mole fractions along the reactor length under various operating conditions, which is shown in Figure 3.1. As expected, the mole fractions of CH_3OH and H_2O decrease, while the mole fractions of H_2, CO and CO_2 increase, as the reactions proceed throughout the length of the reactor.

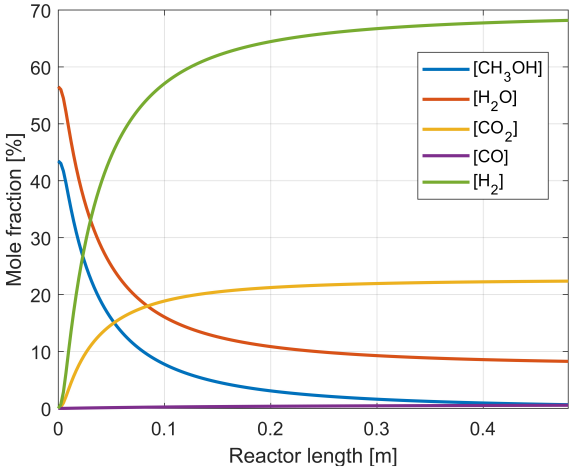

Figure 3.1 Profiles of mole fraction of each component along the reactor length: the contact time $W_{cat}/F_{CH_3OH} = 234.7\ kg\ s\ m^{-1}$*, the inlet temperature of burner gas* $T_{s,0} = 673\ K$*, the inlet temperature of reactants* $T_{t,0} = 433\ K$*, the mass flow of burner gas* $m_{s,0} = 6 \times 10^{-3}\ kg\ s^{-1}$*, and* $S/C = 1.3$

In other MSR models, the energy balance in the shell side is often ignored by setting a constant temperature of the tube wall or burner gas to simplify the calculations. However, the model in this study has taken into account the variations of the shell-side temperature and the local heat transfer coefficient along the length of the reactor. In Figure 3.2, the W_{cat}/F_{CH_3OH} ratio was changed from 132 to 528 kg s m^{-1} by adjusting the value of F_{CH_3OH} while keep the value of W_{cat} constant. As illustrated in Figure 3.2 (a), the effects of W_{cat}/F_{CH_3OH} on the axial temperature profiles in both the tube and shell sides were investigated. The temperature of reactants increases rapidly after entering into the reactor. When the W_{cat}/F_{CH_3OH} is large ($\geq$ 352 kg s m^{-1}), the tube-side temperature keeps increasing along the reactor length until equilibrium is reached. When the W_{cat}/F_{CH_3OH} is small ($\leq$ 264 kg s m^{-1}), the tube-side temperature tends to decline after reaching its peak point. The results also show that as W_{cat}/F_{CH_3OH} increases, the outlet temperature of the reactor rises. Furthermore, as demonstrated in Figure 3.2 (b), the increasing W_{cat}/F_{CH_3OH} increases both the mole fraction of CO in the reformate gas and the methanol conversion at the reactor output.

The axial temperature variation in the catalyst bed is related to the endothermic MSR reactions and the heat provided from the shell side. Because the significant temperature difference between the inside and outside of the reactor tube, the tube-side temperature increases rapidly near the reactor inlet as a result of the substantial heat flux. Simultaneously, the chemical reactions rapidly occur in the front part of the reactor, as evidenced by the dramatic increase in the methanol conversion. When the W_{cat}/F_{CH_3OH} is large ($\geq$ 352 kg s m^{-1}), the methanol conversion gradually

approaches 100%, shown in Figure 3.2 (b), slowing the reaction rates and reducing the heat consumption. Temperatures on both sides then approach the same value when thermal equilibrium is achieved. On the other hand, when the W_{cat}/F_{CH_3OH} is small ($\leq$ 264 kg s m^{-1}), there could be more methanol participating in the reforming process. Because of the higher energy consumption on the tube side, the hot-side temperature drops faster in this case, allowing for less heat to be given to the catalyst bed. Hence, after reaching the highest point, the energy consumed by the endothermic reactions becomes greater than the energy delivered from the hot side, and the tube-side temperature starts to drop. It is widely accepted that a higher operating temperature is favoured for endothermic reactions. When operating under a higher W_{cat}/F_{CH_3OH}, the MSR and MD reaction is enhanced due to the higher tube-side temperature, thus resulting in a higher methanol conversion as shown in Figure 3.2 (b). Furthermore, the rate of the rWGS reaction is enhanced as the operating temperature increases, leading to an increase in the CO selectivity.

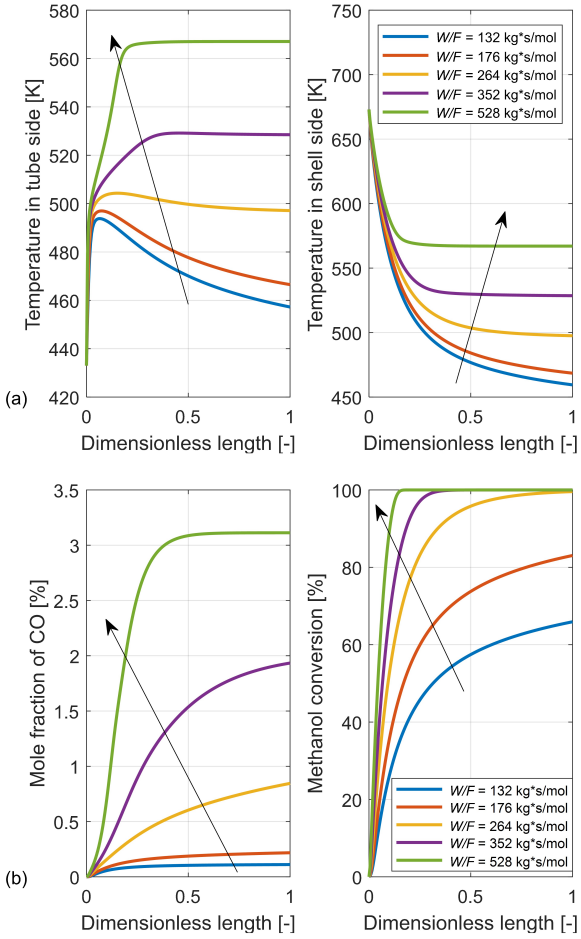

Figure 3.2 Effect of the W_{cat}/F_{CH_3OH} on (a) temperature profiles in tube and shell sides, and (b) CO concentration and methanol conversion along the reactor length: the inlet temperature of burner gas $T_{s,0} = 673$ K, the inlet temperature of reactants $T_{t,0} = 433$ K, the mass flow of burner gas $m_{s,0} = 6 \times 10^{-3}$ kg s^{-1}, and $S/C = 1.3$

Because the tube-side temperature is related to the heat transfer from the shell-side gas, the effect of the inlet temperature of burner gas on the reformer performance is investigated in this study. As can be seen from the simulated axial temperature profiles in Figure 3.3 (a), the tube-side temperature experiences a sharp and temporary rise near the tube inlet. In this sector, the heat provided from the shell side is more than the heat consumed by endothermic reactions. When the inlet temperature of the burner gas is below 673 K, the tube-side temperature starts to decline after this peak temperature point. When the inlet temperature of the burner gas is higher than 723 K, the heat transfer from the shell side can always play a more dominant role compared with the heat consumption by the endothermic reactions. In this case, the tube-side temperature continues to increase along the tube length. Moreover, it is observed that the tube-side temperature rises when the inlet temperature of the burner gas varies from 573 K to 773 K. This is because that, as the hot-side temperature increases, the driving force for heat transfer increases simultaneously. Figure 3.3 (b) represents the axial profiles of CO concentration and methanol conversion under different inlet temperatures of burner gas. The results show that, with a higher inlet temperature of burner gas, both the CO production and the methanol conversion will increase due to the enhanced temperature in the catalyst bed. A methanol conversion of nearly 100% can be achieved at the exit of the reactor when the inlet temperature of the burner gas is above 723 K.

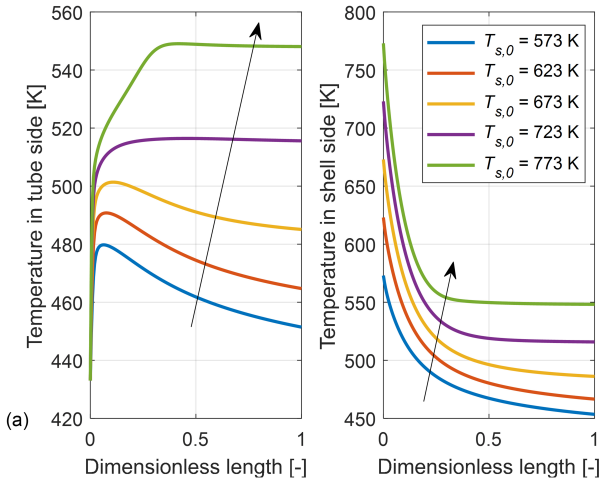

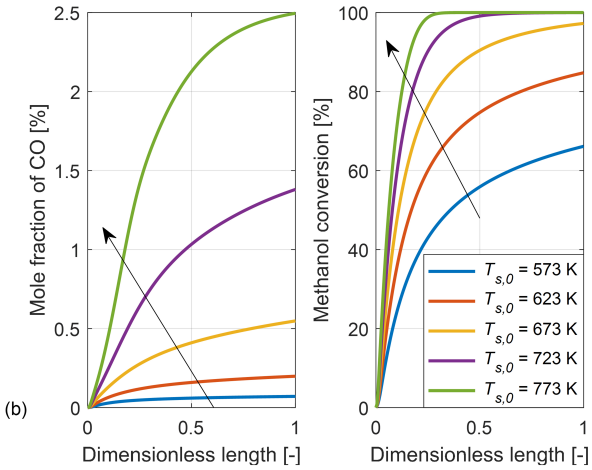

Figure 3.3 Effect of the inlet temperature of burner gas on (a) temperature profiles in tube and shell sides, and (b) CO concentration and methanol conversion along the reactor length: $W_{cat}/F_{CH_3OH} = 234.7\ kg\ s\ m^{-1}$, *the inlet temperature of reactants* $T_{t,0} = 433\ K$, *the mass flow of burner gas* $m_{s,0} = 6 \times 10^{-3}\ kg\ s^{-1}$, *and* $S/C = 1.3$

According to Le Chatelier's principle, the pressure increase shifts the equilibrium to the side of the reaction with fewer moles of gas, while the pressure decrease shifts the equilibrium to the side of reaction with mores mole of gas. Moreover, it is generally accepted that increasing the pressure of reactants will increase the rate of reactions that involve reacting gases. As represented in Figure 3.4, the effect of the operating pressure on the methanol conversion of the reformer is investigated. As the inlet pressure slightly increases from 1 bar to 5 bar, a very small increase of the methanol conversion at the reactor exit could be seen in Figure 3.4 (b). However, when the inlet pressure is above 10 bar, the reactor outlet methanol conversion will decrease with the increase of inlet pressure as shown in Figure 3.4 (a) and (c). Hence, the reformer could operate at atmospheric pressure. There is no need for a high inlet pressure, since increasing the inlet pressure cannot significantly improve the reformer performance.

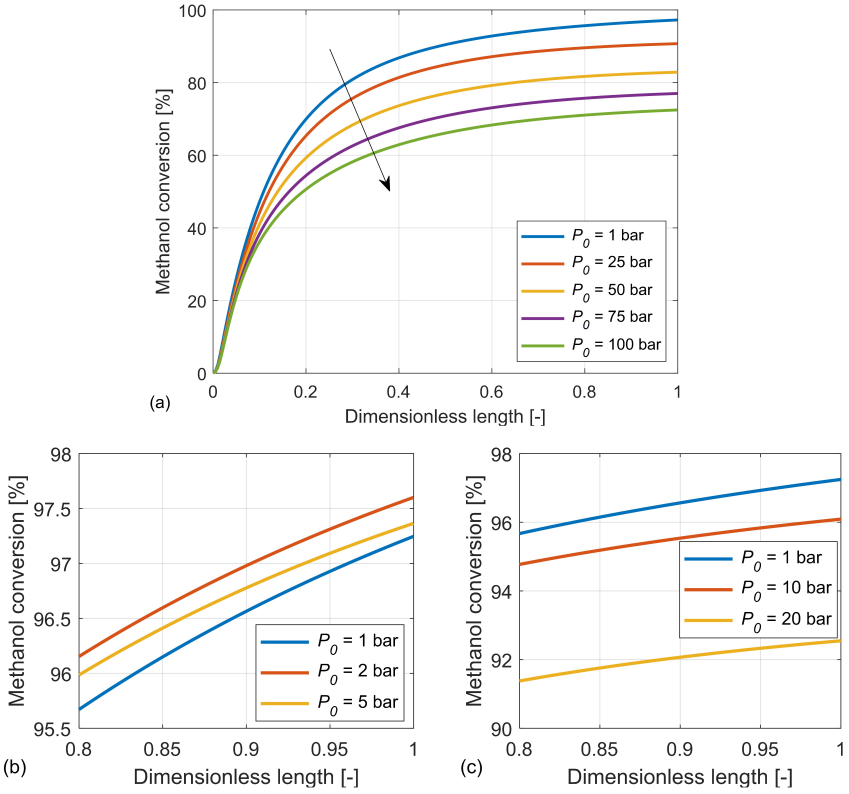

Figure 3.4 Effect of the inlet pressure of the methanol-and-water vapor mixture on the methanol conversion of the reformer: $W_{cat}/F_{CH_3OH} = 234.7\ kg\ s\ m^{-1}$, *the inlet temperature of burner gas* $T_{s,0} = 673\ K$, *the inlet temperature of reactants* $T_{t,0} = 433\ K$, *the mass flow of burner gas* $m_{s,0} = 6 \times 10^{-3}\ kg\ s^{-1}$, *and* $S/C = 1.3$

The S/C is also an important factor that can affect the reformer performance. In Figure 3.5, the value of S/C changes from 1.0 to 3.0 by increasing the flow rate of steam while keep the feeding rate of methanol constant in the inlet gas mixture. It is observed that increasing S/C can decrease the CO concentration in the reformate gas of the reformer. The reduction of CO concentration in the reformate gas is favoured because of the poisoning effect of CO on HT-PEM fuel cells. Moreover, sufficient steam in the reactants can eliminate coke formation during the reforming process, therefore mitigating catalyst deactivation in the catalyst bed caused by coking [136]. Nevertheless, with a higher S/C value, it will also take more energy to evaporate and heat the extra water. Therefore, the methanol conversion is slightly decreased during the MSR process due to the increased heat consumption and reduced temperature in the catalyst bed.

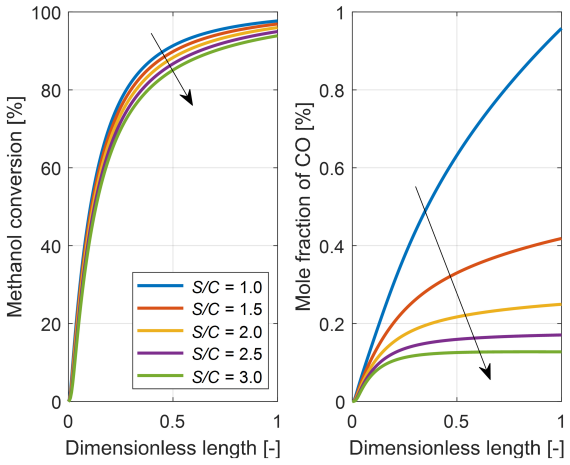

Figure 3.5 Effect of the S/C on the axial profiles of methanol conversion and CO concentration of the reformer: $W_{cat}/F_{CH_3OH} = 234.7\ kg\ s\ m^{-1}$*, the inlet temperature of burner gas* $T_{s,0} = 673\ K$*, the inlet temperature of reactants* $T_{t,0} = 433\ K$*, and the mass flow of burner gas* $m_{s,0} = 6 \times 10^{-3}\ kg\ s^{-1}$

Particle size reduction increases the surface area and the number of pore entrances. Therefore, smaller-sized catalysts perform better and have less deactivation than larger-sized catalysts [137]. However, when smaller-sized catalyst particles are utilized, the pressure drop over the length of the reactor could be significant. The effect of the catalyst particle diameter on pressure drop in the catalyst bed was investigated by changing it from 0.5 mm to 2.0 mm. The catalyst particles packed in the reactor tubes are cylindrical in shape. The pressure drop in this model is estimated using the Ergun equation, which ignores the increasing porosity of the catalyst bed near the tube wall and the viscous friction at the tube wall. As shown in Figure 3.6, the pressure in catalyst bed drops along the axial direction, and the pressure drop is enhanced by the decrease in particle size. Although the pressure variation in catalyst bed does not usually significantly affect the reformer performance, the pressure drop could be an important factor that affect the operation costs. When designing a reactor, it is generally accepted that a pressure drop less than 10% of the reactor inlet pressure is preferred. Therefore, in this case, the catalyst particle with a diameter larger than 0.75 can avoid the occurrence of significant pressure drops in the catalyst bed.

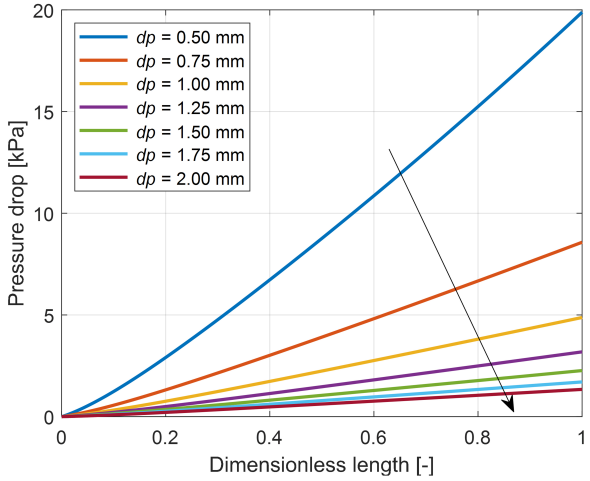

Figure 3.6 Effect of the particle size on the pressure drop along the reactor length: $W_{cat}/F_{CH_3OH} = 234.7\ kg\ s\ m^{-1}$*, the inlet temperature of burner gas* $T_{s,0} = 673\ K$*, the inlet temperature of reactants* $T_{t,0} = 433\ K$*, the mass flow of burner gas* $m_{s,0} = 6 \times 10^{-3}\ kg\ s^{-1}$*, and* $S/C = 1.3$

3.2. SUMMARY

In this chapter, the effects of the W_{cat}/F_{CH_3OH}, inlet temperature of burner gas, pressure, S/C, and particle size on the reformer performance has been investigated. According to the simulation results of the one-dimensional model, the increases in the inlet temperature of burner gas and the W_{cat}/F_{CH_3OH} improved the methanol conversion of the reformer, but also resulted in a high CO concentration in the reformate gas. Additionally, a higher value of S/C led to a lower methanol conversion due to the increased heat consumption for evaporating and heating the increased amount of water. At the same time, the selectivity towards CO during the MSR process was decreased. There was no need for a higher inlet pressure of the reformer, since increasing the inlet pressure cannot significantly improve the reformer performance but increase the pumping cost. Furthermore, in this case, the catalyst particle with a diameter larger than 0.75 can avoid a significant pressure drop (more than 10% of the reactor inlet pressure) along the reactor length.

CHAPTER 4. THE ROLE OF EFFECTIVENESS FACTORS

In general, the experimental and modelling work on catalytic reactions in packed beds can be simply performed assuming finely powdered catalysts [55,129]. As a result, the apparent diffusion limitations within the catalyst particles can be ignored, and the collected reaction rate can be termed as intrinsic. However, the interphase and intraparticle transfer limitations should be taken into account especially for large-sized catalyst particles in catalyst bed. Therefore, the effectiveness factors are introduced in this work to define the relationship between the transport limitations and the reaction rates inside porous catalyst particles.

Typically, there are two methods for estimating the effectiveness factor for cylindrical catalysts. One method is by solving the mass and energy balance equations inside a non-isothermal catalyst pellet which is regarded as spherical. Another method is by expressing the effectiveness factor as a function of the Thiele modulus.

4.1. MODEL VALIDATION

For model validation, an experiment was carried out in a small-scale packed-bed reactor containing catalyst particles for the MSR process. In the case, 3.66 g of $CuO/ZnO/Al_2O_3$ catalyst particles were randomly packed in a 3.6 mL reactor. Cylindrical catalyst particles with a diameter d_p of 1.5 mm and a height h of 1.5 mm were utilized. Figure 4.1 depicts the process flowsheet for the experimental setup. The liquid methanol-and-water mixture was firstly pumped into an evaporator to be evaporated and preheated. A mass flow controller measures and controls the feed rate from the fuel tank. Then the high-temperature vapours pass through a catalyst bed supported by a fine mesh in the small chamber. This small chamber is surrounded by insulating materials and can be heated by electric heaters outside the reactor. The temperature in the catalyst bed was controlled by the PID control of the electric heaters to keep it within a specific range. The temperature of the catalyst bed was measured using two thermocouples at the reactor's entrance and exit. The average value of the recorded temperatures was regarded as the temperature of the catalyst bed. Therefore, it could be assumed as isothermal in the catalyst bed. The main components in the reformate stream from the MSR reactor were analysed by the gas analysers (SIEMENS FIDMAT 6 for CH_3OH, CALOMAT 6 for H_2, ULTRAMAT 6 for CO and CO_2).

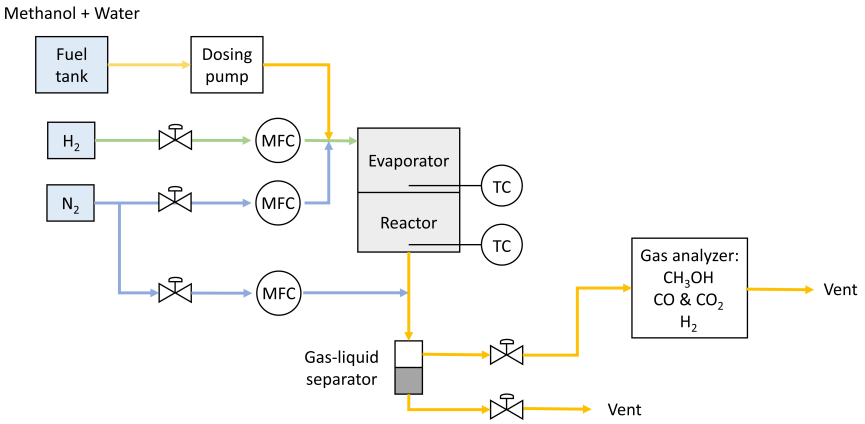

Figure 4.1 Process flowsheet for the experimental setup

The catalyst bed was firstly flushed with the gas mixture containing N_2 with a volumetric flow rate of $Q_{H_2} = 0.1$ cm^{3}min^{-1} and H_2 with a volumetric flow rate of $Q_{N_2} = 2$ cm^{3}min^{-1} (5 vol % of H_2 + 95 vol % of N_2) for at least one hour. The N_2 and H_2 mixture was pumped into the catalyst bed to reduce CuO to Cu, which is the main active component in the catalyst. The operating temperature for this reduction process should be controlled in the range of 433 – 493 K to avoid any thermal sintering of the catalyst. After the reduction process, the liquid methanol-and-water mixture was pumped into the small reactor. The reforming process was carried out under the operating temperatures at 493 K, 513 K and 533 K. The W_{cat}/F_{CH_3OH} varied in the range of 44 – 263 kg s mol^{-1}, which was achieved by changing the volume flow rate of liquid methanol Q_{CH_3OH} from 0.051 to 0.308 cm^3 min^{-1} while keeping a constant catalyst loading. The S/C was selected to be 1.3 to minimise the CO selectivity without wasting much energy in water evaporation [138].

Two models have been developed considering the reaction kinetics and effectiveness factors, calculated by using the distribution method and Thiele modulus method, for MSR reactions in the catalyst bed. Figure 4.2 shows the comparison of methanol conversion between the simulated and experimental results with changes in the operating temperature and W_{cat}/F_{CH_3OH}. There was a good agreement between the experimental data and the simulation results, especially for the model with effectiveness factors calculated by the intraparticle distribution method. Figure 4.3 shows the comparison between the experimental and simulated mole fraction of CO in the reformate gas with different operating temperatures and W_{cat}/F_{CH_3OH}. It can be seen that these two models can be used to estimate the CO content in the reformer with acceptable precision. However, the difference between the experimental and simulation results can be significant in some cases. A possible explanation for this phenomenon is the uneven distribution of temperature and concentrations in the reactor, which influence the local reaction rates. Another possible explanation is that, when the value of W_{cat}/F_{CH_3OH} is high, the feeding rate of reactants can become very

small. This small feeding rate could aggravate the non-uniformity in catalyst bed, and thus, leads to the oscillations of CO concentration in the reformate gas. Additionally, model assumptions, such as the neglect of void fractions near the reactor wall, could also be a cause for the big discrepancies.

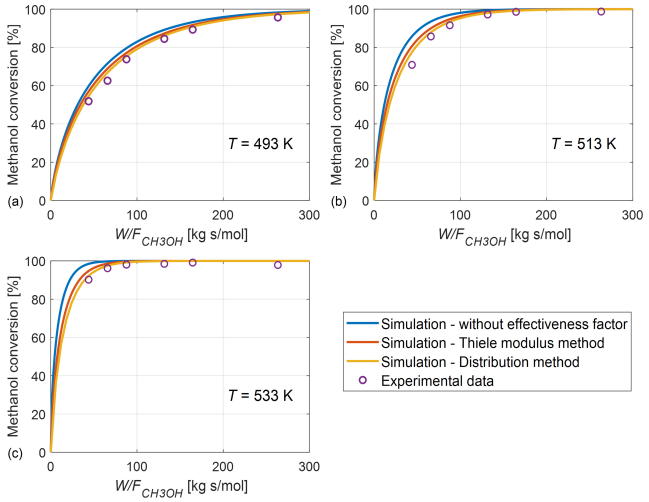

Figure 4.2 Comparison of the methanol conversion of the reactor between the simulation results and the experimental results under different W_{cat}/F_{CH_3OH} and operating temperatures: $S/C = 1.3$ and the catalyst pellet diameter $d_p = 1.5$ mm

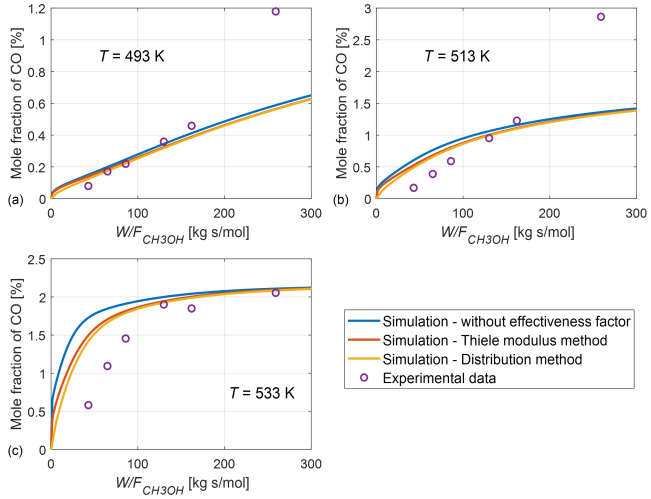

Figure 4.3 Comparison of the mole fraction of CO in the reformate gas between the simulation results and the experimental results under different W_{cat}/F_{CH_3OH} and operating temperatures: $S/C = 1.3$ and the catalyst pellet diameter $d_p = 1.5$ mm

4.2. COMPARING TWO METHODS FOR ESTIMATING EFFECTIVENESS FACTORS

The mass and energy balance equations govern the reaction-diffusion processes inside catalyst pellets. Hence, both the intraparticle temperature and concentration profiles can be evaluated by numerically solving these balance equations. In addition to the internal (intraparticle) diffusion resistance, the external diffusion (interphase diffusion) resistance between the bulk fluid and the exterior surface of the catalyst pellet is considered in this model. Figure 4.4 shows the effect of particle diameter ($d_p = 1.0$ and 2.0 mm) and bulk temperature ($T_b = 493$ and 553 K) on the concentration variations from the bulk fluid (bulk) to the pellet exterior surface ($r/R_p = 1$), and from the pellet exterior surface ($r/R_p = 1$) to the pellet centre ($r/R_p = 0$). The intraparticle diffusion resistance here is reflected as the concentration gradients inside the pellet, while the interphase diffusion resistance is regarded to be responsible for the change in concentrations from the exterior pellet surface to the bulk fluid (given 56.5% vol of H_2O and 43.5% vol of CH_3OH in the bulk fluid). By comparing Figure 4.4 (a) and (c), it can be seen that the concentration gradients inside the catalyst pellet as the bulk temperature rises. At the same time, the interphase diffusion resistance is slightly enhanced, because the concentration gradients from the pellet exterior surface to the bulk phase are greater when the bulk temperature is high. Moreover, as seen from Figure 4.4 (c) and (d), both the external and internal diffusion resistances become more considerable along the pellet radius when the catalyst diameter increases form 1.0 mm to 2.0 mm. Therefore, the effect of the diffusion resistances on the reaction-diffusion processes in porous catalyst particles tends to be more significant with the increasing particle size and bulk fluid temperature.

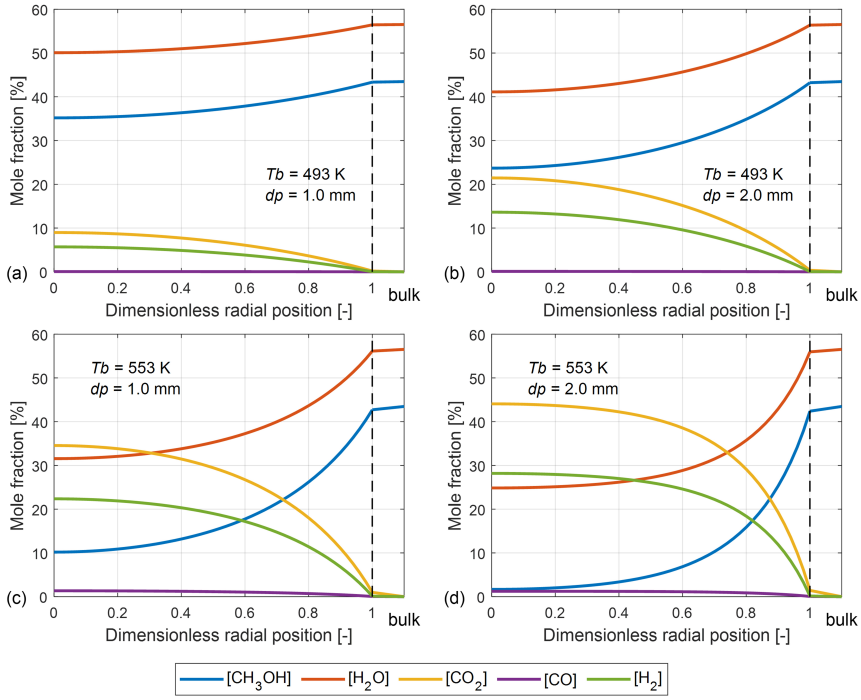

Figure 4.4 Effect of the bulk temperature and the particle diameter on concentration profiles of different components: $S/C = 1.3$ *and the catalyst pellet diameter* $d_p =$ 1.5 mm

With highly endothermic reactions occurring inside the catalyst pellet, heat from the bulk fluid will be brought to the exterior surface of the pellet through the boundary layer and then transferred through the pores inside the pellet to the pellet centre to compensate for the heat loss. This radial temperature distribution can be influenced by the particle diameter and bulk temperature due to external and internal heat transfer resistances. As shown in Figure 4.5 (a) and (b), the temperature difference between the bulk fluid and the exterior pellet surface (the right part of the dotted line) becomes more considerable as the pellet diameter increases from 1.0 mm to 3.0 mm. It represents an increase in the interphase heat transfer resistance. At the same time, the temperature drops more rapidly from the exterior pellet surface towards the pellet centre with a larger pellet diameter due to the higher intraparticle resistance to heat transfer. Furthermore, the variation in bulk temperature impacts the interphase and intraparticle heat transfer resistances. As shown in Figure 4.6, with a higher temperature of the bulk fluid, the external heat transfer resistance becomes more significant, which can be seen as a notable temperate drop from the bulk fluid to the pellet surface. The increasing bulk temperature also leads to an increase in the

temperature gradient inside the catalyst pellet, which is caused by the increased intraparticle heat transfer resistance. The reason could also be the enhanced endothermic reactions due to the increased operating temperature inside the catalyst pellet.

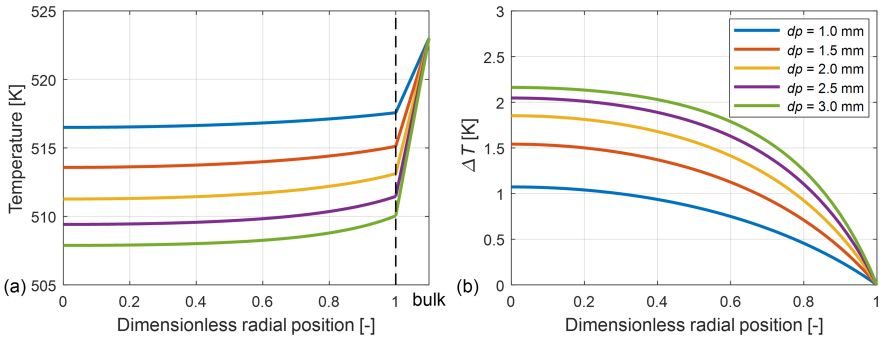

Figure 4.5 Effect of the particle diameter on the profiles of (a) temperature T and (b) temperature difference from the exterior surface of catalyst pellet ($\Delta T = T^s - T$)*:* $S/C =$ 1.3 *and the bulk fluid temperature* $T_b = 523\ K$

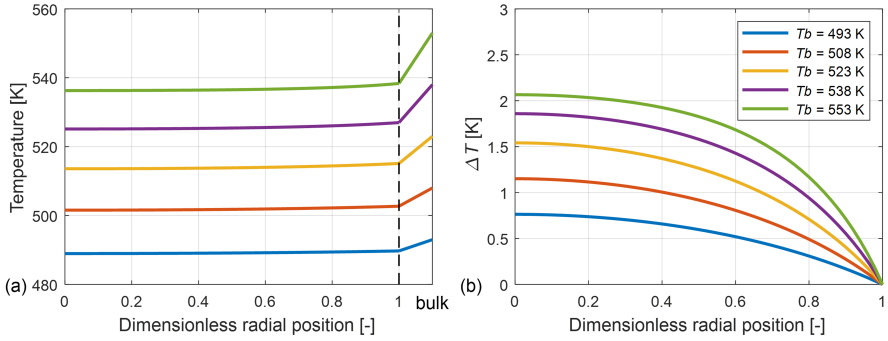

Figure 4.6 Effect of the bulk temperature on the profiles of (a) temperature T and (b) temperature difference from the exterior surface of catalyst pellet ($\Delta T = T^s - T$)*:* $S/C =$ 1.3 *and the catalyst pellet diameter* $d_p = 1.5$ mm

Since the effectiveness factor is derived from the intraparticle distributions of temperature and concentrations, the variations in the pellet size and the bulk temperature could also affect the effectiveness factors in the catalyst bed. Figure 4.7 (a) shows the effect of the pellet diameter on effectiveness factors for the MSR and MD reactions under the given conditions (56.5% vol of H_2O and 43.5% vol of CH_3OH) in bulk fluid at the reactor inlet. As the diameter approaches zero, the effect of both the interphase and intraparticle transfer resistances continues to decrease until there is

none, which is illustrated as the value of effectiveness factors approach 1. When the diameter increases to 3.0 mm, the effectiveness factor for the MSR reaction decreases to 0.17, while the effectiveness factor for the MD reaction decreases to 0.036. It means that, as the diameter increases, less internal catalyst surface is available for chemical reactions inside the porous catalyst pellet, hence the heat and mass transfer resistances become more considerable. As shown in Figure 4.7 (b), the effectiveness factors decrease as the bulk temperature increases from 273 K to 573 K. When the bulk temperature is relatively high (573 K), most of the reactants could be consumed rapidly after diffusing into the catalyst pellet. Only a small amount of reactants can penetrate the interior of the porous pellet. Therefore, as the bulk temperature increases, the effectiveness factors become smaller, and the diffusion rate (the slowest step) more significantly impacts or even dominates the reaction rate.

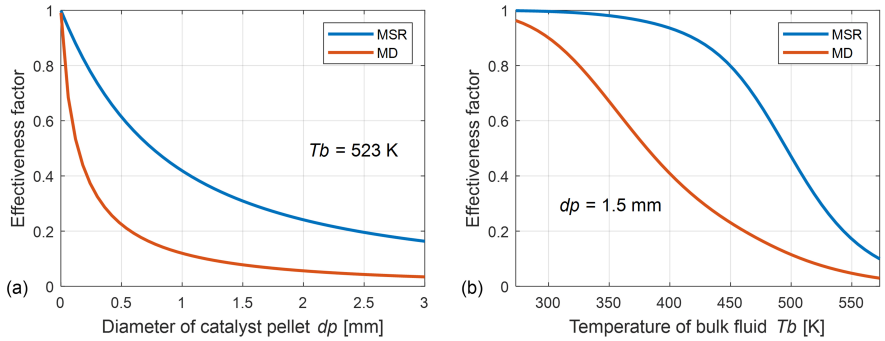

Figure 4.7 Effect of the (a) pellet diameter and (b) bulk fluid temperature on effectiveness factors at the inlet conditions of the reactor: $S/C = 1.3$

Effectiveness factors in the heterogeneous system are affected by the local temperature and concentrations along the reactor length. The axial profiles of effectiveness factors for MSR, MD and WGS reactions simulated by solving intraparticle mass and energy balance equations are shown in Figure 4.8. The effectiveness factors for both the MSR and MD reactions increase along the reactor length due to the variations of temperature and concentrations. However, the effectiveness factor for the WGS reaction shows a hyperbolic trend along the reactor. It reveals that the WGS reaction is reversed at the position of the black dashed line in the reactor.

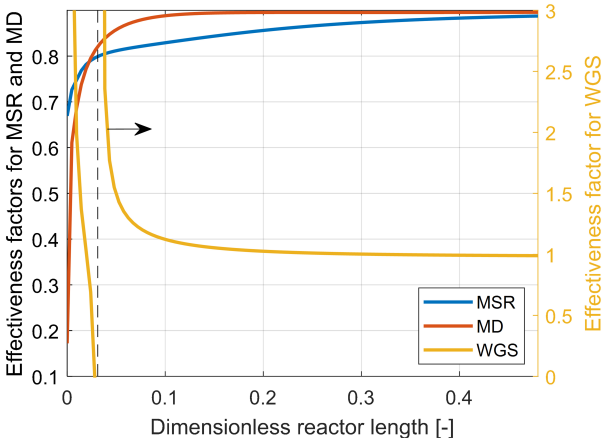

Figure 4.8 Profile of effectiveness factors for the MSR, MD and WGS reactions along the reactor length: $W_{cat}/F_{CH_3OH} = 234.7$ kg s m^{-1}, *the inlet temperature of burner gas* $T_{s,0} = 673$ K, *the inlet temperature of reactants* $T_{t,0} = 433$ K, *the inlet tube-side pressure* $P_{t,o} = 1$ bar, *the catalyst pellet diameter* $d_p = 1.5$ mm, *and* $S/C = 1.3$

By adopting the effectiveness factors for the MSR, MD and MGS reaction in the one-dimensional steady-state model, the performance of the reforming process in the catalyst bed can be more accurately predicted. Figure 4.9 shows the profiles of the mole fraction of different components along the reactor length. The solid lines represent that the intraparticle distribution method is used to calculate the effectiveness factors in this model. The '+' symbols represent that the effectiveness factors are calculated as a function of the Thiele modulus. The simulation results using different methods for the calculation of effectiveness factors are compared with different particle diameters shown in Figure 4.9 (a) and (b), and different temperature of burner gas shown in Figure 4.9 (a) and (c). It can be observed that there are only small differences in the simulation results obtained using the different methods. In this case, both the intraparticle distribution method and the Thiele modulus method could be used to estimate the effectiveness factors if a slight sacrifice of accuracy can be accepted.

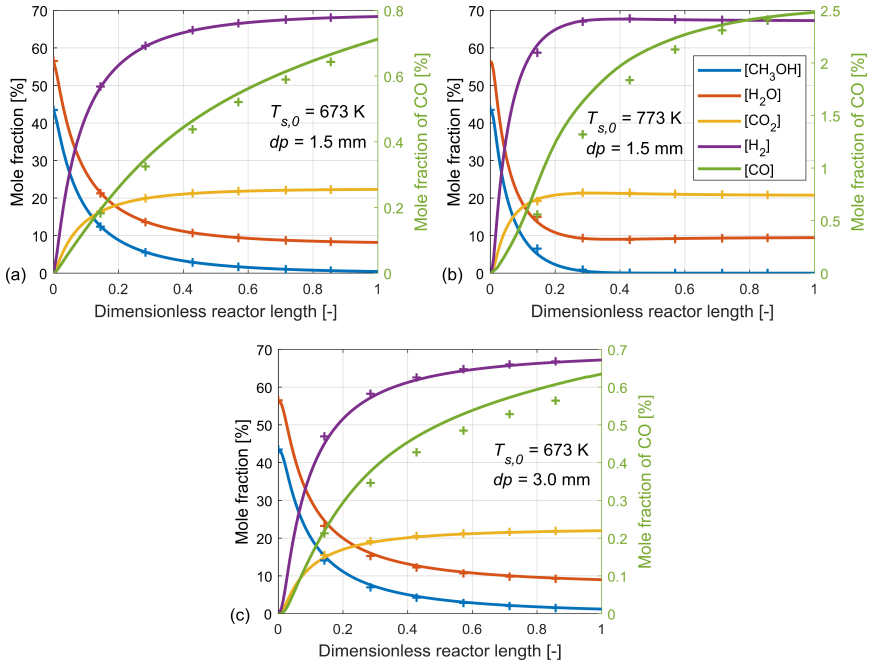

Figure 4.9 Mole fraction profile of each component along the reactor length with effectiveness factors calculated by the intraparticle distribution method (solid lines) and by the Thiele modulus method ('+' symbols): $W_{cat}/F_{CH_3OH} = 234.7$ kg s m^{-1}*, the inlet temperature of reactants* $T_{t,0} = 433$ K*, and* $S/C = 1.3$

4.3. SUMMARY

In this chapter, two typical methods were validated and compared for estimating the effectiveness factors for MSR, WGS and MD reactions in the catalyst bed. One method was by expressing the effectiveness factor as a function of the Thiele modulus. Another method was by solving the mass and energy balance equations inside a non-isothermal catalyst pellet to study the effect of both the interphase and intraparticle transfer resistances. This method provided insight into the interaction between the intrinsic kinetics and the heat and mass transport characteristics of the porous catalyst pellet. According to the simulation results in the particle scale, both the interphase and intraparticle (external and internal) transfer resistances were enhanced with the increasing bulk temperature and catalyst diameter. Therefore, at the inlet conditions of the reactor, it was observed that the effectiveness factors for the MSR and MD reactions decrease with the increasing burner temperature and catalyst diameter. By comparing the simulation results obtained by these two methods, the effectiveness factor estimated by the intraparticle distribution method was more accurate than the

Thiele modulus method. However, the Thiele modulus-effectiveness factor method required a short computation time and could still be used if a slight sacrifice of accuracy (< 5.4% in this study) was acceptable.

CHAPTER 5. SIMULATION RESULTS OF THE TWO-DIMENSIONAL MODEL

The one-dimensional pseudo-homogeneous model can be extended to a two-dimensional pseudo-homogeneous model by considering the radial gradients of temperature and concentrations in the reactor tube. In this two-dimensional model, the mass and energy balance equations are solved in two-dimensional axi-symmetrical cylindrical coordinates. Therefore, the effect of geometric and operating parameters on the radial and axial distributions of temperature and concentrations can be estimated in the catalyst bed. The simulation results obtained from both the one-dimensional model and the two-dimensional model are compared. This demonstrates the importance of introducing a two-dimensional model to evaluate the reformer performance, primarily when temperature and concentrations are non-uniformly distributed in the catalyst bed.

5.1. SIMULATION RESULTS OF THE TWO-DIMENSIONAL MODEL

The simulated profiles of temperature and methanol conversion in a single reactor tube are illustrated in Figure 5.1. It can be observed that, in Figure 5.1 (a), the reactants temperature increases sharply after entering the reactor, especially in the region close to the tube wall. This is because the substantial temperature difference between the tube and shell sides results in a strong heat flux near the reactor entrance. After the sharp increase, the temperature gradually drops along the reactor length due to the strongly endothermic reactions in the catalyst bed. Another reason for the subsequent temperature drop is the decrease in the temperature of the external burner gas. Finally, the temperature can approach a relatively uniform state in the radial direction. The simulated temperature gradient in the radial direction reflects the combined effect of the radial heat transfer and the endothermic reaction rates. Additionally, the hot spot is more likely to be formed in the front region of the reactor and near the tube wall. As shown in Figure 5.1 (b), the distribution of methanol conversion shows a gradually increasing trend along the reactor length. Its radial gradient does not seem to be as significant as the axial gradient. Similar results can be observed in the studies of Ma et al. [132] and Kuncharam et al. [139].

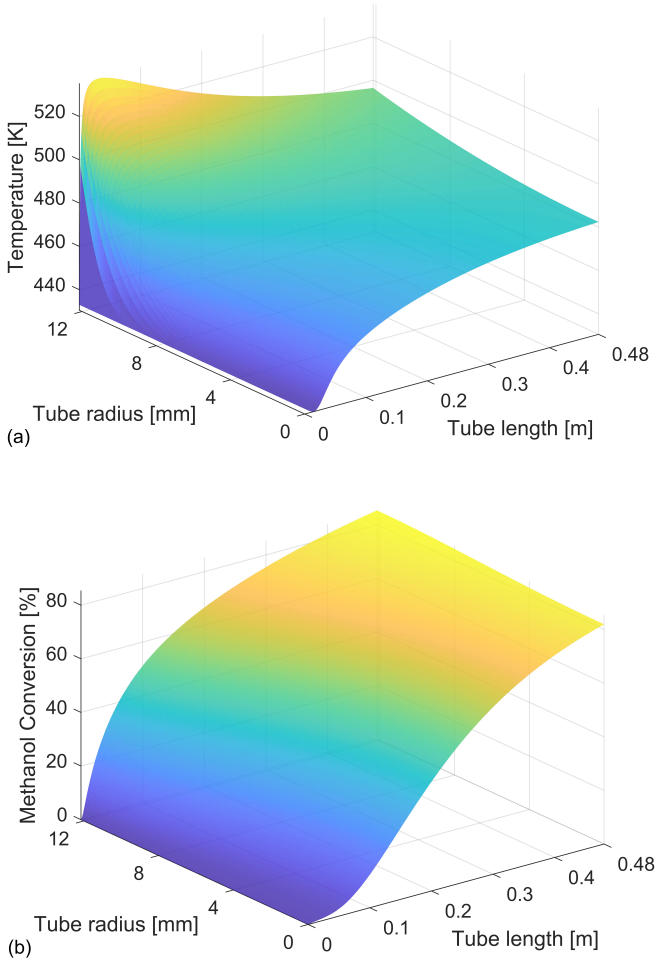

Figure 5.1 Surface plot of the (a) temperature and (b) methanol conversion in a single reactor tube simulated by the two-dimensional model: $W_{cat}/F_{CH_3OH} = 135$ kg s m^{-1}, *the inlet temperature of burner gas* $T_{s,0} = 673$ K, *the inlet temperature of reactants* $T_{t,0} = 433$ K, $S/C = 1.3$, *the tube diameter* $d_t = 24.3$ *mm, and the number of tubes* $N_t = 9$

The comparison of the simulated temperature distributions between the one-dimensional and two-dimensional models is shown in Figure 5.2. In Figure 5.2 (a), there is no radial temperature gradient in the catalyst bed according to the simulation results of the one-dimensional model. Only a rapid variation of temperature exists in the axial direction near the reactor entrance. After that, the temperature gradually increases until it reaches a steady state. As an addition to the one-dimensional model, the effective radial thermal conductivity is considered in the two-dimensional model. Therefore, as shown in Figure 5.1 (b), the simulated temperature in catalyst bed varies in both radial and axial directions.

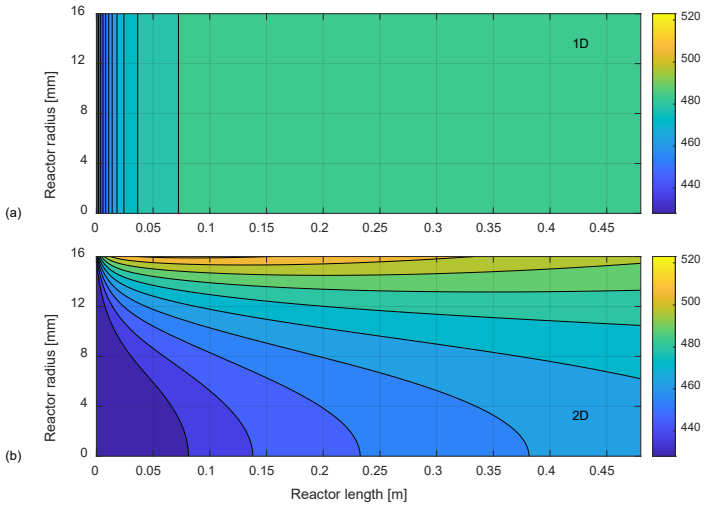

Figure 5.2 Contour plot of the temperature distribution in a single reactor tube simulated by (a) the one-dimensional model and (b) the two-dimensional model: $W_{cat}/F_{CH_3OH} = 135$ kg s m^{-1}, *the inlet temperature of burner gas* $T_{s,0} = 673$ K, *the inlet temperature of reactants* $T_{t,0} = 433$ K, $S/C = 1.3$, *the tube diameter* $d_t = 32.6$ *mm, and the number of tubes* $N_t = 5$

When designing a MSR reformer for the RMFC system, the effects of the operating conditions and the geometric parameters on hydrogen yield, methanol conversion, CO concentration in the reformate gas, as well as the temperature uniformity and hot-spot temperature in the catalyst bed should be considered. As it is shown in the simulation results of the one-dimensional model, the increase in the inlet temperature of burner gas improves the methanol conversion in the catalyst bed. However, when studying the effect of the burner temperature, it is better to take into account the non-uniformity of temperature in the radial direction. Figure 5.3 shows the effect of the inlet temperature of burner gas on the axial profiles of temperature at different radial positions (r/R_t) from the tube wall ($r/R_t = 1$) to the tube centre ($r/R_t = 0$). The results of the one-dimensional model (black dashed lines) and the two-dimensional model (solid lines) are compared in this figure. According to the results of the two-dimensional model, the radial temperature gradients exist in the catalyst bed. The increase of the burner temperature exacerbates the non-uniformity of the temperature in the radial direction. Furthermore, the increased burner temperature can lead to a higher hot-spot temperature in the catalyst bed, which could increase the risk of catalyst deactivation due to the local thermal sintering of catalysts. Therefore, attentions should be paid to the increase of the burner temperature to avoid the excessive radial temperature gradient and hot-spot temperature.

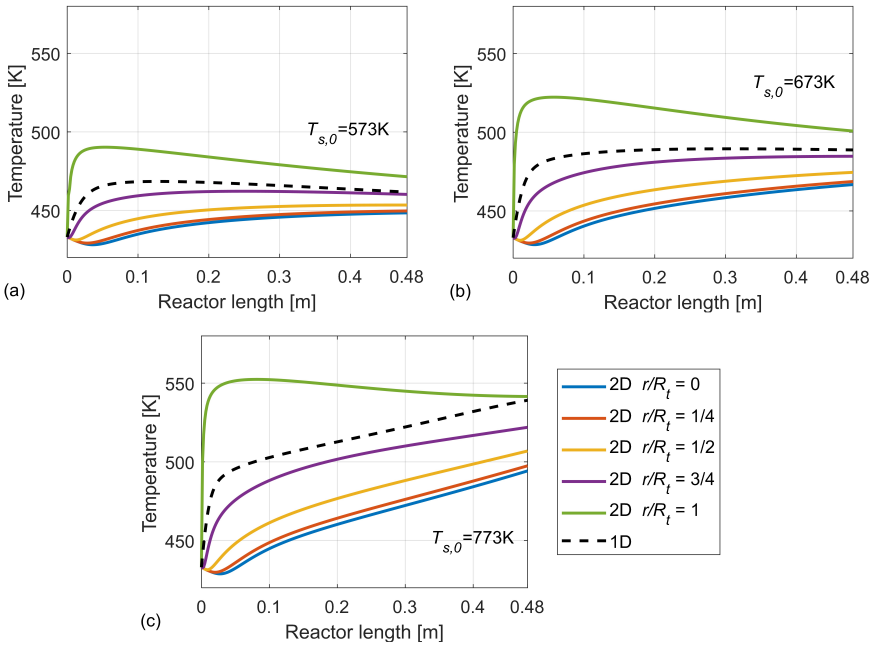

Figure 5.3 Effect of the inlet temperature of burner gas $T_{s,0}$ on the axial profiles of temperature at different radial positions (r/R_t) simulated by the two-dimensional model (solid lines) and the one-dimensional model (black dashed lines): $W_{cat}/F_{CH_3OH} =$ 135 kg s m^{-1}, the inlet temperature of reactants $T_{t,0} = 433$ K, $S/C = 1.3$, and the tube diameter $d_t = 32.6\ mm$

The increase of W_{cat}/F_{CH_3OH} indicates that there is sufficient contact between the reactants and the surface area of the catalyst. It is generally accepted that the rate of surface-catalysed reactions increases with the contact time. The effect of the contact time W_{cat}/F_{CH_3OH} on temperature distributions in the catalyst bed is illustrated in Figure 5.4. In this figure, the W_{cat}/F_{CH_3OH} varies from 135 kg s mol^{-1} to 406 kg s mol^{-1} by changing the number of reactor tubes, while keeping the tube diameter d_t and the reactor length L constant. It can be observed that the radial temperature gradient near the reactor outlet becomes smaller with the increase of W_{cat}/F_{CH_3OH}. This is because the increased contact time accelerates the reaction rates, and the methanol conversion rapidly approaches 100% along the reactor length. After that the endothermic reactions gradually slow down. The temperature, hence, can become more uniformly distributed in the radial direction near the reactor outlet. Moreover, the increase of contact time does not increase the temperature of hot spot in the catalyst bed significantly.

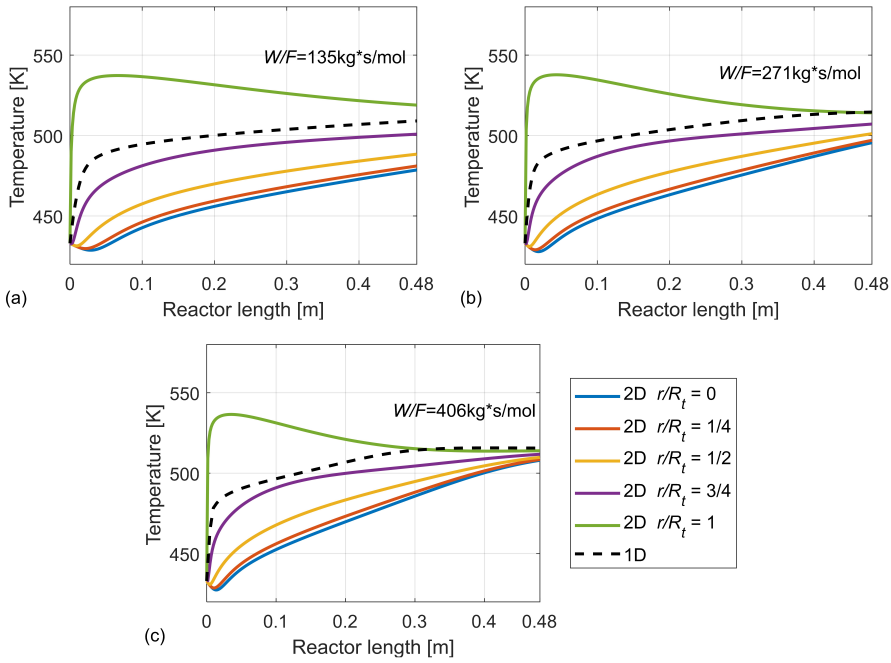

Figure 5.4 Effect of the W_{cat}/F_{CH_3OH} on the axial profiles of temperature at different radial positions (r/R_t) simulated by the two-dimensional model (solid lines) and the one-dimensional model (black dashed lines): the inlet temperature of burner gas $T_{s,0} = 723$ K, the inlet temperature of reactants $T_{t,0} = 433$ K, $S/C = 1.3$, and the tube diameter $d_t = 32.6\ mm$

For a multi-tubular packed-bed reformer with constant reactor volume, both the number of tubes and the number of welding operations can be inversely proportional to the square of the tube diameter. Hence, the use of large-diameter tubes reduces the manufacturing cost of the reformer. However, the increased tube diameter could exacerbate the non-unform distribution of temperature and concentrations in the catalyst bed. The possibility of using fewer reactor tubes with larger tube diameter in the reformer is explored in this study. The temperature profiles estimated by the one-dimensional model and the two-dimensional model are presented in Figure 5.5. Due to the heat transfer resistance and the occurrence of endothermic reactions, the lowest temperature in the catalyst bed appears in the centre of the reactor tube. Besides, the hot spot is formed in a region close to the tube wall and the reactor entrance due to the peak heat flux. It is observed in Figure 5.5 that the increased tube diameter enhances the radial temperature gradient in the reactor tube. This phenomenon implies that, as the tube diameter increases, the heat transfer becomes less efficient due to the decreased surface area per unit volume. Therefore, the temperature is distributed less

evenly over the catalyst bed, which is not helpful for improving the reformer performance. These results agree with the findings of Davieau et al. [140] that the reactor configuration with small-diameter tubes results in relatively ideal diffusion and high methanol conversion in the catalyst bed.

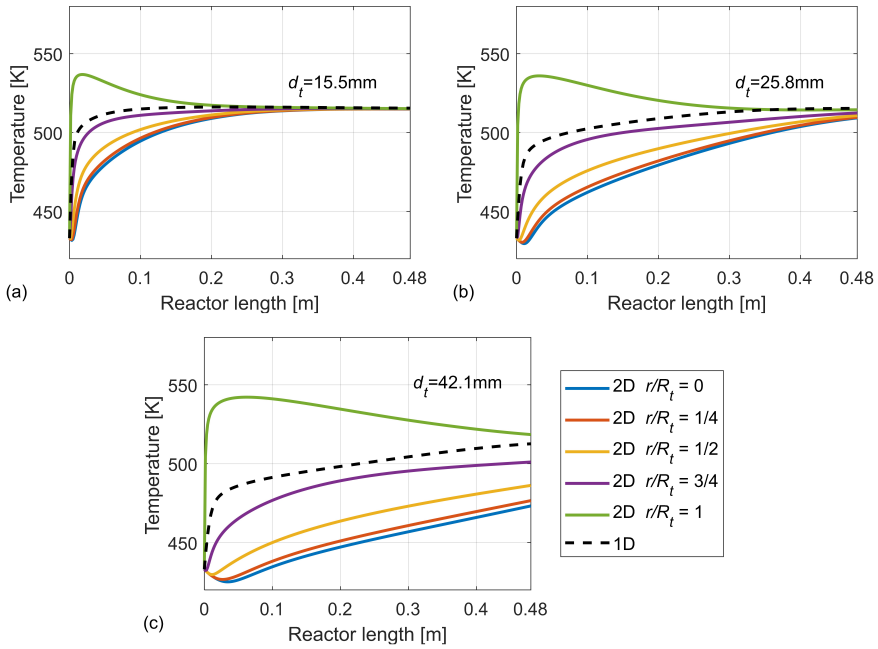

Figure 5.5 Effect of the tube diameter d_t on the axial profiles of temperature at different radial positions (r/R_t) simulated by the two-dimensional model (solid lines) and the one-dimensional model (black dashed lines): $W_{cat}/F_{CH_3OH} = 271$ kg s m^{-1}, the inlet temperature of burner gas $T_{s,0} = 723$ K, the inlet temperature of reactants $T_{t,0} = 433$ K, $S/C = 1.3$

By comparing the simulation results of the one-dimensional model and the two-dimensional model, we can figure out if it is necessary to consider the radial gradients of temperature and concentrations in reactor modelling. Figure 5.6 shows the effect of tube diameter d_t, the inlet temperature of burner gas $T_{s,0}$ and the contact time W_{cat}/F_{CH_3OH} on the methanol conversion and the mole fraction of CO of the reformer. The results reveal that a decrease in tube diameter leads to an increase in the methanol conversion of the reformer. The reason could be that the heat transfer becomes more efficient from the external heat source to the tube centre with a smaller tube diameter. Moreover, a more negligible difference ($< 1.74\%$) in the estimated methanol conversion between the one-dimensional model and the two-dimensional model can be observed when the tube diameter becomes small ($d_t = 13.3$ mm). This

is because, in this case the radial gradients are so small that they can be ignored in the one-dimensional model without much loss of accuracy. However, the estimated mole fraction of CO in the reformate gas does not differ significantly between the one-dimensional model and the two-dimensional model.

As shown in Figure 5.6 (a) and (b), the methanol conversion increases dramatically when the inlet temperature of burner gas increases from 623 K to 723 K. Correspondingly, the mole fraction of CO is also observed to be elevated. It is also observed that when the methanol conversion gets closer to 100%, the difference in the methanol conversion between the one-dimension model and the two-dimensional model becomes less significant. Moreover, in Figure 5.6 (c) and (d), the methanol conversion of the reformer is considerably improved as the W_{cat}/F_{CH_3OH} increases from 135 to 405 kg s mol^{-1}. The mole fraction of CO in the reformate gas also increases with the W_{cat}/F_{CH_3OH}.

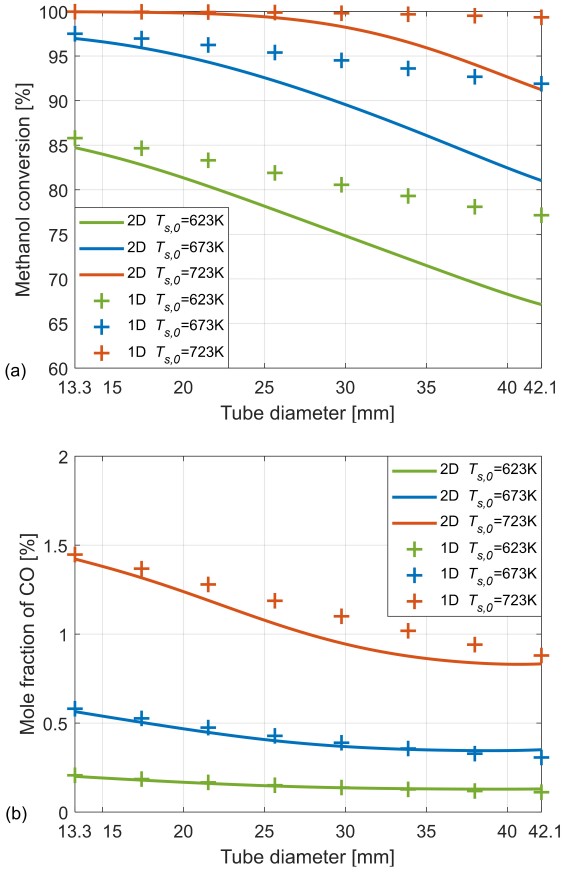

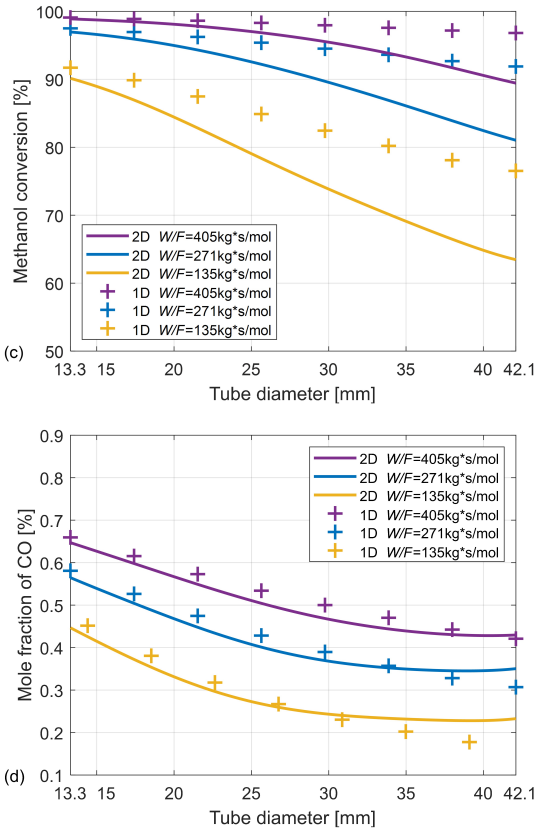

Figure 5.6 Effect of the tube diameter d_t and the inlet temperature of burner gas $T_{s,0}$ on the (a) methanol conversion and (b) mole fraction of CO in the reformate gas: $W_{cat}/F_{CH_3OH} = 271\ kg\,s\,mol^{-1}$; effect of the tube diameter d_t and the contact time W_{cat}/F_{CH_3OH} on the (c) methanol conversion and (d) mole fraction of CO in the reformate gas: $T_{s,0} = 673\ K$.

5.2. OPTIMIZATION OF OPERATING CONDITIONS

The reformer performance is sensitive to the operating parameters such as the inlet temperature of burner gas $T_{s,0}$ and the W_{cat}/F_{CH_3OH}. In this study, the optimal operating conditions are determined by studying the effect of the operating parameters and characterizing the reformer performance using the two-dimensional model. As shown in Figure 5.7, the inlet temperature of burner gas varies from 573 K to 823 K, while the W_{cat}/F_{CH_3OH} varies from 42 to 506 kg s mol^{-1}. The methanol conversion of the reformer can be improved by adopting a higher inlet temperature of burner gas and a higher W_{cat}/F_{CH_3OH}. The results also indicate that the increase in the inlet temperature of burner gas and the W_{cat}/F_{CH_3OH} leads to a higher CO concentration in

the reformate gas of the reformer. Furthermore, the increase in the inlet temperature of burner gas can significantly increase the hot-spot temperature in the catalyst bed.

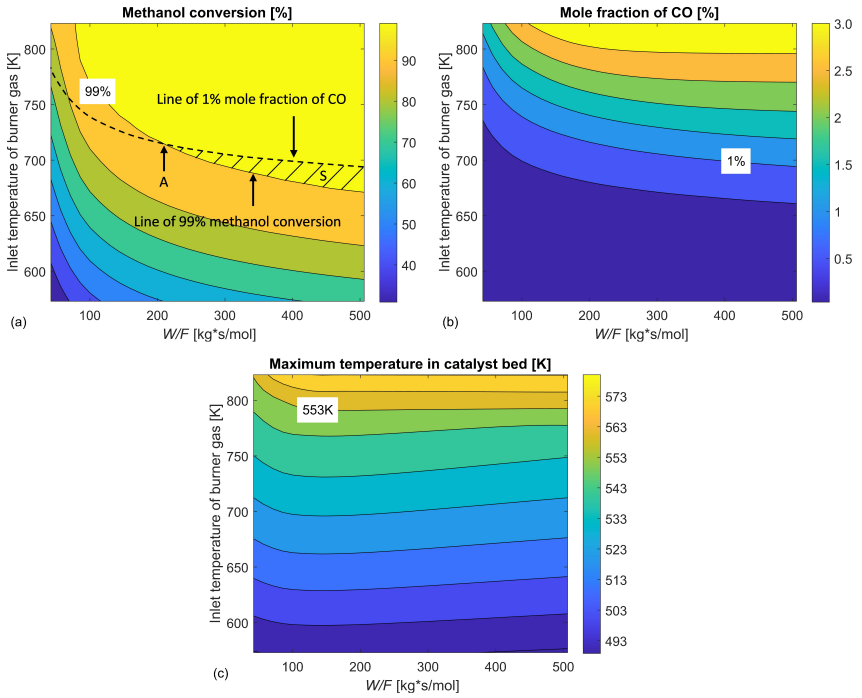

Figure 5.7 Effect of the W/F_{CH_3OH} and the inlet temperature of burner gas $T_{s,0}$ on the (a) methanol conversion, (b) mole fraction of CO and (c) maximum hot-spot temperature of the reformer: $d_t = 18.2\ mm$

When integrating a reformer with an HT-PEM fuel cell stack, the concentrations of CO and methanol in the reformer outlet should be limited to reasonable levels (e.g., below 2% vol for both, preferably below 1% vol) to minimize their poisoning effects on fuel cells. Besides, the hot-spot temperature in the catalyst bed should always be kept below 553 K in order to prevent the subsequent catalyst deactivation by thermal sintering in the hot-spot region. As shown in Figure 5.7 (a), there is a region *S* in the counter plot that is enclosed by the "line of 1% mole fraction of CO" and the "line of 99% methanol conversion". The operating parameters falling into this region can simultaneously ensure that the methanol conversion of the reformer is above 99% and the mole fraction of CO in the reformate gas is below 1% vol. When comparing this region *S* with the contour plot in Figure 5.7 (c), the operating parameters in region *S* can also satisfy the requirement of not exceeding the endurable hot-spot temperature (553 K). Therefore, in this case, the recommended operating conditions for the reformer can be found when the W_{cat}/F_{CH_3OH} is in the range of $216 - 506$ kg s mol^{-1} and the inlet temperature of burner gas is in the range of $671 - 714$ K.

Additionally, the operating parameters falling at point A (with $W_{cat}/F_{CH_3OH} = 216\ \text{kg s mol}^{-1}$ and $T_{s,0} = 714\ \text{K}$) are more recommended for their advantages in minimizing the overall catalyst loading in the reformer.

5.3. SUMMARY

In this section, the simulation results of the two-dimensional model were analysed. The two-dimensional model was developed to get a better understanding of both the radial and axial distributions of temperature and concentrations in the catalyst bed. Moreover, the simulation results of the one-dimensional model and the two-dimensional model were compared, which made it possible to tell the importance of the radial gradients in the catalyst bed under the given geometric parameters and operating conditions. For a tubular reactor with rather non-uniform temperature and concentration distributions in the radial direction, this two-dimensional model can make more accurate predictions of the reformer performance. Furthermore, hot spots in the catalyst beds at temperatures above 280°C could be predicted and avoided in order to prevent severe catalyst deactivation by thermal sintering. Nevertheless, the two-dimensional model requires more computation time than the one-dimensional model.

It was observed that the increase in tube diameter significantly enhanced the non-uniformity of temperature distribution within the reactor tube. Consequently, the tube diameter has been found to be a critical factor that could remarkably affect the difference in the simulation results between the one-dimensional model and the two-dimensional model. This difference also became less noticeable when the methanol conversion of the reformer approached 100%. According to the simulated temperature distribution in the catalyst bed, the lowest temperature appeared at the centre of the reactor tube, and the hot spot was generally formed at the location about 3 cm from the reactor entrance near the tube wall. The increase in the inlet temperature of burner gas significantly enhanced the hot spot temperature of the catalyst bed. Furthermore, the recommended operating conditions falling in the region S could ensure that the CO concentration is less than 1% vol and the methanol conversion is higher than 99% in the reformer outlet.

CHAPTER 6. CONCLUSIONS

This chapter summarizes the main contributions of this research work. This summary includes the model development, the simulation methods used in this work, and the numerical study on the effect of geometric parameters and operating conditions on the reforming performance. The limitations of this research work and suggestions for future work are also given to continue the work to understand the reforming process better and apply it more practically in the industry.

6.1. FINAL REMARKS

In this dissertation, the performance of a multi-tubular packed-bed reformer for the hydrogen production of a 5 kW HT-PEM fuel cell system has been numerically studied. The widely used one-dimensional and two-dimensional steady-state pseudo-homogeneous models have been developed for the MSR process in the packed-bed catalytic reactor.

These one-dimensional and two-dimensional models described the heat and mass transfer phenomena with chemical reactions in the catalyst bed. For the one-dimensional model, the catalyst bed was regarded as non-adiabatic, with heat transferred from the shell side. The reforming reactions took place in a plug-flow tubular reactor, in which the methanol-and-water vapor was fed uniformly into the catalyst bed. This reactor was also assumed to be a pseudo-homogeneous catalyst system. Only concentration and temperature gradients in the axial direction were considered in this model without radial and axial dispersions. A kinetic Langmuir-Hinshelwood model used in this research work was based on the study by Peppley et al. [89,90], where three main reactions (MSR, WGS, and MD) in the reformer process were considered over a commercial catalyst, $CuO/ZnO/Al_2O_3$. In addition, the semiempirical Ergun equation was used to describe the pressure drop in a packed tube. Furthermore, in this model, a non-isothermal co-current heating stream flowing through the shell side was used to provide extra heat for the reactor. The shell-side temperature was considered to vary along the reactor length.

Based on the one-dimensional model, the two-dimensional axisymmetric model has been developed, taking into account the radial gradients of temperature and concentration in the reactor. Therefore, the temperature and concentrations that were non-uniformly distributed over the cross-section, particularly close to the reactor entrance, can be estimated. The PDEs equation systems in the two-dimensional model could be solved in MATLAB® using the pdepe solver or the MOL.

Since cylindrical catalyst particles (1.5 mm × 1.5 mm) are randomly packed in the reactor tubes, the effectiveness factors were introduced to qualify the effect of intraparticle diffusion resistances on the reaction rates. A mathematical model

considering the reaction-diffusion process taking place inside catalyst particles has been developed by regarding the catalyst bed as a heterogeneous catalyst system. Hence, the effectiveness factors can be estimated by solving the mass and energy balance equations inside the catalyst particles. In this study, another approach to estimate the intraparticle reaction-diffusion process in an isothermal simple-shape particle was by calculating the effectiveness factor as a function of the Thiele modulus. Here, the Thiele modulus is a non-dimensional number defined to describe the relationship between diffusion and reaction rate. The bvp4c function in MATLAB® was used in this study to solve the boundary value problem of the reaction-diffusion process inside catalyst particles.

The simulation results in the study of the MSR process over a commercial $CuO/ZnO/Al_2O_3$ catalyst have shown good agreements with the experimental data obtained from a small-scale packed-bed reactor. The effectiveness factor estimated by numerically solving the intraparticle mass and energy balance equations was more accurate than that calculated as a function of the generalized Thiele modulus. However, the Thiele modulus approach was simple and could still be used to estimate the effectiveness factor in the catalyst bed without sacrificing too much accuracy (the maximum percentage discrepancy is 5.4% in this study). When considering the reaction-diffusion processes inside a porous catalyst particle, the interphase and intraparticle heat and mass transfer resistances could be enhanced with the increasing bulk fluid temperature or catalyst diameter. Therefore, at the inlet conditions of the reactor, the effectiveness factors for the MSR and MD reactions would approach 1 when the particle diameter decreased to almost 0 or when the operating temperature was below 273 K. Correspondingly, the effectiveness factors would decrease with the increasing temperature and particle diameter. In addition, the interphase mass transfer resistance was found to be less significant on a particle scale, especially when using such a high flow velocity over the catalyst bed.

According to the simulation results of the one-dimensional model, the temperature and concentration profiles were very sensitive to the change in operating parameters such as the S/C, inlet temperature of burner gas and the W_{cat}/F_{CH_3OH}. The results revealed that with a higher inlet temperature of burner gas, both the CO production and the methanol conversion would increase due to the enhanced temperature in the catalyst bed. It was also observed that the increase in W_{cat}/F_{CH_3OH} improved the methanol conversion of the reformer, but also resulted in a higher CO concentration in the reformate gas. Additionally, the increased S/C was found to decrease the methanol conversion and also decrease the selectivity towards CO during the MSR process.

Compared to the one-dimensional model, the two-dimension model has highlighted the radial heat and mass transfer in the reactor tube. The simulation results revealed that the inlet temperature of burner gas, W_{cat}/F_{CH_3OH} and tube diameter would significantly impact the component and temperature distributions in the radial

direction of the catalyst bed. The lowest temperature appeared at the centre of the reactor tube, and the hot spot was generally formed at the location about 3 cm from the reactor entrance near the tube wall. The difference between the one-dimensional model and the two-dimensional model increased significantly with the increase of the tube diameter. For a reformer that had more tubes (60) with smaller tubes' diameter (13.3 mm), there would be a minimal difference in the simulated methanol conversion between the one-dimensional model and the two-dimensional model, which was about 1.74% in this study. Furthermore, the radial gradients became less critical with a methanol conversion approaching 100% or a relatively small tube diameter. Consequently, in these cases, the simpler one-dimensional model could be used instead of the two-dimensional model for simulating the reformer performance.

6.2. FUTURE WORK

Like most scientific research projects, the research carried out in this study raises more questions that need to be investigated.

Since the degradation problem of HT-PEM fuel cells has attracted widespread attention today, the poisoning effect caused by the improper operations of the reformer on fuel cell stacks should be studied by simulation and experimental studies. Moreover, the online diagnostics of the RMFC system using electrochemical impedance spectroscopy (EIS) technology can provide insights into the condition of the fuel cell stack and can be used to identify specific problems caused by the methanol reformer in the fuel cell system. Systematic fault detection and isolation can be performed based on the characteristic features extracted from the fuel cell EIS that can then be used to control the operating conditions of the reformer based on a robust model, in such a way that alleviates the fuel cell faults.

The catalyst deactivation is not considered currently in our models. The commercial $CuO/ZnO/Al_2O_3$ catalyst will inevitably suffer from the deactivation caused by thermal sintering and carbon deposition during the operating hours. The fresh, partially deactivated and severely deactivated catalysts in the catalyst bed will perform differently in terms of activity and selectivity. The catalyst deactivation can be considered by introducing a general form of the deactivation model, whose constants are optimized with the differential evolution (DE) optimization method.

A dynamic model can be developed to study the transient behaviour of the methanol reformer and make it easier to select optimal operating parameters, especially for the quick start-up and shutdown operations in mobile fuel cell systems. In addition, the dynamic model of the RMFC system can be used to capture the vital dynamic characteristics of the system and design the control system to achieve predetermined control objectives.

REFERENCES

[1] IEA. World Energy Outlook 2021 2021. https://www.iea.org/reports/world-energy-outlook-2021.

[2] Energy Transitions Commission (ETC). The future of fossil fuels: How to steer fossil fuels use in a transition to a low-carbon energy system n.d. https://www.energy-transitions.org/research-paper-the-future-of-fossil-fuels/.

[3] EIA. International Energy Outlook 2021 n.d. https://www.eia.gov/outlooks/ieo/pdf/IEO2021_Narrative.pdf.

[4] European Commission. Questions and Answers on REPowerEU: Joint European action for more affordable, secure and sustainable energy n.d.

[5] Commission E. REPowerEU: Joint European action for more affordable, secure and sustainable energy n.d. https://ec.europa.eu/commission/presscorner/detail/en/ip_22_1511.

[6] Ritchie H, Roser M. Energy. Our World Data 2020.

[7] Perera FP. Multiple threats to child health from fossil fuel combustion: impacts of air pollution and climate change. Environ Health Perspect 2017;125:141–8.

[8] Perera F, Ashrafi A, Kinney P, Mills D. Towards a fuller assessment of benefits to children's health of reducing air pollution and mitigating climate change due to fossil fuel combustion. Environ Res 2019;172:55–72.

[9] United Nations. Adoption of the Paris Agreement 2015.

[10] Johnsson F, Kjärstad J, Rootzén J. The threat to climate change mitigation posed by the abundance of fossil fuels. Clim Policy 2019;19:258–74.

[11] Welsby D, Price J, Pye S, Ekins P. Unextractable fossil fuels in a 1.5 C world. Nature 2021;597:230–4.

[12] Abe JO, Popoola API, Ajenifuja E, Popoola OM. Hydrogen energy, economy and storage: review and recommendation. Int J Hydrogen Energy 2019;44:15072–86.

[13] Bui M, Adjiman CS, Bardow A, Anthony EJ, Boston A, Brown S, et al. Carbon capture and storage (CCS): the way forward. Energy Environ Sci

2018;11:1062–176.

[14] Nyári J, Magdeldin M, Larmi M, Järvinen M, Santasalo-Aarnio A. Techno-economic barriers of an industrial-scale methanol CCU-plant. J CO2 Util 2020;39:101166.

[15] Coralli A, Sarruf BJM, de Miranda PEV, Osmieri L, Specchia S, Minh NQ. Science and Engineering of Hydrogen-Based Energy Technologies: Chapter 2-Fuel Cells 2020.

[16] Alirahmi SM, Assareh E, Chitsaz A, Holagh SG, Jalilinasrabady S. Electrolyzer-fuel cell combination for grid peak load management in a geothermal power plant: Power to hydrogen and hydrogen to power conversion. Int J Hydrogen Energy 2021;46:25650–65.

[17] Jeppesen C. Online Fault Detection for High Temperature Proton Exchange Membrane Fuel Cells: A Data Driven Impedance Approach. 2017. https://doi.org/10.5278/VBN.PHD.ENG.00002.

[18] Cunanan C, Tran M-K, Lee Y, Kwok S, Leung V, Fowler M. A review of heavy-duty vehicle powertrain technologies: Diesel engine vehicles, battery electric vehicles, and hydrogen fuel cell electric vehicles. Clean Technol 2021;3:474–89.

[19] Daiyan R, MacGill I, Amal R. Opportunities and challenges for renewable power-to-X 2020.

[20] Wilberforce T, Alaswad A, Palumbo A, Dassisti M, Olabi A-G. Advances in stationary and portable fuel cell applications. Int J Hydrogen Energy 2016;41:16509–22.

[21] Sengodan S, Lan R, Humphreys J, Du D, Xu W, Wang H, et al. Advances in reforming and partial oxidation of hydrocarbons for hydrogen production and fuel cell applications. Renew Sustain Energy Rev 2018;82:761–80.

[22] Pollet BG, Staffell I, Shang JL. Current status of hybrid, battery and fuel cell electric vehicles: From electrochemistry to market prospects. Electrochim Acta 2012;84:235–49.

[23] Rajashekara K. Propulsion system strategies for fuel cell vehicles. SAE Technical Paper; 2000.

[24] Barbir F. PEM fuel cells: theory and practice. Academic press; 2012.

[25] Sharaf OZ, Orhan MF. An overview of fuel cell technology: Fundamentals and applications. Renew Sustain Energy Rev 2014;32:810–53. https://doi.org/10.1016/j.rser.2014.01.012.

[26] Chandan A, Hattenberger M, El-Kharouf A, Du S, Dhir A, Self V, et al. High temperature (HT) polymer electrolyte membrane fuel cells (PEMFC)-A review. J Power Sources 2013;231:264–78. https://doi.org/10.1016/j.jpowsour.2012.11.126.

[27] Owejan JP, Gagliardo JJ, Sergi JM, Kandlikar SG, Trabold TA. Water management studies in PEM fuel cells, Part I: Fuel cell design and in situ water distributions. Int J Hydrogen Energy 2009;34:3436–44. https://doi.org/10.1016/j.ijhydene.2008.12.100.

[28] Li Q, Oluf J, Savinell RF, Bjerrum NJ. High temperature proton exchange membranes based on polybenzimidazoles for fuel cells. Prog Polym Sci 2009;34:449–77. https://doi.org/10.1016/j.progpolymsci.2008.12.003.

[29] Li Q, Aili D, Hjuler HA, Jensen JO. High temperature polymer electrolyte membrane fuel cells. Springer Switz 2016:387–425.

[30] Iulianelli A, Basile A. Advances in hydrogen production, storage and distribution. Elsevier; 2014.

[31] Eriksson ELV, Gray EMA. Optimization and integration of hybrid renewable energy hydrogen fuel cell energy systems – A critical review. Appl Energy 2017;202:348–64. https://doi.org/10.1016/j.apenergy.2017.03.132.

[32] Dawood F, Anda M, Shafiullah GM. Hydrogen production for energy: An overview. Int J Hydrogen Energy 2020;45:3847–69. https://doi.org/10.1016/j.ijhydene.2019.12.059.

[33] Abdalla AM, Hossain S, Nisfindy OB, Azad AT, Dawood M, Azad AK. Hydrogen production, storage, transportation and key challenges with applications: A review. Energy Convers Manag 2018;165:602–27. https://doi.org/10.1016/j.enconman.2018.03.088.

[34] Sinigaglia T, Lewiski F, Santos Martins ME, Mairesse Siluk JC. Production, storage, fuel stations of hydrogen and its utilization in automotive applications-a review. Int J Hydrogen Energy 2017;42:24597–611. https://doi.org/10.1016/j.ijhydene.2017.08.063.

[35] Ahluwalia RK, Hua TQ, Peng JK. On-board and Off-board performance of hydrogen storage options for light-duty vehicles. Int J Hydrogen Energy

2012;37:2891–910. https://doi.org/10.1016/j.ijhydene.2011.05.040.

[36] Rivard E, Trudeau M, Zaghib K. Hydrogen storage for mobility: a review. Materials (Basel) 2019;12:1973.

[37] Zheng J, Liu X, Xu P, Liu P, Zhao Y, Yang J. Development of high pressure gaseous hydrogen storage technologies. Int J Hydrogen Energy 2012;37:1048–57.

[38] Barbir F, Basile A, Veziroglu TN. Compendium of Hydrogen Energy: Hydrogen Energy Conversion. Woodhead Publishing; 2015.

[39] Sharma S, Ghoshal SK. Hydrogen the future transportation fuel: From production to applications. Renew Sustain Energy Rev 2015;43:1151–8. https://doi.org/10.1016/j.rser.2014.11.093.

[40] Council NR. The hydrogen economy: opportunities, costs, barriers, and R&D needs. National Academies Press; 2004.

[41] Najjar YSH. Hydrogen safety: The road toward green technology. Int J Hydrogen Energy 2013;38:10716–28. https://doi.org/10.1016/j.ijhydene.2013.05.126.

[42] Dutta S. A review on production, storage of hydrogen and its utilization as an energy resource. J Ind Eng Chem 2014;20:1148–56. https://doi.org/10.1016/j.jiec.2013.07.037.

[43] Niaz S, Manzoor T, Pandith AH. Hydrogen storage: Materials, methods and perspectives. Renew Sustain Energy Rev 2015;50:457–69.

[44] Lim KL, Kazemian H, Yaakob Z, Daud WRW. Solid-state materials and methods for hydrogen storage: A critical review. Chem Eng Technol 2010;33:213–26. https://doi.org/10.1002/ceat.200900376.

[45] Züttel A. Hydrogen storage methods. Naturwissenschaften 2004;91:157–72.

[46] Züttel A. Materials for hydrogen storage. Mater Today 2003;6:24–33.

[47] Toyota. 2017 Mirai Product Information n.d. https://pressroom.toyota.com/2017-toyota-mirai-product/.

[48] Khafidz NZAK, Yaakob Z, Lim KL, Timmiati SN. The kinetics of lightweight solid-state hydrogen storage materials: A review. Int J Hydrogen Energy 2016;41:13131–51.

[49] He T, Pachfule P, Wu H, Xu Q, Chen P. Hydrogen carriers. Nat Rev Mater 2016;1:1–17.

[50] Broom DP, Webb CJ, Fanourgakis GS, Froudakis GE, Trikalitis PN, Hirscher M. Concepts for improving hydrogen storage in nanoporous materials. Int J Hydrogen Energy 2019;44:7768–79.

[51] Edlund D. Methanol fuel cell systems: advancing towards commercialization. Pan Stanford; 2016.

[52] Ipsakis D, Voutetakis S, Seferlis P, Papadopoulou S. Dynamic modeling and control issues on a methanol reforming unit for hydrogen production and use in a PEM fuel cell. vol. 7. IFAC; 2009. https://doi.org/10.3182/20090712-4-tr-2008.00134.

[53] Kilner JA, Skinner SJ, Irvine SJC, Edwards PP. Functional materials for sustainable energy applications. Elsevier; 2012.

[54] Krumpelt M, Krause TR, Carter JD, Kopasz JP, Ahmed S. Fuel processing for fuel cell systems in transportation and portable power applications. Catal Today 2002;77:3–16. https://doi.org/10.1016/S0920-5861(02)00230-4.

[55] Iulianelli A, Ribeirinha P, Mendes A, Basile A. Methanol steam reforming for hydrogen generation via conventional and membrane reactors: A review. Renew Sustain Energy Rev 2014;29:355–68. https://doi.org/10.1016/j.rser.2013.08.032.

[56] Karim A, Bravo J, Gorm D, Conant T, Datye A. Comparison of wall-coated and packed-bed reactors for steam reforming of methanol. Catal Today 2005;110:86–91. https://doi.org/10.1016/j.cattod.2005.09.010.

[57] Dalena F, Senatore A, Basile M, Knani S, Basile A, Iulianelli A. Advances in methanol production and utilization, with particular emphasis toward hydrogen generation via membrane reactor technology. Membranes (Basel) 2018;8. https://doi.org/10.3390/membranes8040098.

[58] Selva Roselin L, Chiu HW. Production of hydrogen by oxidative steam reforming of methanol over Cu/SiO2 catalysts. J Saudi Chem Soc 2018;22:692–704. https://doi.org/10.1016/j.jscs.2017.12.001.

[59] Cai F, Lu P, Ibrahim JJ, Fu Y, Zhang J, Sun Y. Investigation of the role of Nb on Pd− Zr− Zn catalyst in methanol steam reforming for hydrogen production. Int J Hydrogen Energy 2019;44:11717–33.

[60] Sá S, Silva H, Brandão L, Sousa JM, Mendes A. Catalysts for methanol steam reforming—A review. Appl Catal B Environ 2010;99:43–57.

[61] Wu G-S, Mao D-S, Lu G-Z, Cao Y, Fan K-N. The role of the promoters in Cu based catalysts for methanol steam reforming. Catal Letters 2009;130:177–84.

[62] Yong ST, Ooi CW, Chai SP, Wu XS. Review of methanol reforming-Cu-based catalysts, surface reaction mechanisms, and reaction schemes. Int J Hydrogen Energy 2013;38:9541–52. https://doi.org/10.1016/j.ijhydene.2013.03.023.

[63] Palo DR, Dagle RA, Holladay JD. Methanol steam reforming for hydrogen production. Chem Rev 2007;107:3992–4021. https://doi.org/10.1021/cr050198b.

[64] Lei Y, Luo Y, Li X, Lu J, Mei Z, Peng W, et al. The role of samarium on Cu/Al2O3 catalyst in the methanol steam reforming for hydrogen production. Catal Today 2018;307:162–8.

[65] Özcan O, Akın AN. Thermodynamic analysis of methanol steam reforming to produce hydrogen for HT-PEMFC: An optimization study. Int J Hydrogen Energy 2019;44:14117–26. https://doi.org/10.1016/j.ijhydene.2018.12.211.

[66] Rosli RE, Sulong AB, Daud WRW, Zulkifley MA, Husaini T, Rosli MI, et al. A review of high-temperature proton exchange membrane fuel cell (HT-PEMFC) system. Int J Hydrogen Energy 2017;42:9293–314.

[67] Kappis K, Papavasiliou J, Avgouropoulos G. Methanol Reforming Processes for Fuel Cell Applications. Energies 2021;14:8442.

[68] Ribeirinha P, Schuller G, Boaventura M, Mendes A. Synergetic integration of a methanol steam reforming cell with a high temperature polymer electrolyte fuel cell. Int J Hydrogen Energy 2017;42:13902–12. https://doi.org/10.1016/j.ijhydene.2017.01.172.

[69] Ribeirinha P, Abdollahzadeh M, Sousa JM, Boaventura M, Mendes A. Modelling of a high-temperature polymer electrolyte membrane fuel cell integrated with a methanol steam reformer cell. Appl Energy 2017;202:6–19. https://doi.org/10.1016/j.apenergy.2017.05.120.

[70] Chein RY, Chen YC, Lin YS, Chung JN. Experimental study on the hydrogen production of integrated methanol-steam reforming reactors for PEM fuel cells. Int J Therm Sci 2011;50:1253–62.

https://doi.org/10.1016/j.ijthermalsci.2011.03.001.

[71] Xing S, Zhao C, Ban S, Su H, Chen M, Wang H. A hybrid fuel cell system integrated with methanol steam reformer and methanation reactor. Int J Hydrogen Energy 2021;46:2565–76.

[72] Justesen KK, Andreasen SJ. Determination of optimal reformer temperature in a reformed methanol fuel cell system using ANFIS models and numerical optimization methods. Int J Hydrogen Energy 2015;40:9505–14.

[73] Justesen KK, Andreasen SJ, Shaker HR. Dynamic modeling of a reformed methanol fuel cell system using empirical data and adaptive neuro-fuzzy inference system models. J Fuel Cell Sci Technol 2014;11.

[74] Justesen KK, Andreasen SJ, Pasupathi S, Pollet BG. Modeling and control of the output current of a Reformed Methanol Fuel Cell system. Int J Hydrogen Energy 2015;40:16521–31. https://doi.org/10.1016/j.ijhydene.2015.10.006.

[75] Ribeirinha P, Abdollahzadeh M, Pereira A, Relvas F, Boaventura M, Mendes A. High temperature PEM fuel cell integrated with a cellular membrane methanol steam reformer: Experimental and modelling. Appl Energy 2018;215:659–69. https://doi.org/10.1016/j.apenergy.2018.02.029.

[76] Ribeirinha P, Alves I, Vázquez FV, Schuller G, Boaventura M, Mendes A. Heat integration of methanol steam reformer with a high-temperature polymeric electrolyte membrane fuel cell. Energy 2017;120:468–77. https://doi.org/10.1016/j.energy.2016.11.101.

[77] Lotrič A, Sekavčnik M, Pohar A, Likozar B, Hočevar S. Conceptual design of an integrated thermally self-sustained methanol steam reformer – High-temperature PEM fuel cell stack manportable power generator. Int J Hydrogen Energy 2017;42:16700–13. https://doi.org/10.1016/j.ijhydene.2017.05.057.

[78] Sahlin SL, Andreasen SJ, Kær SK. System model development for a methanol reformed 5 kW high temperature PEM fuel cell system. Int J Hydrogen Energy 2015;40:13080–9.

[79] Yoshida K, Tanaka S, Hiraki H, Esashi M. A micro fuel reformer integrated with a combustor and a microchannel evaporator. J Micromechanics Microengineering 2006;16. https://doi.org/10.1088/0960-1317/16/9/S04.

[80] Kim T. Micro methanol reformer combined with a catalytic combustor for a PEM fuel cell. Int J Hydrogen Energy 2009;34:6790–8. https://doi.org/10.1016/j.ijhydene.2009.06.024.

[81] Iordanidis AA. Mathematical Modeling of Catalytic Fixed Bed Reactors. 2002.

[82] Zhuang X, Xu X, Li L, Deng D. Numerical investigation of a multichannel reactor for syngas production by methanol steam reforming at various operating conditions. Int J Hydrogen Energy 2020;45:14790–805.

[83] Agrell J, Birgersson H, Boutonnet M. Steam reforming of methanol over a Cu/ZnO/Al2O3 catalyst: a kinetic analysis and strategies for suppression of CO formation. J Power Sources 2002;106:249–57.

[84] Santacesaria E, Carra S. Kinetics of catalytic steam reforming of methanol in a CSTR reactor. Appl Catal 1983;5:345–58.

[85] Tesser R, Di Serio M, Santacesaria E. Methanol steam reforming: A comparison of different kinetics in the simulation of a packed bed reactor. Chem Eng J 2009;154:69–75. https://doi.org/10.1016/j.cej.2009.06.007.

[86] Nehe P, Reddy VM, Kumar S. Investigations on a new internally-heated tubular packed-bed methanol–steam reformer. Int J Hydrogen Energy 2015;40:5715–25.

[87] Suh J-S, Lee M, Greif R, Grigoropoulos CP. A study of steam methanol reforming in a microreactor. J Power Sources 2007;173:458–66.

[88] Pan L, Wang S. Modeling of a compact plate-fin reformer for methanol steam reforming in fuel cell systems. Chem Eng J 2005;108:51–8.

[89] Peppley BA, Amphlett JC, Kearns LM, Mann RF. Methanol–steam reforming on Cu/ZnO/Al2O3 catalysts. Part 2. A comprehensive kinetic model. Appl Catal A Gen 1999;179:31–49. https://doi.org/10.1016/S0926-860X(98)00299-3.

[90] Peppley BA, Amphlett JC, Kearns LM, Mann RF. Methanol-steam reforming on Cu/Zno/Al2O3. Part 1: The reaction network. Appl Catal A Gen 1999;179:21–9. https://doi.org/10.1016/S0926-860X(98)00298-1.

[91] Chein R, Chen Y-C, Chung JN. Axial heat conduction and heat supply effects on methanol-steam reforming performance in micro-scale reformers. Int J Heat Mass Transf 2012;55:3029–42.

[92] Jiang CJ, Trimm DL, Wainwright MS, Cant NW. Kinetic study of steam reforming of methanol over copper-based catalysts. Appl Catal A Gen 1993;93:245–55.

[93] Jiang CJ, Trimm DL, Wainwright MS, Cant NW. Kinetic mechanism for the reaction between methanol and water over a Cu-ZnO-Al2O3 catalyst. Appl Catal A Gen 1993;97:145–58.

[94] Lee JK, Ko JB, Kim DH. Methanol steam reforming over Cu/ZnO/Al2O3 catalyst: kinetics and effectiveness factor. Appl Catal A Gen 2004;278:25–35.

[95] Amphlett JC, Creber KAM, Davis JM, Mann RF, Peppley BA, Stokes DM. Hydrogen production by steam reforming of methanol for polymer electrolyte fuel cells. Int J Hydrogen Energy 1994;19:131–7.

[96] Purnama H, Ressler T, Jentoft RE, Soerijanto H, Schlögl R, Schomäcker R. CO formation/selectivity for steam reforming of methanol with a commercial CuO/ZnO/Al2O3 catalyst. Appl Catal A Gen 2004;259:83–94. https://doi.org/10.1016/j.apcata.2003.09.013.

[97] Sá S, Sousa JM, Mendes A. Steam reforming of methanol over a CuO/ZnO/Al2O3 catalyst, part I: Kinetic modelling. Chem Eng Sci 2011;66:4913–21. https://doi.org/10.1016/j.ces.2011.06.063.

[98] Herdem MS, Mundhwa M, Farhad S, Hamdullahpur F. Multiphysics Modeling and Heat Distribution Study in a Catalytic Microchannel Methanol Steam Reformer. Energy and Fuels 2018;32:7220–34. https://doi.org/10.1021/acs.energyfuels.8b01280.

[99] Yaws CL. Chemical properties handbook: physical, thermodynamic, environmental, transport, safety and health related properties for organic and inorganic chemicals. 1999.

[100] Wan Y, Zhou Z, Cheng Z. Hydrogen production from steam reforming of methanol over CuO/ZnO/Al2O3 catalysts: Catalytic performance and kinetic modeling. Chinese J Chem Eng 2016;24:1186–94.

[101] Fogler HS, Fogler SH. Elements of chemical reaction engineering. Pearson Educación; 1999.

[102] Klaewkla R, Arend M, Hoelderich WF. A review of mass transfer controlling the reaction rate in heterogeneous catalytic systems. vol. 5. INTECH Open Access Publisher Rijeka; 2011.

[103] Lattanzi AM, Pecha MB, Bharadwaj VS, Ciesielski PN. Beyond the effectiveness factor: Multi-step reactions with intraparticle diffusion limitations. Chem Eng J 2020;380. https://doi.org/10.1016/j.cej.2019.122507.

[104] Ziarati M, Ghafouri Roozbahani MA, Khandan N. New method of rigorous modeling and CFD simulation for methanol—steam reforming in packed-bed reactors. Chem Eng Commun 2016;203:1359–73.

[105] Olatunde AO, Olafadehan OA, Usman MA. Computation of effectiveness factor for methanol steam reforming over Cu/ZnO/Al2O3 catalyst pellet. Appl Petrochemical Res 2020;10:35–47.

[106] Taylor R, Krishna R. Multicomponent mass transfer. vol. 2. John Wiley & Sons; 1993.

[107] Agarwal V, Patel S, Pant KK. H2 production by steam reforming of methanol over Cu/ZnO/Al2O3catalysts: Transient deactivation kinetics modeling. Appl Catal A Gen 2005;279:155–64. https://doi.org/10.1016/j.apcata.2004.10.026.

[108] Koning GW. Heat and mass transport in tubular packed bed reactors at reacting and non-reacting conditions: experiments and models. Twente University Press Enschede; 2002.

[109] Gan J, Zhou Z, Yu A. Effect of particle shape and size on effective thermal conductivity of packed beds. Powder Technol 2017;311:157–66. https://doi.org/10.1016/j.powtec.2017.01.024.

[110] Wu J, Zhang H, Ying W, Fang D. Thermal conductivity of cobalt-based catalyst for fischer-tropsch synthesis. Int J Thermophys 2010;31:556–71. https://doi.org/10.1007/s10765-010-0740-x.

[111] Gnielinski V. G9 Fluid-Particle heat transfer in flow through packed beds of solids. VDI Heat Atlas, Springer, Berlin, Heidelberg; 2010, p. 743–4.

[112] Fogler HS. Essentials of Chemical Reaction Engineering: Essenti Chemica Reactio Engi. Pearson Education; 2010.

[113] Yoon HC, Otero J, Erickson PA. Reactor design limitations for the steam reforming of methanol. Appl Catal B Environ 2007;75:264–71. https://doi.org/10.1016/j.apcatb.2007.04.017.

[114] Wesenberg MMH. Gas Heated Steam Reformer Modelling. 2006.

[115] Poling BE, Prausnitz JM, O'connell JP. The properties of gases and liquids. vol. 5. Mcgraw-hill New York; 2001.

[116] Russo V, Mastroianni L, Tesser R, Salmi T, Di Serio M. Intraparticle Modeling of Non-Uniform Active Phase Distribution Catalyst.

ChemEngineering 2020;4:24.

[117] Gallucci F, Basile A. A theoretical analysis of methanol synthesis from CO2 and H2 in a ceramic membrane reactor. Int J Hydrogen Energy 2007;32:5050–8. https://doi.org/10.1016/j.ijhydene.2007.07.067.

[118] Rase HF. Fixed-bed reactor design and diagnostics: gas-phase reactions. Butterworth-Heinemann; 2013.

[119] Zhu J, Araya SS, Cui X, Kær SK. The role of effectiveness factor on the modeling of methanol steam reforming over CuO/ZnO/Al2O3 catalyst in a multi-tubular reactor. Int J Hydrogen Energy 2022.

[120] Ipsakis D, Ouzounidou M, Papadopoulou S, Seferlis P, Voutetakis S. Dynamic modeling and control analysis of a methanol autothermal reforming and PEM fuel cell power system. Appl Energy 2017;208:703–18.

[121] Jiang J, Li X, Deng Z, Yang J, Zhang Y, Li J. Control-oriented dynamic model optimization of steam reformer with an improved optimization algorithm. Int J Hydrogen Energy 2013;38:11288–302.

[122] Jeon SW, Yoon WJ, Jeong MW, Kim Y. Optimization of a counter-flow microchannel reactor using hydrogen assisted catalytic combustion for steam reforming of methane. Int J Hydrogen Energy 2014;39:6470–8.

[123] Ghouse JH, Adams II TA. A multi-scale dynamic two-dimensional heterogeneous model for catalytic steam methane reforming reactors. Int J Hydrogen Energy 2013;38:9984–99.

[124] Li M, Duraiswamy K, Knobbe M. Adsorption enhanced steam reforming of methanol for hydrogen generation in conjunction with fuel cell: Process design and reactor dynamics. Chem Eng Sci 2012;67:26–33.

[125] Jokar SM, Parvasi P, Basile A. The performance evaluation of an industrial membrane reformer with catalyst-deactivation for a domestic methanol production plant. Int J Hydrogen Energy 2019;44:25730–9.

[126] Alopaeus V, Laavi H, Aittamaa J. A dynamic model for plug flow reactor state profiles. Comput Chem Eng 2008;32:1494–506.

[127] Karim A, Bravo J, Gorm D, Conant T, Datye A. Comparison of wall-coated and packed-bed reactors for steam reforming of methanol. Catal Today 2005;110:86–91.

[128] Ribeirinha P, Boaventura M, Lopes JCB, Sousa JM, Mendes A. Study of different designs of methanol steam reformers: Experiment and modeling. Int J Hydrogen Energy 2014;39:19970–81. https://doi.org/10.1016/j.ijhydene.2014.10.029.

[129] Chougule A, Sonde RR. Modelling and experimental investigation of compact packed bed design of methanol steam reformer. Int J Hydrogen Energy 2019;44:29937–45.

[130] McCabe WL, Smith JC, Harriott P. Unit operations of chemical engineering. vol. 5. McGraw-hill New York; 1993.

[131] Mears DE. Diagnostic criteria for heat transport limitations in fixed bed reactors. J Catal 1971;20:127–31.

[132] Ma H, Zhou M, Ying W, Fang D. Two-dimensional modeling of a plant-scale fixed-bed reactor for hydrogen production from methanol steam reforming. Int J Hydrogen Energy 2016;41:16932–43.

[133] Rafiq MH, Jakobsen HA, Schmid R, Hustad JE. Experimental studies and modeling of a fixed bed reactor for Fischer–Tropsch synthesis using biosyngas. Fuel Process Technol 2011;92:893–907.

[134] Cui X, Kær SK. A comparative study on three reactor types for methanol synthesis from syngas and CO2. Chem Eng J 2020;393:124632. https://doi.org/10.1016/j.cej.2020.124632.

[135] Schiesser WE, Griffiths GW. A compendium of partial differential equation models: method of lines analysis with Matlab. Cambridge University Press; 2009.

[136] Sherif SA, Goswami DY, Stefanakos EKL, Steinfeld A. Handbook of hydrogen energy. CRC Press; 2014.

[137] Mochizuki H, Yokoi T, Imai H, Watanabe R, Namba S, Kondo JN, et al. Facile control of crystallite size of ZSM-5 catalyst for cracking of hexane. Microporous Mesoporous Mater 2011;145:165–71. https://doi.org/10.1016/j.micromeso.2011.05.011.

[138] Zhuang X, Xia X, Xu X, Li L. Experimental investigation on hydrogen production by methanol steam reforming in a novel multichannel micro packed bed reformer. Int J Hydrogen Energy 2020;45:11024–34. https://doi.org/10.1016/j.ijhydene.2020.02.034.

[139] Kuncharam BVR, Dixon AG. Multi-scale two-dimensional packed bed reactor model for industrial steam methane reforming. Fuel Process Technol 2020;200:106314.

[140] Davieau DD, Erickson PA. The effect of geometry on reactor performance in the steam-reformation process. Int J Hydrogen Energy 2007;32:1192–200.

Nomenclature

Symbols

a_v	external particle surface area per unit reactor volume	m^{-1}
Bi	tube Biot number, $h_w d_t/(2/\lambda_{er})$	
Bi_f	fluid/wall Biot number, $h_{fw} d_t/(2/\lambda_{er})$	
Bi_s	solid/wall Biot number, $h_{sw} d_t/(2/\lambda_{er})$	
c_p	specific heat capacity	$\mathrm{J\ kg^{-1}K^{-1}}$
C_i	concentration of component i in the fluid phase	$\mathrm{mol\ m^{-3}}$
C_i^s	concentration of component i in the solid phase	$\mathrm{mol\ m^{-3}}$
C_{Si}^T	concentrations of active sites i	$\mathrm{mol\ m^{-2}}$
C_{WP}	Weisz-Prater parameter	
d_{lm}	log-mean diameter	m
d_p	particle diameter	m
d_p^s	surface-equivalent spherical diameter	m
d_p^v	volume-equivalent spherical diameter	m
d_s	diameter of the reformer shell	m
d_t	tube diameter	m
$d_{t,i}$	inner diameter of tube	m
$d_{t,o}$	outer diameter of tube	m
$\bar{d}$	average pore diameter	m
D_{er}	effective radial mass diffusion coefficient	$\mathrm{m^2\ s^{-1}}$
$D_{i,ep}$	particle effective diffusivity of component i	$\mathrm{m^2\ s^{-1}}$
$D_{i,f}$	gas diffusivity of species i	$\mathrm{m^2\ s^{-1}}$
D_{ij}	diffusivity for a binary mixture of i and j	$\mathrm{m^2}\ s^{-1}$
$D_{i,M}$	effective multicomponent diffusion coefficient of component i	$\mathrm{m^2}\ s^{-1}$
$D_{i,K}$	Knudsen diffusivity of component i	$\mathrm{m^2}\ s^{-1}$
D_s	diameter of reformer shell	m
f_b	area fraction of baffle plate that is window	
G	superficial mass velocity	$\mathrm{kg\ m^{-2}s^{-1}}$
G_b	mass velocity through the baffle window	$\mathrm{kg\ m^{-2}s^{-1}}$

G_e	mass velocity of gas mixture	$\mathrm{kg\ m^{-2}s^{-1}}$
G_p	mass velocity for crossflow perpendicular to the tubes	$\mathrm{kg\ m^{-2}s^{-1}}$
h	tube height	m
h_{fs}	heat transfer coefficient between fluid bulk and catalyst particle	$\mathrm{W\ m^{-2}\ K^{-1}}$
h_s	heat transfer coefficient of the shell-side film	$\mathrm{W\ m^{-2}\ K^{-1}}$
h_t	heat transfer coefficient of the tube-side film	$\mathrm{W\ m^{-2}\ K^{-1}}$
k	thermal conductivity	$\mathrm{W\ m^{-1}K^{-1}}$
$k_{i,fs}$	mass transfer coefficient of component i between the fluid phase and solid phase	$\mathrm{m\ s^{-1}}$
k_j	rate constant of reaction j	$\mathrm{m^2\ s^{-1}mol^{-1}}$
k_m	thermal conductivity of gas mixture	$\mathrm{W\ m^{-1}K^{-1}}$
k_s	thermal conductivity of the shell-side fluid	$\mathrm{W\ m^{-1}K^{-1}}$
k_w	thermal conductivity of the tube wall	$\mathrm{W\ m^{-1}K^{-1}}$
K_j^{eq}	equilibrium constant of reaction j	
K^*	adsorption coefficient	$\mathrm{bar^{-0.5}}$
L	reactor length	m
M_i	molar mass of component i	$\mathrm{g\ mol^{-1}}$
N_b	number of baffle plates	
N_t	number of tubes	
Nu_{fs}	fluid/solid Nusselt number, $h_f d_p/\lambda_f$	
p_i	partial pressure of component i	Pa
p_t	tube pitch	m
P	pressure	Pa
P_b	baffle spacing	m
Pe	Peclet number	
Pe_h^0	Peclet number for heat transfer	
$\mathrm{Pe}_{h,r}^{\infty}$	Peclet radial heat transfer for fully developed turbulent flow	
Pr	Prandtl number, $c_p\mu/\lambda$	
r_i	production (consumption) rate of component i	$\mathrm{mol\ s^{-1}kg^{-1}}$
r_j	reaction rate of reaction j	$\mathrm{mol\ m^{-2}s^{-1}}$
r_p	radius of the catalyst pellet	m
R	gas constant	$\mathrm{J\ mol^{-1}K^{-1}}$

R_i	production (consumption) rate of component i per unit reactor volume	$\mathrm{mol\ m^{-3} s^{-1}}$
R_T	heat generation per unit reactor volume	$\mathrm{J\ m^{-3} s^{-1}}$
Re	Reynolds number, $d_p \rho_f u_s / \mu$	
S_{ba}	area for shell-side fluid flow through the baffle window	$\mathrm{m^2}$
Sc	Schmidt number	
S_c	surface area per unit mass of fresh catalyst	$\mathrm{m^2\ kg^{-1}}$
Sh	Sherwood number	
S_{pe}	interstitial area for crossflow perpendicular to the bank of tubes at the widest point in the shell side	$\mathrm{m^2}$
S_p	external surface area of a single non-spherical particle	$\mathrm{m^2}$
T	temperature	K
u_s	superficial fluid velocity	$\mathrm{m\ s^{-1}}$
U_w	overall heat transfer coefficient	$\mathrm{W\ m^{-2} K^{-1}}$
x_i	mole fraction of component i	
x_w	thickness of the tube wall	m
z	axial variable	m

Greek symbols

ΔH	heat of reaction	$\mathrm{J\ mol^{-1}}$
ΔS	entropy	$\mathrm{J\ mol^{-1} K^{-1}}$
ε	porosity	
η	effectiveness factor	
λ_{er}	effective radial thermal conductivity in the catalyst bed	$\mathrm{W\ m^{-1}\ K^{-1}}$
λ_{ep}	particle effective thermal conductivity	$\mathrm{W\ m^{-1}\ K^{-1}}$
λ_f	thermal conductivity of the fluid	$\mathrm{W\ m^{-1}\ K^{-1}}$
λ_i	thermal conductivity of the component i	$\mathrm{mW\ m^{-1} K^{-1}}$
λ_r^0	stagnant thermal conductivity in packed bed	$\mathrm{W\ m^{-1}\ K^{-1}}$
λ_p	thermal conductivity of catalyst particle	
μ	fluid viscosity	Pa s
ν_{ij}	stoichiometric coefficient of the component i in reaction j	
ξ	radial variable for catalyst particle	m
ρ	density	$\mathrm{kg\ m^{-3}}$

ϕ	Thiele modulus
Ω_D	collision integral for diffusion

Subscripts

cat / c	catalyst
b	bulk fluid
f	fluid
lam	laminar flow
p	catalyst particle
s	shell side
t	tube side
$turb$	turbulent flow
w	tube wall

Superscripts

s	surface

Papers

Paper A

Modeling and Design of a Multi-Tubular Packed-Bed Reactor for Methanol Steam Reforming over a $Cu/ZnO/Al_2O_3$ Catalyst

Jimin Zhu, Samuel Simon Araya, Xiaoti Cui, Simon Lennart Sahlin, and Søren Knudsen Kær

The paper has been published in Energies 13, no. 3 (2020): 610.

Modeling and Design of a Multi-Tubular Packed-Bed Reactor for Methanol Steam Reforming over a $Cu/ZnO/Al_2O_3$ Catalyst

Jimin Zhu *, Samuel Simon Araya, Xiaoti Cui, Simon Lennart Sahlin and Søren Knudsen Kær

Department of Energy Technology, Aalborg University, Pontoppidanstræde 111, 9220 Aalborg Ø, Denmark

Abstract

Methanol as a hydrogen carrier can be reformed with steam over $Cu/ZnO/Al_2O_3$ catalysts. In this paper a comprehensive pseudo-homogenous model of a multi-tubular packed-bed reformer has been developed to investigate the impact of operating conditions and geometric parameters on its performance. A kinetic Langmuir-Hinshelwood model of the methanol steam reforming process was proposed. In addition to the kinetic model, the pressure drop and the mass and heat transfer phenomena along the reactor were taken into account. This model was verified by a dynamic model in the platform of ASPEN. The diffusion effect inside catalyst particles was also estimated and accounted for by the effectiveness factor. The simulation results showed axial temperature profiles in both tube and shell side with different operating conditions. Moreover, the lower flow rate of liquid fuel and higher inlet temperature of thermal air led to a lower concentration of residual methanol, but also a higher concentration of generated CO from the reformer exit. The choices of operating conditions were limited to ensure a tolerable concentration of methanol and CO in H_2-rich gas for feeding into a high temperature polymer electrolyte membrane fuel cell (HT-PEMFC) stack. With fixed catalyst load, the increase of tube number and decrease of tube diameter improved the methanol conversion, but also increased the CO concentration in reformed gas. In addition, increasing the number of baffle plates in the shell side increased the methanol conversion and the CO concentration.

Keywords: methanol steam reforming; multi-tubular packed-bed reformer; hydrogen production; temperature profile; geometric parameter

* Corresponding author.

Email address: jzu@energy.aau.dk (Jimin Zhu)

Preprint submitted to Energies *January 24, 2020*

1. Introduction

The contribution of hydrogen to the promotion of green energy is mainly driven by recent achievements, especially polymer electrolyte membrane (PEM) fuel cells, where hydrogen is used as the fuel. One obstacle for the development of the hydrogen economy is the safe storage and transportation challenge presented by hydrogen. Therefore, special attention has been paid to the development of economical hydrogen production methods by chemically converting hydrocarbons or alcohols to a hydrogen-rich synthesis gas stream. This process, generically called reforming, requires oxidizing agents. When water is used as the oxidant, the process is known as steam reforming [1]. Among various hydrogen carriers, methanol stands out because of its properties of being liquid at ambient conditions and infinitely miscible with water. Moreover, methanol has a low boiling point (65°C) for vaporization, a relatively high H/C ratio (4:1), a low reforming temperature (200-300°C) owing to the absence of a strong C–C bond, and is producible from various carbon-based feedstocks, such as natural gas, biomass, and CO_2 [2–4]. Under appropriate conditions, the most favored reaction stoichiometry is the methanol steam reforming (MSR) reaction. One of the major advantages of the MSR reaction is that 1/3 of the hydrogen product can be derived from water. In addition to the MSR reaction, there are normally other two reactions that happen during the reforming process: the water-gas shift (WGS) reaction and the methanol decomposition (MD) reaction. The three main reactions that take place within the methanol steam reformer are shown in the following equations [5]:

Methanol steam reforming reaction (MSR):

$$CH_3OH + H_2O \leftrightarrow CO_2 + 3H_2 \qquad \Delta H = +\,49.7\ \left(kJ\ mol^{-1}\right), \tag{1}$$

Water-gas shift reaction (WGS):

$$CO + H_2O \leftrightarrow CO_2 + H_2 \qquad \Delta H = -\,41.2\ \left(kJ\ mol^{-1}\right), \tag{2}$$

Methanol decomposition reaction (MD):

$$CH_3OH \leftrightarrow CO + 2H_2 \qquad \Delta H = +\,90.2\ \left(kJ\ mol^{-1}\right), \tag{3}$$

Although hydrogen is the only desired product, other by-products are inevitably formed in reformate gas mixture, such as carbon dioxide (CO_2), small amounts of carbon monoxide (CO), unconverted water and methanol vapor. The fractions of methanol, CO_2 and especially CO in the reformate gas should be minimized because of their poisoning effect on fuel cells [6,7]. Catalysts used for methanol steam reforming are supposed to have as main properties good activity and fast kinetics at low temperature, high selectivity to suppress CO production, good stability and long lifetime [5]. The most widely used commercial catalysts for the MSR process are Cu-

based catalysts, especially $Cu/ZnO/Al_2O_3$, due to their relatively high activity and selectivity [8].

Methanol reforming methods carried out experimentally and industrially in packed-bed reactors will inevitably result in high investment and operating costs. Therefore, there are numerous studies on the kinetics and mechanisms of MSR over commercial $Cu/ZnO/Al_2O_3$ catalysts. Jiang et al. [9] proposed an expression of reaction rates based on power rate law kinetics. It is assumed that there was only one kind of active site for reactions and the methyl formate was the intermediate. Peppley et al. [10] studied the reaction network of MSR on the catalyst BASF K3-110. They assumed two distinct types of active sites, one type for MSR and WGS reactions and the other for MD reaction. And a comprehensive kinetic model was developed considering the surface mechanism of the catalyst. Agrell et al. [11] investigated the MSR over a $Cu/ZnO/Al_2O_3$ catalyst from Süd-Chemie (G-66 MR) and developed a kinetic model. With operating temperatures below 220 °C, an Arrhenius-type function was used; and with higher temperatures, the mass transport hindered the reaction kinetics, hence a fifth degree polynomial was used instead of the Arrhenius expression. Sandra et al. [12] and Herdem et al. [13] compared several kinetic rate expressions of the MSR process. They found that a kinetic Langmuir-Hinshelwood model which was developed by Peppley et al. [10] presented the best fit to the experimental data.

Another dominant factor for the reforming process is the reformer design. Conventional packed-bed reformers use catalyst particles in the form of pellets or cylinders, which are versatile for application at both the laboratory and industrial scale owing to their relatively low cost and easy operation [14]. Nevertheless, one disadvantage of packed-bed reformers is the radial temperature gradient in the catalyst bed [3]. Recent progress in micro-processing make it possible to manufacture wall-coated micro-channel reactors and membrane reactors, which present fewer heat and mass transfer limitations, less pressure drop, better selectivity, but also a drawback of lower specific catalyst load [2,9,15,16]. However, potential barriers for the commercialization of micro-channel and membrane reactors, such as high costs and low mechanical resistance, make packed-bed reformers still the most widely used types in the chemical industry for extracting hydrogen from methanol.

Because of the endothermic characteristic of the reforming process, an external heating source is needed to activate the reaction sites and prevent temperature drops in the catalyst bed. For on-site applications, it means that the reformer should be integrated with a heat supply unit, usually called a catalytic combustor or burner [17–19]. In this system, a flow of thermal fluid is needed to transfer heat from the burner to the catalyst bed. Reaction rates of methanol reforming predominately depend on the local concentration and temperature correlated to heat and mass transfer mechanisms, which should be investigated when designing a reactor. Yoon et al. [20] analyzed the dominant limiting mechanisms (heat transfer, mass transfer and chemical kinetics) in the methanol steam reformer theoretically and experimentally. Results

showed that with the diminishing of catalyst size, the heat transfer limitation increased and the mass transfer limitation decreased. Also with the diameter of the reactor diminished, the heat and mass transfer were enhanced. Vadlamudi et al. [21] analyzed a packed-bed reactor for autothermal reforming of methanol to produce sufficient hydrogen for a 100 W fuel cell stack. They developed a 1-D non-isothermal model considering the steady state mass and energy balance. The simulated results agreed well with experimental data and the pressure drop was considered to be negligible. Ma et al. [22] investigated the hydrogen output and thermal behavior of a plant-scale fixed-bed reformer for methanol steam reforming based on a 2-D pseudo-homogenous model. The results showed that there was no obvious concentration gradients in the radial direction. Moreover, with a larger tube diameter, the limited heat transfer would lead to a larger radial temperature gradient in the catalyst bed. A similar result has been reported in [23] that the small ratio of tube to particle diameter (D/dp) and low reactant velocity introduced a large heat transport resistance between the tube wall and the catalyst particles. Mears et al. [23] developed a criterion to evaluate the importance of radial temperature gradients in fixed bed catalytic reactors. Results showed that the heat transfer resistance between the wall and the catalyst bed cannot be neglected when $D/dp > 100$. Furthermore, the increased porosity of the bed near the wall caused a limited number of contact points between catalyst particles and the reactor wall. Hence, the major cause of the heat transport resistance between the catalyst bed and the reactor wall could be regarded as the gas film [24], which has been considered in this study. Vázquez et al. [25] employed a tubular-quartz reactor and a multichannel micro packed-bed reactor to perform the kinetic model of methanol steam reforming. The results represented both axial and radial temperature gradients in the catalyst bed. But for a small-scale multichannel reactor with a large length to width ratio ($L/W = 50$), the radial temperature gradients in the catalyst bed can be considered negligible at an almost isothermal condition. The study proved that convective heat transfer properties in the catalyst bed could be improved by increasing the length to width ratio of reactors to increase the gas velocity and the contact surface of gas flow in reactors. Montebelli et al. [26] compared the performance of two highly conductive structured multi-tubular reactors with a commercial multi-tubular packed-bed reactor for methanol synthesis. They concluded that the packed-bed reactor had a better performance than structured systems due to the effective convective heat transfer mechanism in the catalyst bed, which is shown as lower hot-spot temperatures and higher radial heat transfer rates. The effectiveness factor for catalysts in commercial size has been widely investigated owing to the strong effect of internal diffusion on reaction rates. Lee et al. [27] estimated the effectiveness factor of catalyst particles to investigate the effect of the particle internal diffusion limitations and obtain the intrinsic kinetics of methanol steam reforming over $Cu/ZnO/Al_2O_3$ catalyst. Tesser et al. [28] tested different kinetics of steam reforming of methanol in packed bed reactor, considering both mass and heat balance along the length of reactor and inside the catalyst particles.

The multi-tubular packed-bed reformer is normally represented as an entire tube bundle immersed in an external heating source with a uniform and constant temperature when developing a mathematical model. However, in practical applications, the temperature of thermal fluid in inter-tubular space is variable along the length and has significant effect on the performance of the reformer. Therefore, the temperature profiles of both tube side and shell side along the reactor should be taken into consideration. Compared to the large heat transfer resistance between the tube wall and the catalyst bed, the convective and conductive heat transfer inside the catalyst bed is relatively efficient. Hence, with a large L/W of the reactor, we took into account the heat transfer resistance of gas film, and neglected the radial temperature gradient inside catalyst bed to simplify the model. The catalyst effectiveness factor is generally introduced for taking into account the internal diffusion resistance in commercial catalyst particles, especially when large size particles are used. In this paper, the Weisz-Prater Criterion was used to check if there were diffusion limitations, and the effectiveness factor was estimated for the reaction.

In this work, a one-dimensional pseudo-homogenous model for multi-tubular packed-bed reformer was established in MATLAB taking into account the main chemical reactions, and the mass and heat transfer phenomena in both tube side and shell side. In the radial direction, the overall heat transfer coefficient between catalyst bed and external heating source was considered, including the conductive heat transfer through the tube wall, the convective heat transfer from reactant to the inner wall of the tube, and the convective heat transfer from the outer tube wall to the outside fluid. Effects of the pressure drop along the reactor and the intraparticle diffusion limitation were also included in this model. A dynamic model of the multi-tubular methanol steam reformer was developed in ASPEN to verify the MATLAB model. The thermal behavior of both tube side and shell side was represented in the term of temperature profile. The influence of operating conditions such as flow rate of methanol-and-water mixture and inlet temperature of external thermal air on the methanol conversion and CO concentration of reformed gas was investigated. In addition, the impact of geometric parameters of reactor design, such as the diameter and number of tubes as well as the spacing and number of baffles, has been investigated on the reformer performance. This model of MSR is expected to be integrated with the high temperature polymer electrolyte membrane fuel cell (HT-PEMFC) in a combined stack arrangement to investigate the thermal integration of the system for further study.

2. Description of Methanol Steam Reformer

Generally, a reformed methanol fuel cell (RMFC) system is composed of a burner, an evaporator, several thermal fluid circuits, a methanol steam reformer and a fuel cell stack. Firstly, the mixture of methanol and water is pumped into the evaporator where the fuel is evaporated. The vapor fuel is then fed into the catalyst bed in the reformer and converted into hydrogen-rich gas by chemical reactions. The hydrogen-rich gas from the reformer is sent to the anode side of the fuel cell stack. The fuel cells utilize

the hydrogen from anode side together with the oxygen from the cathode side to generate electricity by electrochemical reactions. The exhaust gas from the fuel cell stack is directed to the burner, where the residual hydrogen and methanol react with air in the burner. The generated heat is transferred into the catalyst bed by thermal fluid circuit. In this work, the methanol steam reformer as a subsystem of the RMFC system has been studied.

The reformer for MSR in this study is a multi-tubular packed-bed reformer. The structure of the heat-exchanger type reformer, including baffles, tubes and a shell, is presented in Figure 1. The reactor shell is usually surrounded by thermal insulation materials to avoid any significant amount of heat loss. Tubes packed with $Cu/ZnO/Al_2O_3$ catalyst are arranged in equilateral triangle tube bundles and installed inside the shell. The baffle plates are used to support the tube bundles, increase the flow distribution in the inter-tubular space and for an effective heat transfer between the tube side and shell side.

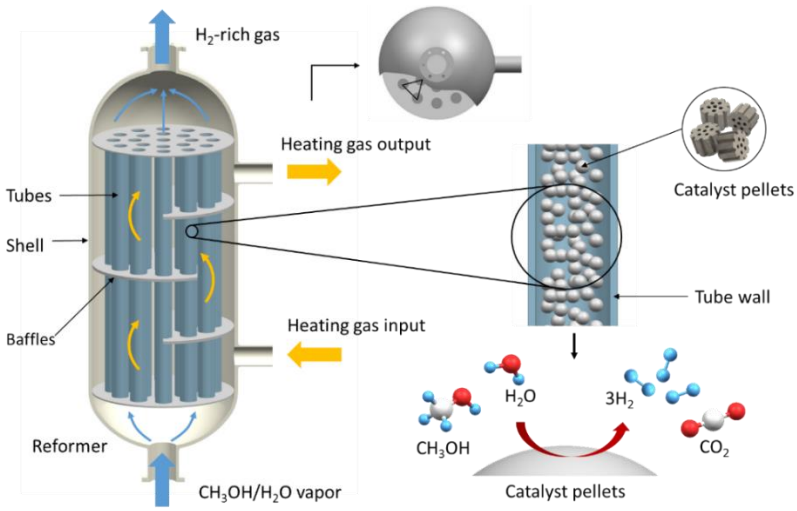

Figure 1. Structure of the multi-tubular packed-bed reformer for methanol steam reforming.

The heating gas from the burner flows through the shell side of the reformer, thereby providing an external heat source for the reactions. In the tube side, reactants flow through the catalyst bed, where the steam reforming reactions occur.

3. Model of the Methanol Steam Reformer

3.1. Kinetic Model of Reaction Rates

In this study, the process of methanol steam reforming consists of three reversible overall reactions: MSR, WGS and MD. For kinetic analysis of the reforming process over $Cu/ZnO/Al_2O_3$ catalyst, the Langmuir-Hinshelwood macro kinetic model based on the study of Peppley et al. [10] is used. This classic and comprehensive kinetic model is developed on the basis of several assumptions: hydrogen and oxygen-containing species adsorb on different active sites; the active sites for MD reaction are different from those for SRM and WGS reaction; the rate-determining step for both MSR and MD is the dehydrogenation of the adsorbed methoxy, while for WGS reaction the RDS is the formation of an intermediate formate species [12]. According to the Langmuir-Hinshelwood model, the rate expressions for three key reactions involved in the process can be expressed as follows:

$$r_R = \frac{k_R K^*_{CH_3O^{(1)}} \left(p_{CH_3OH}/p_{H_2}^{\frac{1}{2}}\right)\left(1 - p_{H_2}^3 p_{CO_2}/K_R^{eq} p_{CH_3OH} p_{H_2O}\right) C_{S_1}^T C_{S_{1a}}^T}{\left(1 + K^*_{CH_3O^{(1)}}\left(p_{CH_3OH}/p_{H_2}^{\frac{1}{2}}\right) + K^*_{HCOO^{(1)}} p_{CO_2} p_{H_2}^{\frac{1}{2}} + K^*_{OH^{(1)}}\left(p_{H_2O}/p_{H_2}^{\frac{1}{2}}\right)\right)\left(1 + K_{H^{(1a)}}^{\frac{1}{2}} p_{H_2}^{\frac{1}{2}}\right)}, \quad (4)$$

$$r_W = \frac{k_W K^*_{OH^{(1)}}\left(p_{CO} p_{H_2O}/p_{H_2}^{\frac{1}{2}}\right)\left(1 - p_{H_2} p_{CO_2}/K_W^{eq} p_{CO}\, p_{H_2O}\right) C_{S_1}^{T^2}}{\left(1 + K^*_{CH_3O^{(1)}}\left(p_{CH_3OH}/p_{H_2}^{\frac{1}{2}}\right) + K^*_{HCOO^{(1)}} p_{CO_2} p_{H_2}^{\frac{1}{2}} + K^*_{OH^{(1)}}\left(p_{H_2O}/p_{H_2}^{\frac{1}{2}}\right)\right)^2}, \quad (5)$$

$$r_D = \frac{k_D K^*_{CH_3O^{(2)}}\left(p_{CH_3OH}/p_{H_2}^{\frac{1}{2}}\right)\left(1 - p_{H_2}^2 p_{CO}/K_D^{eq} p_{CH_3OH}\right) C_{S_2}^T C_{S_{2a}}^T}{\left(1 + K^*_{CH_3O^{(2)}}\left(p_{CH_3OH}/p_{H_2}^{\frac{1}{2}}\right) + K^*_{OH^{(2)}}\left(p_{H_2O}/p_{H_2}^{\frac{1}{2}}\right)\right)\left(1 + K_{H^{(2a)}}^{\frac{1}{2}} p_{H_2}^{\frac{1}{2}}\right)}, \quad (6)$$

where k_j and K_j^{eq} are the rate constant and equilibrium constant of reaction j ($j = R, W, D$) respectively, K^* is the adsorption coefficient, p_i is the partial pressure of component i ($i = CO_2, CO, H_2, CH_3OH$ and H_2O), $C_{S_1}^T$, $C_{S_{1a}}^T$, $C_{S_2}^T$ and $C_{S_{2a}}^T$ are the total site concentrations of site '1', '1a', '2', and '2a' respectively. The required parameters for the comprehensive kinetic model of methanol steam reforming can be found in [10]. The temperature dependence of each constants can be expressed using the Arrhenius expression [10,29,30]:

$$k_R = k_R^{\infty}\, exp\left(\frac{-E_R}{RT}\right), \quad (7)$$

$$k_D = k_D^{\infty}\, exp\left(\frac{-E_D}{RT}\right), \quad (8)$$

$$k_w = k_R^{\infty}\, exp\left(\frac{-E_W}{RT}\right), \quad (9)$$

$$K_R^{eq} = \exp\left(-\frac{50240 - 170.98T - 2.64 \times 10^{-2}T^2}{RT}\right), \quad (10)$$

$$K_W^{eq} = \exp\left(-\frac{-41735 + 46.66T - 7.55 \times 10^{-3}T^2}{RT}\right), \quad (11)$$

$$K_D^{eq} = \frac{K_R^{eq}}{K_W^{eq}}, \quad (12)$$

$$K^*_{CH_3O^{(1)}} = exp\left(\frac{\Delta S^*_{CH_3O^{(1)}}}{R} - \frac{\Delta H^*_{CH_3O^{(1)}}}{RT}\right), \quad (13)$$

$$K^*_{HCOO^{(1)}} = exp\left(\frac{\Delta S^*_{HCOO^{(1)}}}{R} - \frac{\Delta H^*_{HCOO^{(1)}}}{RT}\right), \quad (14)$$

$$K^*_{OH^{(1)}} = exp\left(\frac{\Delta S^*_{OH^{(1)}}}{R} - \frac{\Delta H^*_{OH^{(1)}}}{RT}\right), \quad (15)$$

$$K_{H^{(1a)}} = exp\left(\frac{\Delta S_{H^{(1a)}}}{R} - \frac{\Delta H_{H^{(1a)}}}{RT}\right), \quad (16)$$

$$K^*_{CH_3O^{(2)}} = exp\left(\frac{\Delta S^*_{CH_3O^{(2)}}}{R} - \frac{\Delta H^*_{CH_3O^{(2)}}}{RT}\right), \quad (17)$$

$$K^*_{OH^{(2)}} = exp\left(\frac{\Delta S^*_{OH^{(2)}}}{R} - \frac{\Delta H^*_{OH^{(2)}}}{RT}\right), \quad (18)$$

$$K_{H^{(2a)}} = exp\left(\frac{\Delta S_{H^{(2a)}}}{R} - \frac{\Delta H_{H^{(2a)}}}{RT}\right), \quad (19)$$

To calculate the rate r_i (mol s^{-1}(kg of catalyst)$^{-1}$) of production i per time per mass of catalyst, it is necessary to combine the rate expressions r_j (mol $s^{-1}m^{-2}$) for each individual reaction j and multiply by the surface area per unit mass of fresh catalyst S_c (m^2kg^{-1}):

$$r_{CO_2} = (r_R + r_W)S_c, \quad (20)$$

$$r_{CO} = (r_D - r_W)S_c, \quad (21)$$

$$r_{H_2} = (3r_R + 2r_D + r_W)S_c, \quad (22)$$

$$-r_{CH_3OH} = (r_R + r_D)S_c, \tag{23}$$

$$-r_{H_2O} = (r_R + r_W)S_c, \tag{24}$$

3.2. Pressure Drop in Catalyst Bed of the Packed-Bed Reformer

As a fluid passes through a packed bed, it experiences pressure loss. Especially when the size of tablets is small, the pressure drop in the catalyst bed has to be taken into consideration. In this paper, we assume that a set of porous cylindrical catalyst particles of uniform size are packed in cylindrical tubes. It is widely accepted that the pressure drop can be approximated by the semiempirical Ergun equation [31]:

$$\frac{dP}{dz} = -\frac{G}{\rho_t D_p}\left(\frac{1-\phi}{\phi^3}\right)\left[\frac{150(1-\phi)\eta_t}{D_p} + 1.75G\right], \tag{25}$$

Inside the packed bed, the viscosity of the gas mixture η_t (Pa s) as well as the density of the gas mixture ρ_t (kg m^{-3}) can be described as a function of reactor length z (m); P (Pa) is the pressure in the catalyst bed; ϕ is the void fraction of the catalyst bed; D_p (m) is the diameter of catalyst particles; G (kg m^{-2}s^{-1}) is the superficial mass velocity. The first-order solution for viscosity of pure gas η_i (Pa s) can be expressed by using the Chun et al. method [32,33]:

$$\eta_i = 40.785\frac{F_c(M_iT)^{\frac{1}{2}}}{V_c^{\frac{2}{3}}\Omega_v}, \tag{26}$$

$$F_c = 1 - 0.2756\omega + 0.059035\mu_r^4 + \kappa, \tag{27}$$

$$\kappa = 0.682 + 4.704[(number\ of - OH\ groups)/(molecular\ weight)], \tag{28}$$

$$\mu_r = 131.3\frac{\mu}{(V_cT_c)^{\frac{1}{2}}}, \tag{29}$$

$$T^* = 1.2593\frac{T}{T_c}, \tag{30}$$

$$\Omega_v = [A(T^*)^{-B}] + C[\exp(-DT^*)] + E[\exp(-FT^*)], \tag{31}$$

Where $A = 1.16145$, $B = 0.14874$, $C = 0.52487$, $D = 0.77320$, $E = 2.16178$ and $F = 2.43787$.

In this study, Herning and Zipperer's method [34] was utilized to estimate the gas mixture viscosity η_m (Pa s) in the methanol steam reformer:

$$\eta_m = \sum_{i=1}^{5} \frac{x_i \eta_i}{\sum_{j=1}^{5} x_j \Phi_{ij}}, \tag{32}$$

$$\Phi_{ij} = \left(\frac{M_j}{M_i}\right)^{\frac{1}{2}} = {\Phi_{ji}}^{-1}, \tag{33}$$

The properties of each gas component are listed in Table 1.

Table 1. Basic constants values for the calculation of viscosity of gases.

Gas Components	V_c ($\mathbf{cm^3\ mol^{-1}}$)	T_c (K)	ω	μ (D)
CH_3OH	118.00	512.64	0.565	1.70
H_2O	55.95	647.14	0.344	1.84
H_2	64.20	32.98	-0.217	0
CO	93.10	132.85	0.045	0.122
CO_2	94.07	304.12	0.225	0

3.2. Effectiveness Factor

The use of large catalyst size can reduce the pressure drop in the catalyst bed along the length, but may lead to a significant effect of intraparticle diffusion limitation on reaction rates. The reforming mixture in catalyst bed consists of five components: carbon dioxide (CO_2), hydrogen (H_2), water (H_2O), methanol (CH_3OH), carbon monoxide (CO). In catalyst bed, reactants transfer from the bulk fluid to the external surface of catalyst particle with reforming reactions taking place. Then the reactants will diffuse from the external surface with a higher concentration to reach the pores surface inside the catalyst through the pore tortuosity. The effective diffusivity is defined to describe the diffusion, which affects the chemical reactions inside catalyst particles. The effective diffusivity $D_{i,\text{eff}}$ ($\text{m}^2\ s^{-1}$) is estimated using the Maxwell-Stefan equation [35]:

$$\frac{1}{D_{i,\text{eff}}} = \sum_{\substack{j=1 \\ j \neq i}}^{n} \frac{x_j}{D_{ij}} \left(1 - \frac{x_i N_j}{x_j N_i}\right) + \frac{1}{D_{i,K}}, \tag{34}$$

where D_{ij} ($\text{m}^2\ s^{-1}$) is the diffusivity for a binary mixture of i and j. The Chapman-Enskog equation is used for the binary diffusivity at low density:

$$D_{ij} = 0.0018583 \frac{T^{3/2}\left(1/M_i + 1/M_j\right)^{1/2}}{P\sigma_{ij}^2 \Omega_D}, \tag{35}$$

$$\sigma_{ij} = \frac{\sigma_i + \sigma_j}{2}, \tag{36}$$

$$\sigma = 0.841 V_c^{1/3}, \tag{37}$$

$$\frac{\varepsilon}{k} = 0.75 T_c, \tag{38}$$

$$\Omega_D = \left(44.54 T_{ij}^{*-4.909} + 1.911 T_{ij}^{*-1.575}\right)^{0.10}, \tag{39}$$

$$T_{ij}^* = \frac{kT}{\varepsilon_{ij}}, \tag{40}$$

$$\varepsilon_{ij} = \left(\varepsilon_i \varepsilon_j\right)^{1/2}, \tag{41}$$

where T (K) is the operating temperature, P (atm) is the pressure, M_i (kg mol^{-1}) is the molar mass of component i, Ω_D is the collision integral for diffusion. The Knudsen diffusivity $D_{i,K}$ (m^2 s^{-1}) of component i is calculated by:

$$D_{i,K} = \frac{\bar{d}}{3}\sqrt{\frac{8RT}{\pi M_i}}, \tag{42}$$

where $\bar{d}$ (m) is the average pore diameter (6.4×10^{-9} m) [36].

The effectiveness factor η (ranging from 0 to 1) is defined to describe the relative importance of diffusion and reaction limitations. For a first order reaction, the expression of the effectiveness factor is:

$$\eta\phi_1^2 = 3(\phi_1 \coth \phi_1 - 1), \tag{43}$$

where ϕ_1 is the Thiel modulus for a first-order reaction. The left-hand side is also called the Weisz-Prater parameter C_{WP}, which is used to determine whether the diffusion is limiting the reactions. The shape of catalyst particles used in this study is cylindrical.

$$C_{WP} = \eta\phi_1^2, \tag{44}$$

$$\phi_1^2 = \frac{-r_{js}\rho_c r_p^2}{4D_{i,\text{eff}}C_{is}}, \tag{45}$$

where r_{js} $(mol\ s^{-1}(g\ of\ catalyst)^{-1})$ and C_{is} $(mol\ m^{-3})$ are the rate of reaction j and the concentration of component i if the entire interior surface were exposed; r_p (m) is the radius of catalyst particle. If $C_{WP} \ll 1$, the diffusion limitation and concentration gradient within the catalyst particle is supposed to be negligible. However, if $C_{WP} \gg 1$, the internal diffusion limitation should be considered.

3.3. Mass and Energy Balance in Tube Side and Shell Side of the Packed-Bed Reformer

In this study, a comprehensive mathematical model is developed to evaluate the performance of the MSR process in the reformer. Tubes packed with catalyst particles were placed inside the reformer shell. Chemical reactions take place on the surface of $Cu/ZnO/Al_2O_3$ catalyst in the tube side of reformer. There is also a sweep of heating gas through the shell side, where no reaction happens. The model developed for the performance of the MSR process in the catalyst bed of one single tube can be extended to all tubes. The transport phenomena in the reactor-heat supply system can be described by the concentration of reactants and thermal profiles along the length of thereactor. In the radial direction of the methanol steam reformer, the convective heat transfer on both surfaces of the tube and the conductive heat transfer through the tube wall are considered. To simplify the mathematical model, major assumptions can be listed as follows:

- steady-state conditions;
- ideal gas behavior;
- the radial mass and thermal dispersions in the tube side and shell side are negligible;
- the methanol steam reaction is regarded as a first-order reaction;
- the reformer-heat supply system is adiabatic from the surrounding.

In the catalyst bed, it is assumed that the reforming reactions are affected by internal diffusion of reactants. The effectiveness factor is set to be η for the catalyst. Therefore, the continuity equations for specie i is given by the following mole-balance equations:

$$\frac{dF_i}{dz} = \eta r_i \rho_c A_c, \tag{46}$$

where F_i $(\text{mol} \cdot \text{s}^{-1})$ is the molar flow rate of component i, ρ_c $(\text{kg} \cdot m^{-3})$ is the density of catalyst, A_c (m^2) is the area of cross section of the catalyst bed.

A steady state energy balance along the axis of catalyst bed leads to the following equation [31]:

$$\frac{dT_t}{dz} = \frac{U_t a \Delta T + \sum r_j \Delta H_j S_c \rho_c}{\sum F_i C_{pi}} A_c, \tag{47}$$

where C_{pi} (J mol^{-1}K^{-1}) is the specific heat of gas component i, which can be calculated from Table 2; ΔH_j (J mol^{-1}) is the enthalpy change of reaction j, which can be calculated from Table 3; ΔT (K) is the temperature difference between shell side and tube side at length z (m); a is the ratio of the heat transfer area inside the reactor to the reactor volume; U_t (Wm^{-2}K^{-1} or Js^{-1}m^{-2}K^{-1}) is the overall heat transfer coefficient of tube side.

A steady state energy balance along the axis of the shell side is written as:

$$\frac{dT_s}{dz} = \frac{N_t U_s A_o \Delta T}{F_s C_{ps} L}, \tag{48}$$

where U_s (W m^{-2}K^{-1} or J s^{-1}m^{-2}K^{-1}) is the overall heat transfer coefficient outside the tube, A_o (m^2) is the heat transfer area outside the reactor tube, F_s (mol $\cdot$ s^{-1}) is the molar flow rate of heating air, C_{ps} (J kg^{-1}K^{-1}) is the specific heat of heating air, L (m) is the total length of the packed-bed reactor, and N_t is the number of tubes in the reformer.

Table 2. Specific heat of gases.

Species	**Specific Heat (J/mol · K)**
H_2	$C_{PH_2} = a_1 + b_1\left(\frac{T}{1000}\right) + c_1\left(\frac{T}{1000}\right)^2 + d_1\left(\frac{T}{1000}\right)^3 + e_1\left(\frac{1000}{T}\right)^2$,
H_2O	$C_{PH_2O} = a_2 + b_2\left(\frac{T}{1000}\right) + c_2\left(\frac{T}{1000}\right)^2 + d_2\left(\frac{T}{1000}\right)^3 + e_2\left(\frac{1000}{T}\right)^2$,
CO_2	$C_{PCO_2} = a_3 + b_3\left(\frac{T}{1000}\right) + c_3\left(\frac{T}{1000}\right)^2 + d_3\left(\frac{T}{1000}\right)^3 + e_3\left(\frac{1000}{T}\right)^2$,
CO	$C_{PCO} = a_4 + b_4\left(\frac{T}{1000}\right) + c_4\left(\frac{T}{1000}\right)^2 + d_4\left(\frac{T}{1000}\right)^3 + e_4\left(\frac{1000}{T}\right)^2$,
CH_3OH	$C_{PCH_3OH} = 63.4$.

$a_1 = 33.066178$	$a_2 = 30.92000$	$a_3 = 24.99735$	$a_4 = 25.56759$
$b_1 = -11.363417$	$b_2 = 6.832514$	$b_3 = 55.18696$	$b_4 = 6.096130$
$c_1 = 11.432816$	$c_2 = 6.7934356$	$c_3 = -33.69137$	$c_4 = 4.054656$
$d_1 = -2.772874$	$d_2 = -2.534480$	$d_3 = 7.948387$	$d_4 = -2.671301$
$e_1 = -0.158558$	$e_2 = 0.0821398$	$e_3 = -0.136638$	$e_4 = 0.131021$

Table 3. Enthalpy change of reactions.

$\Delta H_R = 4.95 \times 10^4 + \left(C_{PCO_2} + 3C_{PH_2} - C_{PCH_3OH} - C_{PH_2O}\right)(T - 298)$ J/mol

$$\Delta H_D = 9.07 \times 10^4 + \left(C_{P\mathrm{CO}} + 2C_{P\mathrm{H_2}} - C_{P\mathrm{CH_3OH}}\right)(T - 298)\ \mathrm{J/mol}$$

$$\Delta H_W = -4.12 \times 10^4 + \left(C_{P\mathrm{CO_2}} + C_{P\mathrm{H_2}} - C_{P\mathrm{H_2O}} - C_{P\mathrm{CO}}\right)(T - 298)\ \mathrm{J/mol}$$

Figure 2 shows the cross section of a single tube and the radial temperature profile near the tube wall. There are three regions, where the temperature varies sharply, corresponding to three resistances to heat transfer: 1) the fluid film of the inner side of the tube, 2) the tube wall and 3) the fluid film outside the tube.

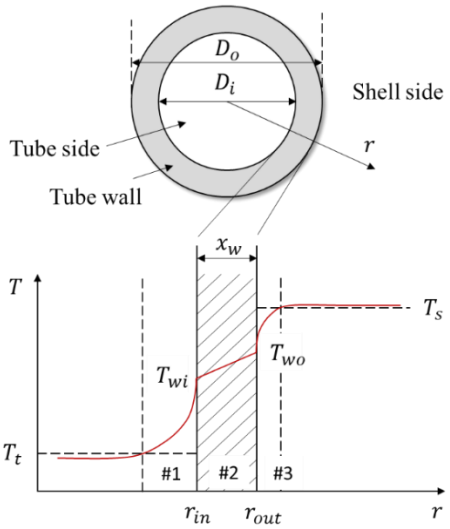

Figure 2. Cross section of single tube and radial temperature profile.

Therefore, the overall driving force can be decomposed into the sum of three separate temperature drops in each region:

$$\Delta T = T_s - T_t = (T_s - T_{wo}) + (T_{wo} - T_{wi}) + (T_{wi} - T_t), \tag{49}$$

Film coefficients h_t and h_s are used to describe the convective heat-transfer rate between the fluid flow and tube wall in #1 and #3 fluid films separately. The film heat-transfer coefficient h_t of the fluid film in tube side is defined as a proportionality constant between the heat flux dq/dA_i and driving force $(T_{wi} - T_t)$:

$$dq = h_t dA_i (T_{wi} - T_t), \tag{50}$$

Similarly, the film heat-transfer coefficient of the fluid film in shell side h_s is defined as:

$$dq = h_s dA_o (T_s - T_{wo}), \tag{51}$$

The heat transfer occurs in the region #2 is pure conduction through the tube wall. This process can be described as:

$$dq = \frac{k_w}{x_w} dA_{lm} (T_{wo} - T_{wi}), \tag{52}$$

where x_w (m) is the thickness of tube wall; A_i and A_o are the internal and external surface areas of the tube wall separately; dA_{lm} is the log-mean of dA_i and dA_o:

$$dA_{lm} = \frac{dA_o - dA_i}{ln\left(\frac{A_o}{A_i}\right)} = \frac{\pi(D_o - D_i)dL}{ln\left(\frac{D_o}{D_i}\right)} = \pi D_{lm} dL, \tag{53}$$

Assuming the steady-state heat transfer, the overall heat-transfer coefficient of the shell side U_s and of the tube side U_t can be described by [37]:

$$\frac{1}{U_s} = \frac{1}{h_t}\frac{D_o}{D_i} + \frac{x_w}{k_w}\frac{D_o}{D_{lm}} + \frac{1}{h_s}, \tag{54}$$

$$\frac{1}{U_t} = \frac{1}{h_t} + \frac{x_w}{k_w}\frac{D_i}{D_{lm}} + \frac{1}{h_s}\frac{D_i}{D_o}, \tag{55}$$

To calculate the overall heat-transfer coefficients, the heat transfer coefficient of the inner film h_t can be estimated as:

$$h_t = \left(0.4 R_e^{\frac{1}{2}} + 0.2 R_e^{\frac{2}{3}}\right) P_r^{0.4} \frac{1-\phi}{\phi}\frac{k_m}{D_p}, \tag{56}$$

where D_p (m) is the diameter of the catalyst particle, ϕ is the void fraction, P_r is the Prandtl number, k_m ($\mathrm{W\,m^{-1}K^{-1}}$) is the average thermal conductivity of the gas mixture inside tubes.

For packed beds, the Reynolds number is defined by:

$$R_e = \frac{D_p G}{\eta_m}\frac{1}{1-\phi}, \tag{57}$$

For a conventional packed-bed reformer in the form of shell-and-tube heat exchanger, the outer film coefficient h_s is determined by the geometric parameters of reformer tubes and baffles inside the shell, which is shown in Figure 3. The bundle of tubes in a heat-and-tube heat exchanger reformer can be stacked in the triangular pitch which allows the tubes to be more tightly packed. The center-to-center distance between

adjacent tubes is called the tube pitch, p_t (m). For tubes packed in triangular pitch, the general requirement is that, $p_t \geq 5/4\, D_i$. A commonly used technique for increasing the heat transfer coefficient h_s is to install baffle plates inside the shell, which partially block the cross-sectional area. The reduction of the cross-section area available for flow will increase the mass flux or velocity of the flow, also can prevent the formation of large stagnant regions, and thereby enhance h_s. The baffle plate is a disc whose diameter is equal to the inner diameter of the reformer shell D_s (m) with holes for tubes to pass through. The part of the baffle plate called baffle window is formed by cutting off this part of plate to make a cross section available for the shell-side flow. Series of baffle plates are arranged inside shell along the length of the reformer with the baffle window alternately placed on top and bottom. The spacing between the baffle plates is baffle pitch, P_b (m). Typical baffle pitch is a fraction of the shell diameter, $0.2 < P_b/D_s < 1$. In the design of reformer, many geometric parameters should be taken into account with respect to the optimum solution of arrangements of baffles and tubes.

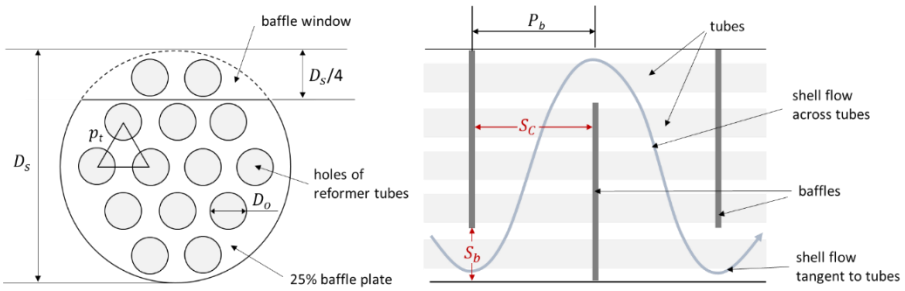

Figure 3. Arrangement of tubes and baffles in the shell of reformer.

A generally used equation for estimating the heat transfer coefficient in the shell-side film h_s in a shell-tube heat exchanger is the Donohue equation:

$$h_s = 0.2\left(\frac{D_o G_e}{\eta_s}\right)^{0.6}\left(\frac{C_{ps}\eta_s}{k_s}\right)^{0.33}\frac{k_s}{D_o}, \tag{58}$$

where mass velocity G_e (kg $m^{-2}s^{-1}$) is calculated by:

$$G_e = \sqrt{G_b G_p}, \tag{59}$$

G_b (kg $m^{-2}s^{-1}$) is the mass velocity through the baffle window:

$$G_b = \frac{\dot{m}_s}{S_b}, \tag{60}$$

where S_b (m^2) is the area available for shell-side fluid flow through the baffle window:

$$S_b = f_b\left(\frac{\pi D_s^2}{4}\right) - N_b\left(\frac{\pi D_o^2}{4}\right), \tag{61}$$

G_p (kg $m^{-2}s^{-1}$) is the mass velocity for crossflow perpendicular to the tubes:

$$G_p = \frac{\dot{m}_s}{S_p}, \tag{62}$$

where S_p (m^2) is the interstitial area available for crossflow perpendicular to the bank of tubes at the widest point in the shell:

$$S_p = P_b D_s\left(1 - \frac{D_o}{p_t}\right), \tag{63}$$

where k_s (W $m^{-1}K^{-1}$) is average thermal conductivity of shell-side gas, $\dot{m}_s$ (kg s^{-1}) is the mass flow rate of shell-side gas, η_s (Pa s) is the average viscosity of shell-side gas.

4. Results and Discussion

4.1. Comparison betweeen counter-current and co-current reactor

In a methanol steam reformer, the packed bed reactor for endothermic reactions is always coupled with a combustor, which provides an external heating source by the flow of thermal air passing through the adjacent shell side. When the reactant and thermal air flow in opposite directions, the reactor is known as counter-current reactor. For co-current reactor, the flows are in the same direction. The thermal performance of both co-current and counter-current reactors was simulated with the inlet methanol-and-steam-mixture temperature of 433K and the inlet thermal air temperature of 673K. Results of methanol conversion are both above 95%. The CO concentration in the exit gas is 0.99% of the counter-current reactor and 0.34% of the co-current reactor. As Figure 4**a** represents, the methanol and steam mixture is fed from the entrance of the reactor in a low temperature, and the thermal air flows into the shell side from the opposite side of the reformer with a high temperature. The small temperature difference in the "cold side" leads to a diminished heat transfer so that a lower tube-side temperature. Therefore, the reaction rates of methanol reforming in the former part are limited. In the "hot side" of reactor, the temperature of catalyst bed increases rapidly. The increased operating temperature results to a high methanol conversion but also a higher CO concentration in the exit gas. In Figure 4**b**, the temperature profiles show that the tube-side temperature increases sharply after entering into the reactor. Due to the boosted endothermic reactions and reduced temperature difference,

the temperature of tube side decreases gradually after the peak temperature around 500 K. The maximum temperature in co-current reactor is lower than counter-current reactor, which leads to a better performance in CO control and less catalyst deactivation. Moreover, the larger temperature difference drives a more efficient heat transfer, which benefits the higher reaction rate in the front part of the reactor. Therefore, co-current heat exchanger reformers are more favored.

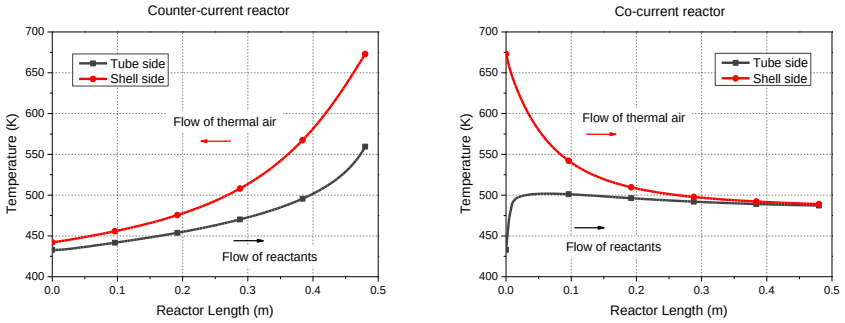

Figure 4. Temperature profiles of both tube side and shell side in a (**a**) counter-current reactor, and a (**b**) co-current reactor along the length of the reactor.

4.2. Pressure Drop in Catalyst Bed

It is shown that the smaller-sized catalyst performs better than larger-sized catalyst and suffers from less deactivation, owing to the increase in the surface area and number of pore entrances caused by the decrease in the particle size [38]. However, in small-scale packed bed reformer, especially when smaller size of catalyst tablet is chosen, the effect of pressure drop becomes significant and has to be taken into consideration during the construction of the reactor. The effect of the particle size on the pressure along the catalyst bed is investigated by changing the particle diameter from 0.5 mm to 2.0 mm, which is shown in Figure 5. The particles packed in reformer tubes are nearly monodispersed in size and cylindrical in shape. As expected, the pressure decreases along the length of catalyst bed, and the decrease is favored at smaller particle sizes of catalyst. Additionally, the pressure drop is calculated based on Ergun equation without taking into account the increased porosity of the bed near the wall and the viscous friction at the wall. It is indicated that the value of actual pressure drop may reach 20% higher than the pressure drop calculated by Ergun equation when the tube-to-particle-diameter ratio D/d_p is quite small [39]. In this study, the particle size of 1.5 mm is used. As recommended by BASF Catalyst Selectra®, when the particle size of catalyst is 1.5 mm, the pressure drop should be taken into consideration during the development of the reformer model.

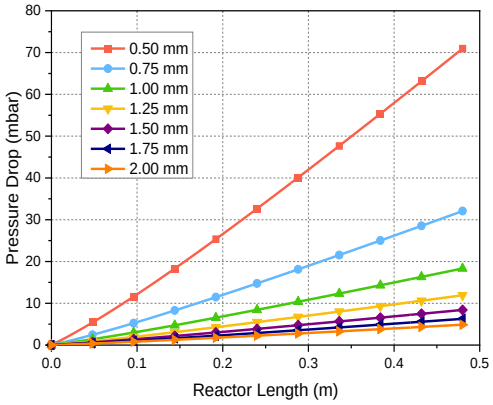

Figure 5. Pressure drop along the length of reactor with different particle sizes.

4.3. Model Verification and the Effectiveness Factor

The reformer used for MSR in this paper is a multi-tubular fixed bed reactor. The external thermal air in the shell side is used for providing heat source for reforming reactions inside tubes. The overall heat transfer between shell side and tube side gas is similar to the case of shell-and-tube heat exchanger. The geometrical parameters and operating conditions of the reformer are shown in Table 4. The development of the reformer model is of high importance to predict the performance of the small-scale methanol steam reformer and consequently optimize the design. Essentially, the simulation model needs to be verified. Without taking into consideration of the effectiveness factor of reforming reactions, the simulation model built in MATLAB-Simulink platform was verified using data from a dynamic model of the methanol steam reformer in ASPEN. The comparison of methanol conversions calculated by Simulink model and ASPEN model is shown in Table 5, where a good agreement is be observed.

Table 4. Reactor specification and operating conditions of the reformer in this study.

Parameters	Value
Catalyst particle diameter, D_p (mm)	1.5
Catalyst density, ρ_b (kg m^{-3})	1300
Surface area of fresh catalyst, S_c (m^2 kg^{-1})	102000
Void fraction ϕ	0.38

Operating temperature of catalyst (K)	503 – 563
Molar ratio of steam to methanol S/C	1.5
Pressure, P (bar)	1
Tube dimension (m)	0.016 × 0.001
Number of tubes, N_t	36
Inner diameter of reformer shell, D_s (m)	0.24
Reactor length, L (m)	0.48

Table 5. Comparison of the methanol conversions calculated by Simulink model and Aspen model.

Parameters	**Value**								
	Case 1	**Case 2**	**Case 3**	**Case 4**	**Case 5**	**Case 6**	**Case 7**	**Case 8**	**Case 9**
Mass flow rate of liquid fuel (L/h)	4.5	6	7.5	4.5	4.5	4.5	4.5	4.5	4.5
Mass flow rate of thermal air (g/s)	6	6	6	4	2	6	6	6	6
Inlet temperature of vapor fuel (K)	433	433	433	433	433	453	413	433	433
Inlet temperature of thermal air (K)	673	673	673	673	673	673	673	623	573
	Result of Methanol Conversion								
Simulink model (%)	95.34	80.03	66.75	76.92	45.74	96.63	93.85	81.52	62.71
ASPEN model (%)	95.18	79.10	65.71	77.21	46.38	96.42	93.78	81.31	62.81
Relative error (%)	0.17	1.16	1.56	-0.38	-1.40	0.22	0.07	0.26	-0.16

As the simulation results can be affected by internal diffusion of the catalyst particles, the effectiveness factor should be taking into consideration. In this paper, the cylinder catalyst particles with the size of 1.5 mm are used. To estimate the effectiveness factor by Equation (43), it is necessary to check the value of Weisz-Prater parameter C_{WP} to learn if the diffusion limitation is significant within the catalyst particle. For both WGS and MD reactions, the value of C_{WP} simulated under normal operating conditions is shown to be much smaller than 1. However, for the

MSR reaction, C_{WP} ranges from 0.5 to 6.45. Therefore, the intraparticle diffusion limitation of the WGS and MD reactions can be ignored and it of the MSR reaction should be considered in this model. The effectiveness factor profiles of MSR reaction are shown in Figure 6 as a function of the inlet flow rate of fuel and the position in the length of the catalyst bed.

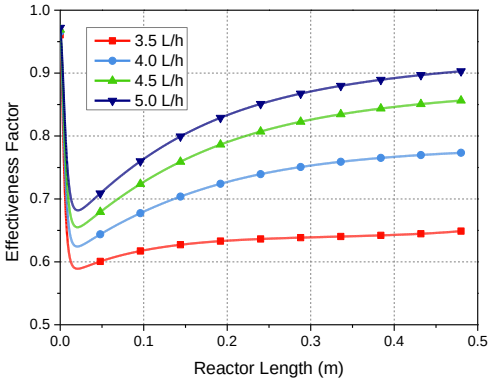

Figure 6. Effectiveness factor of MSR reaction along the length of reactor with the inlet flow rate of fuel ranging from 3.5 to 5.0 L/h. The particle size of catalyst is 1.5 mm.

4.4. Reformer Performance

The developed mathematical model in this study allows predicting the mole fractions of different species exiting the reformer under different conditions. The mole fractions of different species along the length of the reactor are presented in Figure 7, with the inlet fuel flow rate of methanol and water mixture at 4.5 L/h, the inlet temperature of thermal air at 673 K and the inlet temperature of vapor fuel at 433 K. The reforming process starts with only methanol and steam. As the reactions proceed along the length of the reactor, the mole fractions of methanol and steam reduction, while the mole fractions of reforming products including H_2, CO and CO_2 increase continuously.

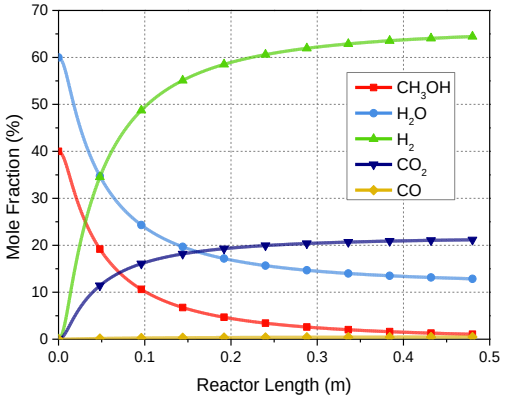

Figure 7. Profiles of mole fraction of each components along the length of reactor.

In existing models of methanol steam reformer, the temperature of heating gas is usually considered constant along the reactor length, so that a separate energy balance of the shell side can be ignored to simplify the mathematical model. In order to simulate the operating performance of the reformer more accurately, the radial heat transfer and thermal behavior of the shell side have been considered in this work. As shown in Figure 8**a**, the effect of fuel flow rate on axial temperature profiles in both tube side and shell side was investigated. The flow rate of liquid water-and-methanol mixture varies from 3 to 6 L/h, with the mass flow rate of thermal air at 6 g/s, the inlet temperature of vapor fuel and thermal air at 433 K and 673 K, respectively. The temperature variation of catalyst bed inside tubes is related to the endothermic reaction of methanol steam reforming and the external heat from the shell side. With a lower flow rate of liquid fuel at 3 L/h, the tube-side temperature near the entrance of the reactor increases more rapidly compared to the higher flow rate cases. Because less methanol is participating in the reforming reactions, the energy absorbed by endothermic process is less than the energy transferred to the tube side depending on the temperature difference. It is widely accepted that the MSR process is favored at higher temperatures according to its thermodynamic characteristics. Therefore, the enhanced endothermic reactions due to a higher tube-side temperature results in a higher methanol conversion, which achieves nearly 100% at the exit of reactor as shown in Figure 8**b**. When operating with higher flow rates of vapor fuel at 5 and 6 L/h, the tube-side temperatures experience a momentary increase and then decrease along the length of reactor. With significant heat consumption by reactions inside tubes, the radial heat transfer gradually becomes hard to compensate for the heat loss because the drive force of temperature difference between the shell side and tube side tends to be smaller. In addition, with a lower operating temperature in the catalyst bed and a higher W/F_{CH_3OH} (ratio of catalyst weight to molar flow rate of methanol, $kg\,s/mol$), the methanol conversion with higher fuel flow rate is lower than other cases.

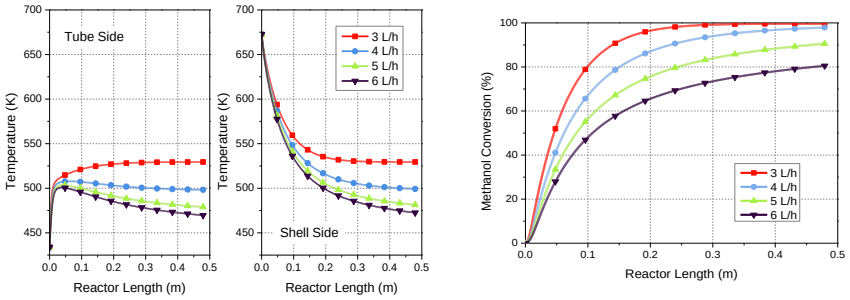

Figure 8. The effect of the mass flow rate of methanol-and-water mixture ranging from 3 to 6 L/h on (**a**) the temperature profile of both tube side and shell side, and (**b**) the methanol conversion along the length of reactor.

The effect of inlet temperature of the thermal air on the performance of reformer was investigated, and the axial temperature profiles in both tube side and shell side were illustrate in Figure 9**a**. The methanol conversion along the length of the reactor at different inlet temperature of the thermal air is represented in Figure 9**b**. The inlet temperature of the thermal air varies in the range of 573−723 K with the inlet temperature of vapor fuel at 433 K, the inlet flow rate of liquid fuel at 4.5 L/h, and the inlet flow rate of the thermal air at 6 g/s. As can be seen from the temperature profiles, the increasing temperature of the thermal air raises both the tube-side and the shell-side temperature along the reactor length. There is a sharp and momentary increase of tube-side temperature near the entrance of tube. In this part, the large driving force caused by temperature difference leads to a significant heat transfer from the shell side to the tube side. After the tube-side temperature has been increased, the increasing tendency slows down with the inlet temperature of thermal air at 723 K. It is known that higher operating temperature favors MSR process, and hence with a higher inlet temperature of thermal air, the reaction rate of MSR is enhanced, which leads to more absorption of energy owing to the endothermic process. However, the driving force of radial heat transfer due to the temperature difference increases simultaneously. The enhanced heat transfer provides sufficient heat and has an overwhelming effect on the temperature distribution compared with the effect of heat absorption. However, with the inlet temperature of thermal air lower than 673 K, the radial heat transfer is diminished due to the reduce driving force of radial heat transfer. The endothermic process still plays the critical role compared with the effect of heat transfer. Therefore, after a sharp increase at the entrance of the reactor, the temperature subsequently decreases with a lower inlet temperature of thermal air. Figure 9**b** represents the methanol conversion profile along the length of the reactor. With a higher inlet temperature of thermal air, the methanol conversion increases due to the enhanced reaction rate. The methanol conversion achieves nearly 100% at the exit of reactor with the inlet temperature of thermal air at 723 K.

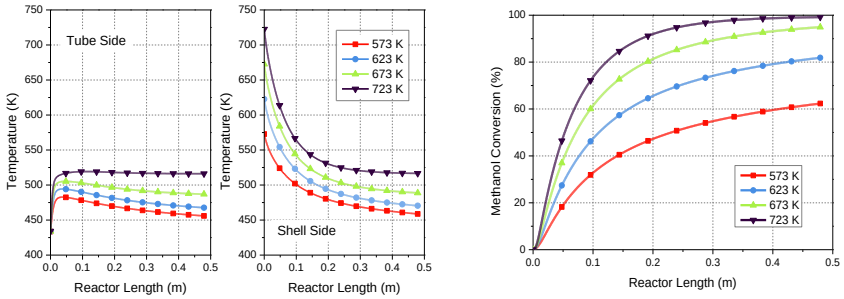

(**a**) (**b**)

Figure 9. The effect of the inlet temperature of thermal air ranging from 573 to 723 K on (**a**) the temperature profile of both tube side and shell side, and (**b**) the methanol conversion along the length of reactor.

For the application of HT-PEMFCs, the composition of produced H_2-rich gas requires a high concentration of H_2, and low concentrations of both methanol and CO. Araya et al. [40] has analyzed the effect of methanol and water vapor on the degradation of HT-PEMFC by polarization curves and impedance spectra. The work showed that the HT-PEMFC operated with 5% and 8% concentration of methanol in the anode gas had significant performance degradation. The results also showed that a 3% or lower methanol concentration in the anode gas feed showed a negligible impact on the performance of HT-PEMFC, which indicated that the HT-PEMFC had a tolerance of methanol concentration of up to about 3%. Therefore, 2% methanol concentration in the reformed gas could be a relatively low content to ensure the performance of the HT-PEMFC. With the acid-doped PBI electrolytes, the poisoning effect of CO has been studied by Li et al. [41,42], and found that the effect is very temperature-dependent and can be sufficiently suppressed at elevated temperature. The results showed that 3% CO can be tolerated when operating at 200℃, and for 1% above 175℃, and for 0.5% above 150℃. Similar results have been achieved in [43] that when the HT-PEM fuel cell operated at 180°C or above, the reformate gas with a higher CO concentration of 2−5% can be accepted. In addition, elevated concentration of CO has been reported to cause unexpected coke deposition over the catalyst of methanol steam reformer and covers the copper sites, which will have a negative effect on the reformer performance [36].

The developed mathematical model in this study allows analyzing the mole fraction profiles of residual methanol and CO as a byproduct in the reactant mixture when gave the operating parameters of the reformer. It is especially important to predict the concentration of different components in the exit gas which is fed into the fuel cell stack. The contours of methanol concentration in the exit gas of reformer are indicated in Figure 10**a** with different inlet temperatures of thermal air and different flow rates of liquid fuel. It can be seen that a higher temperature of thermal air leads to a lower

mole fraction of methanol in the exit gas of the methanol steam reformer. Simultaneously, the increasing flow rate of fuel mixture causes an obvious increase of methanol concentration. As mentioned above, a higher methanol concentration due to lower inlet temperature of heating gas and a higher flow rate of fuel is unfavorable to the performance of HT-PEM fuel cell stack. In this paper, concentration lower than 2% is preferred to ensure a considerably low content of methanol.

The mole fraction profiles of CO in the exit gas of the reformer were illustrated in Figure 10**b**. As expected, with increasing inlet temperature of thermal air, the methanol decomposition reaction is promoted and the water-gas shift reaction is diminished, which leads to a sharply increasing trend of mole fraction of CO. In addition, increasing the flow rate of fuel mixture leads to a decrease of the CO mole fraction. Likewise, a higher CO concentration due to lower flow rate of fuel and higher temperature of heating gas should be controlled to a tolerable level. Generally, the CO concentration lower than 1% is acceptable. Therefore, to ensure that the reformate composition from the reformer is suitable for an HT-PEMFC, the operating parameters represented by the lines in the respective contours in Figures 10**a,b** are recommended.

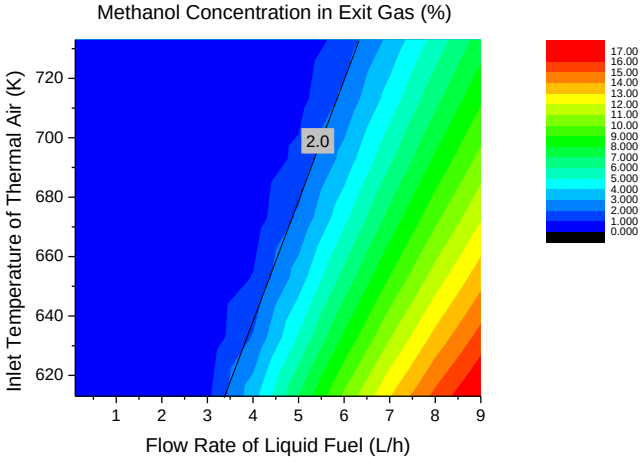

(**a**)

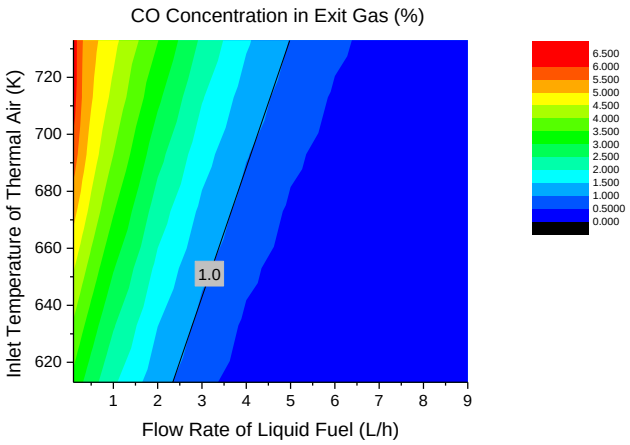

(**b**)

Figure 10. Profiles of (**a**) methanol concentration, and (**b**) CO concentration in the exit gas of reformer with different inlet flow rate of fuel mixture and inlet temperature of thermal air. .

4.4. Influence of Geometric Parameters in the Multi-Tubular Packed-Bed Reactor

It is widely accepted that the W/F_{CH_3OH} associate with the dominating convective heat transfer properties can strongly affect the performance of reformer. By keeping the overall weight of catalyst W (kg) constant, which is substantially attained by setting the total volume of tubes invariant in the reformer, the impact of geometric parameters can be investigated. With the fixed overall catalyst load, the number of tubes will increase by a factor equal to the square of the factor by which the radius of tubes decreases. For the packed-bed reformer in the current work, the geometric parameters used to simulate the performance of the reformer are listed in Table 6 and Table 7.

Table 6. Geometric parameters of the packed-bed reformer with variation in the number and diameter of tubes.

Parameters	**Value**			
	Case 1	**Case 2**	**Case 3**	**Case 4**
Number of reactor tubes, N_t	144	36	16	9
Inner diameter of the tubular reactor, D_i (m)	0.008	0.016	0.024	0.032

Outer diameter of the tubular reactor, D_o (m)	0.010	0.018	0.026	0.034
Tube pitch, p_t (m)	0.015	0.027	0.039	0.051
Number of baffle plates, N_b	4			
Spacing between baffle plates, P_b (m)	0.12			
Length of the reactor, L (m)	0.48			
Area fraction of baffle plate that is window, f_b (for 25% baffle plate)	0.1955			

Table 7. Geometric parameters of the packed-bed reformer with variation in the number and pitch of baffles.

Parameters	**Value**			
	Case 1	**Case 2**	**Case 3**	**Case 4**
Number of baffle plates, N_b	3	4	6	8
Spacing between baffle plates, P_b (m)	0.16	0.12	0.08	0.06
Number of reactor tubes, N_t	16			
Inner diameter of the tubular reactor, D_i (m)	0.024			
Outer diameter of the tubular reactor, D_o (m)	0.026			
Tube pitch, p_t (m)	0.039			
Length of the reactor, L (m)	0.48			
Area fraction of baffle plate that is window, f_b (for 25% baffle plate)	0.1955			

Axial temperature profiles in catalyst bed with the variations of tube number and tube diameter in Table 6 are evaluated for the same mass of catalyst. The increase of tube diameter will lead to the reduction of tube number in the reformer correspondingly, which boosts the overall heat exchange area of reformer as well as the surface-to-volume ratio of a single cylindrical tube. As shown in Figure 11, tube-side temperatures have a sharp increase near the entrance of reformer owing to the driving

force of temperature difference between the internal and external fluid. After the initial increase, the reformer with less tubes and larger tube diameter (case 4) results to a roughly constant tube-side temperature along the length of reactor. For the reformer with more tubes and smaller tube diameter (case 1), the tube-side temperature maintains the increasing trend until the maximum value, then progressively decreases along the length and reaches a final temperature at the exit of reformer even lower than the other cases. The temperature profiles in the catalyst bed are determined by the interplay between the rates of heat transfer and endothermic reaction. The decrease of tube diameter promotes the heat transfer, which favors the approach of catalyst bed to a higher temperature, hence increases the endothermic reaction rates. When the heat consumption of the endothermic reaction overcomes the heat supply from the external heating source, the temperature will progressively drop.

The variation of methanol conversion is directly related to the temperature profile in the catalyst bed. As shown in Figure 12**a**, the geometric parameters in case 1 lead to higher methanol conversion mainly because of its short pre-heat length and high operating temperature in catalyst bed. However, later the temperature drop limits the efficiency of MSR process and eventually results to an inconspicuously lower methanol conversion at the outlet of the reformer. Figure 12**b** shows the CO concentration profiles inside tubes along the length of the reactor. Accordingly, the geometric parameters of more tubes and smaller tube diameter contribute to a clear increase in CO concentration due to the higher operating temperature.

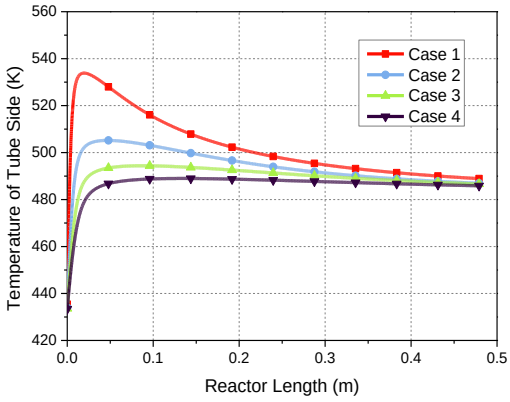

Figure 11. Temperature profiles of tube side along the length of reactor with different number and diameter of tubes.

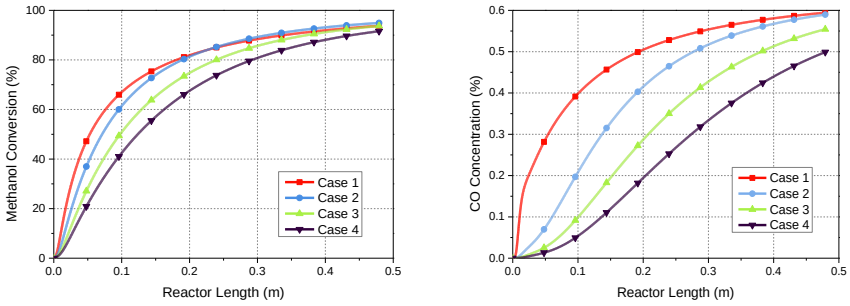

(**a**) (**b**)

Figure 12. Profiles of (**a**) methanol conversion, (**b**) CO concentration along the length of reactor with different number and diameter of tubes.

The number of tubes and welding operations of the reformer, due to the decrease in the tube diameter at fixed catalyst load, will increase the investment and industrial costs. In addition, the CO concentration of the outlet gas mixture is also higher in this case. Therefore, there is a tendency to investigate the possibility of adopting reactor tubes with a larger diameter [44]. However, the adoption of reformer with larger tube diameter may cause larger radial temperatures gradients and cold-spot inside the catalyst bed [22], which means that the heat supplied from external thermal air cannot effectively compensate the heat consumed by the reforming process, and this results in lower methanol conversion. Furthermore, for tubes with smaller diameter, especially for ratios D/dp smaller than 6, the impact of the porosity change near the tube walls cannot be neglected then [45]. Therefore, the choice of geometric parameters should be a trade-off between reformer performance and manufacturing costs.

One of the methods to improve the heat transfer properties of the reformer with fixed flow rate of thermal air is to increase the external heat transfer coefficient by installing baffle plates by increasing turbulence in shell-side fluid. The axial profiles of methanol conversion and CO concentration inside tubes are shown in Figure 13. With the constant length of tubes, the added number of baffle plates is associated with the reduction of baffle spacing. For the reformer with smaller baffle spacing and more baffle plates (case 4), a higher methanol conversion is attained with an increase in CO concentration at reformer outlet. This change can be explained by the increased operating temperature in catalyst bed due to the effective radial heat transfer of reformer. However, the larger number of baffles in the shell-side of reformer makes the fabrication more expensive.

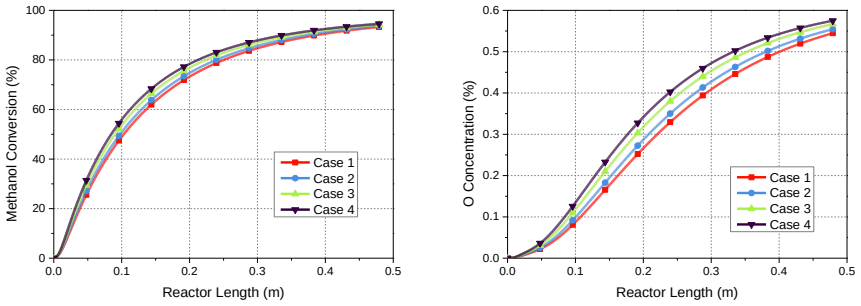

(**a**) (**b**)

Figure 13. Profiles of (**a**) methanol conversion, (**b**) CO concentration along the length of reactor with different number and pitch of baffles.

5. Conclusions

Simulation based on a comprehensive pseudo-homogenous model of a conventional packed-bed reformer has been developed to investigate the effects of operating conditions and geometric parameters on temperature distribution, methanol conversion and CO concentration along the axis of the multi-tubular methanol steam reformer. The model took into account the main chemical reactions, and the mass and heat transfer phenomena in both tube side and shell side of the reformer. In the radial direction, the overall heat transfer coefficient including the convective heat transfer near the internal and external surfaces of the tube wall, and the conductive heat transfer through the tube wall has been considered. The Ergun equation was used to calculate the pressure drop inside catalyst bed. A dynamic model of the multi-tubular methanol steam reformer was developed in the platform of ASPEN. Good agreement of methanol conversion was achieved between the data of the MATLAB model and the ASPEN model. The performance of a counter-current reactor and a co-current reactor has been compared. Results showed that the reactor in the form of a co-current heat exchanger had a lower CO concentration and better heat transfer efficiency. The intraparticle diffusion limitation for MSR reaction was considered by taking into account the effectiveness factor along the reactor. Axial temperature profiles of both tube side and shell side with different flow rate of liquid fuel and different inlet temperature of thermal air were represented in this paper. The developed mathematical model also allowed analyzing the mole fractions along the length of reformer of residual methanol and generated CO in the gas mixture. The results revealed that lower flow rate of liquid fuel and higher inlet temperature of thermal air led to a better methanol conversion, but also a higher CO concentration in outlet gas mixture. Because the generate hydrogen through steam reforming is intended for use in HT-PEMFCs, the composition of the H_2-rich gas requires a concentration of methanol lower than 2% and CO lower than 1%. Therefore, the operating conditions should be limited to a certain region, where a suitable composition of reformed gas for feeding into an HT-PEM fuel cell stack can be achieve. With fixed catalyst load,

the increase in the number of tubes and decrease in the tube diameter improved the methanol conversion, while also increasing the CO concentration. In addition, the reformer with more baffle plates in the shell side achieved better methanol conversion at the cost of higher CO concentration. Therefore, the choice of geometric parameters should be a trade-off between the manufacturing costs and the reformer performance.

Author Contributions: Conceptualization, J.Z., S.S.A. and S.L.S.; data curation, J.Z.; formal analysis, J.Z. and S.S.A.; funding acquisition, S.K.K.; investigation, J.Z. and X.C.; methodology, J.Z., S.S.A. and S.L.S.; project administration, S.S.A. and S.K.K.; resources, S.K.K.; software, J.Z., S.L.S. and X.C.; supervision, S.S.A. and S.K.K.; validation, J.Z., S.S.A. and X.C.; visualization, J.Z.; writing, original draft, J.Z.; writing, review and editing, J.Z., S.S.A., X.C., S.L.S. and S.K.K..

Funding: The research leading to these results has received funding from the Chinese scholarship council (CSC) and from the Danish Energy Technology Development and Demonstration Program (EUDP) through the COmmercial BReakthrough of Advanced fuel cells (COBRA Drive) project, grant number 64018-0118.

Conflicts of Interest: The authors declare no conflict of interest.

Nomenclature

$\boldsymbol{a}$	ratio of the heat transfer area inside the reactor to the reactor volume (m^{-1})
$\boldsymbol{A_c}$	area of cross section of catalyst bed (m^2)
$\boldsymbol{A_i}$	internal surface area of tube (m^2)
$\boldsymbol{A_o}$	external surface area of tube (m^2)
$\boldsymbol{C_{pi}}$	specific heat of gas component i $(\mathrm{Jmol}^{-1}\mathrm{K}^{-1})$
$\boldsymbol{C_{S_i}^T}$	total surface concentration of site i $(\mathrm{mol\ m}^{-2})$
$\boldsymbol{C_{is}}$	surface concentration of component i $(\mathrm{mol\ m}^{-3})$
$\boldsymbol{C_{WP}}$	Weisz-Prater parameter
$\boldsymbol{D_p}$	diameter of the catalyst particle in the reformer (m)
$\boldsymbol{D_s}$	diameter of the reformer shell (m)
$\boldsymbol{D_i}$	inner diameter of tube (m)
$\boldsymbol{D_{ij}}$	diffusivity for a binary mixture of i and j $(\mathrm{m}^2 s^{-1})$
$\boldsymbol{D_{i,K}}$	Knudsen diffusivity of component i $(\mathrm{m}^2 s^{-1})$
$\boldsymbol{D_{i,\mathrm{eff}}}$	effective diffusivity $(\mathrm{m}^2 s^{-1})$
$\boldsymbol{D_o}$	outer diameter of tube (m)
$\boldsymbol{f_b}$	area fraction of baffle plate that is window (for 25% baffle plate, $f_b = 0.1955$)

$\boldsymbol{E_j}$	activation energy for rate constant of reaction j ($\mathrm{kJmol^{-1}}$)
$\boldsymbol{F_i}$	molar flow rate of component i ($\mathrm{mol\ s^{-1}}$)
$\boldsymbol{G}$	superficial mass velocity ($\mathrm{m\ s^{-1}}$)
$\boldsymbol{G_e}$	mass velocity of shell-side fluid
$\boldsymbol{G_b}$	mass velocity through the baffle window ($\mathrm{kg\ m^{-2}s^{-1}}$)
$\boldsymbol{G_p}$	mass velocity for crossflow perpendicular to the tubes ($\mathrm{kg\ m^{-2}s^{-1}}$)
$\boldsymbol{h}$	individual heat transfer coefficient ($\mathrm{Wm^{-2}K^{-1}}$ or $\mathrm{Js^{-1}m^{-2}K^{-1}}$)
$\boldsymbol{k}$	thermal conductivity ($\mathrm{Wm^{-1}K^{-1}}$)
$\boldsymbol{k_j}$	rate constant of reaction j ($j = \mathrm{R, D\ or\ W}$) ($\mathrm{m^2\ s^{-1}mol^{-1}}$)
$\boldsymbol{K_i^*}$	adsorption coefficient of specie i ($\mathrm{bar^{-0.5}}$)
$\boldsymbol{K_j^{eq}}$	equilibrium constant of reaction j ($j = \mathrm{R, D\ or\ W}$)
$\boldsymbol{L}$	length of the packed-bed reactor (m)
$\boldsymbol{M}$	molecular weight ($\mathrm{kg\ mol^{-1}}$)
$\boldsymbol{N_t}$	number of tubes
$\boldsymbol{N_b}$	number of baffles
$\boldsymbol{p_i}$	partial pressure of component i (bar)
$\boldsymbol{P}$	pressure of the catalyst bed (bar)
$\boldsymbol{P_b}$	baffle spacing (m)
$\boldsymbol{P_r}$	Prandtl number
$\boldsymbol{p_t}$	tube pitch (m)
$\boldsymbol{r_i}$	rate of formation of component i ($\mathrm{mol\ s^{-1}(kg\ of\ catalyst)^{-1}}$), the number of moles of i reacting per unit time per unit mass of catalyst
$\boldsymbol{r_j}$	rate of reaction j ($j = \mathrm{R, D\ or\ W}$)($\mathrm{mol\ s^{-1}m^{-2}}$), the number of moles of reaction per time per unit surface area
$\boldsymbol{R}$	gas constant ($\mathrm{Jmol^{-1}K^{-1}}$)
$\boldsymbol{R_e}$	Reynolds number
$\boldsymbol{S_b}$	area available for shell-side fluid flow through the baffle window ($\mathrm{m^2}$)
$\boldsymbol{S_c}$	surface area per unit mass of fresh catalyst ($\mathrm{m^2kg^{-1}}$)
$\boldsymbol{S_p}$	interstitial area available for crossflow perpendicular to the bank of tubes at the widest point in the shell ($\mathrm{m^2}$)
$\boldsymbol{U}$	overall heat transfer coefficient ($\mathrm{Wm^{-2}K^{-1}}$ or $\mathrm{Js^{-1}m^{-2}K^{-1}}$)
$\boldsymbol{V_c}$	critical volume ($\mathrm{cm^3mol^{-1}}$)
$\boldsymbol{W}$	weight of catalyst (kg)

x_i	mole fraction of specie i
x_w	thickness of the tube wall (m)
μ_r	dimensionless dipole moment (D)
η_i	viscosity of fluid (Pa s)
η	effectiveness factor
ρ	density (kg m^{-3})
ϕ	void fraction
ϕ_1	Thiel modulus for a first-order reaction
ω	acentric factor
κ	special correction for highly polar substances
ΔH	enthalpy change ($Jmol^{-1}$)
ΔS_i	entropy change of adsorption for species i ($Jmol^{-1}K^{-1}$)
ΔT	temperature difference (K)

Subscripts

m	gas mixture
c	catalyst
t	tube side of the reformer
s	shell side of the reformer
wi	inner side of tube wall
wo	outer side of tube wall
w	tube wall

References

[1] Edlund D. Methanol fuel cell systems: advancing towards commercialization. Pan Stanford; 2016.

[2] Iulianelli A, Ribeirinha P, Mendes A, Basile A. Methanol steam reforming for hydrogen generation via conventional and membrane reactors: A review. Renew Sustain Energy Rev 2014;29:355–68. https://doi.org/10.1016/j.rser.2013.08.032.

[3] Karim A, Bravo J, Gorm D, Conant T, Datye A. Comparison of wall-coated and packed-bed reactors for steam reforming of methanol. Catal Today

2005;110:86–91. https://doi.org/10.1016/j.cattod.2005.09.010.

[4] Dalena F, Senatore A, Basile M, Knani S, Basile A, Iulianelli A. Advances in methanol production and utilization, with particular emphasis toward hydrogen generation via membrane reactor technology. Membranes (Basel) 2018;8. https://doi.org/10.3390/membranes8040098.

[5] Sá S, Silva H, Brandão L, Sousa JM, Mendes A. Catalysts for methanol steam reforming-A review. Appl Catal B Environ 2010;99:43–57. https://doi.org/10.1016/j.apcatb.2010.06.015.

[6] Araya SS, Zhou F, Liso V, Sahlin SL, Vang JR, Thomas S, et al. A comprehensive review of PBI-based high temperature PEM fuel cells. Int J Hydrogen Energy 2016;41:21310–44. https://doi.org/10.1016/j.ijhydene.2016.09.024.

[7] Zhou F, Andreasen SJ, Kær SK, Park JO. Experimental investigation of carbon monoxide poisoning effect on a PBI/H3PO4 high temperature polymer electrolyte membrane fuel cell: Influence of anode humidification and carbon dioxide. Int J Hydrogen Energy 2015;40:14932–41. https://doi.org/10.1016/j.ijhydene.2015.09.056.

[8] Papavasiliou J, Avgouropoulos G, Ioannides T. Steady-state isotopic transient kinetic analysis of steam reforming of methanol over Cu-based catalysts. Appl Catal B Environ 2009;88:490–6. https://doi.org/10.1016/j.apcatb.2008.10.018.

[9] Jiang CJ, Trimm DL, Wainwright MS, Cant NW. Kinetic study of steam reforming of methanol over copper-based catalysts. Appl Catal A, Gen 1993;93:245–55. https://doi.org/10.1016/0926-860X(93)85197-W.

[10] Peppley BA, Amphlett JC, Kearns LM, Mann RF. Methanol–steam reforming on Cu/ZnO/Al2O3 catalysts. Part 2. A comprehensive kinetic model. Appl Catal A Gen 1999;179:31–49. https://doi.org/10.1016/S0926-860X(98)00299-3.

[11] Agrell J, Birgersson H, Boutonnet M. Steam reforming of methanol over a Cu/ZnO/Al2O3 catalyst: A kinetic analysis and strategies for suppression of CO formation. J Power Sources 2002;106:249–57. https://doi.org/10.1016/S0378-7753(01)01027-8.

[12] Sá S, Sousa JM, Mendes A. Steam reforming of methanol over a CuO/ZnO/Al2O3catalyst, part I: Kinetic modelling. Chem Eng Sci 2011;66:4913–21. https://doi.org/10.1016/j.ces.2011.06.063.

[13] Herdem MS, Mundhwa M, Farhad S, Hamdullahpur F. Multiphysics Modeling and Heat Distribution Study in a Catalytic Microchannel Methanol Steam Reformer. Energy and Fuels 2018;32:7220–34. https://doi.org/10.1021/acs.energyfuels.8b01280.

[14] Lee M tsang, Greif R, Grigoropoulos CP, Park HG, Hsu FK. Transport in packed-bed and wall-coated steam-methanol reformers. J Power Sources 2007;166:194–201. https://doi.org/10.1016/j.jpowsour.2007.01.007.

[15] Bravo J, Karim A, Conant T, Lopez GP, Datye A. Wall coating of a CuO/ZnO/Al2O3 methanol steam reforming catalyst for micro-channel reformers. Chem Eng J 2004;101:113–21. https://doi.org/10.1016/j.cej.2004.01.011.

[16] Cui X, Kær SK. Two-dimensional thermal analysis of radial heat transfer of monoliths in small-scale steam methane reforming. Int J Hydrogen Energy 2018;43:11952–68. https://doi.org/10.1016/j.ijhydene.2018.04.142.

[17] Yoshida K, Tanaka S, Hiraki H, Esashi M. A micro fuel reformer integrated with a combustor and a microchannel evaporator. J Micromechanics Microengineering 2006;16. https://doi.org/10.1088/0960-1317/16/9/S04.

[18] Chein RY, Chen YC, Lin YS, Chung JN. Experimental study on the hydrogen production of integrated methanol-steam reforming reactors for PEM fuel cells. Int J Therm Sci 2011;50:1253–62. https://doi.org/10.1016/j.ijthermalsci.2011.03.001.

[19] Kim T. Micro methanol reformer combined with a catalytic combustor for a PEM fuel cell. Int J Hydrogen Energy 2009;34:6790–8. https://doi.org/10.1016/j.ijhydene.2009.06.024.

[20] Davieau DD, Erickson PA. The effect of geometry on reactor performance in the steam-reformation process. Int J Hydrogen Energy 2007;32:1192–200. https://doi.org/10.1016/j.ijhydene.2006.11.029.

[21] Vadlamudi VK, Palanki S. Modeling and analysis of miniaturized methanol reformer for fuel cell powered mobile applications. Int J Hydrogen Energy 2011;36:3364–70. https://doi.org/10.1016/j.ijhydene.2010.12.062.

[22] Ma H, Zhou M, Ying W, Fang D. Two-dimensional modeling of a plant-scale fixed-bed reactor for hydrogen production from methanol steam reforming. Int J Hydrogen Energy 2016;41:16932–43. https://doi.org/10.1016/j.ijhydene.2016.07.117.

[23] Mears DE. Diagnostic criteria for heat transport limitations in fixed bed reactors. J Catal 1971;20:127–31. https://doi.org/10.1016/0021-9517(71)90073-X.

[24] Karim A, Bravo J, Datye A. Nonisothermality in packed bed reactors for steam reforming of methanol. Appl Catal A Gen 2005;282:101–9. https://doi.org/10.1016/j.apcata.2004.12.006.

[25] Vidal Vázquez F, Simell P, Pennanen J, Lehtonen J. Reactor design and catalysts testing for hydrogen production by methanol steam reforming for fuel cells applications. Int J Hydrogen Energy 2016;41:924–35. https://doi.org/10.1016/j.ijhydene.2015.11.047.

[26] Montebelli A, Visconti CG, Groppi G, Tronconi E, Ferreira C, Kohler S. Enabling small-scale methanol synthesis reactors through the adoption of highly conductive structured catalysts. Catal Today 2013;215:176–85. https://doi.org/10.1016/j.cattod.2013.02.020.

[27] Lee JK, Ko JB, Kim DH. Methanol steam reforming over Cu/ZnO/Al2O3 catalyst: Kinetics and effectiveness factor. Appl Catal A Gen 2004;278:25–35. https://doi.org/10.1016/j.apcata.2004.09.022.

[28] Tesser R, Di Serio M, Santacesaria E. Methanol steam reforming: A comparison of different kinetics in the simulation of a packed bed reactor. Chem Eng J 2009;154:69–75. https://doi.org/10.1016/j.cej.2009.06.007.

[29] Wan Y, Zhou Z, Cheng Z. Hydrogen production from steam reforming of methanol over CuO/ZnO/Al2O3 catalysts: Catalytic performance and kinetic modeling. Chinese J Chem Eng 2016;24:1186–94. https://doi.org/10.1016/j.cjche.2016.02.006.

[30] Yaws CL. Chemical properties handbook. McGraw-Hill,; 1999.

[31] Scott Fogler H. Elements of chemical reaction engineering. vol. 42. Prentice-Hall International London; 1987. https://doi.org/10.1016/0009-2509(87)80130-6.

[32] Chung TH, Ajlan M, Lee LL, Starling KE. Generalized multiparameter correlation for nonpolar and polar fluid transport properties. Ind Eng Chem Res 2005;27:671–9. https://doi.org/10.1021/ie00076a024.

[33] Chung TH, Lee LL, Starting KE. Applications of Kinetic Gas Theories and Multiparameter Correlation for Prediction of Dilute Gas Viscosity and Thermal Conductivity. Ind Eng Chem Fundam 1984;23:8–13.

https://doi.org/10.1021/i100013a002.

[34] Poling BE, Prausnitz JM, O'connell JP. The properties of gases and liquids. vol. 5. Mcgraw-hill New York; 2001.

[35] Taylor R, Krishna R. Multicomponent mass transfer. vol. 2. John Wiley & Sons; 1993.

[36] Agarwal V, Patel S, Pant KK. H2 production by steam reforming of methanol over Cu/ZnO/Al2O3catalysts: Transient deactivation kinetics modeling. Appl Catal A Gen 2005;279:155–64. https://doi.org/10.1016/j.apcata.2004.10.026.

[37] McCabe WL, Smith JC, Harriott P. Unit operations of chemical engineering. 6th ed. vol. 1130. McGraw-hill New York; 2001.

[38] Mochizuki H, Yokoi T, Imai H, Watanabe R, Namba S, Kondo JN, et al. Facile control of crystallite size of ZSM-5 catalyst for cracking of hexane. Microporous Mesoporous Mater 2011;145:165–71. https://doi.org/10.1016/j.micromeso.2011.05.011.

[39] Winterberg M, Tsotsas E. Impact of tube-to-particle-diameter ratio on pressure drop in packed beds. AIChE J 2000;46:1084–8. https://doi.org/10.1002/aic.690460519.

[40] Araya SS, Grigoras IF, Zhou F, Andreasen SJ, Kær SK. Performance and endurance of a high temperature PEM fuel cell operated on methanol reformate. Int J Hydrogen Energy 2014;39:18343–50. https://doi.org/10.1016/j.ijhydene.2014.09.007.

[41] Li Q, He R, Gao JA, Jensen JO, Bjerrum NJ. The CO poisoning effect in PEMFCs operational at temperatures up to 200°C. J Electrochem Soc 2003;150:1599–605. https://doi.org/10.1149/1.1619984.

[42] Li Q, Oluf J, Savinell RF, Bjerrum NJ. High temperature proton exchange membranes based on polybenzimidazoles for fuel cells. Prog Polym Sci 2009;34:449–77. https://doi.org/10.1016/j.progpolymsci.2008.12.003.

[43] Das SK, Reis A, Berry KJ. Experimental evaluation of CO poisoning on the performance of a high temperature proton exchange membrane fuel cell. J Power Sources 2009;193:691–8. https://doi.org/10.1016/j.jpowsour.2009.04.021.

[44] Montebelli A, Visconti CG, Groppi G, Tronconi E, Kohler S. Optimization

of compact multitubular fixed-bed reactors for the methanol synthesis loaded with highly conductive structured catalysts. Chem Eng J 2014;255:257–65. https://doi.org/10.1016/j.cej.2014.06.050.

[45] Arab S, Commenge JM, Portha JF, Falk L. Methanol synthesis from CO2 and H2 in multi-tubular fixed-bed reactor and multi-tubular reactor filled with monoliths. Chem Eng Res Des 2014;92:2598–608. https://doi.org/10.1016/j.cherd.2014.03.009.

Paper B

The role of effectiveness factor on the modeling of methanol steam reforming over $CuO/ZnO/Al_2O_3$ catalyst in a multi-tubular reactor

Jimin Zhu, Samuel Simon Araya, Xiaoti Cui, Søren Knudsen Kær

The paper has been available online in International Journal of Hydrogen Energy, 2022.

The role of effectiveness factor on the modeling of methanol steam reforming over $Cu/ZnO/Al_2O_3$ catalyst in a multi-tubular reactor

Jimin Zhu*, Samuel Simon Araya, Xiaoti Cui, Søren Knudsen Kær

AAU Energy, Aalborg University, Pontoppidanstraede 111, 9220 Aalborg øst, Denmark

Abstract

A pseudo-homogeneous model for the methanol steam reforming process was developed based on reaction kinetics over a $CuO/ZnO/Al_2O_3$ catalyst and non-adiabatic heat and mass transfer performances in a co-current packed-bed reactor. A Thiele modulus method and an intraparticle distribution method were applied for predicting the effectiveness factors for main reactions and providing insights into the diffusion-reaction process in a cylindrical catalyst pellet. The results of both methods are validated and show good agreements with the experimental data, but the intraparticle distribution method provides better predictions. Results indicate that increases in catalyst size and bulk fluid temperature amplify the impact of intraparticle diffusion limitations, showing a decrease in effectiveness factors. To satisfy the requirements of a high temperature polymer electrolyte membrane fuel cell stack, the optimized operating conditions, which bring the methanol and CO concentrations to less than 1% vol in the reformate stream, are determined based on the simulation results.

Keywords: methanol steam reforming, intraparticle diffusion, Thiele modulus, effectiveness factor, hydrogen production

*Corresponding author
Email address: jzu@energy.aau.dk (Jimin Zhu)

1. Introduction

Hydrogen is a clean and promising energy carrier and plays an essential role in hydrogen-based energy systems, especially in polymer electrolyte membrane (PEM) fuel cell systems. Among PEM fuel cells, high-temperature polymer electrolyte membrane (HT-PEM) fuel cells show advantages in enhanced electrode kinetics and easier heat and water management [1, 2]. By operating at a higher temperature (393−473 K), HT-PEM fuel cells also have an improved tolerance towards carbon monoxide (CO) up to 3−5 % vol [3–5].

Hydrogen, however, has a low volumetric density and shows limitations in terms of storage, transportation, and distribution, which are existing barriers to the growth of the hydrogen market [6, 7]. Reforming of carbon-based fuels such as natural gas, methane and methanol is a promising technology for hydrogen production [8]. Among all these fuels, methanol is a good hydrogen source because it is in liquid form under standard conditions and has a high hydrogen to carbon ratio (4:1). Methanol has both a high gravimetric energy density (22.4 $\mathrm{MJ\,kg^{-1}}$ vs. less than 1 $\mathrm{MJ\,kg^{-1}}$ for batteries or pumped hydro storage) and a high volumetric energy density (17.8 $\mathrm{MJ\,L^{-1}}$ vs. 0.01 $\mathrm{MJ\,L^{-1}}$ and 0.03 $\mathrm{MJ\,L^{-1}}$ for hydrogen and methane, respectively) [9]. The high energy density and stability of methanol at ambient conditions make it cheap and easy for long-term storage. A lower reforming temperature (473−573 K) than other carbon-based fuels such as methane (1073−1273 K) also makes it suitable for stack integration with HT-PEM fuel cells [4, 8]. Moreover, methanol can be produced from renewable energies and captured carbon dioxide (CO_2), which benefits from the extensive studies of power-to-methanol technology. Therefore, it can be considered as a decarbonized energy carrier [9, 10]. The most commonly used reforming method for methanol is catalytic steam reforming. Compared with other methanol-reforming methods, the methanol steam reforming (MSR) process provides the highest concentration of hydrogen per mole of methanol [11, 12]. The following three reactions are considered to represent the kinetics of the MSR process [13, 14]:

Methanol steam reforming reaction (MSR)

$$CH_3OH + H_2O \leftrightarrow CO_2 + 3H_2 \quad \Delta H = +49.7\ (\text{kJ mol}^{-1}) \tag{1}$$

Water-gas shift reaction (WGS)

$$CO + H_2O \leftrightarrow CO_2 + H_2 \quad \Delta H = -41.2\ (\text{kJ mol}^{-1}) \tag{2}$$

Methanol decomposition reaction (MD)

$$CH_3OH \leftrightarrow CO + 2H_2 \quad \Delta H = +90.2\ (\text{kJ mol}^{-1}) \tag{3}$$

The most commonly used catalysts for MSR process are copper-based catalysts, especially $CuO/ZnO/Al_2O_3$ catalysts, because of their high activity and selectivity [8, 15, 16]. Inside a porous catalyst pellet, chemical reactions and heat and mass transfer take place simultaneously. Typically, experiments reported in the literature were conducted on finely powdered catalysts [8, 17]. Hence, the intraparticle diffusion resistances can be ignored and the reaction rates are referred to as intrinsic. In industrial-scale applications, however, it is not possible to use such tiny catalyst pellets without causing significant pressure drops [18].

Diffusion limitations inside catalyst pellets can affect the local reaction rates and selectivity, especially for larger particle sizes and at higher operating temperatures [19]. To accurately predict the reforming performance of the catalyst bed, the effectiveness factor (η) should be introduced. The effectiveness factor is used to quantify the effect of intraparticle diffusion limitations on reaction rates. It is defined as the ratio of the actual reaction rate in the catalyst particle to the calculated rate that exists in the absence of diffusion limitations [20–23].

$$\eta = \frac{\text{Actual overall rate of reaction}}{\begin{array}{c}\text{Rate of reaction that would result if entire interior surface were} \\ \text{exposed to the external pellet surface conditions } C_{is},\ T_s\end{array}} \tag{4}$$

One of the most commonly used methods to calculate the effectiveness factor is using the Thiele modulus by assuming an isothermal, first-order reaction [21, 24–26]. The Thiele modulus is a non-dimensional number representing

the relationship between the diffusion rate and the reaction rate in a porous catalyst pellet. Another way to estimate the effectiveness factor is by considering the temperature and concentration distributions inside the catalyst particle, known as intraparticle distribution method. In this method, the equations of reaction rates and mass and energy balances are numerically solved to obtain the temperature and concentration distributions and the local reaction rates within the catalyst particle [27–30].

Hafeez et al. [26] developed a heterogeneous model to predict the performance of both a packed bed and a coated wall microreactor over a commercial $CuO/ZnO/Al_2O_3$ catalyst. In their study, the effectiveness factor was calculated using the Thiele modulus. The MSR and MD reactions were considered irreversible, and the WGS reaction was neglected. Ziarati et al. [28] developed a dynamic model of the MSR process in a packed-bed reactor considering the contributions of all molecular and convective terms of momentum, heat and mass transfer, and the effectiveness factors. They used the species continuity equations to calculate the intraparticle concentration distributions of methanol, hence to estimate the effectiveness factor for the MSR reaction. However, the WGS reaction was neglected. The effectiveness factor for the MD reaction was also considered as equal to one. Olatunde et al. [29] numerically investigated the non-isothermal effectiveness factor for the catalytic MSR process over a commercial $CuO/ZnO/Al_2O_3$ catalyst. The concentration distribution of key components (methanol and hydrogen) and the temperature distribution inside a spherical catalyst pellet was estimated. However, they neglected the external diffusion resistances between gas and solid phase. The existence of CO was also neglected in the reforming mixture. Tesser et al. [30] conducted the experimental work on an internal loop gradient-less Berty CSTR reactor and a pilot-scale tubular packed-bed reactor for MSR. A reactor model taking into account the reaction kinetics and mass and heat transfer effects was also developed. The effectiveness factor was considered for a commercial catalyst in the size of $3-7\,\mathrm{mm}$. The effectiveness factor was calculated by solving mass and

heat balance equations governing the simultaneous reactions and diffusion in a catalyst particle. However, the reaction mechanisms for CO formation were not considered in their study. Indeed, most studies regard the MSR process as a first-order reaction when calculating the effectiveness factor. Some studies ignore the external mass transfer limitations. Moreover, some researches do not appropriately deal with complex reaction networks inside the catalyst particle [25].

In our previous work [31], a one-dimensional pseudo-homogeneous model for the MSR process in a packed bed reactor was proposed. The effectiveness factor for the MSR reaction was calculated by using an empirical equation of the Thiele modulus. However, the effectiveness factors for the WGS and MD reactions were ignored. Moreover, the role of the intraparticle diffusion resistances as well as the effectiveness factors on the performance of the reactor are not well investigated, adding to the novelty of this work.

In the current study, a one-dimensional steady-state model of a multi-tubular packed-bed reformer was developed for the steam reforming of methanol on a commercial $CuO/ZnO/Al_2O_3$ catalyst. A comprehensive kinetic Langmuir-Hinshelwood model was proposed to express the rate of MSR, WGS and MD reactions. The effectiveness factor for the MSR reaction was calculated as a function of the Thiele modulus, which could be seen from our previous work [31]. For comparison purposes, a rigorous reaction-diffusion model in catalyst pellets was also developed to estimate the effectiveness factors. The effects of key operating parameters (temperature and particle size) on the intraparticle distributions of temperature and concentration were studied and discussed. As opposed to previous pseudo-homogeneous models, this model provided an understanding of the role of the external and internal heat and mass transfer resistances in effectiveness factors, and appropriately dealt with the transport phenomena and complex reaction networks inside catalyst particles. In addition, experiments were conducted in this study to validate the kinetic model and the effectiveness factors. To bring both the methanol and

CO concentrations to less than 1% vol in the reformate stream, the optimized operating conditions were determined based on the simulation results.

2. Design of methanol steam reformer

Generally, a reformed methanol fuel cell (RMFC) system is composed of a burner, an evaporator, several thermal fluid circuits, a methanol steam reformer, and a high temperature PEM fuel cell stack. During the operation, a mixture of methanol and water is pumped into the evaporator, where the fuel is evaporated and then fed into the catalyst bed in the reformer. The reactants in the bulk fluid first travel to the external surface of the catalyst pellets, then diffuse from the external surface into and through the pores within the pellets, where the reactions take place on the exposed surface of catalyst. After that, the produced hydrogen-rich gas is sent to the anode side of the fuel cell stack. The fuel cells utilize the hydrogen from the anode side together with the oxygen from the cathode side to generate electricity by electrochemical reactions. The exhaust gas from the fuel cell stack anode is directed to the burner, where the residual carbon monoxide, hydrogen, and methanol react with air to generate thermal energy through the combustion process. The generated heat is provided into the catalyst bed by the thermal fluid passing through the shell side of the reactor. In this work, the methanol steam reformer as a subsystem of the RMFC system has been studied.

The shell-and-tube reformer for MSR in this study consists of baffles and tubes inside a cylindrical shell. The structure of the multi-tubular packed-bed reactor is illustrated in Figure 1. The reactor shell is usually surrounded by thermal insulation materials to avoid any significant amount of heat loss. Tubes packed with $CuO/ZnO/Al_2O_3$ catalyst are installed inside the shell and arranged in equilateral triangle tube bundles. The baffle plates are used to support the tube bundles, increase the flow distribution in the inter-tubular space, and for an effective heat transfer between tube and shell sides. The gas from the burner flows through the shell side of the reformer, thereby providing

an external heat source to drive the reactions in the catalyst bed. In the tube side, reactants flow through the catalyst bed, where the steam reforming reactions and pressure drop occur.

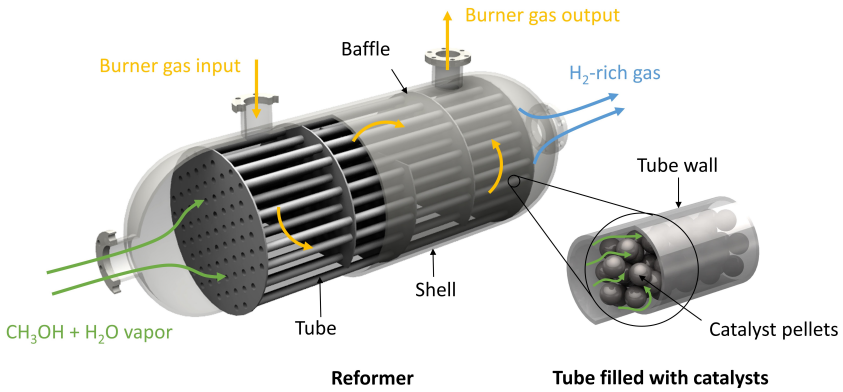

Figure 1: Schematic diagram of a multi-tubular packed-bed reactor for methanol steam reforming.

3. Experiment

3.1. Experimental setup

Experiments for the MSR process were performed at atmospheric pressure in a small-scale packed-bed reactor made of stainless steel. The commercial $CuO/ZnO/Al_2O_3$ catalyst particles were loaded in the reactor. The feeding rate of fuel (liquid methanol-water mixture) from the fuel tank was measured and controlled by a mass flow controller (MFC). The methanol-water mixture was first pumped into the evaporator, where the mixture was heated and evaporated. The high-temperature steam and methanol vapor then passed through the catalyst bed, where a fine mesh grid supported the catalysts. The reactor was surrounded by thermal insulation materials and heated by electric heaters outside the reactor. Therefore, this packed-bed reactor is assumed to be isothermal. The electric heaters were regulated by PID control of the

electric heaters to maintain the temperature in the fixed bed within a specific range. Temperatures at the inlet and outlet of the reactor were measured by two thermocouples. The average value of the measured inlet and outlet temperatures was regarded as the temperature of the catalyst bed. The gas analyzer (SIEMENS FIDMAT 6 for CH_3OH, CALOMAT 6 for H_2, and ULTRAMAT 6 for CO and CO_2) was used to analyze the main components of the reformate stream from the MSR reactor. The basic schematic of the experimental setup is shown in Figure 2.

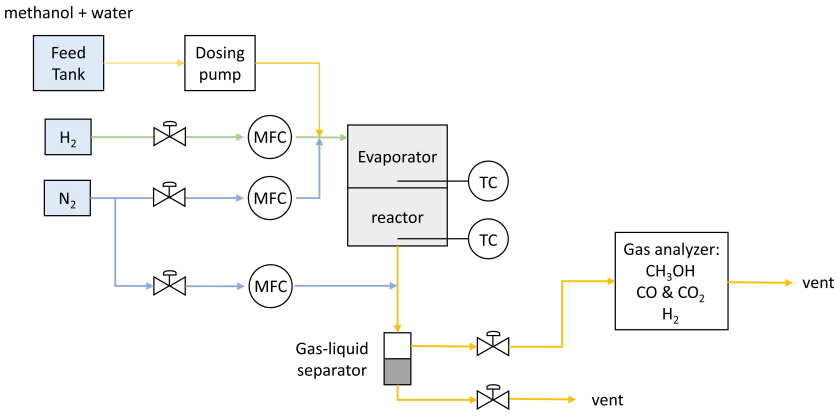

Figure 2: Processflow-sheet for the experimental setup.

3.2. Experimental procedure

The reactor was loaded with 3.66 g of the commercial $CuO/ZnO/Al_2O_3$ catalyst in a volume of 3.6 mL. Cylindrical catalyst particles with a diameter of 1.5 mm were used. The catalyst was flushed firstly in situ with a volumetric flow rate of hydrogen $Q_{H_2} = 0.1\,\mathrm{cm^3\,min^{-1}}$, and a volumetric flow rate of dinitrogen $Q_{N_2} = 2\,\mathrm{cm^3\,min^{-1}}$ (5% vol of H_2 diluted with N_2) for 1 hour to reduce CuO to Cu (the main active component in the catalyst). The reduction reaction rate was kept low in order to avoid any sintering of catalyst by controlling the operating temperature in the range of 433−493 K. The reforming process

was carried out at temperatures of 493 K, 513 K and 533 K and a ratio of catalyst weight to the molar flow rate of methanol (W/F_{CH_3OH}) in the range of $44-263\,\mathrm{kg\,s\,mol^{-1}}$. The variation of W/F_{CH_3OH} was achieved by changing the volumetric flow rate of liquid methanol Q_{CH_3OH} from 0.051 to $0.308\,\mathrm{cm^3\,min^{-1}}$ while keeping a constant catalyst loading. Test at each operating condition was kept for at least 30 minutes of continuous running to make sure the steady state was achieved. The value of the steam to carbon ration (S/C) was selected to be 1.3 to maximize the methanol conversion without wasting much energy in water evaporation [32].

4. Mathematical model

The phenomena occurring in the catalytic packed-bed reactor for MSR can be characterized according to the reaction kinetics, pressure drop, internal and external diffusion resistances of catalyst pellets, heat and mass transfer in both tube and shell sides, and heat exchange between the tube side and shell side through the tube wall. Therefore, the one-dimensional pseudo-homogeneous model is developed taking into account the reaction kinetics, effectiveness factors, species continuity equation, thermal energy equation, and pressure drop.

4.1. Reaction kinetics

According to the studies of Sá et al. [33] and Herdem et al. [34], the kinetic Langmuir-Hinshelwood model based on the work of Peppley et al. [13, 14] has been proved to present the best agreement between the mathematical model and the experimental data for the commercial $CuO/ZnO/Al_2O_3$ catalyst. Peppley et al. [13, 14] developed a comprehensive model for the process of MSR on a $CuO/ZnO/Al_2O_3$ catalyst. The surface mechanisms for all three reversible reactions (MSR, WGS, and MD) were proposed based on the following assumptions: hydrogen adsorption doesn't compete for the same active sites with the adsorption of oxygen-containing species; the type of active sites for the MD

reaction is different from the type of active sites for the MSR and WGS reactions; the rate-determining step for both the MSR reaction and MD reaction is the dehydrogenating of adsorbed methoxy groups; the rate-determining step for the WGS reaction is the formation of an intermediate formate species. The detailed derivations of the rate expressions are reported in [35]. Based on the Langmuir-Hinshelwood model, the rate expressions for the three main reactions (MSR, WGS and MD) involved in the process can be expressed as:

$$r_R = \frac{k_R K^*_{CH_3O^{(1)}} \left(p_{CH_3O\ H}/p_{H_2}^{1/2}\right)\left(1 - p_{H_2}^3 p_{Co_2}/K_R^{eq} p_{CH_3\ OH}\, p_{H_2o}\right) C_{S_1}^T C_{S_{1a}}^T}{\left(1 + K^*_{CH_3O^{(1)}}\left(p_{CH_3O\ H}/p_{H_2}^{1/2}\right) + K^*_{HCO\ O^{(1)}} p_{CO_2} p_{H_2}^{1/2} + K^*_{OH^{(1)}}\left(p_{H_2O}/p_{H_2}^{1/2}\right)\right)\left(1 + K_{H^{(1a)}}^{1/2} p_{H_2}^{1/2}\right)} \tag{5}$$

$$r_W = \frac{k_W K^*_{OH^{(1)}} \left(p_{CO} p_{H_2O}/p_{H_2}^{1/2}\right)\left(1 - p_{H_2} p_{CO_2}/K_W^{eq} p_{CO} p_{H_2o}\right) C_{S_1}^{T\,2}}{\left(1 + K^*_{CH_3O^{(1)}}\left(p_{CH_3O\ H}/p_{H_2}^{1/2}\right) + K^*_{HCO\ O^{(1)}} p_{CO_2} p_{H_2}^{1/2} + K^*_{OH^{(1)}}\left(p_{H_2o}/p_{H_2}^{1/2}\right)\right)^2} \tag{6}$$

$$r_D = \frac{k_D K^*_{CH_3O^{(2)}} \left(p_{CH_3O\ H}/p_{H_2}^{1/2}\right)\left(1 - p_{H_2}^2 p_{CO}/K_D^{eq} p_{CH_3O\ H}\right) C_{S_2}^T C_{S_{2a}}^T}{\left(1 + K^*_{CH_3O^{(2)}}\left(p_{CH_3O\ H}/p_{H_2}^{1/2}\right) + K^*_{OH^{(2)}}\left(p_{H_2O}/p_{H_2}^{1/2}\right)\right)\left(1 + K_{H^{(2a)}}^{1/2} p_{H_2}^{1/2}\right)} \tag{7}$$

where r_j ($\mathrm{mol\,m^{-2}\,s^{-1}}$) is the rate of reaction j ($j = R$, W and D); k_j and K_j^{eq} ($\mathrm{m^2\,s^{-1}\,mol^{-1}}$) are the equilibrium constant of reaction j, respectively; and K^* ($\mathrm{bar^{-0.5}}$) is the adsorption coefficient; p_i (bar) is the partial pressure of component i ($i = \mathrm{CO_2}$, CO, $\mathrm{H_2}$, $\mathrm{CH_3OH}$ and $\mathrm{H_2O}$). Based on the reaction mechanisms, the elementary surface processes for the MSR and the WGS reactions occur on the Type 1 active sites, and the MD reaction occurs on the distinct Type 2 active site. Therefore, the $C_{s_1}^T$, $C_{s_{1a}}^T$, $C_{s_2}^T$ and $C_{s_{2a}}^T$ in equations (5) to (7) are defined as the concentrations of distinct active sites '1', '1a', '2', and '2a' on the surface of the catalyst ($\mathrm{mol\,m^{-2}}$), where the '1' and '1a' sites are assumed to be active for the MSR and WGS reactions and the '2' and '2a' sites are for the MD reaction [14].

4.2. Effectiveness factor

When there are considerable heat and mass transfer resistances inside the porous catalyst particle, the reaction rates on the catalyst particle can be non-uniform. To account for variations in the reaction rates throughout the pellet,

a parameter known as the effectiveness factor is introduced. The effectiveness factor η is defined as the ratio of the actual reaction rate in the catalyst particle to the reaction rate at the external surface of the pellet [21]. It can be obtained as a function of the Thiele modulus for first-order kinetics in a spherical catalyst pellet. Another approach is to calculate the effectiveness factor numerically by considering the concentration and temperature distributions within catalyst pellets.

4.2.1. Thiele modulus method

A Thiele modulus-effectiveness factor method is applied to provide insight into the interplay of intraparticle mass transfer and intrinsic adsorption kinetics [36]. For a first-order reaction in spherical catalyst pellets, the expression of the effectiveness factor as a function of Thiele modulus is:

$$\eta = \frac{3}{\phi_1^2}\left(\phi_1 \coth \phi_1 - 1\right) \tag{8}$$

where ϕ_1 is the Thiele modulus for a first-order reaction, which can be expressed as:

$$\phi_1^2 = \frac{r_{js}\rho_c r_p^2 S_c}{D_{i,\mathrm{ep}} c_{is}} \tag{9}$$

where r_{js} ($\mathrm{mol\,m^{-2}\,s^{-1}}$) and c_{is} ($\mathrm{mol\,m^{-3}}$) are the rate of reaction j and the concentration of component i if the entire interior surface was exposed; r_p (m) is the radius of the catalyst pellet; ρ_c ($\mathrm{kg\,m^{-3}}$) is the density of catalyst bed; and $D_{i,ep}$ ($\mathrm{m^2\,s^{-1}}$) is the effective diffusivity of component i, which is defined to describe the diffusion that affects the chemical reactions inside catalyst particles.

The catalyst particle used in this study is cylindrical with an aspect ratio of 1. For such a non-spherical particle, the volume-equivalent (surface-equivalent) particle diameter, defined as the diameter of a single spherical pellet having the same volume (surface) as the non-spherical particle, is introduced in this study. For a cylinder catalyst with a diameter d and a height h, the volume-equivalent

particle diameter d_p^v can be calculated by:

$$d_p^v = \left(\frac{6V_{pa}}{\pi}\right)^{\frac{1}{3}} = d\left(\frac{3}{2}\frac{h}{d}\right)^{\frac{1}{3}} \tag{10}$$

where V_{pa} (m^3) is the volume of a single catalyst particle. The surface-equivalent sphere diameter d_p^s (m) can be calculated by:

$$d_p^s = \left(\frac{S_{pa}}{\pi}\right)^{\frac{1}{2}} \tag{11}$$

where S_{pa} (m^2) is the surface area of a single catalyst particle.

4.2.2. Intraparticle distribution method

In the catalyst bed, the mass transfer of reactants first takes place from the bulk fluid to the external surface of catalyst pellets. Then the reactants diffuse into and through pores inside the pellets, with reactions occurring on the pore surface. This two-step diffusion process, including the external and internal diffusion in the porous catalyst pellets, is shown in Figure 3. Expecting an analogous behavior between the mass diffusion and the heat transfer, the model of the intraparticle heat and mass balances can be developed. A non-isothermal condition is assumed throughout the spherical particle. It is also assumed that the molecular diffusion occurs only in the radial direction within the pellet, and the catalyst particles are spherical or equal to their volume equivalent sphere.

The local reaction rate inside the porous catalyst pellet depends predominately on the local composition and temperature. Hence, the effectiveness factor η_j for reaction j (j = MSR, MD and WGS) is regarded as the ratio of the average rate of reaction j with diffusion inside the catalyst pellet to the rate of reaction in the bulk stream. The average reaction rate can be calculated by the integral of the local reaction rate with respect to the catalyst volume and then divided by the catalyst volume. The effectiveness factor can be approximated by the intraparticle distribution method:

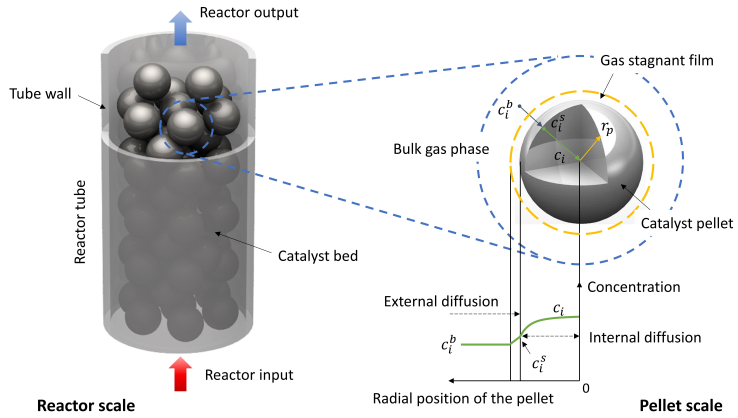

Figure 3: Diffusion processes in a catalytic pellet.

$$\eta_j = \frac{\int_0^{r_p} 4\pi\xi^2 r_j\left(c_i, T\right) d\xi}{(4/3)\pi r_p^3 r_j\left(c_i^b, T^b\right)} \tag{12}$$

where ξ (m) is the radial distance of pellet; $r_j\left(c_i, T\right)$ $(\mathrm{mol\,m^{-2}\,s^{-1}})$ indicates the local rate of reaction j with the temperature T (K) and the concentration c_i $(\mathrm{mol\,m^{-3}})$ of component i inside the pellet; and $r_j\left(c_i^b, T^b\right)$ $(\mathrm{mol\,m^{-2}\,s^{-1}})$ indicates the intrinsic rate of reaction j in the bulk fluid condition with the temperature T^b (K) and the concentration c_i^b $(\mathrm{mol\,m^{-3}})$ of component i.

The temperature and concentration profiles inside a spherical catalyst particle can be calculated according to the following mass and heat balance equations:

Intraparticle mass balance

$$D_{i,ep}\left(\frac{\partial^2 c_i}{\partial\xi^2} + \frac{2}{\xi}\frac{\partial c_i}{\partial\xi}\right) = \rho_c \sum_{j=1}^{N_R} v_{ij} r_j S_c \tag{13}$$

Intraparticle heat balance

$$\lambda_{ep}\left(\frac{\partial^2 T}{\partial\xi^2} + \frac{2}{\xi}\frac{\partial T}{\partial\xi}\right) = \rho_c \sum_{j=1}^{N_R} \left(-\Delta H_j\right) r_j S_c \tag{14}$$

where $D_{i,ep}$ ($\mathrm{m^2\,s^{-1}}$) is the particle effective diffusivity of component i; λ_{ep} ($\mathrm{W\,m^{-1}\,K^{-1}}$) is the particle effective thermal conductivity; ν_{ij} is the stoichiometric coefficient of species i in the reaction j; N_R is the number of main reactions; and r_j ($\mathrm{mol\,m^{-2}\,s^{-1}}$) is the local rate of reaction j within the catalyst particle.

The boundary conditions are:

at $\xi = 0$,

$$\frac{\partial c_i}{\partial \xi} = 0 \tag{15}$$

$$\frac{\partial T}{\partial \xi} = 0 \tag{15}$$

at $\xi = \frac{d_p^v}{2}$,

$$-D_{i,ep}\frac{\partial c_i}{\partial \xi} = k_{i,fs}\left(c_i - c_i^b\right) \tag{15}$$

$$-\lambda_{ep}\frac{\partial T}{\partial \xi} = h_{fs}\left(T - T^b\right) \tag{16}$$

where $k_{i,fs}$ ($\mathrm{m\,s^{-1}}$) is the mass transfer coefficient between the bulk fluid and catalyst particle; h_{fs} ($\mathrm{W\,m^{-2}\,K^{-1}}$) is the heat transfer coefficient, considering both the external and internal heat transfer, between the bulk fluid and catalyst particle; and d_p^v (m) is the volume-equivalent sphere diameter, which equals the diameter of a sphere with the same volume as the particle.

4.3. Species continuity equation

To develop a one-dimensional steady-state model of a multi-tubular packed-bed reactor for the MSR process, the following assumptions are made:

1) the whole system is adiabatic and under steady-state conditions;
2) all reacting species are in the gas phase and behave as the ideal gas;
3) plug flow occurs in a packed bed with no axial mixing;

4) the temperature and concentration gradients in the radial direction are neglected;
5) the catalyst size and packed bed porosity are considered to be uniform.

This model considers the effectiveness factors, pressure drop, heat and mass transfer in tube and shell sides along the reactor length, and heat exchange between the tube side and shell side through the tube wall. The continuity equation for specie i along the axis of the catalyst bed is given by:

$$\frac{dF_i}{dz} = \eta_i r_i \rho_b A_c \tag{17}$$

where F_i ($\mathrm{mol\,s^{-1}}$) is the molar flow rate of species i at the axial location z (m), A_c ($\mathrm{m^2}$) is the cross-sectional area of the catalyst bed, r_i ($\mathrm{mol\,kg_{catalyst}^{-1}\ s^{-1}}$) is the production rate of component i, $C_{P,i}$ ($\mathrm{J\,mol^{-1}\,K^{-1}}$) is the specific heat of gas component i, and ρ_b ($\mathrm{kg\,m^{-3}}$) is the density of catalyst bed.

4.4. Thermal energy equation

The steady state energy balance along the axis of the catalyst bed leads to the following equation:

$$\frac{dT_t}{dz} = \frac{U_t a \Delta T + \sum r_j \rho_b \Delta H_j S_c}{\sum F_i C_{P,i}} A_c \tag{18}$$

where U_t ($\mathrm{W\,m^{-2}\,K^{-1}}$ or $\mathrm{J\,s^{-1}\,m^{-2}\,K^{-1}}$) is the overall heat transfer coefficient in tube side, a is the surface-to-volume ratio in the thermal conductivity of a single tube, ΔT (K) is the temperature difference between shell side and tube side, ΔH_j ($\mathrm{J\,mol^{-1}}$) is the reaction enthalpy of reaction j, and r_j ($\mathrm{mol\,m^2\,s^{-1}}$) is the rate of reaction j.

A steady state energy balance along the axis in shell side is written as:

$$\frac{dT_s}{dz} = \frac{N_s U_s A_o \Delta T}{F_s C_{Ps} L} \tag{19}$$

where U_s ($\mathrm{W\,m^{-2}\,K^{-1}}$ or $\mathrm{J\,s^{-1}\,m^{-2}\,K^{-1}}$) is the overall heat transfer coefficient outside the tube, A_o ($\mathrm{m^2}$) is the heat transfer area outside the reactor tube, F_s ($\mathrm{mol\,s^{-1}}$) is the molar flow rate of burner gas, $C_{P,s}$ ($\mathrm{J\,kg^{-1}\,K^{-1}}$) is the specific

heat of burner gas, L (m) is the total length of the packed-bed reactor, and N_t is the number of tubes in the reformer.

4.5. Pressure drop

It is assumed that a set of porous catalyst pellets of uniform size are packed in the cylindrical tubes. The pressure drop along the reactor length can be approximated by the semi-empirical Ergun equation [21]:

$$\frac{dP}{dz} = -\frac{G}{\rho_f d_p}\left(\frac{1-\phi}{\phi^3}\right)\left[\frac{150(1-\phi)\mu_f}{d_p} + 1.75G\right] \tag{21}$$

where μ_f (Pa s) is the viscosity of gas mixture, ρ_f (kg m^{-3}) is the density of gas mixture, ϕ is the void fraction of the catalyst bed, and G (kg m^{-2} s^{-1}) is superficial mass velocity. The parameters for modeling in this study are listed in Table 1.

5. Results and discussion

5.1. Model validation

To validate the kinetic model and the effectiveness factor calculated by two different methods (Thiele modules method and intraparticle distribution method) described in section 4, an experiment was conducted in a small-scale reactor loaded with porous catalyst particles for MSR reactions. The experimental results were compared with the simulation results of (1) the kinetic model only, (2) the kinetic model + effectiveness factor calculated by the Thiele modules method, and (3) the kinetic model + effectiveness factor calculated by the intraparticle distribution method. Simulation results in terms of the methanol conversion and CO concentration in reformed gas were compared with the experimental data at the operating temperatures of 493 K, 513 K and 533 K, and the W/F_{CH_3OH} ratios of 0−300 kg s mol^{-1}. The operating parameters for simulations and experiments are shown in Table 2.

As shown in Figure 4, there is a good agreement between the experimental data and the calculated methanol conversions of the model using the intraparticle distribution method, where a percentage discrepancy of less than

Table 1: Properties of catalyst and geometric parameters of the reactor.

Parameter	Value
Density of catalyst bed, ρ_b ($\mathrm{kg\,m^{-3}}$)	1300
BET area, S_c ($\mathrm{m^2\,kg^{-1}}$)	102000
Average pore diameter, Å (m)	6.4×10^{-9}
Void fraction of catalyst bed, ϕ	0.37
Diameter of cylindrical catalyst particle, d_p (m)	0.0015
Height of cylindrical catalyst particle, h (m)	0.0015
Site concentrations of site '1', C^T_{S1} ($\mathrm{mol\,m^{-2}}$)	7.5×10^{-6}
Site concentrations of site '1a', C^T_{S1a} ($\mathrm{mol\,m^{-2}}$)	7.5×10^{-6}
Site concentrations of site '2', C^T_{S2} ($\mathrm{mol\,m^{-2}}$)	7.5×10^{-6}
Site concentrations of site '2a', C^T_{S2a} ($\mathrm{mol\,m^{-2}}$)	7.5×10^{-6}
Number of reactor tubes, N_t	36
Inner diameter of the tubular reactor, D_t (m)	0.016
Outer diameter of the tubular reactor, D_o (m)	0.018
Tube pitch, p_t (m)	0.027
Number of baffle plates, N_b	4
Spacing between baffle plates, p_b (m)	0.12
Length of the reactor, L (m)	0.48
Area fraction of baffle plate that is window, f_b (for 25% baffle plate)	0.1955

Table 2: Geometricand operating parameters for simulations and experiments.

Parameter	Value
Mass of catalyst (g)	3.66
Volume of catalyst bed (mL)	3.6
Feeding rate of methanol liquid ($cm^3\,min^{-1}$)	$0.051 - 0.308$
Operating temperature (K)	$493 - 533$
Operating pressure (bar)	1
Steam/methanol ratio (S/C) (mol/mol)	1.3
Catalyst size (mm)	1.5×1.5
W/F_{CH_3OH} ($kg\,s\,mol^{-1}$)	$0 - 300$

3.3% is observed. The kinetic model with effectiveness factors calculated by Thiele modulus also agrees well with the experimental data of methanol conversion, where the maximal percentage discrepancy is 5.4%. Furthermore, for the kinetic model without considering effectiveness factors, a more considerable difference appears between the predicted methanol conversion and the experimental results. Therefore, for cylindrical catalyst particles (1.5 mm diameter with an aspect ratio of 1) used in this study, the effect of catalyst particle size on methanol conversion should be considered owing to the significant effect of intraparticle diffusion on reaction rates.

Figure 5 shows the comparison between the experimental results and simulated CO concentration in the reformed gas with changes under the operating temperatures and W/F_{CH_3OH}. As we can see, these models can approximately predict the CO concentration under most conditions. However, there are two unexpected jumps of CO concentration in the experimental data when the temperature is at 493 K and 513 K, and the W/F_{CH_3OH} is at $259\,kg\,s\,mol^{-1}$. A possible explanation for this might be the non-uniform distributions of temperature and concentration in the reactor, which affect the local reaction rates. Another possible explanation is that, in our experiments, a very small feeding

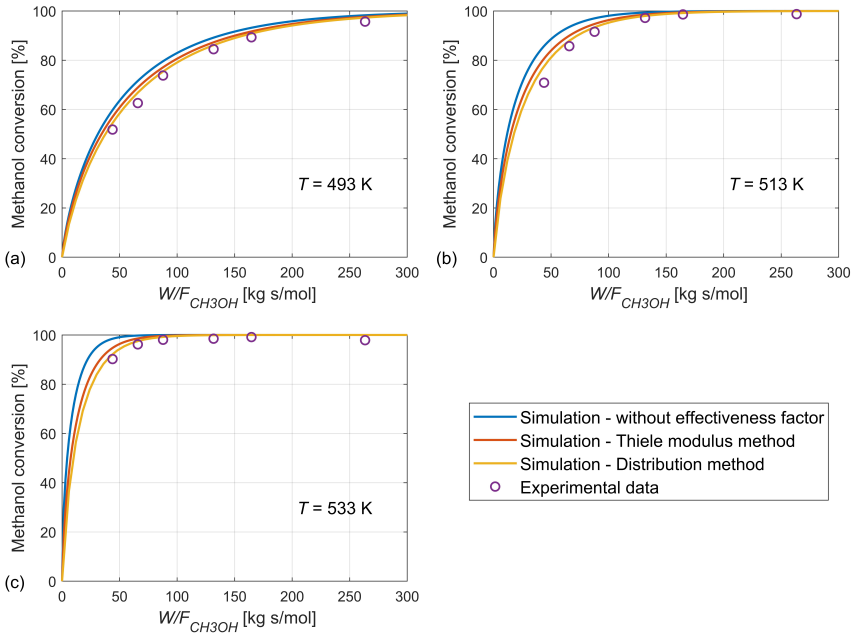

Figure 4: Comparison of methanol conversion between the simulation results and the experimental results under different $W/F_{\mathrm{CH_3OH}}$ and operating temperatures of catalyst bed.

rate of methanol is introduced to obtain a large $W/F_{\mathrm{CH_3OH}}$ in the reactor. This extremely small feeding rate of liquid methanol ($0.051\,\mathrm{cm^3 min^{-1}}$) could intensify the effect of non-uniform distributions and lead to the oscillations of CO production at the large $W/F_{\mathrm{CH_3OH}}$ value. Moreover, the large void fractions near the reactor wall, which were not investigated in this study, could also be a possible reason.

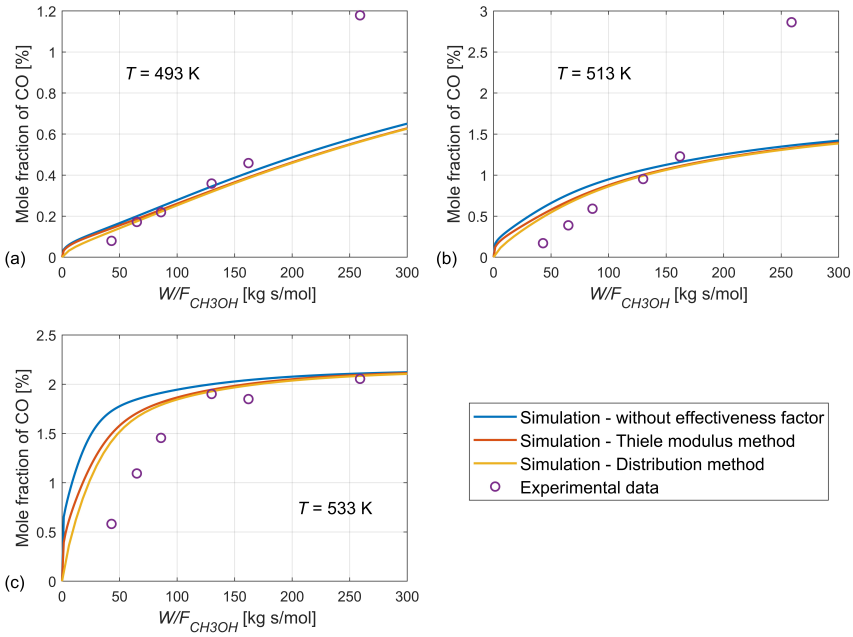

Figure 5: Comparison of the mole fraction of CO in the reformed gas between the simulation results and the experimental results under different $W/F_{\mathrm{CH_3OH}}$ and operating temperatures of catalyst bed.

5.2. Intraparticle diffusion

According to the above analysis, the intraparticle distribution method provides a better prediction of effectiveness factors in the catalyst bed. Therefore, this method for the calculation of the effectiveness factors is utilized in this section by solving the mass and heat balance equations governing both the reactions and diffusion inside catalyst pellets. The numerical solutions of the

mass and heat balance equations allow the evaluation of both temperature and concentration profiles inside the pellet. Figure 6 shows the intraparticle profiles of concentration as function of the dimensionless radial position (r/R). To study the intraparticle diffusion phenomena, the concentration profiles are discussed for varying particle diameter ($d_p = 1.0, 2.0\,\mathrm{mm}$) and varying bulk temperature ($T_b = 493, 553\,\mathrm{K}$) at the inlet condition ($S/C = 1.3$) of the catalyst bed. By comparing Figure 6 (a) with (b), the changes in concentration become more rapid from the external surface ($r/R = 1$) to the pellet center ($r/R = 0$) when the diameter increases from 1.0 mm to 2.0 mm. In addition, as the bulk temperature increases from 493 K to 553 K, the changes in concentrations also become more dramatic along the pellet radius. Therefore, the process tends to be more diffusion-limited with increasing particle size and temperature. The methanol conversion is generally reduced due to these diffusion limitations within the catalyst particles. The effect of external mass transfer limitations is also investigated by considering the mass transfer coefficient $k_{i,fs}$ from the gas to solid phase. The mass transfer coefficient is represented as the difference between concentrations on the external catalyst surface and the given values (reactor inlet condition) in the bulk fluid. As shown in Figure 6, the effect of the external mass transfer resistance is represented as the difference between the concentrations of the diffusing species in the the bulk fluid (with 56.5% vol of H_2O and 43.5% vol of CH_3OH) and those on the external surface (when $r/R = 1$). The results show that there are negligible external mass transfer resistances for this gas–solids system in these operating conditions, due to the small concentration differences ($< 1.08\%$) between the bulk fluid and the external surface. In addition, these concentration differences become slightly larger (from 0.13% to 1.08%) when the bulk fluid temperature is higher and the particle size is larger. Similar results have also been obtained in the study of Hafeez et al. [26] and Zhang et al. [37].

Due to the heat transfer limitations, the effects of particle diameter on the dimensionless profiles of temperature and temperature drop ΔT from the exter-

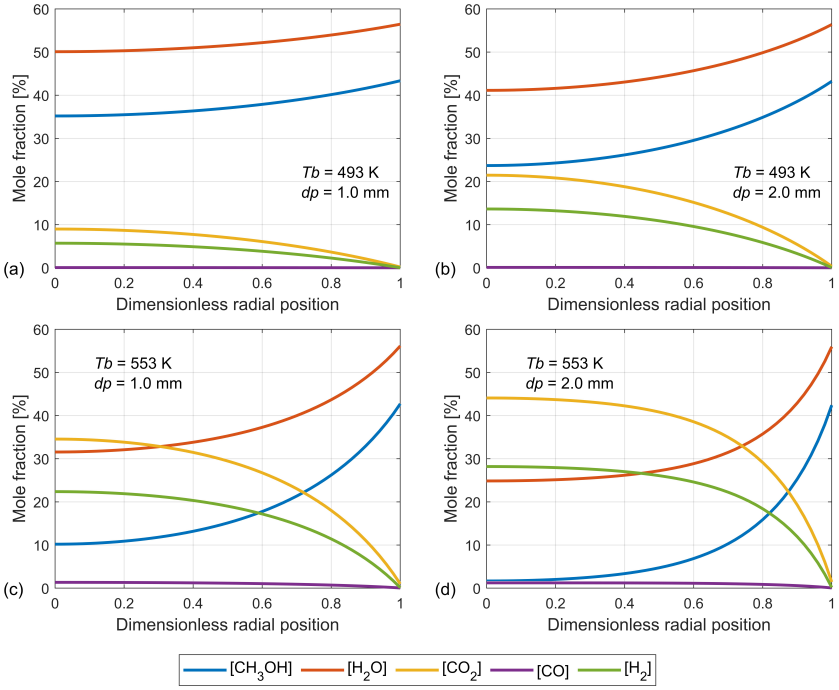

Figure 6: Simulated intraparticle profiles of mole fractions from the pellet center to the external radius of the pellet at the inlet condition for varying temperature T_b and diameter of catalyst particle d_p: (a) $T_b = 493\,\mathrm{K}$, $d_p = 1.0\,\mathrm{mm}$; (b) $T_b = 493\,\mathrm{K}$, $d_p = 2.0\,\mathrm{mm}$; (c) $T_b = 553\,\mathrm{K}$, $d_p = 1.0\,\mathrm{mm}$; and (d) $T_b = 553\,\mathrm{K}$, $d_p = 2.0\,\mathrm{mm}$.

nal surface at the inlet condition ($S/C = 1.3$) of the reactor were investigated in this study. With highly endothermic reactions that happen inside porous catalyst particles, heat will be transferred from the bulk fluid through the thermal boundary layer to the external surface of the pellet and then diffuse along the radial direction to the pellet center. Therefore, in Figure 7 (a) and (b), temperatures drop from the external surface to the pellet center due to the heat transfer characteristics and endothermic nature of the MSR process inside the porous catalyst pellet. As the particle diameter increases, temperatures decline more rapidly towards the pellet center due to the greater limitations in internal heat transfer. As can be seen in Figure 7 (a), there exists a temperature difference between the external surface and the bulk fluid ($T_b = 523\,\mathrm{K}$). This temperature difference increases significantly with the increase in particle size. Therefore, the heat transfer coefficient across the gas-solid interface region due to the external heat transfer limitation can not be neglected. Moreover, the intraparticle distribution of temperature is affected not only by the particle size but also by the bulk fluid temperature. The effects of bulk temperature on the dimensionless profiles of temperature and temperature drop from the external surface (ΔT) are studied. In Figure 8, the ΔT shows a steeper declining trend from the external surface to the pellet center when a higher temperature of bulk fluid is introduced in the reactor. The reason could be that the increased temperature of the catalyst pellet enhances reaction rates.

Since the effectiveness factor is derived from the intraparticle profiles of concentrations and temperature, the changes in particle size and bulk temperature will also affect the effectiveness factor for each reaction. In Figure 9, the effects of changes in particle diameter and bulk temperature on the effectiveness factors for MSR and MD reactions are presented at the reactor inlet condition ($S/C = 1.3$). As shown in Figure 9 (a), when the diameter of catalyst particle approaches zero, the effect of intraparticle diffusion resistances is reduced to the minimum, which is illustrated by the effectiveness factors approaching unity. At this point, the exposure of the catalyst surface to reactants is max-

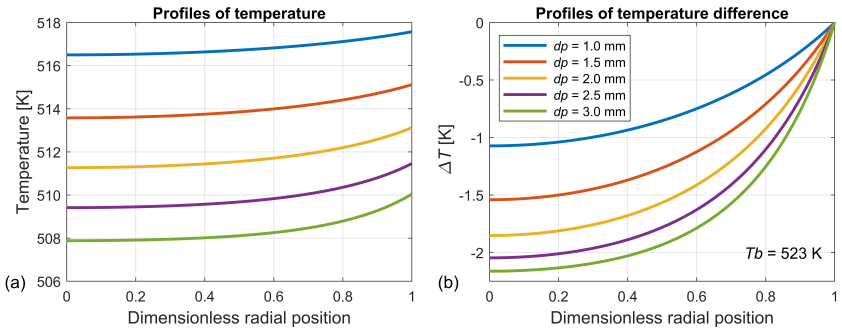

Figure 7: Intraparticle profiles of (a) temperature and (b) temperature difference from the pellet center to the external radius of the pellet at the inlet condition for varying diameter of catalyst particle d_p.

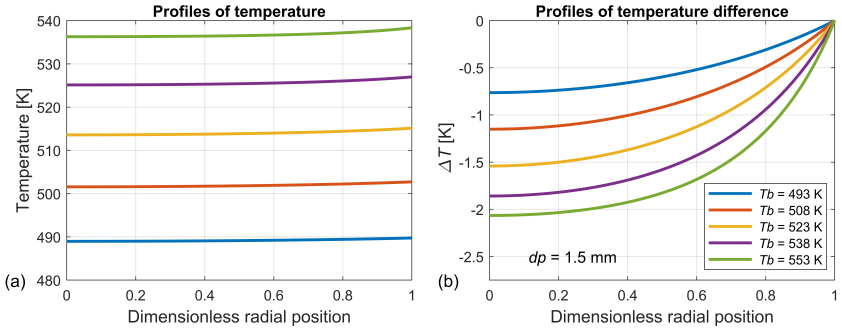

Figure 8: Intraparticle profiles of (a) temperature and (b) temperature difference from the pellet center to the external radius of the pellet at the inlet condition for varying bulk fluid temperature T_b.

imized for the reactions to take place. As the particle diameter increases to 3.0 mm, there will be considerable increases in the heat and mass transfer limitations within the pellet. Hence, the effectiveness factor for the MSR reaction decreases to 0.17, and the effectiveness factor for the MD reaction decreases to 0.036. This implies that for a larger particle diameter, the effect of intraparticle diffusion limitations becomes more predominant. Hence, less surface area in the catalyst is available for the reactions, and, on the contrary, most of the reactions occur near the external surface of the catalyst particle. As shown in Figure 9 (b), when the bulk fluid temperature increases from 273 K to 573 K, the effectiveness factor for the MSR reaction decreases from almost 1 to 0.1, and the effectiveness factor for the MD reaction decreases from 0.96 to 0.03. For a very high temperature in the bulk fluid, the reaction rate is enhanced and becomes more significant than the diffusion rate. Thus the effectiveness factors become smaller, and the process is regarded as diffusion-limited. Most of the reactants are consumed very fast near the outer surface when diffusing towards the pellet center. Therefore, only a very small amount of reactants can penetrate the interior of the pellet.

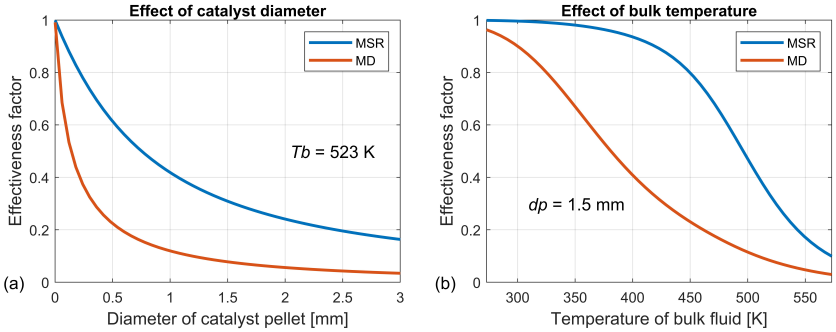

Figure 9: Effects of (a) catalyst diameter d_p and (b) bulk fluid temperature T_b variations on effectiveness factors for MSR and MDreactions at the reactor inlet condition.

5.3. Reformer performance

By developing the one-dimensional pseudo-homogeneous model, the performance of the MSR process on a multi-tubular packed-bed reformer is predicted. The MSR process in this reformer operates under the given conditions that the W/F_{CH_3OH} is $235\,kg\,s\,mol^{-1}$, the inlet temperature of shell-side gas is 673 K, and the inlet temperature of water-methanol vapor mixture is 473 K. In Figure 10, the solid lines show the simulation results with effectiveness factors calculated by the intraparticle distribution method and the '+' plus signs refer to the simulation results with effectiveness factors using the Thiele modulus method. There are only slight differences between the profiles by these two methods, which indicates that both the intraparticle distribution method and the Thiele modulus method can be used to predict the effectiveness factors for the MSR process in this reactor. Other results comparisons between these two methods under different temperatures of the burner gas and different particle sizes can be found in the Appendix. The concentration profiles of reactants and products along the reactor length are displayed in Figure 10 (a). As can be seen, the methanol-steam mixture is fed into the reactor with an S/C of 1.3. As the reaction proceeds, the mole fractions of reforming products constantly increase along the reactor length. After reactants pass through the catalyst bed, a methanol conversion of 98% is obtained. However, about 90% of the methanol is converted by the MSR process in the front section of the tube, which can be seen in Figure 10 (c). Figure 10 (b) shows a transient rise of temperature in the catalyst bed and a transient decrease of temperature in the burner gas near the tube entrance. This is due to the considerable temperature difference between the shell and tube sides, enhancing the heat transfer. Figure 10 (d) shows the profiles of effectiveness factors for MSR, MD and WGS reactions under the same operating conditions. The change of the effectiveness factor for the MSR reaction represents a similar trend with that for the MD reaction, while it shows a hyperbolic trend along the reactor for the WGS reaction. This could be due to the fact that the WGS reaction is reversed along

the reactors.

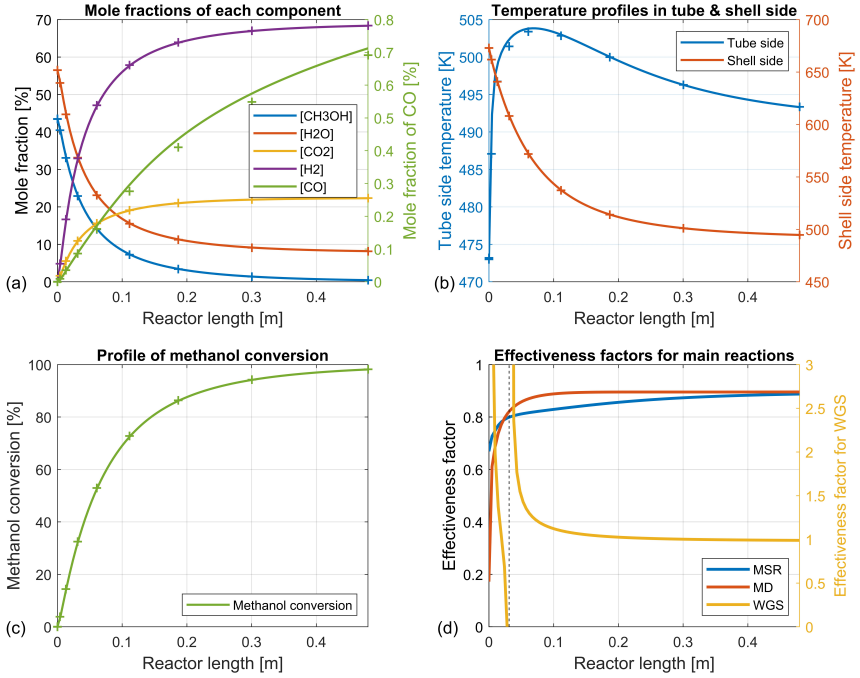

Figure 10: Profiles of (a) mole fractions of each component, (b) temperature in both tube and shell sides, (c) methanol conversion and (d) effectiveness factors for MSR, MD and WGS reactions along the reactor length with effectiveness factors calculated by the intraparticle distribution method (solid line) and Thiele modulus method ('+' plus sign).

Due to the effect on the intraparticle diffusion limitations, the change in particle diameter d_p is observed to have effects on the profiles of the methanol conversion and pressure drop through the length of the catalyst bed, which is presented in Figure 11. The inlet temperature of burner gas in the shell side T_s is 673 K, the inlet temperature of water/methanol vapor T_t is 433 K, and the $W/F_{\mathrm{CH_3OH}}$ is 235 $\mathrm{kg\,s\,mol^{-1}}$ in this reactor. In Figure 11 (a), it is found that the methanol conversion is slightly increased from 94.92% to 97.16% when the diameter of the catalyst particle decreases from 2.5 mm to 0.5 mm. This is caused by the decrease of intraparticle diffusion resistances. However, as shown in Figure 11 (b), a remarkable increase of pressure drop along the reactor

length is observed when using a smaller particle size. Excessive pressure drop or pressure loss in the reactor tubes should generally be avoided, because it will result in poor system performance and excessive pump power consumption. A catalyst particle diameter of less than 1.5 mm is acceptable for the reaction process as it is still within the allowed 10% (difference from the initial pressure) pressure drop for the packed-bed reactor [24].

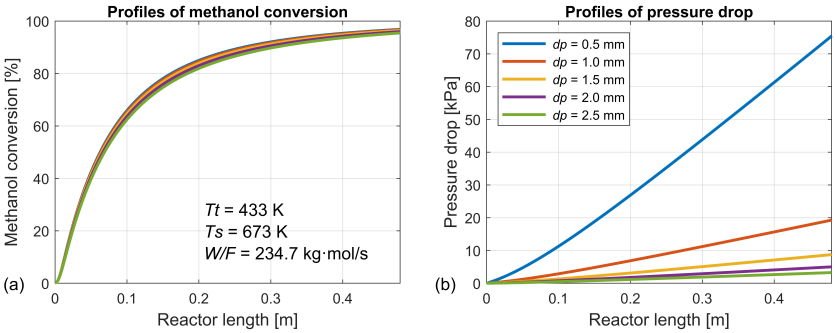

Figure 11: Effects of the diameter of catalyst particles d_p on distributions of (a) the methanol conversion, and (b) the pressure drop along the reactor length.

5.4. Optimization of operating parameters

As additional heat is provided from the burner gas in the shell side as the reactants flow through the catalyst bed, the inlet temperature of burner gas can affect the methanol conversion and CO concentration by affecting the heat transfer through the tube wall. In Figure 12 (b), the methanol conversion is improved when increasing the inlet temperature of burner gas from 573 K to 773 K because more heat is provided to the catalyst bed. However, as shown in Figure 12 (a), there is also a dramatic increase of CO concentration in the reformed gas due to the increased temperature of burner gas. The increase in temperature favors endothermic reactions (MD and reverse WGS), which leads to the accelerated CO production rate. Figure 12 (a) and (b) also illustrate the changes in methanol conversion and CO concentration with the $W/F_{\mathrm{CH_3OH}}$ ranging from 100 to 350 $\mathrm{kg\,s\,mol^{-1}}$, where the inlet flow of methanol is changed

at constant catalyst loading. The methanol conversion is increased by increasing the W/F_{CH_3OH}, so does the CO concentration in the reformed gas. This is because less methanol is fed into the catalyst bed to gain a larger value of W/F_{CH_3OH}, which leads to the reduction in the energy consumption by the MSR reforming process. Therefore, the increased temperature in the catalyst bed enhances the selectivity of CO.

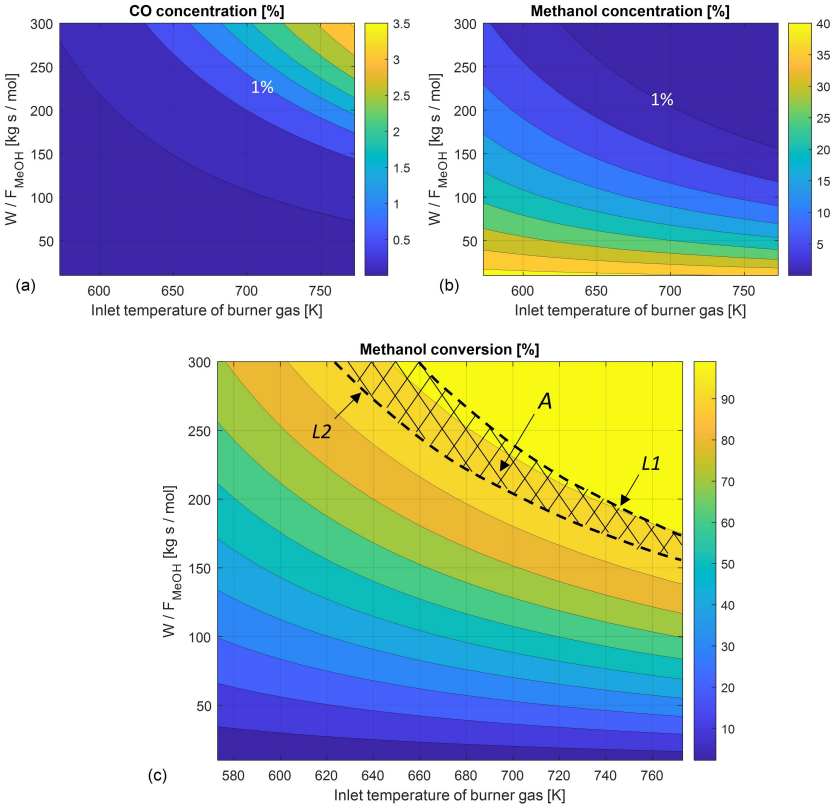

Figure 12: Effects of the W/F_{CH_3OH} and the inlet temperature of the burner gas on profiles of (a) the CO concentration, (b) the methanol concentration and (c) methanol conversion in the reformate gas

Many studies have been conducted on the poisoning effects of methanol-based reformate impurities on the PBI-based HT-PEM fuel cells. Generally,

a CO concentration of $2-3\%$ vol and a methanol concentration of 3% vol in the anode stream can be tolerated without leading to a significant degradation in the performance of the HT-PEM fuel cell [38–40]. However, the poisoning effects can deteriorate due to the possible interdependence among the effects of different impurities and can have more long-term severe durability effects on the fuel cell [39]. Therefore, keeping the concentrations of CO and methanol to less than 1% vol in the reformate gas is expected to be a good compromise and is used to optimize the operating parameters of the MSR process in the reformer. In Figure 12 (a) and (b), the 1% vol line of CO and methanol concentration is highlighted in each profile, which corresponds to $L1$ and $L2$ in Figure 12 (c), respectively. In Figure 12 (c), the area on the left side of $L1$ corresponds to CO concentration lower than 1% vol, and the area on the right side of $L2$ corresponds to methanol concentration lower than 1% vol. Therefore, the operating conditions in area A between $L1$ and $L2$ bring both methanol and CO concentration lower than 1% vol, which fulfill the requirement of HT-PEM fuel cells. For example, with the $W/F_{\mathrm{CH_3OH}}$ at $300\,\mathrm{kg\,s\,mol^{-1}}$, the recommended inlet temperature of burner gas should be in the range of $624-661\,\mathrm{K}$; and with the inlet temperature of burner gas at $773\,\mathrm{K}$, the recommended values of $W/F_{\mathrm{CH_3OH}}$ are in the range of $156-174\,\mathrm{kg\,s\,mol^{-1}}$.

6. Conclusions

A one-dimensional steady-state model of a multi-tubular packed-bed reactor was developed for the MSR on a commercial $\mathrm{CuO/ZnO/Al_2O_3}$ catalyst. This model took into account the reaction kinetics, pressure drop, internal and external diffusion resistances of catalyst pellets, heat and mass transfer in both tube and shell sides, and heat exchange between the tube and shell sides through the tube wall. To predict the effectiveness factors for main reactions, both the intraparticle distribution method and the Thiele modulus method were adopted and compared in this work. The computational results of both methods showed good agreements with the experimental results for

methanol conversion and CO concentration, but the intraparticle distribution method provided better predictions. Therefore, the effect of the particle size on the one-dimensional profiles of methanol conversion and CO concentration were investigated by the intraparticle distribution method. The results indicated that the methanol conversion was improved with the decrease in particle size, which also brings a higher pressure drop over the catalyst bed. Moreover, the effects of the inlet temperature of burner gas and $W/F_{\mathrm{CH_3OH}}$ on methanol conversion and CO concentration in the reformate gas were analyzed. It was observed that the increase in the inlet temperature of burner gas and the increase in $W/F_{\mathrm{CH_3OH}}$ could improve the methanol conversion, but also lead to a higher CO concentration in the products. Based on the computational results, the optimized operation conditions that bring both methanol and CO concentration lower than 1% vol in products were determined. With the $W/F_{\mathrm{CH_3OH}}$ at $300\,\mathrm{kg\,s\,mol^{-1}}$, the recommended inlet temperature of burner gas should be in the range of $624-661\,\mathrm{K}$; and with the inlet temperature of burner gas at $773\,\mathrm{K}$, the recommended values of $W/F_{\mathrm{CH_3OH}}$ are in the range of $156-174\,\mathrm{kg\,s\,mol^{-1}}$.

Acknowledgements

The research leading to these results has received funding from the Chinese scholarship council (CSC) and from the Danish Energy Technology Development and Demonstration Program (EUDP) through the COmmercial BReakthrough of Advanced fuel cells (COBRA Drive) project, grant number 64018-0118.

References

[1] H. Lan, L. Yang, F. Zheng, C. Zong, S. Wu, X. Song, Analysis and optimization of high temperature proton exchange membrane (ht-pem) fuel cell based on surrogate model, International Journal of Hydrogen Energy 45 (22) (2020) 12501–12513.

[2] M. Bodner, H. R. García, T. Steenberg, C. Terkelsen, S. M. Alfaro, G. S. Avcioglu, A. Vassiliev, S. Primdahl, H. A. Hjuler, Enabling industrial production of electrodes by use of slot-die coating for ht-pem fuel cells, international journal of hydrogen energy 44 (25) (2019) 12793–12801.

[3] L. Xia, C. Zhang, M. Hu, S. Jiang, C. S. Chin, Z. Gao, Q. Liao, Investigation of parameter effects on the performance of high-temperature pem fuel cell, International Journal of Hydrogen Energy 43 (52) (2018) 23441–23449.

[4] O. Özcan, A. N. Akın, Thermodynamic analysis of methanol steam reforming to produce hydrogen for HT-PEMFC: An optimization study, International Journal of Hydrogen Energy 44 (27) (2019) 14117–14126. doi:10.1016/j.ijhydene.2018.12.211.
URL https://dx.doi.org/10.1016/j.ijhydene.2018.12.211

[5] S. K. Das, A. Reis, K. J. Berry, Experimental evaluation of CO poisoning on the performance of a high temperature proton exchange membrane fuel cell, Journal of Power Sources 193 (2) (2009) 691–698. doi:10.1016/j.jpowsour.2009.04.021.
URL https://dx.doi.org/10.1016/j.jpowsour.2009.04.021

[6] J. O. Abe, A. Popoola, E. Ajenifuja, O. Popoola, Hydrogen energy, economy and storage: review and recommendation, International journal of hydrogen energy 44 (29) (2019) 15072–15086.

[7] F. Dawood, M. Anda, G. Shafiullah, Hydrogen production for energy: An overview, International Journal of Hydrogen Energy 45 (7) (2020) 3847–3869.

[8] A. Chougule, R. R. Sonde, Modelling and experimental investigation of compact packed bed design of methanol steam reformer, International Journal of Hydrogen Energy 44 (57) (2019) 29937–29945.

doi:10.1016/j.ijhydene.2019.09.166.
URL https://dx.doi.org/10.1016/j.ijhydene.2019.09.166

[9] G. Léonard, D. Giulini, D. Villarreal-Singer, Design and evaluation of a high-density energy storage route with CO2 re-use, water electrolysis and methanol synthesis, Comput. Aided Chem. Eng 38 (2016) 1797–802.

[10] S. Simon Araya, V. Liso, X. Cui, N. Li, J. Zhu, S. L. Sahlin, S. H. Jensen, M. P. Nielsen, S. K. Kær, A review of the methanol economy: the fuel cell route, Energies 13 (3) (2020) 596.

[11] S. T. Yong, C. W. Ooi, S. P. Chai, X. S. Wu, Review of methanol reforming-Cu-based catalysts, surface reaction mechanisms, and reaction schemes, International Journal of Hydrogen Energy 38 (22) (2013) 9541–9552. doi:10.1016/j.ijhydene.2013.03.023.
URL https://dx.doi.org/10.1016/j.ijhydene.2013.03.023

[12] W. H. Chen, Y. Q. Su, B. J. Lin, J. K. Kuo, P. C. Kuo, Hydrogen production from partial oxidation and autothermal reforming of methanol from a cold start in sprays, Fuel 287 (2021) 1–9.

[13] B. A. Peppley, J. C. Amphlett, L. M. Kearns, R. F. Mann, Methanol–steam reforming on Cu/ZnO/Al2O3. Part 1: the reaction network, Applied Catalysis A: General 179 (1-2) (1999) 21–29. doi:10.1016/s0926-860x(98)00298-1.
URL https://dx.doi.org/10.1016/s0926-860x(98)00298-1

[14] B. A. Peppley, J. C. Amphlett, L. M. Kearns, R. F. Mann, Methanol–steam reforming on Cu/ZnO/Al2O3 catalysts. Part 2. A comprehensive kinetic model, Applied Catalysis A: General 179 (1-2) (1999) 31–49. doi:10.1016/s0926-860x(98)00299-3.
URL https://dx.doi.org/10.1016/s0926-860x(98)00299-3

[15] D. R. Palo, R. A. Dagle, J. D. Holladay, Methanol steam reforming for hydrogen production, Chemical reviews 107 (10) (2007) 3992–4021.

[16] C. Azenha, T. Lagarteira, C. Mateos-Pedrero, A. Mendes, Production of hydrogen from methanol steam reforming using cupd/zro2 catalysts–influence of the catalytic surface on methanol conversion and co selectivity, International Journal of Hydrogen Energy 46 (33) (2021) 17490–17499.

[17] V. Agarwal, S. Patel, K. K. Pant, H2 production by steam reforming of methanol over Cu/ZnO/Al2O3 catalysts: transient deactivation kinetics modeling, Applied Catalysis A: General 279 (1-2) (2005) 155–164. doi:10.1016/j.apcata.2004.10.026.
URL https://dx.doi.org/10.1016/j.apcata.2004.10.026

[18] C. I. Méndez, J. Ancheyta, F. Trejo, Modeling of Catalytic Fixed-Bed Reactors for Fuels Production by Fischer–Tropsch Synthesis, Energy & Fuels 31 (12) (2017) 13011–13042. doi:10.1021/acs.energyfuels.7b01431.
URL https://dx.doi.org/10.1021/acs.energyfuels.7b01431

[19] H. Purnama, T. Ressler, R. E. Jentoft, H. Soerijanto, R. Schlögl, R. Schomäcker, CO formation/selectivity for steam reforming of methanol with a commercial CuO/ZnO/Al2O3 catalyst, Applied Catalysis A: General 259 (1) (2004) 83–94. doi:10.1016/j.apcata.2003.09.013.
URL https://dx.doi.org/10.1016/j.apcata.2003.09.013

[20] B. M. Cruz, J. D. D. Silva, A two-dimensional mathematical model for the catalytic steam reforming of methane in both conventional fixed-bed and fixed-bed membrane reactors for the Production of hydrogen, Int J Hydrogen Energy 42 (2017) 23670–90.

[21] H. S. Fogler, Essentials of Chemical Reaction Engineering: Essenti Chemica Reactio Engi, Pearson Education, 2010.

[22] S. Pathak, A. Goswami, S. Upadhyayula, Kinetic modeling and simulation of catalyst pellet in the high temperature sulfuric acid decomposition section of iodine-sulfur process, International Journal of Hydrogen Energy 44 (59) (2019) 30850–30864.

[23] S. Saeidi, S. Najari, G. Gróf, F. Gallucci, Effect of operating conditions and effectiveness factor on hydrogenation of co2 to hydrocarbons, International Journal of Hydrogen Energy 44 (54) (2019) 28586–28602.

[24] A. A. Iordanidis, Mathematical modeling of catalytic fixed bed reactors, Twente University Press Enschede, The Netherlands, 2002.

[25] A. M. Lattanzi, M. B. Pecha, V. S. Bharadwaj, P. N. Ciesielski, Beyond the effectiveness factor: Multi-step reactions with intraparticle diffusion limitations, Chemical Engineering Journal 380 (2020) 122507.

[26] S. Hafeez, E. Aristodemou, G. Manos, S. M. Al-Salem, A. Constantinou, Modelling of packed bed and coated wall microreactors for methanol steam reforming for hydrogen production, RSC Advances 10 (68) (2020) 41680–41692. doi:10.1039/d0ra06834a.
URL https://dx.doi.org/10.1039/d0ra06834a

[27] X. Cui, S. K. Kær, A comparative study on three reactor types for methanol synthesis from syngas and CO2, Chemical Engineering Journal 393 (2020) 124632–124632. doi:10.1016/j.cej.2020.124632.
URL https://dx.doi.org/10.1016/j.cej.2020.124632

[28] M. Ziarati, M. A. G. Roozbahani, N. Khandan, New Method of Rigorous Modeling and CFD Simulation for Methanol—Steam Reforming in Packed-Bed Reactors, Chemical Engineering Communications 203 (10) (2016) 1359–1373. doi:10.1080/00986445.2016.1198333.
URL https://dx.doi.org/10.1080/00986445.2016.1198333

[29] A. O. Olatunde, O. A. Olafadehan, M. A. Usman, Computation of effectiveness factor for methanol steam reforming over Cu/ZnO/Al2O3 catalyst pellet, Applied Petrochemical Research 10 (1) (2020) 35–47. doi:10.1007/s13203-020-00244-w.
URL https://dx.doi.org/10.1007/s13203-020-00244-w

[30] R. Tesser, M. D. Serio, E. Santacesaria, Methanol steam reforming: A comparison of different kinetics in the simulation of a packed bed reactor, Chemical Engineering Journal 154 (1-3) (2009) 69–75. doi:10.1016/j.cej.2009.06.007.
URL https://dx.doi.org/10.1016/j.cej.2009.06.007

[31] J. Zhu, S. S. Araya, X. Cui, S. L. Sahlin, S. K. Kær, Modeling and Design of a Multi-Tubular Packed-Bed Reactor for Methanol Steam Reforming over a Cu/ZnO/Al2O3 Catalyst, Energies 13 (3) (2020) 610–610. doi:10.3390/en13030610.
URL https://dx.doi.org/10.3390/en13030610

[32] X. Zhuang, X. Xia, X. Xu, L. Li, Experimental investigation on hydrogen production by methanol steam reforming in a novel multichannel micro packed bed reformer, Int J Hydrogen Energy 45 (2020) 11024–11058.

[33] S. Sá, J. M. Sousa, A. Mendes, Steam reforming of methanol over a CuO/ZnO/Al2O3 catalyst, part I: Kinetic modelling, Chemical Engineering Science 66 (20) (2011) 4913–4921. doi:10.1016/j.ces.2011.06.063.
URL https://dx.doi.org/10.1016/j.ces.2011.06.063

[34] M. S. Herdem, M. Mundhwa, S. Farhad, F. Hamdullahpur, Multiphysics Modeling and Heat Distribution Study in a Catalytic Microchannel Methanol Steam Reformer, Energy & Fuels 32 (6) (2018) 7220–7234. doi:10.1021/acs.energyfuels.8b01280.
URL https://dx.doi.org/10.1021/acs.energyfuels.8b01280

[35] B. A. D. Peppley, A comprehensive kinetic model of methanol-steam reforming on cu/zno/al o catalyst, Ph.D. thesis, Royal Military College of Canada (1998).

[36] R. T. Driessen, S. R. Kersten, D. W. Brilman, A Thiele Modulus Approach for Nonequilibrium Adsorption Processes and Its Application to CO2 Capture, Industrial & Engineering Chemistry Research 59 (15) (2020) 6874–

6885. doi:10.1021/acs.iecr.9b05503.
URL https://dx.doi.org/10.1021/acs.iecr.9b05503

[37] G. Zhang, J. Zhao, Q. Wang, T. Yang, Q. Zhang, L. Zhang, Fast start-up structured cufemg/al2o3 catalyst applied in microreactor for efficient hydrogen production in methanol steam reforming, Chemical Engineering Journal (2021) 130644.

[38] F. Zhou, S. J. Andreasen, S. K. Kær, J. O. Park, Experimental investigation of carbon monoxide poisoning effect on a PBI/H3PO4 high temperature polymer electrolyte membrane fuel cell: Influence of anode humidification and carbon dioxide, International Journal of Hydrogen Energy 40 (43) (2015) 14932–14941. doi:10.1016/j.ijhydene.2015.09.056.
URL https://dx.doi.org/10.1016/j.ijhydene.2015.09.056

[39] S. Araya, S. Andreasen, S. Kær, Experimental Characterization of the Poisoning Effects of Methanol-Based Reformate Impurities on a PBI-Based High Temperature PEM Fuel Cell, Energies 5 (11) (2012) 4251–4267. doi:10.3390/en5114251.
URL https://dx.doi.org/10.3390/en5114251

[40] S. S. Araya, I. F. Grigoras, F. Zhou, S. J. Andreasen, S. K. Kær, Performance and endurance of a high temperature PEM fuel cell operated on methanol reformate, International Journal of Hydrogen Energy 39 (32) (2014) 18343–18350. doi:10.1016/j.ijhydene.2014.09.007.
URL https://dx.doi.org/10.1016/j.ijhydene.2014.09.007

Paper C

Comparison between 1D and 2D numerical models of a multi-tubular packed-bed reactor for methanol steam reforming

Jimin Zhu, Xiaoti Cui, Samuel Simon Araya

The paper has been submitted to International Journal of Hydrogen Energy, 2022.

Comparison between 1D and 2D numerical models of a multi-tubular packed-bed reactor for methanol steam reforming

Jimin Zhu*, Xiaoti Cui, Samuel Simon Araya

AAU Energy, Aalborg University, Pontoppidanstræde 111, 9220 Aalborg, Denmark

Abstract

The hydrogen-rich gas produced in-situ by methanol steam reforming (MSR) reactions significantly affects the performance and endurance of the high-temperature polymer electrolyte membrane (HT-PEM) fuel cell stack. A numerical study of MSR reactions over a $CuO/ZnO/Al_2O_3$ catalyst coupling with the heat and mass transfer performance in a co-current packed-bed reactor is conducted. The simulation results of a 1D and a 2D reactor model are compared, which indicates the importance of radial gradients in the catalyst bed. The effects of geometry and operating parameters on the steady-state performance of the reactor are investigated. The simulation results show that the increases in the inlet temperature of burner gas and the tube diameter significantly increase the radial temperature differences in reformer tubes. Moreover, with a methanol conversion approaching 100% or a relatively small tube diameter, the simplified 1D model can be used instead of the 2D model to estimate the reactor performance.

Keywords: methanol steam reforming, hydrogen production, packed-bed reactor, thermal behaviour, reactor modelling

1. Introduction

Hydrogen is a clean and renewable energy source that plays an essential role in hydrogen-based energy systems, especially in polymer electrolyte membrane (PEM) fuel cell systems. As we know, the PEM fuel cell is a compact electrochemical device that converts the chemical energy in hydrogen and oxygen to electrical energy with high energy efficiency and zero-pollutant emission. According to their ranges of

* Corresponding author

Email address: jzu@energy.aau.dk (Jimin Zhu)

operating temperature, PEM fuel cells can be classified into two categories. The low-temperature polymer electrolyte membrane (LT-PEM) fuel cell generally operates at a temperature below 373 K. This low operating temperature makes a rapid start-up possible but also leads to a high requirement for hydrogen purity. The high-temperature polymer electrolyte membrane (HT-PEM) fuel cell operates at $393 - 473$ K. By operating at a higher temperature, the HT-PEM fuel cell gets an improved tolerance towards carbon monoxide (CO) up to $3 - 5\%$ vol [1], making it suitable to be integrated with an in-situ hydrogen generation system without purification.

Methanol stands out among various hydrogen carriers because it is in liquid form under standard conditions and has a high hydrogen to carbon ratio (4: 1). The high energy density and stability of methanol at ambient conditions make it cheap and easy for long-term storage. In addition, methanol can be produced from renewable energies and captured carbon dioxide (CO_2), which benefits from the extensive studies of power-to-methanol technology [2–4]. Moreover, lower reforming temperature ($200 - 300$℃) than other carbon-based fuels such as methane ($800 - 1000$℃) also makes it suitable for stack integration with HT-PEM fuel cells [1,5]. Compared to other catalytic reactions for hydrogen production, such as methanol decomposition (MD) and partial oxidation of methanol (POM), the methanol steam reforming (MSR) process provides the highest concentration of hydrogen per mole of methanol [6]. Therefore, the on-board hydrogen generation by MSR becomes an efficient and practical option to fuel PEM fuel cells especially for vehicle propulsion. In this process, the methanol and water (steam) mixture is converted into a hydrogen-rich gas by chemical reactions occurring on the surface of catalysts. The three overall reactions for the catalytic MSR process can be written as [7,8]:

Methanol steam reforming (MSR) reaction:

$$CH_3OH + H_2O \leftrightarrow CO_2 + 3H_2 \qquad \Delta H = +49.7 \text{ (kJ mol}^{-1}\text{)} \tag{1}$$

Water-gas shift (WGS) reaction:

$$CO + H_2O \leftrightarrow CO_2 + H_2 \qquad \Delta H = -41.2 \text{ (kJ mol}^{-1}\text{)} \tag{2}$$

Methanol decomposition (MD) reaction:

$$CH_3OH \leftrightarrow CO + 2H_2 \qquad \Delta H = +90.2 \text{ (kJ mol}^{-1}\text{)} \tag{3}$$

The low-temperature reforming of methanol ($473 - 573$ K) is highly desired because it is easier to integrate with HT-PEM fuel cells and can result in a low CO concentration. Therefore, catalysts that provide good activity and fast kinetics at low temperatures are favoured for the MSR [4]. Cu-based catalysts like $Cu/ZnO/Al_2O_3$ are the most widely used commercial catalysts due to their cost-effectiveness, high activity, and selectivity. It is generally accepted that the active component on

$Cu/ZnO/Al_2O_3$ catalyst is copper. The catalyst's activity and selectivity mainly depend on the copper content and its dispersion on the catalyst's surface. Additionally, the effects of ZnO are to promote the reducibility of copper and increase the copper dispersion within the catalyst [9]. However, the biggest problem with the Cu-based catalysts is reported to be easily deactivated by thermal sintering at high operating temperatures [10]. Therefore, Al_2O_3 is used as a structural promoter that can increase copper dispersion and decrease the susceptibility to sintering [11].

The mechanism and kinetics of MSR have been extensively studied theoretically and experimentally [7,8,12]. Jiang et al. [13] derived a Langmuir–Hinshelwood (LH) rate expression for the MSR process based on only one type of active site. They neglected the WGS reaction because the competitive adsorption favoured methanol and methyl formate rather than CO. On the contrary, Lee et al. [14] considered the MD reaction to be negligible, and the CO was assumed to be only produced by the reverse water gas shift (rWGS) reaction. A Langmuir–Hinselwood rate expression was developed based on the assumption of two distinct types of active sites: one for adsorbed methoxy and the other for adsorbed hydrogen. The dehydrogenation of the adsorbed methoxy to the adsorbed oxymethylene was considered as the rate-determining step (RDS). Peppley et al. [7,8] developed a comprehensive model considering MSR, WGS, and MD reactions on a $CuO/ZnO/Al_2O_3$ catalyst. They proposed two distinct types of active sites: one is for the MD reaction, and another is for the MSR and WGS reactions. Moreover, they assumed that the hydrogen adsorption does not compete for the active sites on which the oxygen-containing species adsorb. More recently, Sá et al. [15] and Herdem et al. [16] compared several kinetic rate expressions of the MSR process over a commercial $CuO/ZnO/Al_2O_3$ catalyst. They found that a kinetic Langmuir-Hinshelwood model based on the work of Peppley et al. [7,8] presented the best agreement with their experimental data.

As the catalyst behaviour is strongly influenced by the reactor geometry and operating conditions, the development of a numerical model is essential to estimate the reformer performance and optimize the MSR process. Mainly tubular packed-bed reactors are designed to minimize undesired radial temperature gradients to operate as close to isothermal conditions as possible [17,18]. In these cases, a simplified 1D model can be used to evaluate and analyse the reactor performance without considering the radial heat and mass transfer. Chougule et al. [5] developed a 1D pseudo-homogeneous steady-state model using Engineering Equation Solver (EES) to analyse the MSR in a catalytic packed-bed tubular reactor. The simulation results presented a strong agreement with the experimental data. The effects of operating temperature and steam to carbon molar ratio (S/C) on the reformer performance were investigated. In our previous studies, a 1D pseudo-homogeneous model of a multi-tubular packed-bed reactor for MSR was developed using MATLAB® [19,20]. This model considered the reaction kinetics, pressure drop, effectiveness factors, and heat and mass balances in both the tube and shell sides. The axial and radial dispersion in the plug-flow reactor was assumed to be absent. The model was used to obtain the optimal reactors

configuration and operating conditions. However, very few details of the mass and heat transfer phenomena in the reactor tubes were presented, which may lead to lower accuracy in predicting the formation of hotspots and the reformer performance, especially for large-diameter reactors [21].

The simultaneous heat consumption (endothermic reactions) and heat exchanges with the shell-side gas cause the temperature gradients along the length and across the cross-section of the reactor tube. Moreover, because of the heterogeneous catalytic reactions associated with transport processes, non-adiabatic reactors will also produce radial concentration gradients. Therefore, it is necessary to consider the effect of variations in temperature and concentrations across the reactor in some cases to avoid substantial miscalculations. Ma et al. [22] carried out a 2D pseudo-homogeneous model for a plant-scale fixed-bed MSR reactor using MATLAB®. Effects of the tube diameter and operating conditions on the reactor's hydrogen production and temperature profile were investigated. However, the effectiveness factors for MSR reactions were neglected with a 5-6 mm particle size in this study. Karim et al. [23] developed a 2D pseudo-homogeneous model to study the heat transfer limitation and the catalyst performance in different diameter reactors. It was observed that the decrease of reactor diameter could enhance the methanol conversion of the MSR reactor but also lead to a higher pressure drop through the catalyst bed. Bayat et al. [24] developed a comprehensive 2D steady-state model for a multi-tubular packed-bed MSR reactor. A triple-objective optimization of the MSR reformer was performed using the non-dominated sorting genetic algorithm – II as a robust optimization approach. The optimal operating conditions were determined in this study which enhanced almost 47.04% of hydrogen mass fraction in the MSR reactor. However, the effect of reactor configuration and the formation of hot spots were not considered in this study.

Approach like computational fluid dynamics (CFD) allows more detailed investigations on the reactor performance by developing 3D models for tubular packed-bed reactor for MSR [25,26]. Zhuang et al. [27] established a 3D numerical model to study the heat and mass transfer characteristics as well as the MSR reactions in a multichannel reactor. The effects of S/C, weight hourly space velocity (WHSV), operating temperature, and catalyst layer thickness on the reformer performance were evaluated and discussed. However, it is computationally expensive and time consuming for building such complex models. In addition to the above mentioned methods, Zheng et al. [28] used an error backpropagation algorithm and a genetic algorithm to establish a mathematical model for different microreactors and optimize the methanol steam reforming performance of a cylindrical microreactor. Justesen et al. [29] proposed a method for predicting the constituents of the reformed gas from a methanol steam reformer in a reformed methanol fuel cell system. The method is based on Adaptive Neuro-Fuzzy-Inference-System, which was trained on experimental data. One significant drawback of these methods is that a big amount of data is needed for training. In addition, since catalyst degradation is not included in

these models, an increase in the mean absolute error could be observed when the experiment is repeated after a period of operation.

The present work aims to compare the simulation results of the simplified 1D model and the 2D model in predicting the performance of the reformer. The packed-bed shell-and-tube reactor is designed to be integrated with a 5 kW HT-PEM fuel cell stack. A numerical study of the heat and mass transfer processes coupled with the reaction kinetics in the catalyst bed is conducted. The co-current stream of burner gas on the shell side, which is non-isothermal, is modelled as the external heat source using a 1D model. The simulation results of the comprehensive kinetic model and effectiveness factors show a good agreement with the experimental data obtained in a small-scale packed-bed reactor for the MSR process. The 1D steady-state, pseudo-homogeneous model of the plug-flow reactor is developed without considering the radial heat and mass transfer. In comparison, the resistances to heat and mass transfer in the radial direction of reactor tubes are highlighted and introduced in a 2D model. Therefore, the temperature and composition gradients in both axial and radial coordinates are considered. The effects of the geometry and operating conditions are investigated on the reformer performance in terms of the distributions of methanol conversion, CO mole fraction, operating temperature, and maximum temperature difference. A parametric study is also carried out to obtain the optimal operating conditions for the reformer.

2. Modelling approach

The integration of hydrogen production in-situ by MSR with HT-PEM fuel cells is already used in power supplies. In this study, a shell-and-tube reformer for MSR, which consists of baffles and tubes inside a cylindrical shell, is illustrated in Figure 1. The reactor shell is usually surrounded by thermal insulation materials to avoid significant heat loss. Reactor tubes, packed with porous cylindrical catalyst pellets, are arranged in an equilateral triangle tube bundle, and installed inside the shell. The gas from the burner passes through the shell side of the reformer, thereby providing an external heat source to drive the reactions in the catalyst bed. Methanol and water mixture are evaporated before entering the reformer. This gas mixture flows through the catalyst bed in the tube side, where the reforming reactions occur on the solid surface of catalyst particles.

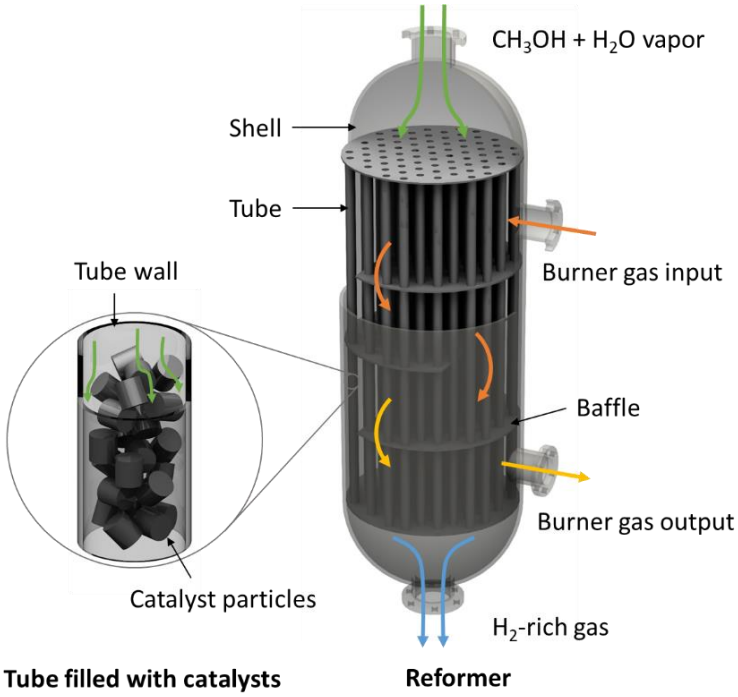

Figure 1. Structure of a multi-tubular packed-bed reactor for methanol steam reforming

The mathematical model was derived by adopting the following assumptions in this study:

- The absence of axial heat and mass dispersion (plug flow).
- The absence of temperature and concentration gradients between the external surface of the particles and the adjacent layer of fluid (pseudo-homogeneous).
- Temperature of burner gas as a function of the reactor length in the non-adiabatic case.
- The absence of temperature and concentration gradients within catalyst particles.
- Uniform size, porosity, and activity of catalyst particles.
- Constancy of bed void fraction throughout the entire catalyst bed.

- Effectiveness factors for main reactions as a function of Thiele modulus.
- No deactivation of catalysts due to the sintering of catalysts and carbon deposition on the catalytic surface.

2.1. Reaction kinetics

A comprehensive kinetic model developed by Peppley et al. [7,8] was used in this study to describe the MSR process over the $Cu/ZnO/Al_2O_3$ catalyst. The Langmuir-Hinshelwood model is based on assumptions: (a) hydrogen and oxygen-containing species adsorb on different active sites; (b) the active site for the MD reaction is different from that for the MSR and WGS reaction; (c) the rate-determining step (RDS) for both the MSR reaction and the MD reaction is the dehydrogenation of adsorbed methoxy groups; (d) the RDS for the WGS reaction is the formation of an intermediate formate species. The rates r_j (mol $m^{-2}s^{-1}$) for three key reactions (MSR, WGS and MD) involved in the process can be expressed as:

$$r_R = \frac{k_R K^*_{CH_3O^{(1)}} \left(p_{CH_3OH}/p^{\frac{1}{2}}_{H_2}\right)\left(1 - p^3_{H_2} p_{CO_2}/K^{eq}_R p_{CH_3OH} p_{H_2O}\right) C^T_{S_1} C^T_{S_{1a}}}{\left(1 + K^*_{CH_3O^{(1)}}\left(p_{CH_3OH}/p^{\frac{1}{2}}_{H_2}\right) + K^*_{HCOO^{(1)}} p_{CO_2} p^{\frac{1}{2}}_{H_2} + K^*_{OH^{(1)}}\left(p_{H_2O}/p^{\frac{1}{2}}_{H_2}\right)\right)\left(1 + \right.} \quad (4)$$

$$r_W = \frac{k_W K^*_{OH^{(1)}} \left(p_{CO} p_{H_2O}/p^{\frac{1}{2}}_{H_2}\right)\left(1 - p_{H_2} p_{CO_2}/K^{eq}_W p_{CO}\, p_{H_2O}\right) C^{T^2}_{S_1}}{\left(1 + K^*_{CH_3O^{(1)}}\left(p_{CH_3OH}/p^{\frac{1}{2}}_{H_2}\right) + K^*_{HCOO^{(1)}} p_{CO_2} p^{\frac{1}{2}}_{H_2} + K^*_{OH^{(1)}}\left(p_{H_2O}/p^{\frac{1}{2}}_{H_2}\right)\right)^2}, \quad (5)$$

$$r_D = \frac{k_D K^*_{CH_3O^{(2)}} \left(p_{CH_3OH}/p^{\frac{1}{2}}_{H_2}\right)\left(1 - p^2_{H_2} p_{CO}/K^{eq}_D p_{CH_3OH}\right) C^T_{S_2} C^T_{S_{2a}}}{\left(1 + K^*_{CH_3O^{(2)}}\left(p_{CH_3OH}/p^{\frac{1}{2}}_{H_2}\right) + K^*_{OH^{(2)}}\left(p_{H_2O}/p^{\frac{1}{2}}_{H_2}\right)\right)\left(1 + K^{\frac{1}{2}}_{H^{(2a)}} p^{\frac{1}{2}}_{H_2}\right)}, \quad (6)$$

where k_j ($m^2\, s^{-1} mol^{-1}$) and K^{eq}_j are the rate constant and the equilibrium constant of reaction j, respectively; K^* ($bar^{-0.5}$) is the adsorption coefficient; p_i (bar) is the partial pressure of component i ($i = CO_2, CO, H_2, CH_3OH$ and H_2O); and $C^T_{S_1}$, $C^T_{S_{1a}}$, $C^T_{S_2}$ and $C^T_{S_{2a}}$ (mol m^{-2}) are the total site concentrations of site '1', '1a', '2', and '2a', respectively, where the '1' and '1a' sites are assumed to be active for the MSR and WGS reactions and the '2' and '2a' sites are for the MD reaction. Further details on these constants can be found in the Appendix.

The production rate of component i per time per mass of catalyst r_i (mol s^{-1} (kg of catalyst)$^{-1}$) can be calculated considering the rate expression r_j (mol s^{-1} m^{-2}) for individual reaction j and the surface area per unit mass of fresh catalyst S_c (m^2 kg^{-1}) [19]:

$$r_{CO_2} = (r_R + r_W)S_c, \tag{7}$$

$$r_{CO} = (r_D - r_W)S_c, \tag{8}$$

$$r_{H_2} = (3r_R + 2r_D + r_W)S_c, \tag{9}$$

$$-r_{CH_3OH} = (r_R + r_D)S_c, \tag{10}$$

$$-r_{H_2O} = (r_R + r_W)S_c, \tag{11}$$

2.2. Effectiveness factor

The effectiveness factor, η, is estimated as the ratio of the actual reaction rate in the catalyst particle to the calculated rate that exist in the absence of diffusion limitations [30]. In our previous study [20], the Thiele modulus method and the intraparticle distribution methods were applied and compared for predicting the effectiveness factors for main reactions of MSR. The comparison results indicated that both methods could be used when the diameter of cylindrical catalyst particles is set to 1.5 mm. For a first-order reaction in a spherical catalyst pellet, a easier expression for the effectiveness factor η as a function of the Thiele modulus can be derived as [31]:

$$\eta = \frac{3}{\phi_1^2}(\phi_1 \coth \phi_1 - 1) \tag{12}$$

where ϕ_1 is the Thiel modulus for a first-order reaction, which can be expressed as:

$$\phi_1^2 = \frac{r_{jp}\rho_c r_p^2 S_c}{D_{i,\mathrm{ep}} c_{ip}} \tag{13}$$

where r_{jp} (mol m^{-2} s^{-1}) and c_{ip} (mol m^{-3}) are the rate of reaction j and the concentration of component i, respectively, if the entire interior surface is exposed; r_p (m) is the radius of the catalyst pellet; and ρ_c (kg m^{-3}) is the density of catalyst bed.

Catalysts in the form of porous cylindrical particles with an aspect ratio of 1 are utilized in this study. For a non-spherical particle, the volume-equivalent particle diameter d_p^v (m), defined as the diameter of a single spherical pellet having the same volume as the non-spherical particle, is usually used instead of its actual diameter

d_p (m). For a cylinder catalyst with a diameter of d (m) and a height of h (m), the volume-equivalent particle diameter d_p^v can be calculated by:

$$d_p^v = \left(\frac{6V_{pa}}{\pi}\right)^{\frac{1}{3}} = d\left(\frac{3}{2}\frac{h}{d}\right)^{\frac{1}{3}} \tag{14}$$

where V_{pa} is the volume of a single catalyst particle (m^3).

2.3. Steady-state mass and heat balance equations on the tube side

To predict the MSR performance in the plug-flow reactor, two steady-state models (1D and 2D) considering the typical transport and chemical reaction phenomena in the catalyst bed are developed in this study. For the 1D model, it is assumed that no axial mixing occurs in the plug-flow reactor, and the radial gradients are neglected. For the 2D model, the heat and species dispersions in the radial direction are considered. Therefore, uniform temperature and concentration distributions in the cross-section can be estimated.

One-dimensional plug flow

Mass balance

$$u_s \frac{dc_i}{dz} = \eta_i \rho_c r_i \tag{15}$$

where c_i (mol m^{-3}) is the concentration of component i in the fluid, u_s (m s^{-1}) is the superficial velocity of the fluid in axial direction, ρ_c (kg m^{-3}) is the density of catalyst bed, and r_i (mol s^{-1} (kg of catalyst)$^{-1}$) is the rate of consumption or formation of the component i.

Heat balance

$$u_s \rho_f C_{p,f} \frac{dT_t}{dz} = a_s U_t \Delta T + \sum \eta_j \rho_c \left(-\Delta H_j\right) r_j S_c \tag{16}$$

where $C_{p,f}$ (J $\mathrm{kg}^{-1}\mathrm{K}^{-1}$) is the specific heat specific heat of pseudo-fluid, ρ_f (kg m^{-3}) is the pseudo-fluid density, ΔH_j (J mol^{-1}) is the enthalpy change of reaction j, ΔT (K) is the temperature difference between shell side and tube side at length z (m), a_s (m^2 m^{-3}) is the surface-to-volume ratio of a single tube, U_t ($\mathrm{Wm}^{-2}\mathrm{K}^{-1}$ or $\mathrm{Js}^{-1}\mathrm{m}^{-2}\mathrm{K}^{-1}$) is the overall heat transfer coefficient in the tube side.

Two-dimensional plug flow

Figure 2 displays the schematic diagram of a single reactor tube, which is axisymmetric with the inner radius of tubes R_t and the length L. The 2D steady-state model in the catalyst bed is solved in axi-symmetrical cylindrical coordinates with variations of temperature and concentrations in both the axial (z) and radial (r) directions. The variations in the angular direction around the central axis are assumed to be negligible. In this rectangular region, the lower boundary is the line of symmetry (centreline). At the upper boundary, the heat transfer from the shell side to the tube side is accounted for and modelled by using the film theory. The uniform initial conditions are given at the left boundary. The mass and heat balances in the packed-bed reactor with con-current configuration are expressed by the following equations:

Mass balance

$$u_s \frac{\partial c_i}{\partial z} = D_{er}\left(\frac{\partial^2 c_i}{\partial r^2} + \frac{1}{r}\frac{\partial c_i}{\partial r}\right) + \eta_i \rho_c r_i \tag{17}$$

Energy balance

$$u_s \rho_f C_{p,f} \frac{\partial T_t}{\partial z} = \lambda_{er}\left(\frac{\partial^2 T_t}{\partial r^2} + \frac{1}{r}\frac{\partial T_t}{\partial r}\right) + \sum \eta_j \rho_c \left(-\Delta H_j\right) r_j S_c \tag{18}$$

where D_{er} ($\mathrm{m^2\ s^{-1}}$) is the effective radial mass diffusion coefficient, λ_{er} ($\mathrm{W\ m^{-1}\ K^{-1}}$) is the effective thermal conductivity in the radial direction. Further details on the calculation of D_{er} and λ_{er} can be found in the Appendix.

Initial and boundary conditions

$$c = c_0, T = T_0 \qquad \text{at } z = 0, 0 \le r \le R_t$$

$$\frac{\partial c}{\partial r} = 0 \qquad \text{at } r = 0 \text{ and } r = R_t$$

$$\frac{\partial T}{\partial r} = 0 \qquad \text{at } r = 0, \text{ all } z$$

$$\frac{\partial T}{\partial r} = -\frac{U_t}{\lambda_{er}}(T - T_s) \qquad \text{at } r = R_t$$

In addition, all the tubes within the tube bundle are subject to the same external conditions at the same cross section of the reformer. It means that the temperature profiles within a single tube can represent the performance of all the tubes in the reformer.

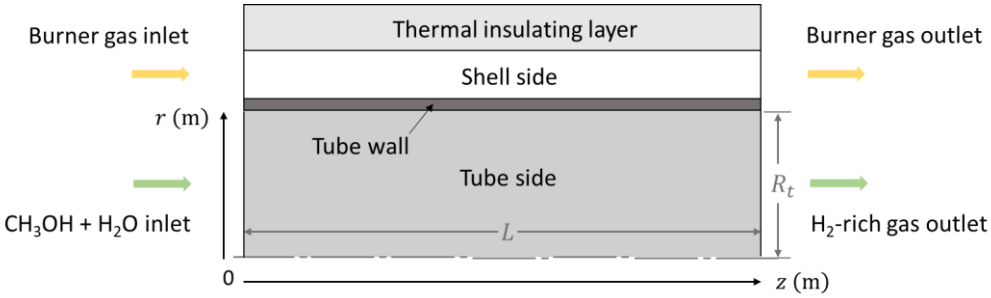

Figure 2. Schematic representation of a single reactor tube packed with $CuO/ZnO/Al_2O_3$ catalyst used for the simulation study

2.4. Steady-state heat balance equation on the shell side

The reactor tubes are heated by a co-current stream of burner gas on the shell side. The temperature of the burner gas on the shell side was considered as non-isothermal in the axial direction of the reactor. A simple 1D steady-state model is developed in this study to consider the heat balance for the burner gas:

$$u_{s,s}\rho_{f,s}C_{p,s}\frac{dT_s}{dz} = a_s U_s \Delta T \tag{19}$$

whereU_s (W $m^{-2}K^{-1}$ or J $s^{-1}m^{-2}K^{-1}$) is the overall heat transfer coefficient in the shell side, $C_{p,s}$ (J $kg^{-1}K^{-1}$) is the specific heat of burner gas, $\rho_{f,s}$ (kg m^{-3}) is the density of burner gas, $u_{s,s}$ (m s^{-1}) is the superficial velocity of the burner gas in the axial direction, D_o (m) is the outer diameter of the tubular reactor, and N_t is the number of tubes in the reformer. The values of parameters in the reformer models can be found in the Table 1. Further details on the model equations can be found in the Appendix.

Table 1. Properties of catalyst and geometric parameters of the reactor

Parameter	Value
Density of catalyst bed, ρ_c (kg m^{-3})	1300
BET area, S_c (m^2 kg^{-1})	102000
Average pore diameter Å, (m)	6.4×10^{-9}
Void fraction of catalyst bed, ϕ	0.37
Diameter of cylindrical catalyst particle, d_p (m)	0.0015

Height of cylindrical catalyst particle, h (m)	0.0015
Site concentrations of site '1', $C_{S_1}^T$ (mol m^{-2})	7.5×10^{-6}
Site concentrations of site '1a', $C_{S_{1a}}^T$ (mol m^{-2})	1.5×10^{-5}
Site concentrations of site '2', $C_{S_2}^T$ (mol m^{-2})	7.5×10^{-6}
Site concentrations of site '2a', $C_{S_{2a}}^T$ (mol m^{-2})	1.5×10^{-5}
Number of reactor tubes, N_t	9
Inner diameter of the tubular reactor, D_i (m)	0.0243
Outer diameter of the tubular reactor, D_o (m)	0.0263
Tube pitch, p_t (m)	0.039
Number of baffle plates, N_b	4
Spacing between baffle plates, p_b (m)	0.12
Length of the reactor, L (m)	0.48
Area fraction of baffle plate that is window, f_b (for 25% baffle plate)	0.1955

2.5. Simulation method

The model of MSR, in which the concentrations of the major gas species and the temperature in catalyst bed were defined as functions of radial and axial coordinates, was implemented in MATLAB®. For the 2D model, heat and mass transfer phenomena are described by a set of partial differential equations (PDEs). Therefore, the method of lines (MOL) was applied to solve the PDEs in this study [32]. The basic idea of this MOL was to replace the PDE spatial (boundary-value) partial derivatives with algebraic approximations by using finite differences (FDs). In this model, a second-order upwind FD approximation was applied. Thus, with only one remaining independent variable, in this case, a system of ordinary differential equations (ODEs) approximated the original PDE system. Besides, the PDE solver *pdepe* in MATLAB® can also be used for solving the system of PDEs.

3. Experiments

Experiments for the MSR process were performed at the atmospheric pressure in a small-scale reactor. The reactor was loaded with 3.66 g of the commercial $CuO/ZnO/Al_2O_3$ catalyst in a volume of 3.6 mL. Cylindrical catalyst particles with a diameter of 1.5 mm and an aspect ratio of 1 were used. The feeding rate of the liquid methanol/water mixture from the fuel tank was measured and controlled by a mass

flow controller. This mixture was first pumped into an evaporator to be evaporated and preheated. Then the high temperature vapor of fuel passed through the catalyst bed which was supported by a fine mesh grid. The reactor was surrounded by thermal insulation materials and was heated by electric heaters outside the reactor. Therefore, this packed-bed reactor was assumed isothermal. The temperature in the fixed bed was regulated by PID control of the electric heaters to maintain it within a specific range. Two thermocouples were used to measure the inlet and outlet temperatures of the reactor, and the average temperature was regarded as the temperature of the catalyst bed. The main components of the reformate stream from the MSR reactor were analyzed by the gas analyzer (SIEMENS FIDMAT 6 for CH_3OH, CALOMAT 6 for H_2, and ULTRAMAT 6 for CO and CO_2).

The catalyst bed was firstly flushed with the N_2/H_2 mixture for 1 hour, where the volumetric flow rates of H_2 and N_2 were $0.1\ \mathrm{cm^3\ min^{-1}}$ and $2\ \mathrm{cm^3\ min^{-1}}$, respectively. The N_2/H_2 mixture was introduced to the catalyst bed to reduce CuO to Cu (the main active component in the catalyst). The operating temperature for this reduction process was controlled in the range of $433 - 493\ \mathrm{K}$. Therefore, the reduction reaction rate can be kept relatively low so as to avoid any sintering of catalyst. Then, the liquid methanol/water mixture was pumped into the reformer by a dosing pump. The reforming process was carried out with different operating temperatures at 493 K, 513 K and 533 K and the ratio of catalyst weight to the molar flow rate of methanol (W/F_{CH_3OH}) in the range of $44 - 263\ \mathrm{kg\ s\ mol^{-1}}$. The variation of W/F_{CH_3OH} was achieved by changing the volumetric flow rate of liquid methanol from 0.051 to $0.308\ \mathrm{cm^3\ min^{-1}}$ while keeping a fixed loading of catalysts. The S/C was selected to be 1.3 to maximize the methanol conversion without wasting much energy in water evaporation [33].

4. Result and discussion

4.1. Model validation

Kinetic study for MSR process has been made over a commercial $CuO/ZnO/Al_2O_3$ catalyst. Typically, catalyst kinetic experiments are performed on finely powdered catalysts [5,17]. Hence, obvious diffusion limitations within catalyst particles can be avoided, and the collected reaction rates could be referred to as intrinsic. However, cylindrical catalyst particles with a diameter of 1.5 mm were used in this study. Inside the porous catalyst pellets, chemical reactions and heat and mass transfer take place simultaneously. Effectiveness factors were introduced to qualify the effect of intraparticle diffusion limitations on reaction rates. The effectiveness factor describes the relationship between the diffusive reaction rate and the reaction rate in the bulk stream. In this study, the effectiveness factors for MSR, WGS and MD reactions were calculated as a function of Thiele modulus.

To validate the kinetic model and the effectiveness factors, an experiment was conducted in a small-scale reactor loaded with catalyst particles for MSR process. Comparisons between the simulation results and the experimental results on the methanol conversion and the mole fraction of CO were carried out with varying W/F_{CH_3OH} in the range of $0-300$ kg s mol^{-1} and operating temperatures at 493 K, 513 K and 533 K. The operating parameters for simulations and experiments are shown in Table 2.

Table 2. Geometric and operating parameters for simulations and experiments

Parameter	Value
Mass of catalyst (g)	3.66
Volume of catalyst bed (mL)	3.6
Feeding rate of methanol liquid (cm^3 min^{-1})	$0.051-0.308$
Temperature (K)	$493-533$
Pressure (bar)	1
Steam/methanol ratio (mol/mol)	1.3
Catalyst size (mm)	1.5×1.5
W/F_{CH_3OH} (kg s mol^{-1})	$0-300$

As shown in Figure 3 (a), there is a good agreement on methanol conversion between the experimental data and the simulation results of the kinetic model with effectiveness factors. A percentage discrepancy less than 5.4% is observed. The methanol conversion increases with increasing temperature in catalyst bed. In addition, increasing the W/F_{CH_3OH} can also improve the methanol conversion. Figure 3 (b) shows the experimental and simulated mole fractions of CO in the reformate gas with varying temperature in catalyst bed and W/F_{CH_3OH}. As we can see, the CO production increases with respect to W/F_{CH_3OH} in the reactor. As the operating temperature increases, the mole fraction of CO in the reformate gas also increases. This model can approximately predict the CO concentration under most conditions, except for two data points in the experimental results that lie outside the overall distribution of the dataset. These two unexpected jumps of CO concentration occurred when the W/F_{CH_3OH} was 259 kg s mol^{-1}and the temperature was 493 K and 513 K. It might be caused by the non-uniform distributions of temperature and concentration in the reactor. Therefore, the local reaction rates were affected during the experiment. Another possible explanation is that, a very small feeding rate of liquid methanol (0.051 cm^3 min^{-1}) was introduced to obtain a large value of $W/F_{CH_3OH}=$

259 kg s mol^{-1} in the experiment. This small feeding rate of reactants intensified the effect of non-uniform distributions, which hence led to the oscillations of CO production at the large W/F_{CH_3OH} value. Morever, the large void fraction near the reactor wall was also a possible reason. However, the radial void fraction profile has not been considered in the model.

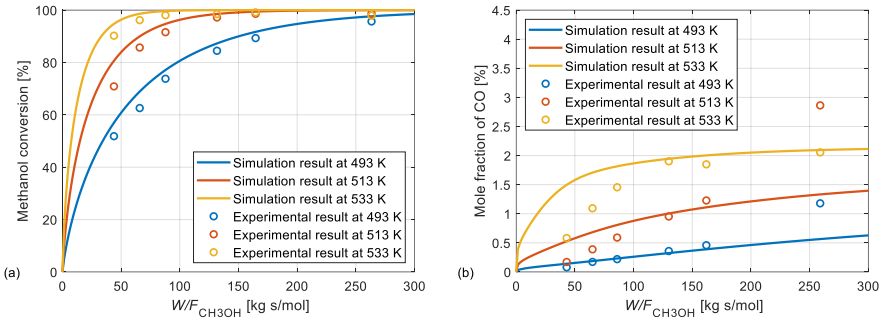

Figure 3. Comparison of the (a) methanol conversion and the (b) mole fraction of CO between simulation results and experimental results under different W/F_{CH_3OH} and operating temperatures of catalyst bed

4.2. Temperature and methanol conversion distribution

In the 1D steady-state model, the absence of radial variations in velocity, concentration, temperature, and reactions is assumed in the tubular packed-bed reactor. To better understand the temperature and concentration gradients in both the axial and radial directions in the catalyst bed, the 2D model is developed using the axisymmetric coordinate system. Figure 4 (a) shows the simulated profile of temperature, while Figure 4 (b) shows the corresponding profile of methanol conversion in a single reactor tube obtained with the 2D model. In this case, the reformer consists of 9 reactor tubes with the length $L = 0.48$ m, the inner tube diameter $D_t = 32.6$ mm and the thickness of tube wall $x_w = 2$ mm; the catalyst contact time is $W/F_{CH_3OH} = 135$ kg s mol^{-1}; the inlet temperature of the fuel vapor is set as $T_f = 433\ K$ and the inlet temperature of burner gas is set as $T_b = 673$ K. As shown in Figure 4 (a), the temperature near the tube wall ($r = R_t$), where the external heat source was applied, shows a sharp increase followed by a gradual drop in the axial direction. The sharp temperature increase is caused by the fact that the inlet temperature of reactants (433 K) is below the inlet temperature of external burner gas (673 K). The substantial temperature difference results to a significant heat transfer from the burner gas. The subsequent temperature drop is due to the strongly endothermic reactions occurring along the catalyst bed. Another reason for this temperature drops along the reactor length is the temperature decrease of the external burner gas. The observed temperature gradients in the radial direction reflect the combined effects of the radial thermal conductivity and the strongly endothermic reactions. A gradual increase of

temperature is observed along the central axial line of the tube ($r = 0$ mm). The temperature, then, reaches a relatively stable state, while the radial temperature distribution becomes nearly uniform. Therefore, a hot spot is most likely to appear near the tube wall and in the early or middle part of the reactor. Under the given conditions, the temperature reaches up to 522.44 K at the hot spot, and the average temperature at the reactor outlet is observed to be 483.00 K. As shown in Figure 4 (b), the methanol conversion increases along the reactor while the reforming reactions of methanol occur in catalyst bed. The average methanol conversion at the reactor outlet reaches 71.36%.

Figure 5 shows the comparison of temperature profiles as a function of the radius and length of a single reactor tube predicted by the 1D model and the 2D model. The geometric and operating conditions are the same as in Figure 4. As shown in Figure 5 (a), no temperature gradient occurs in the radial direction according to the results of the 1D model. Hence, only a short and rapid temperature increase in the axial direction is observed near the reformer inlet. Afterwards, the temperature increases gradually and eventually reaches a stable state. In comparison, a temperature contour plot obtained by the 2D model is shown in Figure 5 (b). The radial temperature gradients can be observed, owing to the consideration of effective radial thermal conductivity of catalyst bed. Therefore, the variations of bed temperature can be accurately modelled by the 2D model.

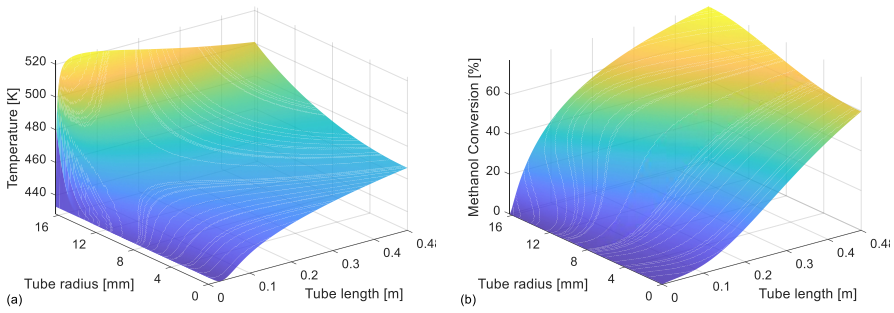

Figure 4. Surface plot of (a) temperature and (b) methanol conversion in a single reactor tube by the 2D model: $D_t = 32.6$ mm, $W/F_{CH_3OH} = 135$ kg s mol^{-1}, $T_b = 673$ K.

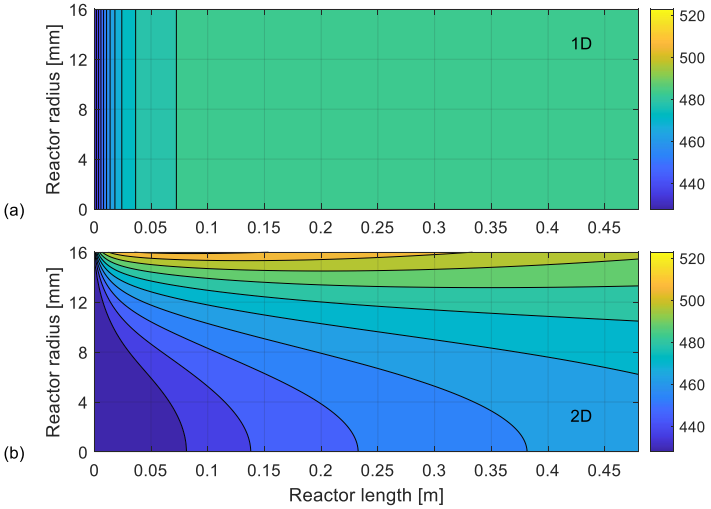

Figure 5. Contour plot of temperature in a single reactor tube by the (a) 1D model and the (b) 2D model: $D_t = 32.6$ mm, $W/F_{CH_3OH} = 135$ kg s mol^{-1}, $T_b = 673$ K.

4.3. Effects of geometry and operation conditions

For a 5 kW HT-PEM fuel cell system, the liquid methanol-water mixture with a feeding rate at 4.225 L h^{-1} and a steam-to-carbon ratio (S/C) at 1.3 is provided for hydrogen production. According to the negative effects of impurities on the fuel cells, it is also necessary to limit the mole fraction of CO and methanol to (or less than) $2-3\%$ vol and 3% vol in the reformate gas, respectively [34–36]. Therefore, the performance of the reformer should be evaluated to satisfy the requirements of the HT-PEM fuel cell system.

4.3.1. Effect of the inlet temperature of burner gas T_b

The effects of the inlet temperature of burner gas and W/F_{CH_3OH} on axial profiles of methanol conversion and mole fraction of CO are investigated. As shown in Figure 6, the inlet temperature of burner gas T_b is assigned to be 573 K, 673 K and 773 K, the inner tube diameter D_t is 32.6 mm, the W/F_{CH_3OH} is set as 135 kg s mol^{-1}, while other parameters are kept the same as those of the case in Figure 4. For the results of 2D model in Figure 6 (a) and (b), the average methanol conversion at the reactor outlet increases dramatically from 42.0 % to 92.8 %, the average mole fraction of CO produced also increases from 0.35% to 1.20%, while the inlet temperature of burner gas is elevated from 573 K to 773 K. Correspondingly, for the results of 1D model, the methanol conversion at the reactor outlet is improved from 48.6% to 99.3%, and the mole fraction of CO is observed to increase from 0.35% to 1.32%. The distinctions of the methanol conversion and the mole fraction of CO between these

two models are owing to the different distributions of temperature calculated in the catalyst bed.

To better understand of the overall temperature activity within the reactor tubes, the axial profiles of the maximum temperature difference of reactor tubes in the radial direction ΔT $(T_{max} - T_{min})$ are illustrated in Figure 6 (c). In addition, the temperature profiles along the reactor tube at different radial positions are provided in Figure 7 (a) (b) (c). Due to the radial heat and mass transfer resistances, the thermal behaviour in the catalyst bed evaluated by the 2D model can be different from that which is evaluated by the 1D model. As shown in Figure 7 (a) (b) (c), the temperature distribution in the catalyst bed is non-uniform and has a sharp rise to the peak near the tube wall in the entrance region. The formation of hot spots could induce the potential risk of local catalyst deactivation due to the thermal sintering. When the inlet temperature of burner gas increases from 573 K to 773 K, the hot-spot temperature observed near the tube wall ($r/R_t = 1$) increases from 490.25 K to 552.40 K. This increase of hot-spot temperature could be caused by the increase of the inlet temperature difference between the shell side and the tube side. It is also observed that the temperature gradient from the tube wall ($r/R_t = 1$) to the tube centre ($r/R_t = 0$) exists in the catalyst bed due to the endothermic reactions and the resistance to heat transfer. As shown in Figure 6 (c), the elevated inlet temperature of burner gas tends to increase the non-uniformity of the radial temperature distribution in the packed catalyst bed. The reason could be that the higher heat flux amplifies the static temperature gradient along the radial direction.

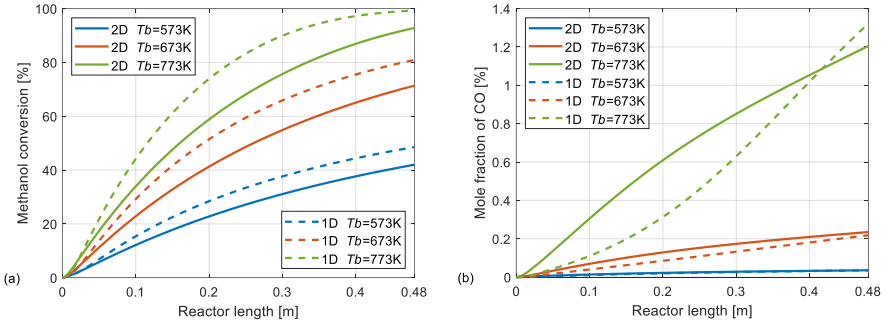

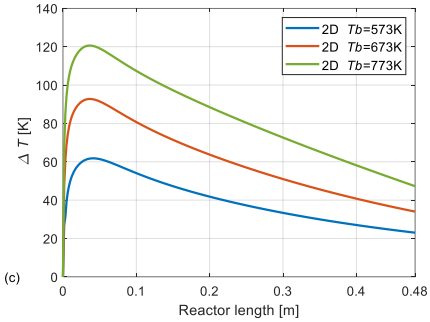

Figure 6. Effect of the inlet temperature of burner gas T_b on axial profiles of (a) the methanol conversion, (b) the mole fraction of CO, and (c) the maximum temperature difference in radial direction ΔT $(T_{max} - T_{min})$: $D_t = 32.6$ mm, $W/F_{CH_3OH} = 135$ kg s mol^{-1}.

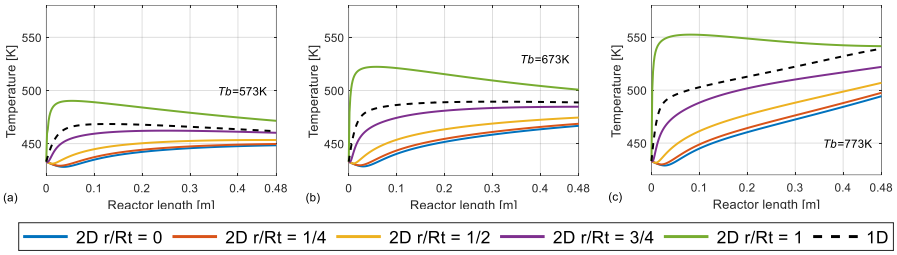

Figure 7. Effect of the inlet temperature of burner gas T_b on axial temperature profiles at different radial positions (r/R_t): $D_t = 32.6$ mm, $W/F_{CH_3OH} = 135$ kg s mol^{-1}.

4.3.2. Effect of the contact time W/F_{CH_3OH}

The increase in W/F_{CH_3OH} means that the surface area of the catalyst in contact with the reactants is increased. Figure 8 (a) and (b) represent the effects of the W/F_{CH_3OH} on the methanol conversion and the mole fraction of CO along the reactor length, respectively. In this figure, the inlet temperature of burner gas is fixed at 723 K. By varying the tube number in the reformer while keeping both the tube diameter D_t and tube length L constant, the value of W/F_{CH_3OH} is changed without changing the fuel feeding rate. Based on the results of the 2D model, the average methanol conversion at the reactor outlet is improved from 83.7% to 99.7% as the W/F_{CH_3OH} increases from 135 to 406 kg s mol^{-1}. Correspondingly, the average mole fraction of CO at the reactor outlet increases from 0.56% to 1.17%. For the results of the 1D model, the methanol conversion increases from 93.2% to 100%, and the mole fraction of CO increases from 0.55% to 1.36% while the W/F_{CH_3OH} increases from 135 to 406 kg s mol^{-1}. These results indicate that the rate of the MSR reactions is increased

due to the higher values of W/F_{CH_3OH}. It is also shown that, when the methanol conversion is approaching 100%, the differences in methanol conversion and mole fraction of CO between these two models become less significant. Figure 8 (c) represents the effects of the W/F_{CH_3OH} on axial profiles of the maximum temperature difference in the radial direction ΔT $(T_{max} - T_{min})$ of reactor tubes. The change in W/F_{CH_3OH} is proved to have no significant effect on the highest value of the maximum temperature difference in the radial direction ΔT $(T_{max} - T_{min})$ over the entire reactor.

Figure 9 demonstrates the comparison of temperature profiles obtained from the 1D model and the 2D model under different W/F_{CH_3OH}. It is shown that the radial temperature gradient at the reactor outlet becomes shallower with the increase of W/F_{CH_3OH}. Figure 8 (a) indicates that, as the W/F_{CH_3OH} increases to 406 kg s mol^{-1}, the rate of methanol steam reforming reactions becomes greater. The increased reaction rates lead to a higher methanol conversion in the catalyst bed. While the methanol conversion approaches 100%, the speed of the endothermic reactions gradually slows down. Therefore, the temperature in the radial direction can become more uniformly distributed at the reactor outlet, as shown in Figure 9 (c).

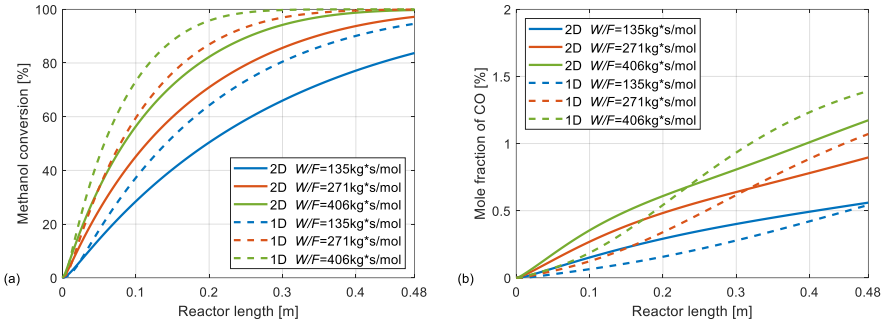

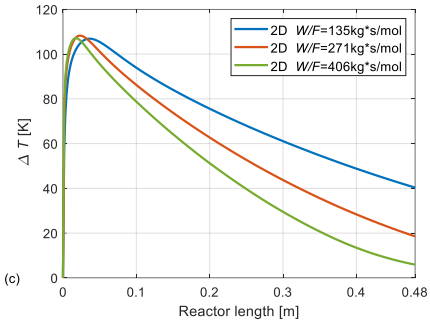

Figure 8. Effect of the W/F_{CH_3OH} on axial profiles of (a) the methanol conversion, (b) the mole fraction of CO, and (c) the maximum temperature difference in radial direction ΔT $(T_{max} - T_{min})$: $D_t = 32.6$ mm, $T_b = 723$ K.

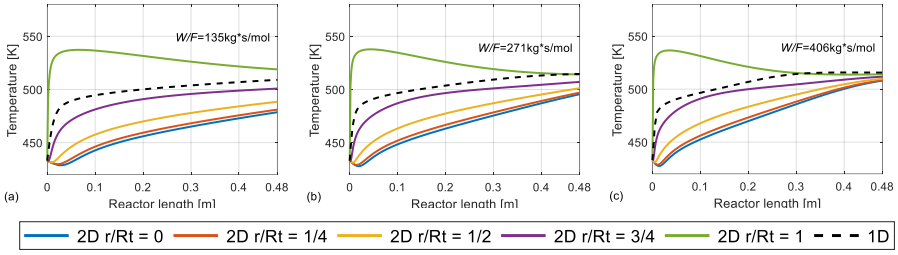

Figure 9. Effect of the W/F_{CH_3OH} on axial temperature profiles at different radial positions (r/R_t): $D_t = 32.6$ mm, $T_b = 723$ K.

4.3.3. Effect of the tube diameter D_t

The successful design of a polite-scale MSR reformer is to obtain a high methanol conversion and low CO concentration in the hydrogen-rich reformate. In this section, the possibility of adopting fewer reactor tubes with a larger diameter in the multi-tubular packed-bed reformer is investigated in this study. For a reformer with a fixed catalyst inventory, both the number of tubes and the number of welding operations can be inversely proportional to the square of the diameteir. Therefore, the use of large-diameter tubes would reduce the investment cost of the reactor [37]. However, the inner diameter of reactor tubes can profoundly affect the temperature non-uniformity in the catalyst bed. Hence, the 2D model was developed in this study to estimate the effect of tube diameter D_t on the reformer performance.

Figure 10 (a) and (b) represent the effect of the tube diameter D_t and the inlet temperature of burner gas T_b on the methanol conversion and the mole fraction of CO of the reformer. As the inner tube diameter D_t increases from 13.3 mm to 42.1 mm, the number of tubes should be changed from 60 to 6 to maintain the same overall

catalyst load in the reactor. Therefore, the W/F_{CH_3OH} is kept constant at $271\ \mathrm{kg\ s\ mol^{-1}}$. Figure 10 (c) and (d) represent the effect of the tube diameter D_t, and the W/F_{CH_3OH} on the methanol conversion and the mole fraction of CO of the reformer. In Figure 10 (c) and (d), the inlet temperature of burner gas is kept constant at $673\ \mathrm{K}$, while the W/F_{CH_3OH} is set as $135 - 405\ \mathrm{kg\ s\ mol^{-1}}$. It is observed that a decrease in diameter leads to an increase in the methanol conversion for this externally heated multi-tubular reactor. The reason could be that, for a small tube diameter, the external heat source can provide sufficient heat throughout the reactor during operation, allowing for relatively ideal diffusion and chemical kinetics to reach a higher methanol conversion. Figure 10 also indicates that, in these cases, a smaller difference of the methanol conversion (less than 1.74%) between these two models can be observed when the tube diameter decreases to $13.3\ \mathrm{mm}$ due to the smaller radial temperature gradients. Therefore, in these cases, it could be concluded that it is sufficient to use a simpler 1D model to estimate the performance of a steam methane reforming reactor when the tube diameter is less than $13.3\ \mathrm{mm}$.

Figure 10 (e) shows the effect of the tube diameter on axial profiles of the maximum temperature difference in the radial direction ΔT $(T_{max} - T_{min})$ of reactor tubes. In these cases, the W/F_{CH_3OH} is kept constant at $271\ \mathrm{kg\ s\ mol^{-1}}$, and the inlet temperature of burner gas is set at $723\ \mathrm{K}$. It is apparent from this figure that the increased tube diameter tends to increase the non-uniformity of the radial temperature distribution in the packed catalyst bed. When the inner diameter is $15.5\ \mathrm{mm}$, the maximum radial temperature difference of $97.5\ \mathrm{K}$ is developed in the reactor tube; and when the inner diameter is increased to $42.1\ \mathrm{mm}$, a maximum radial temperature difference of $116.1\ \mathrm{K}$ is observed.

To better understand the overall temperature activity within the reactor tubes, the temperature profiles estimated by the 1D model and the 2D model are provided in Figure 11. Due to the endothermicity of the MSR process, the lowest temperature appears at the centre of the reactor tube. Besides, the hot spot arises near the tube wall in the entrance region of the reactor due to the peak heat flux. It is also visible in Figure 11 (a), (b) and (c) that large tube diameters can enhance the radial temperature gradients when analysing the temperature profiles in the catalyst bed. This phenomenon implies that the heat transfer will be more efficient with the decrease of tube diameter because the surface area per volume is increased. Hence, the temperature is distributed more evenly over the catalyst bed, and the efficiency of the chemical reactions is improved. These results agree with the findings of Davieau et al. [38] that the reactor configurations with a smaller diameter allow a relatively ideal diffusion and nearly complete methanol conversion in catalyst beds.

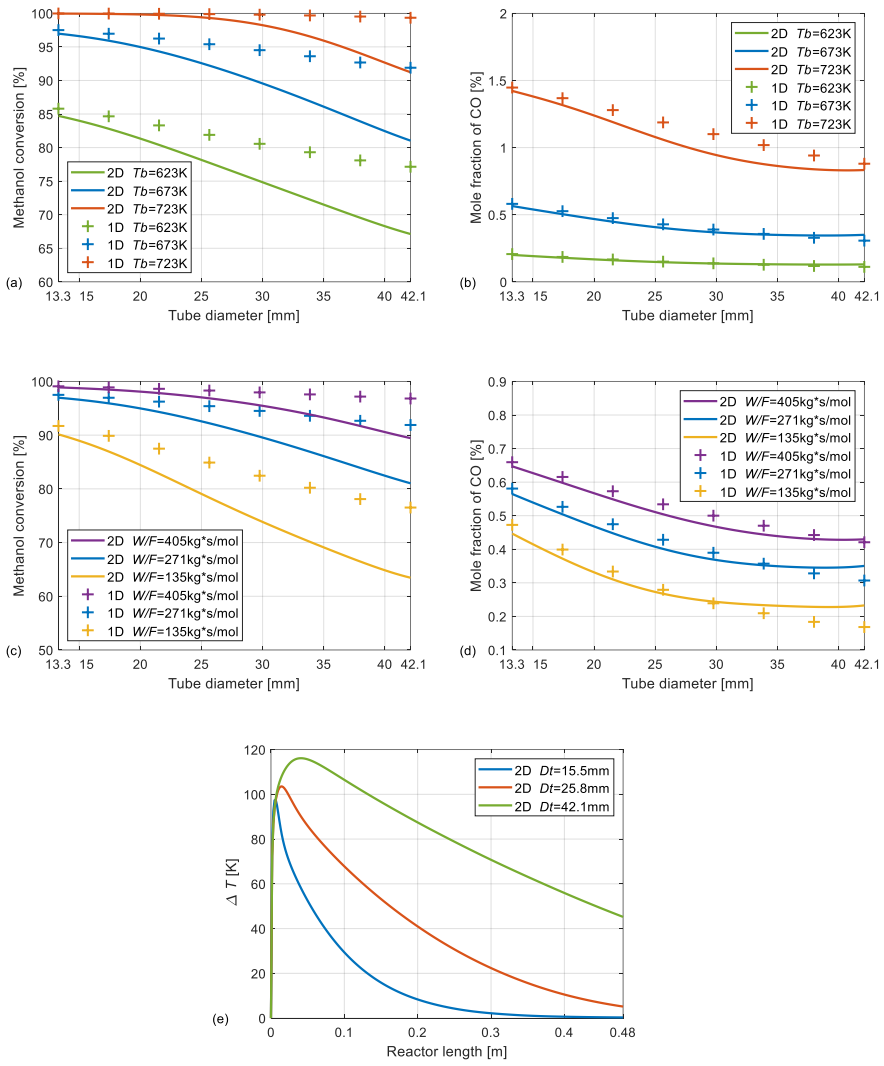

Figure 10. Effect of the tube diameter D_t and the inlet temperature of burner gas T_b on axial profiles of (a) the methanol conversion, and (b) the mole fraction of CO: $W/F_{CH_3OH} = 271$ kg s mol^{-1}; effect of the tube diameter D_t and the W/F_{CH_3OH} on axial profiles of (c) the methanol conversion, and (d) the mole fraction of CO: $T_b = 673$ K; and effect of the tube diameter D_t on axial profiles of (e) the maximum temperature difference in radial direction ΔT $(T_{max} - T_{min})$: $T_b = 723$ K, $W/F_{CH_3OH} = 271$ kg s mol^{-1}.

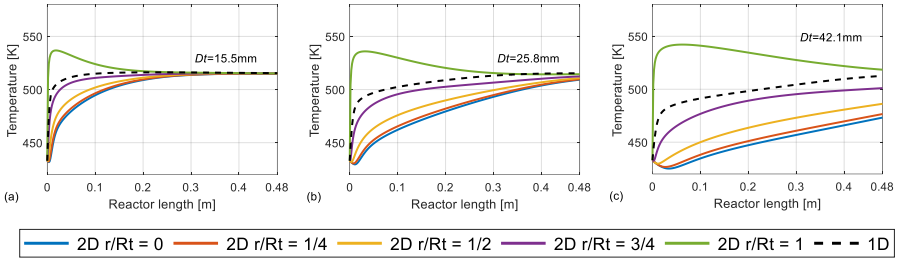

Figure 11. Effect of the tube diameter D_t on axial temperature profiles at different radial positions (r/R_t): $T_b = 723$ K, $W/F_{CH_3OH} = 271$ kg s mol^{-1}.

4.4. Optimization of operating parameters

The operating parameters are sensitive parameters for achieving the optimal performance of the reformer. In this study, the effects of the inlet temperature of burner gas and the W/F_{CH_3OH} are evaluated by characterizing the performance of the reformer using the 2D model. In Figure 12, the tube diameter is set to 18.2 mm. By choosing a smaller tube diameter, a more uniform radial temperature distribution can be obtained in the catalyst bed. The number of tubes changes from 5 to 40. Correspondingly, the W/F_{CH_3OH} varies from 42 kg s mol^{-1} to 506 kg s mol^{-1}. As shown in Figure 12 (a), the methanol conversion can be improved by adopting a higher W/F_{CH_3OH} and a higher inlet temperature of burner gas. The effects of the inlet temperature of burner gas and the W/F_{CH_3OH} on the the mole fraction of CO are illustrated in Figure 12 (b). The results indicate that the increase in the inlet temperature of burner gas and in the W/F_{CH_3OH} will lead to higher CO concentrations in the reformate gas. As shown in Figure 12 (c), the increase in the inlet temperature of burner gas significantly increases the maximum hot-spot temperature within the catalyst bed.

Based on the demands of an HT-PEM fuel cell system, the reformer should reach a methanol conversion of over 99%. Moreover, the mole fraction of CO in the reformate gas should be limited to a reasonable level (e.g., 1% vol). To prevent the risk of hot-spot formation and subsequent catalyst thermal sintering in certain areas of the reactor, the temperature in catalyst beds should always be kept below the safe limit of 553 K. As shown in Figure 12 (a), there is a region S that is enclosed by the line of "1% mode fraction of CO" and the line of "99% methanol conversion". Therefore, the operating conditions in the region S can simultaneously bring the methanol conversion to above 99% and the mole fraction of CO to lower than 1% vol in the reformer. Compared with the contour plot in Figure 12 (c), the operating conditions within the region S also ensure that the maximum hot-spot temperature in the catalyst bed will not exceed the limits of its endurable temperature (553 K). Therefore, it can be concluded that the inlet temperature of burner gas in the range of 671 K to 694 K could be recommended when the W/F_{CH_3OH} is set to 506 kg s mol^{-1}. Additionally, when the

W/F_{CH_3OH} is set to 216 kg s mol^{-1}, the inlet temperature of burner gas could be set to 714 K (point A) to minimize the overall catalyst loading in the reformer.

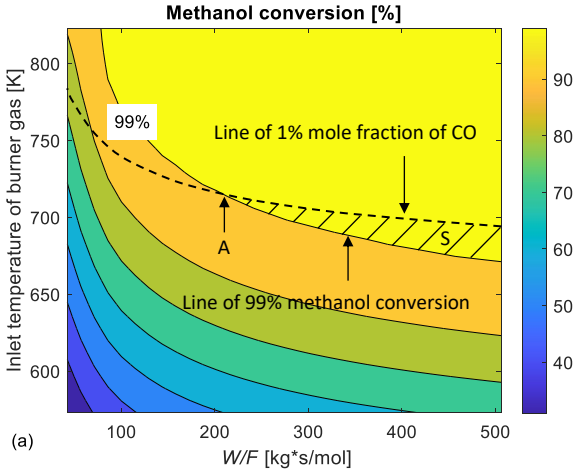

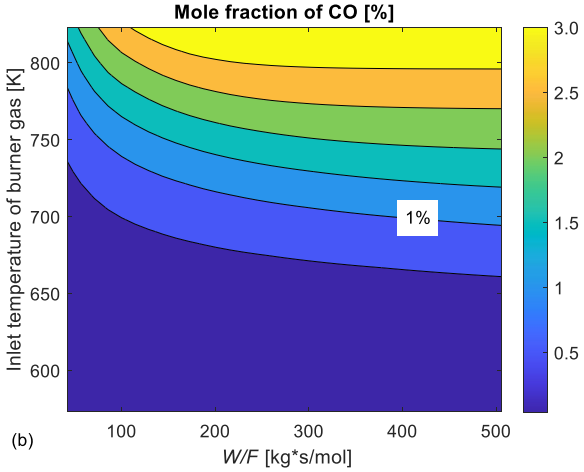

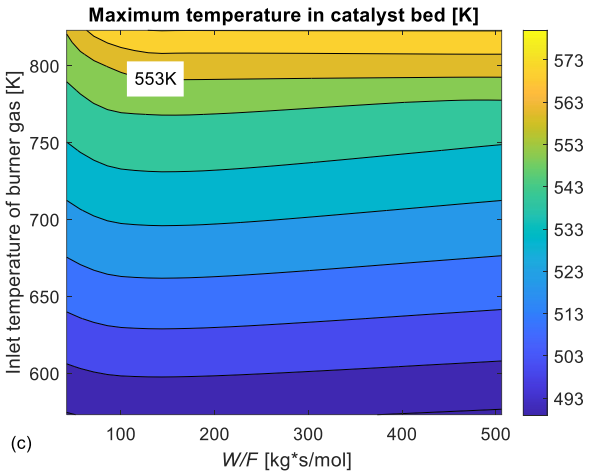

Figure 12. Effect of the W/F_{CH_3OH} and the inlet temperature of burner gas on the (a) methanol conversion, (b) mole fraction of CO and (c) maximum hot-spot temperature of the reformer: $D_t = 18.2$ mm.

5. Conclusions

The numerical study comparing a 1D model and a 2D model for the methanol steam reforming process in a multi-tubular packed-bed reformer has been conducted. The steady-state 1D and 2D models have considered the heat and mass transfer processes coupled with the reaction kinetics in the catalyst bed. Besides, the burner gas flowing through the shell side has been modelled as an external heat source using a 1D non-isothermal model. The simulation results of the kinetic model and effectiveness factors have shown good agreement with the experimental data obtained in a small-scale packed-bed reactor for the MSR process. The 1D model has been developed without considering the radial heat and mass transfer. In comparison, the resistances to the radial heat and mass transfer of the reformer tube have been highlighted and introduced in the 2D model.

The simulation results revealed that the overall methanol conversion and the mole fraction of CO in the reformate gas were enhanced by the elevated inlet temperatures of burner gas and W/F_{CH_3OH}. It was also recognized that the overall methanol conversion and the mole fraction of CO in the reformate gas increased as the tube diameter became larger with a fixed catalyst loading in the reformer. Comparisons of the 1D and the 2D models indicated the importance of radial gradients from the centreline to the tube wall in packed-bed reactors. The study showed that the increases in the inlet temperature of burner gas and the tube diameter significantly amplified the maximum radial temperature differences in the catalyst bed. Hot spots were formed near the tube wall in the entrance region. The increase of the inlet temperature of

burner gas resulted in a significant increase of the hot-spot temperature inside the catalyst bed. Moreover, with a methanol conversion approaching 100% or a relatively small tube diameter, the simple 1D plug-flow model could be used instead of the 2D model to estimate the performance of the pilot-scale MSR reactor in these cases.

Acknowledgements

The research leading to these results has received funding from the Chinese scholarship council (CSC) and from the Danish Energy Technology Development and Demonstration Program (EUDP) through the Commercial BReakthrough of Advanced fuel cells (COBRA Drive) project, grant number 64018-0118.

Nomenclature

a_s	surface-to-volume ratio, $m^2\ m^{-3}$
C_p	specific heat capacity, $J\ kg^{-1}K^{-1}$
$C_{S_m}^T$	total catalyst surface concentration of site m, $mol\ m^{-2}$
c_i	concentration of species i, $mol\ m^{-3}$
D_{er}	effective radial diffusion coefficient, $m^2\ s^{-1}$
D_i	inner diameter of reactor tube, m
D_o	outer diameter of reactor tube, m
d_p	diameter of catalyst particle, m
d_p^v	volume-equivalent particle diameter, m
E_j	activation energy for rate constant of reaction j, $kJ\ mol^{-1}$
f_b	area fraction of baffle plate that is window
h_s	heat transfer coefficient in the shell-side film, $W\ m^{-2}\ K^{-1}$
h_t	heat transfer coefficient in the tube-side film, $W\ m^{-2}\ K^{-1}$
K_i^*	adsorption coefficient of surface species i
K_j^{eq}	reaction equilibrium constant of reaction j

k_j	rate constant for reaction, $m^2 s^{-1} mol^{-1}$
M_i	molecular weight of species i, kg mol^{-1}
N_b	number of baffle plates
N_t	number of tubes
P	operating pressure, Pa
p_b	spacing between baffle plates, m
p_i	partial pressure of species i, Pa
p_t	tube pitch, m
R	universal gas constant, J $K^{-1} mol^{-1}$
r	radial coordinate, m
r_i	production rate of species i, mol $s^{-1} kg^{-1}$
r_j	reaction rate of reaction j, mol $m^{-2} s^{-1}$
r_p	radius of the catalyst pellet, m
S_c	surface area per unit mass of fresh catalyst, m^2 kg^{-1}
S/C	steam to carbon molar ratio
T	operating temperature, K
T_b	inlet temperature of burner gas, K
U_t	heat transfer coefficient in the tube side, W $m^{-2} K^{-1}$
U_s	heat transfer coefficient in the shell side, W $m^{-2} K^{-1}$
u_s	superficial velocity, m s^{-1}
W/F_{CH_3OH}	ratio of catalyst weight to the molar flow rate of methanol, kg s mol^{-1}

x_i	mole fraction of species i
z	axial position in the tube, m

Greek symbols

μ	viscosity, Pa s
ΔH_j	reaction heat of reaction j, J mol^{-1}
ΔT	temperature difference, K
η	effectiveness factor
λ_{er}	effective radial thermal conductivity, W m^{-1} K^{-1}
ρ	density, kg m^{-3}
ϕ	void fraction of catalyst bed
ϕ_1	Thiel modulus for a first-order reaction

Superscript and subscript

c	catalyst bed
er	effective radial parameter
i	species including CH_3OH, H_2O, H_2, CO_2 and CO
j	reactions including MSR, WGS and MD
p	catalyst particle
x, y, x	coordinates

References

[1] Özcan O, Akın AN. Thermodynamic analysis of methanol steam reforming to produce hydrogen for HT-PEMFC: An optimization study. Int J Hydrogen Energy 2019;44:14117–26. https://doi.org/10.1016/j.ijhydene.2018.12.211.

[2] Léonard G, Giulini D, Villarreal-Singer D. Design and evaluation of a high-density energy storage route with CO2 re-use, water electrolysis and methanol synthesis. Comput. Aided Chem. Eng., vol. 38, Elsevier; 2016, p. 1797–802.

[3] Cui X, Kær SK, Nielsen MP. Energy analysis and surrogate modeling for the green methanol production under dynamic operating conditions. Fuel 2022;307. https://doi.org/10.1016/j.fuel.2021.121924.

[4] Araya SS, Liso V, Cui X, Li N, Zhu J, Sahlin SL, et al. A review of the methanol economy: The fuel cell route. Energies 2020;13. https://doi.org/10.3390/en13030596.

[5] Chougule A, Sonde RR. Modelling and experimental investigation of compact packed bed design of methanol steam reformer. Int J Hydrogen Energy 2019;44:29937–45. https://doi.org/10.1016/j.ijhydene.2019.09.166.

[6] Chen WH, Su YQ, Lin BJ, Kuo JK, Kuo PC. Hydrogen production from partial oxidation and autothermal reforming of methanol from a cold start in sprays. Fuel 2021;287:1–9. https://doi.org/10.1016/j.fuel.2020.119638.

[7] Peppley BA, Amphlett JC, Kearns LM, Mann RF. Methanol-steam reforming on Cu/Zno/Al2O3. Part 1: The reaction network. Appl Catal A Gen 1999;179:21–9. https://doi.org/10.1016/S0926-860X(98)00298-1.

[8] Peppley BA, Amphlett JC, Kearns LM, Mann RF. Methanol–steam reforming on Cu/ZnO/Al2O3 catalysts. Part 2. A comprehensive kinetic model. Appl Catal A Gen 1999;179:31–49. https://doi.org/10.1016/S0926-860X(98)00299-3.

[9] Yong ST, Ooi CW, Chai SP, Wu XS. Review of methanol reforming-Cu-based catalysts, surface reaction mechanisms, and reaction schemes. Int J Hydrogen Energy 2013;38:9541–52. https://doi.org/10.1016/j.ijhydene.2013.03.023.

[10] Sá S, Silva H, Brandão L, Sousa JM, Mendes A. Catalysts for methanol steam reforming-A review. Appl Catal B Environ 2010;99:43–57. https://doi.org/10.1016/j.apcatb.2010.06.015.

[11] Palo DR, Dagle RA, Holladay JD. Methanol steam reforming for hydrogen production. Chem Rev 2007;107:3992–4021. https://doi.org/10.1021/cr050198b.

[12] Pashchenko D. Effect of the geometric dimensionality of computational

domain on the results of CFD-modeling of steam methane reforming. Int J Hydrogen Energy 2018;43:8662–73. https://doi.org/10.1016/j.ijhydene.2018.03.183.

[13] Jiang CJ, Trimm DL, Wainwright MS, Cant NW. Kinetic mechanism for the reaction between methanol and water over a Cu-ZnO-Al2O3 catalyst. Appl Catal A, Gen 1993;97:145–58. https://doi.org/10.1016/0926-860X(93)80081-Z.

[14] Lee JK, Ko JB, Kim DH. Methanol steam reforming over Cu/ZnO/Al2O3 catalyst: Kinetics and effectiveness factor. Appl Catal A Gen 2004;278:25–35. https://doi.org/10.1016/j.apcata.2004.09.022.

[15] Sá S, Sousa JM, Mendes A. Steam reforming of methanol over a CuO/ZnO/Al2O3 catalyst, part I: Kinetic modelling. Chem Eng Sci 2011;66:4913–21. https://doi.org/10.1016/j.ces.2011.06.063.

[16] Herdem MS, Mundhwa M, Farhad S, Hamdullahpur F. Multiphysics Modeling and Heat Distribution Study in a Catalytic Microchannel Methanol Steam Reformer. Energy and Fuels 2018;32:7220–34. https://doi.org/10.1021/acs.energyfuels.8b01280.

[17] Iulianelli A, Ribeirinha P, Mendes A, Basile A. Methanol steam reforming for hydrogen generation via conventional and membrane reactors: A review. Renew Sustain Energy Rev 2014;29:355–68. https://doi.org/10.1016/j.rser.2013.08.032.

[18] Vidal Vázquez F, Simell P, Pennanen J, Lehtonen J. Reactor design and catalysts testing for hydrogen production by methanol steam reforming for fuel cells applications. Int J Hydrogen Energy 2016;41:924–35. https://doi.org/10.1016/j.ijhydene.2015.11.047.

[19] Zhu J, Araya SS, Cui X, Sahlin SL, Kær SK. Modeling and design of a multi-tubular packed-bed reactor for methanol steam reforming over a Cu/ZnO/Al2O3 catalyst. Energies 2020;13:610.

[20] Zhu J, Araya SS, Cui X, Kær SK. The role of effectiveness factor on the modeling of methanol steam reforming over CuO/ZnO/Al2O3 catalyst in a multi-tubular reactor. Int J Hydrogen Energy 2022. https://doi.org/https://doi.org/10.1016/j.ijhydene.2021.12.223.

[21] Rase HF. Fixed-bed reactor design and diagnostics: gas-phase reactions. Butterworth-Heinemann; 2013.

[22] Ma H, Zhou M, Ying W, Fang D. Two-dimensional modeling of a plant-scale fixed-bed reactor for hydrogen production from methanol steam reforming. Int J Hydrogen Energy 2016;41:16932–43. https://doi.org/10.1016/j.ijhydene.2016.07.117.

[23] Karim A, Bravo J, Datye A. Nonisothermality in packed bed reactors for steam reforming of methanol. Appl Catal A Gen 2005;282:101–9. https://doi.org/10.1016/j.apcata.2004.12.006.

[24] Bayat M, Garmroodi Asil A. Robust multi-objective optimization of methanol steam reforming for boosting hydrogen production. Int J Hydrogen Energy 2021;46:29795–811. https://doi.org/10.1016/j.ijhydene.2021.06.164.

[25] Wang F, Li L, Liu Y. Effects of flow and operation parameters on methanol steam reforming in tube reactor heated by simulated waste heat. Int J Hydrogen Energy 2017;42:26270–6. https://doi.org/10.1016/j.ijhydene.2017.09.002.

[26] Dixon AG. Local transport and reaction rates in a fixed bed reactor tube: Endothermic steam methane reforming. Chem Eng Sci 2017;168:156–77. https://doi.org/10.1016/j.ces.2017.04.039.

[27] Zhuang X, Xu X, Li L, Deng D. Numerical investigation of a multichannel reactor for syngas production by methanol steam reforming at various operating conditions. Int J Hydrogen Energy 2020;45:14790–805. https://doi.org/10.1016/j.ijhydene.2020.03.207.

[28] Zheng T, Zhou W, Yu W, Ke Y, Liu Y, Liu R, et al. Methanol steam reforming performance optimisation of cylindrical microreactor for hydrogen production utilising error backpropagation and genetic algorithm. Chem Eng J 2019;357:641–54. https://doi.org/10.1016/j.cej.2018.09.129.

[29] Justesen KK, Andreasen SJ, Shaker HR, Ehmsen MP, Andersen J. Gas composition modeling in a reformed methanol fuel cell system using adaptive neuro-fuzzy inference systems. Int J Hydrogen Energy 2013;38:10577–84. https://doi.org/10.1016/j.ijhydene.2013.06.013.

[30] Cruz BM, da Silva JD. A two-dimensional mathematical model for the catalytic steam reforming of methane in both conventional fixed-bed and fixed-bed membrane reactors for the Production of hydrogen. Int J Hydrogen Energy 2017;42:23670–90. https://doi.org/10.1016/j.ijhydene.2017.03.019.

[31] Fogler HS. Essentials of Chemical Reaction Engineering: Essenti Chemica

Reactio Engi. Pearson Education; 2010.

[32] Schiesser WE, Griffiths GW. A compendium of partial differential equation models: method of lines analysis with Matlab. Cambridge University Press; 2009.

[33] Zhuang X, Xia X, Xu X, Li L. Experimental investigation on hydrogen production by methanol steam reforming in a novel multichannel micro packed bed reformer. Int J Hydrogen Energy 2020;45:11024–34. https://doi.org/10.1016/j.ijhydene.2020.02.034.

[34] Zhou F, Andreasen SJ, Kær SK, Park JO. Experimental investigation of carbon monoxide poisoning effect on a PBI/H3PO4 high temperature polymer electrolyte membrane fuel cell: Influence of anode humidification and carbon dioxide. Int J Hydrogen Energy 2015;40:14932–41. https://doi.org/10.1016/j.ijhydene.2015.09.056.

[35] Araya SS, Andreasen SJ, Kær SK. Experimental characterization of the poisoning effects of methanol-based reformate impurities on a PBI-based high temperature PEM fuel cell. Energies 2012;5:4251–67. https://doi.org/10.3390/en5114251.

[36] Araya SS, Grigoras IF, Zhou F, Andreasen SJ, Kær SK. Performance and endurance of a high temperature PEM fuel cell operated on methanol reformate. Int J Hydrogen Energy 2014;39:18343–50. https://doi.org/10.1016/j.ijhydene.2014.09.007.

[37] Montebelli A, Visconti CG, Groppi G, Tronconi E, Kohler S. Optimization of compact multitubular fixed-bed reactors for the methanol synthesis loaded with highly conductive structured catalysts. Chem Eng J 2014;255:257–65. https://doi.org/10.1016/j.cej.2014.06.050.

[38] Davieau DD, Erickson PA. The effect of geometry on reactor performance in the steam-reformation process. Int J Hydrogen Energy 2007;32:1192–200. https://doi.org/10.1016/j.ijhydene.2006.11.029.

SUMMARY

Fuel cells, especially the high temperature polymer electrolyte membrane (HT-PEM) fuel cell, are attracting more attention in backup power, transportation and stationary applications. The HT-PEM fuel cells convert hydrogen directly into electricity, making it possible to have a higher efficiency than conventional generators. Nevertheless, technical problems in hydrogen storage and transportation are still the essential obstacles to the widespread adoption of hydrogen powered fuel cell systems. As an alternative method, the methanol steam reforming (MSR) process has been considered promising for the in-situ hydrogen generation in HT-PEM fuel cell systems. The hydrogen-rich gas produced in-situ by the MSR process has a significant impact on the performance and durability of the HT-PEM fuel cell stack. Hence, the performance of the reformer should be studied. Special attentions should be paid to the contents of carbon monoxide and methanol in the reformate. The experiments for the reformer provide us the direct and concise results of the system. However, it can be costly and time-consuming, especially when multiple variables should be tested. The tested results could also be affected by certain objective factors such as unnoticed catalyst deactivation, errors in measuring devices (e.g., incorrect fitting of the measuring scale), and inappropriate research design. The mathematical modelling of packed bed reactors allows a deep insight into the chemical reactions and transport processes in the reactor. A multi-tubular packed-bed MSR reformer for hydrogen production is designed to be integrated with a 5 kW HT-PEM fuel cell stack in this study. A co-current stream of burner gas passes by the shell side of the reformer acting as an external heat source for the catalyst bed. Simultaneously, the reactants flow through the tubular packed-bed reactor with MSR reactions occurring on the commercial CuO/ZnO/Al2O3 based catalyst. As the reactants flow through the packed bed, complex physical and chemical phenomena at different scales occur in the reactor. Several assumptions are made to simplify the modeling of packed bed reactors. The one-dimensional pseudo-homogeneous model considers the reforming reactions and the axial transfer phenomena in the reactor. Since no mixing in the axial direction and complete mixing in the radial direction are assumed, this model is referred as an ideal plug-flow model. The effectiveness factor in this model is calculated as a function of the Thiele modulus. The pressure drop in the axial direction through the catalyst bed is also considered, though it generally does not significantly affect the overall reformer performance. Hence, based on the one-dimensional model, the effect of operating parameters such as the steam to carbon ratio (S/C), the contact time (Wcat/FCH3OH) and the inlet temperature of burner gas can be investigated. According to the simulation results of the one-dimensional model, the increase in the inlet temperature of burner gas and Wcat/FCH3OH is observed to improve the methanol conversion of the reformer. Simultaneously, the CO concentration in the reformate gas is also increased due to the enhanced temperature in the catalyst bed. Additionally, a higher S/C value leads to a lower methanol conversion due to the increased heat consumption for evaporating and heating the additional steam. This will also reduce the amount of CO in the MSR process. The one-dimensional pseudo-homogeneous model can be extended to a two-dimensional pseudo-homogeneous model by additionally considering the radial gradients of temperature and concentrations in the reactor tube. For a tubular reactor with rather non-uniformly distributed temperature and concentration in the radial direction, this two-dimensional model can make more accurate predictions of the reformer performance. Moreover, the two-dimensional model can be used to estimate the hot-spot temperature and the local catalyst deactivation when the reactor operates at relatively high temperature. Nevertheless, it requires slightly more computation time than the one-dimensional model. According to the simulated temperature distributions in the catalyst bed, the lowest temperature appears at the centre of the reactor tube, and the hot spot is generally formed at the location about 3 cm from the reactor entrance near the tube wall. The increase in the inlet temperature of the burner gas significantly enhances the hot spot temperature of the catalyst bed. In addition, the tube diameter is found to be the most important factor that affects the difference of the simulation results between the one-dimensional model and the two-dimensional model. Besides, this difference between these two models becomes less noticeable when the methanol conversion of the reformer is approaching 100%. Due to the porous structure of the catalyst, not all the catalytically active surface are exposed to the bulk conditions. Therefore, the reaction-diffusion process within a catalyst particle is modelled considering the interphase and intraparticle transfer resistances. Therefore, the effectiveness factor can be calculated by solving the intraparticle mass and energy balance equations. This method provides an insight into the interaction between the intrinsic kinetics and the heat and mass transport characteristics of the porous catalyst pellet. According to the simulation results in the particle scale, the interphase and intraparticle heat and mass transfer resistances are enhanced with the increasing bulk fluid temperature and the catalyst diameter. Therefore, at the inlet conditions of the reactor, it can be observed that the effectiveness factors for the MSR and MD reactions decrease with the increasing burner temperature and particle diameter. Another method used to estimate the effectiveness factor in this study is by regarding the effectiveness factor as a function of the Thiele modulus. This Thiele modulus-effectiveness factor method requires shorter computation time but is less accurate for the calculation of effectiveness factors.

ISSN (online): 2446-1636
ISBN (online): 978-87-7573-914-1

AALBORG UNIVERSITY PRESS